Free surface flows over submerged obstructions

A thesis submitted to the School of Computing Sciences of the University of East Anglia in partial fulfilment of the requirements for the degree of Doctor of Philosophy

By Charlotte Page

August 2015

Abstract

Steady and unsteady two-dimensional free surface flows subjected to one or multiple disturbances are considered. Flow configurations involving either a single fluid or two layers of fluid of different but constant densities, are examined. Both the effects of gravity and surface tension are included. Fully nonlinear boundary integral equation techniques based on Cauchy's integral formula are used to derive integro-differential equations to model the problem. The integro-differential equations are discretised and solved iteratively using Newton's method.

Both forced solitary waves and critical flow solutions, where the flow upstream is subcritical and downstream is supercritical, are obtained. The behaviour of the forced wave is determined by the Froude and Bond numbers and the orientation of the disturbance. When a second disturbance is placed upstream in the pure gravity critical case, trapped waves have been found between the disturbances. However, when surface tension is included, trapped waves are shown only to exist for very small values of the Bond number. Instead, it is shown that the disturbance must be placed downstream in the gravity-capillary case to see trapped waves. The stability of these critical hydraulic fall solutions is examined. It is shown that the hydraulic fall is stable, but the trapped wave solutions are only stable in the pure gravity case.

Critical, flexural-gravity flows, where a thin sheet of ice rests on top of the fluid are then considered. The flows in the flexural-gravity and gravity-capillary cases are shown to be similar. These similarities are investigated, and the physical significance of both configurations, examined.

When two fluids are considered, the situation is more complex. The rigid lid approximation is assumed, and four types of critical flow are investigated. Trapped wave solutions are found to exist in some cases, depending on the Froude number in the lower layer.

Acknowledgements

First and foremost I would like to express my profound gratitude to my supervisor, Dr Emilian Părău, who has supported and mentored me throughout my PhD studies. Your tremendous guidance and enthusiasm has been invaluable to me and has helped to make me a much more confident person.

I would like to express my appreciation and thanks to my former supervisor Dr Scott Grandison, not only for your academic support, but for keeping me sane and motivated during the difficult times in my first year. Special thanks go to Dr Stephen Laycock for taking over as my supervisor when Scott left, despite working on a different research area to mine.

My thanks extend to both my examiners; Dr Mark Cooker and Dr Matthew Turner. Your meticulous attention to detail has helped to ensure that this thesis is that much more reader friendly.

On a more personal note, I would like to express my sincere gratitude to my uncle, Keith Hood. Without your persuasion and encouragement to continue my research, I would be unlikely to have completed this PhD.

My thanks go to my parents, my brother and my sister for the tremendous support you have all provided me in my academic journey. I would also like to acknowledge my friends who have supported and helped me with the onerous task of proof reading this thesis.

Finally, but by no means least, my thanks go to my amazing partner Michael Anson. You are the person who has seen me at my most frustrated during this journey but you have always continued to believe in me and help me through the difficult times. Your love and support has changed me for the better throughout the past couple of years, and you will always have my gratitude.

Contents

List of tables

List of figures

CHAPTER ONE

INTRODUCTION

Fluid mechanics is a vastly researched branch of continuum mechanics. It concerns the study of continuous materials which flow in the presence of a deforming force. These materials do not support shear stresses and so, when at rest, are defined by the shape of their retaining container. The study of fluid mechanics is so extensive partially because of the substantial range of industrial fields it has applications to: from aerodynamics in economising wind farms, to the flow of oil through pipes in the ocean. Jets, waves and wakes are all of interest under this broad field.

It is well known that interest in fluid mechanics goes back a long way. Even before 200BC, the Greek mathematician Archimedes was laying the foundations of modern day hydrostatics. In 1687 Isaac Newton determined the three laws of motion for classical mechanics, which were then also applied to fluid mechanics. Following this pioneering work, Leonard Euler [47] discovered the famous Euler equations describing the conservation of mass and momentum in an inviscid fluid. Claude-Louis Navier [86] and George Stokes [112] then added the effects of viscosity to the Euler equations, introducing the Navier-Stokes equations. The well known Bernoulli equation relating the pressure in a fluid to its velocity, was discovered by Daniel Bernoulli [15]. It shows that the pressure of an inviscid fluid, or the potential energy in thr fluid, will increase when the speed of the fluid decreases. The work presented in this thesis relies on these pioneering discoveries.

1.1 Free surface flows

Free-boundary problems describe the range of problems in which an unknown function is sought in some unknown region Ω, with unknown boundary $\delta\Omega$. The boundary is 'free' and so must be sought as part of the solution. Free-boundaries are found in many everyday situations; waves on the beach at the seaside, oil spillages in the ocean, ice cubes

in a drink (or glaciers in the ocean), water in a bath, or simply on a flying kite. The free-boundary is the interface between the water and the air in the first and fourth examples, the two liquids of different densities in the second example, the melting surface of the ice-cube (or glacier) and the water-air interface in the third example, and the surface of the kite in the final example. All these scenarios therefore involve a free-boundary and so can be modelled as a free-boundary problem.

Free surface problems are a subset of the free-boundary problems. They consist of the problems in which the boundary describes the unknown surface or interface bounding a fluid. The surface can move with the fluid and so must be found as part of the solution. Examples include (i) the interface between two different liquids such as oil settled on top of water, (ii) the interface between a liquid and a gas (such as where the atmosphere meets the sea), and (iii) a change of state, for example melting ice.

Free surfaces are sometimes classified according to whether they have an intersection with a rigid surface or not. A ship moving through the ocean is the classical example of such an intersection. The free surface intersects the hull of the ship. Other examples include flow under a sluice gate and flow past a groyne at the seaside. Free surfaces which do not intersect a rigid surface include flows over submerged obstacles; where the obstacle is either on the bottom of the channel (for example, the flow over rocks on the seabed) or moving through the fluid (for example, a submarine), flows past a localised pressure distribution (for example, due to meteorological conditions), and pure solitary waves.

The study of free surface flows consequently has a wide range of practical applications, both in industrial and scientific settings, as well as in every-day situations. One tries to determine how the unknown free surface moves and changes position with time, subject to numerous boundary conditions.

1.2 Surface Tension

Surface tension is a force which is caused by the interaction of molecules on a free surface. A molecule in a fluid is attracted to neighbouring molecules of the same type by a cohesive force. However, for those molecules which are on the free surface, surrounding molecules of the same type do not exist on all sides. Therefore, a molecule on the free surface is attracted to its neighbouring molecules on the free surface much more strongly. This creates a ‘film’ on the free surface, and surface tension is then the force required to break the film. Surface tension is thus dependent on the molecules in the fluid, and so is dependent on the temperature (which affects the movement/energy of the molecules), as well as on the fluid itself. On a plane horizontal free surface, the surface tension will therefore act horizontally. However, when the free surface is curved, the curvature means

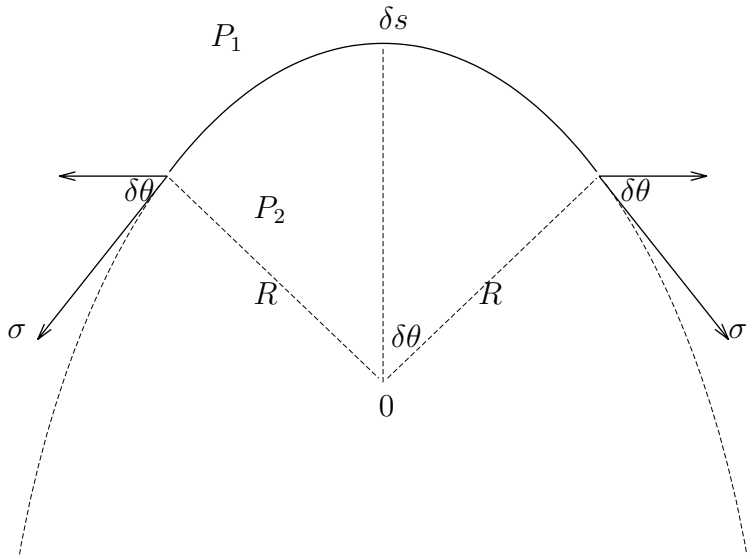

Figure 1.1: Small segment of the free surface of length δs. The magnitude of the surface tension is given by σ, acting in the directions indicated. The pressures in the two fluids separated by the free surface are denoted by P_1 and P_2.

that the surface tension acts tangentially to the free surface. See for example de Gennes, Brochard-Wyart and Quere [34]. In the diagram shown in figure 1.1, the angle between the direction of the surface tension σ and the horizontal, is denoted by $\delta\theta$.

The surface tension is commonly described in terms of the pressure jump across the free surface. Here we consider a two-dimensional small segment δs of a free surface separating two fluids. The pressure in one fluid is denoted by P_1 and the pressure in the other by P_2, as shown in figure 1.1. We therefore want to obtain a relationship between P_1 and P_2. This relationship is determined by the shape of the free surface, and so we take R to represent the principal radius of the curvature of the free surface. Next, we balance the forces across the segment of the free surface. We consider the triangle formed by the direction of the surface tension and the horizontal, shown in figure 1.2(a), to obtain the magnitude of the forcing action normal to the free surface. This gives $x = \sigma \sin(\delta\theta)$. Thus, in the normal direction we obtain

$$2\sigma \sin(\delta\theta) + P_1 \delta s = P_2 \delta s. \tag{1.2.1}$$

As we consider a small segment of the free surface, $\delta\theta$ is small, so $\sin(\delta\theta) \approx \delta\theta$. Thus, equation (1.2.1) becomes

$$2\sigma\delta\theta = (P_2 - P_1)\delta s. \tag{1.2.2}$$

Now we consider the triangle approximated by the principal radius R and half of the free

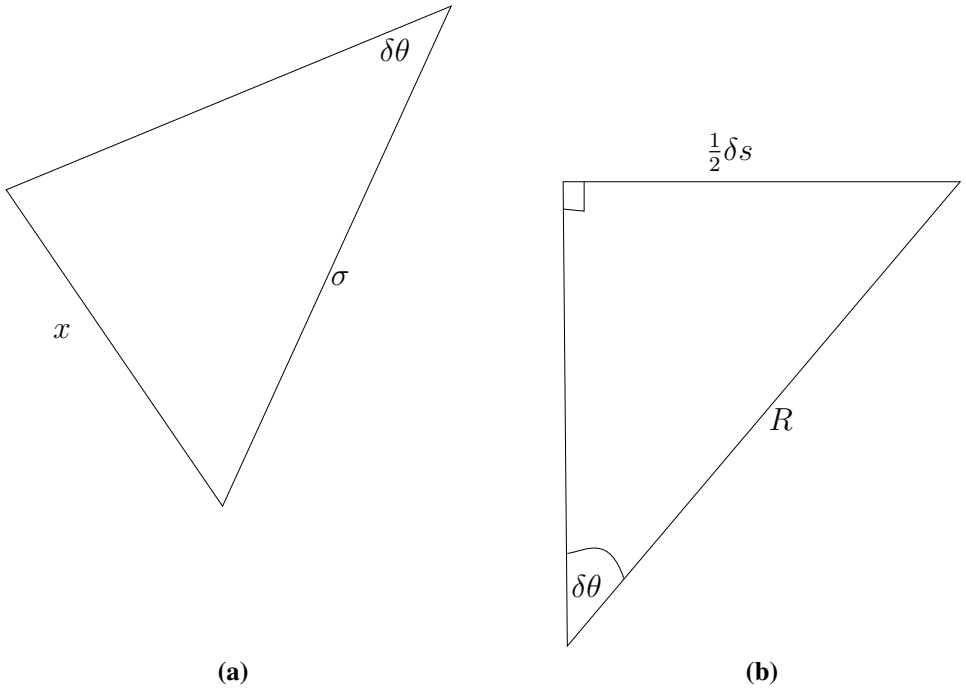

Figure 1.2: Enlarged triangular segments from the free surface segment δs, shown in figure 1.1

surface segment shown in figure 1.2(b). We see that, under the assumption that $\delta\theta$ is small,

$$\frac{1}{2}\delta s = R\sin(\delta\theta), \tag{1.2.3}$$

$$\Rightarrow \frac{1}{2}\delta s \approx R\delta\theta, \tag{1.2.4}$$

$$\Rightarrow \frac{\delta\theta}{\delta s} \approx \frac{1}{2R}. \tag{1.2.5}$$

Then, dividing (1.2.2) by δs and substituting into (1.2.5) we find that

$$\frac{\sigma}{R} = (P_2 - P_1). \tag{1.2.6}$$

Now we need to find R.

To proceed, we denote the free surface by $y = \eta(x)$ and consider the small segment δs in Cartesian coordinates. We then approximate δs with a straight line so that we can consider the triangle formed by δs, δx and δy, shown in figure 1.3. Thus,

$$(\delta x)^2 + (\delta y)^2 = (\delta s)^2, \tag{1.2.7}$$

$$\frac{\delta y}{\delta x} = \tan\alpha, \tag{1.2.8}$$

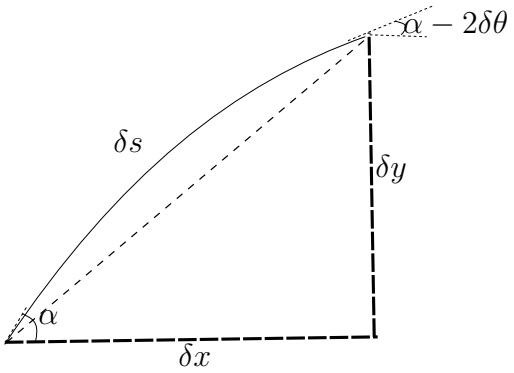

Figure 1.3: Free surface segment δs, shown on the Cartesian plane.

where we define α to be the angle between the tangent to the free surface and the horizontal δx. Dividing (1.2.7) by $(\delta x)^2$, taking the limit as $\delta x \to 0$, and then rearranging for ds/dx gives

$$\frac{ds}{dx} = \sqrt{1 + \left(\frac{d\eta}{dx}\right)^2} = \sqrt{1 + \tan^2\alpha} = \sec\alpha, \tag{1.2.9}$$

having used (1.2.8). Next, we differentiate (1.2.8) with respect to x to obtain

$$\frac{d^2\eta}{dx^2} = \sec^2\alpha \frac{d\alpha}{dx} = \left(1 + \left(\frac{d\eta}{dx}\right)^2\right)\frac{d\alpha}{dx}, \tag{1.2.10}$$

where we have used (1.2.9).

Using (1.2.9) and (1.2.10), we know that

$$\frac{d\alpha}{ds} = \frac{d\alpha}{dx}\frac{dx}{ds} = \frac{d^2\eta}{dx^2}\left(1 + \left(\frac{d\eta}{dx}\right)^2\right)^{-\frac{3}{2}}. \tag{1.2.11}$$

Now we examine $d\alpha/ds$. We consider the diagram shown in figure 1.3. The angle α decreases by $2\delta\theta$ over the small segment, so the change in α is given by

$$\delta\alpha = -2\delta\theta. \tag{1.2.12}$$

Dividing by δs, substituting in $\delta\theta/\delta s$ from (1.2.5), and taking the limit as $\delta s \to 0$ gives

$$\frac{d\alpha}{ds} = -\frac{1}{R}. \tag{1.2.13}$$

Thus, (1.2.11) becomes

$$\frac{-1}{R} = \frac{d^2\eta}{dx^2}\left(1 + \left(\frac{d\eta}{dx}\right)^2\right)^{-\frac{3}{2}}. \tag{1.2.14}$$

Finally, substituting (1.2.14) into (1.2.6) gives

$$P_2 - P_1 = -\sigma \frac{d^2\eta}{dx^2} \left(1 + \left(\frac{d\eta}{dx}\right)^2\right)^{-\frac{3}{2}}. \tag{1.2.15}$$

We can write this more succinctly in terms of the outward unit normal $\mathbf{n}$ to the free surface. If we define $f(x, y) = y - \eta(x)$ to describe the free surface, then, using subscripts to denote partial derivatives, we find that

$$\mathbf{n} = \frac{\nabla f}{|\nabla f|} = \frac{-\eta_x \mathbf{i} + \mathbf{j}}{(\eta_x^2 + 1)^{\frac{1}{2}}}, \tag{1.2.16}$$

and then,

$$\nabla \cdot \mathbf{n} = \frac{-\eta_{xx}}{(\eta_x^2 + 1)^{\frac{1}{2}}} + \frac{\eta_x^2 \eta_{xx}}{(\eta_x^2 + 1)^{\frac{3}{2}}}, \tag{1.2.17}$$

$$= \frac{-\eta_{xx}}{(\eta_x^2 + 1)^{\frac{3}{2}}}. \tag{1.2.18}$$

Equation (1.2.15) therefore becomes

$$P_2 - P_1 = \sigma \nabla \cdot \mathbf{n} = \sigma\kappa. \tag{1.2.19}$$

It is known as the Young-Laplace equation, and describes the pressure difference as some multiple of the surface tension coefficient σ. The multiple κ is known as the curvature term, describing the shape of the free surface $y = \eta(x)$. In two-dimensions it is given by

$$\kappa = -\frac{\eta_{xx}}{(1 + \eta_x^2)^{\frac{3}{2}}}, \tag{1.2.20}$$

see for example Vanden-Broeck [124].

1.3 Waves

A progressive wave is a disturbance or signal travelling in some medium, transferring energy from one point to another. The medium may undergo some oscillation as the wave passes, but the particles in the medium will return to their initial state in the linear case; they will not travel with the wave. There are numerous types and shapes of waves, which can be generated in many different ways. Waves are found in the scientific world and in everyday situations, and can also occur in nature. Examples include sinusoidal waves modelling simple harmonic motion (e.g. light, sound and water waves), stationary waves which stay in the same horizontal position over time, rogue (or freak) waves which

are found in the ocean and are significantly steeper than the other waves close-by, and tsunamis (or tidal waves) which have a significantly longer wavelength than normal ocean waves. In this thesis we are interested in water waves, which can be modelled using free surface fluid mechanics.

Through experimental work on the Union Canal near Edinburgh in 1834, John Scott Russell [103] accidentally discovered the solitary wave.

> "I was observing the motion of a boat which was rapidly drawn along a narrow channel by a pair of horses, when the boat suddenly stopped - not so the mass of water in the channel which it had put in motion; it accumulated round the prow of the vessel in a state of violent agitation, then suddenly leaving it behind, rolled forward with great velocity, assuming the form of a large solitary elevation, a rounded, smooth and well-defined heap of water, which continued its course along the channel apparently without change of form or diminution of speed. I followed it on horseback, and overtook it still rolling on at a rate of some eight or nine miles an hour, preserving its original figure some thirty feet long and a foot to a foot and a half in height. Its height gradually diminished, and after a chase of one or two miles I lost it in the windings of the channel. Such, in the month of August 1834, was my first chance interview with that singular and beautiful phenomenon which I have called the Wave of Translation."

The 'Wave of Translation' or solitary wave, is a stable wave which has an amplitude that decays to zero both far up and downstream of the wave peak. As Russell observed, solitary waves are waves of permanent form. They can travel great distances without changing speed or shape. Unlike other waves, due to the balancing of the nonlinear and dispersive effects on the wave, solitary waves are also able to pass through each other without merging or changing form. They are then known as solitons and possess the property that a small amplitude wave will be overtaken by a larger wave. Solitary waves and solitons can occur on the free surface of a canal or riverbed (as observed by John Scott Russell), or in the atmosphere (such as the Morning Glory wave cloud, observable in Northern Australia), or as internal waves under the sea.

Due to the complexity of the fully nonlinear wave problem, many studies use a range of simplifying assumptions. The classic assumptions of potential flow theory, assuming that the fluid is incompressible and inviscid, and the flow irrotational, provide a common simplification. The effects of gravity and/or surface tension may also be neglected, and waves are thus classifiable accordingly. Pure gravity waves are governed by the influences of gravity alone. The effects of surface tension are neglected, so that when a wave particle is displaced from its equilibrium, gravity alone acts as the restoring force, trying to return

the particle to equilibrium. Stokes [112, 113] found that such waves have slightly broader troughs than crests, with the sharpness of the crest increasing with the amplitude of the wave. Stokes further conjectured that as the velocity of the wave increases, the amplitude of the crest approaches a limiting configuration with an angle of 120°. This was proved almost a century later by Toland [117] and Amick, Fraenkel and Toland [3].

When gravity is neglected so that only the effects of surface tension on the free surface are considered, the resulting waves are typically of very small wavelength and are known as pure capillary waves. The ripples found when a rain droplet falls into a puddle are a classical example of such waves. Waves dominated by capillarity have broader crests than troughs, and thus, are easily distinguishable from pure gravity waves. In 1957, Crapper [33] found unique exact nonlinear solutions for pure capillary waves in water of infinite depth. He showed that for a given wavenumber k, as the steepness of the waves increases, a limiting configuration is approached, where the trough touches itself and a small trapped bubble is formed.

When both the effects of gravity and surface tension are considered, the waves are classified as gravity-capillary waves.

Another type of wave that will be considered in this research are flexural-gravity waves. Such waves can occur on the interface between a fluid and a (thin) layer of ice floating on top of the fluid. The ice plate is approximated as a thin elastic shell, and so the restoring forces in such circumstances are the gravitational acceleration and the flexural elasticity of the ice.

In the following chapters, the free surface fluid mechanics problem in which a fluid flows past some form of disturbance, is studied. Most of the work focuses on the gravity-capillary problem, but where appropriate, previously found pure gravity solutions are also discussed, alongside the presentation of some new results. The complexity of some of the problems is then increased by considering comparable solutions in the flexural-gravity problem of a fluid under a floating ice plate. Furthermore, a second disturbance is added to the flow configuration to allow for a much wider range of new solutions. The text is arranged as follows.

In chapter 2 a review of the extensive existing literature is presented. Both weakly nonlinear and fully nonlinear solutions are discussed.

Chapter 3 uses a fully nonlinear method to investigate subcritical gravity-capillary solitary wave solutions. Many of the results in this chapter have been published by the author and coworkers [91].

In chapter 4, critical flow (hydraulic fall) solutions are discussed in detail, using fully nonlinear methods, supported by the linear and weakly nonlinear theory. Several new results and ideas are presented, most of which have been published by the author and coworkers [88].

In chapter 5 the effect of a thin continuous ice sheet floating on top of the fluid is investigated. Critical flow flexural-gravity solutions are sought and comparisons are made with the gravity-capillary solutions found in chapter 4. The key findings presented in this chapter have been published by the author and Dr Părău [89].

A two-layer flow is studied in chapter 6, where the upper fluid is bounded above and the lower fluid is bounded below, by horizontal rigid walls. The chapter focuses on the critical flow case, with the solutions presented being much richer than those found in the single layer case discussed in chapter 4. There are several avenues of possible future work left open in this chapter.

The stability of forced solitary waves and the critical flow results presented in chapter 4 are investigated in chapter 7. The fully time dependent problem is therefore considered here, and the steady wave solutions are followed forward in time in order to deduce their stability. The main results in this chapter have been published by the author and Dr Părău [90].

Finally, in chapter 8 a conclusion is presented, drawing together all the new free surface flows results obtained in chapters 3-7 for flow past one or multiple disturbances in a channel of finite depth. A brief insight into possible avenues of future work stemming from this research is given.

CHAPTER TWO

LITERATURE REVIEW/BACKGROUND

A classical area of free surface fluid mechanics is the study of flows past disturbances in a channel of finite depth. There are many naturally occurring physical situations that such a problem can model, as the disturbance can take one of many different forms: a fully submerged obstacle on the channel bottom (for example the flow generated by a rock on the river bed), a submerged body not touching the bottom of the channel (for example a submarine under water), a surface piercing obstruction such as a ship sailing in the water, or even a localised applied pressure distribution on the free surface (for example an atmospheric disturbance caused by a storm or high winds). The free surface flows resulting from these disturbances are qualitatively similar, so just one form generally needs to be considered. The history of the work in this area is vast and so whilst a brief summary of some of the important results are given in this chapter, the interested reader may also be referred to the monographs of Baines [9] and Vanden-Broeck [124] for example.

Both weakly nonlinear model equations and fully nonlinear numerical schemes have been studied and extensively developed, in order to solve this type of problem.

2.1 The Korteweg-de Vries equation

The Korteweg-de Vries (KdV) equation,

$$\eta_t + c\eta_x + \frac{3}{2}\sqrt{\frac{g}{H}}\eta\eta_x + \frac{cH^2}{6}\left(1 - \frac{\tau}{3}\right)\eta_{xxx} = 0, \tag{2.1.1}$$

was derived by Diederik Korteweg and Gustav de Vries [74] in 1895 to model waves on the free surface of shallow water. Here $\eta(x,t)$ is the surface elevation, g is the acceleration due to gravity, H is the height of the channel downstream as $x \to -\infty$, $c = \sqrt{gH}$ is the wave speed, and τ is the dimensionless Bond number defining the ratio of surface tension

forces to gravitational forces. It is given by

$$\tau = \frac{\sigma}{\rho g H^2}, \tag{2.1.2}$$

where ρ is the fluid density and σ is the surface tension coefficient.

The KdV equation is a nonlinear partial differential equation which balances the effects of weak dispersion (from the η_{xxx} term) with those of weak nonlinearity (from the $\eta\eta_x$ term). If we choose a frame of reference moving with the wave (i.e. with speed c), then after some rescaling (see for example Whitham [128]), one can obtain the classical nondimensional KdV equation;

$$\eta_t + 6\eta\eta_x + \eta_{xxx} = 0. \tag{2.1.3}$$

This equation can be solved exactly to give a weakly nonlinear model for small amplitude waves on the free surface, valid in the long-wave regime. It admits both periodic cnoidal wave train solutions and solitary wave solutions of the form

$$u = A\,\mathrm{sech}^2\left(k(x - vt)\right), \tag{2.1.4}$$

where $k \propto A^{\frac{1}{2}}$. The form of the solitary wave was found independently in 1876 by Lord Rayleigh [101] and in 1871 by Boussinesq [21]. It has the property that the speed, v, of the wave is proportional to the wave amplitude, A. Thus, one can deduce that tall thin waves travel faster than broader shorter waves. Therefore, as solitary waves are capable of colliding and passing through each other without changing form, a large wave will inevitably overtake a small wave, without merging into it.

In 1967, Gardner, Greene, Kruskal and Miura [56] discovered that the KdV equation is integrable via the inverse scattering transform method, and so it became understood that the solitary wave is a key feature in describing long weakly nonlinear waves.

In 1984, Akylas [1] derived the forced KdV (fKdV) equation,

$$\eta_t + \lambda\eta_x - \frac{1}{6}\eta_{xxx} - \frac{3}{2}\eta\eta_x = \frac{1}{2}b_x, \tag{2.1.5}$$

to model the free surface of a flow subjected to a localised pressure distribution. Here, the effects of surface tension have been neglected, and the parameter λ is proportional to $F - 1$, where F is the dimensionless Froude number defining the ratio of flow speed to the linear shallow water wave speed $c = \sqrt{gH}$. It is given by

$$F = \frac{U}{\sqrt{gH}}, \tag{2.1.6}$$

where g is the acceleration due to gravity, U is the downstream velocity of the fluid, and

H is the constant downstream fluid depth.

The fKdV equation includes the balancing effects of weak nonlinearity and dispersion, as well as the effects of forcing (for example, by some underlying topography $b(x)$ or some applied pressure distribution $p(x)$). Further derivations of the fKdV equation have since been given for a more general underlying topographic forcing, for example, see Grimshaw and Smyth [65] and Shen [108]. In the absence of forcing, i.e. with $b(x) = 0$, the equation reduces to the classical KdV equation.

An extensive amount of research has been devoted to the stationary fKdV equation (sfKdV), given by

$$\lambda\eta_x - \frac{1}{6}\eta_{xxx} - \frac{3}{2}\eta\eta_x = \frac{1}{2}b_x, \tag{2.1.7}$$

where the free surface is independent of time.

The literature surrounding this rich topic is vast. Pratt [95] conducted experiments on the flow over two submerged obstacles. The height and lengths of the obstacles were chosen so that the flow would take the form of long waves, so he was able to interpret his results in terms of the weakly nonlinear KdV model equation. Shen, Shen and Sun [105] modelled the flow over a semi-circular obstruction using the sfKdV equation, and Shen [106] used the sfKdV equation to find a free surface flowing over a channel of arbitrary cross section, subjected to an externally applied pressure distribution.

The validity of the sfKdV equation, as a model for the free surface flow past a disturbance, has been studied by Shen [108]. He compared the results of the sfKdV model with those of computational and experimental work, and concluded that the sfKdV equation is an accurate model for the problem under certain assumptions; the amplitude of the forcing must be small (i.e. less than half of the depth of the fluid upstream), and the length of the forcing must be less than twice the amplitude of forcing. Furthermore, in order to simplify the problem, it has been shown that it is possible to approximate the forcing using a Dirac delta function. If the forcing is centred around $x = x_o$ then the forcing term $F(x)$ can be described by

$$F(x) \approx Q\delta(x_o), \tag{2.1.8}$$

where Q is a constant describing the area of the shape of the forcing.

Dias and Vanden-Broeck [38] used the sfKdV equation to determine the number of independent parameters required for a new form of free surface flow solution over a semi-circular obstruction: the generalised hydraulic fall, described later in section 2.3. They then confirmed their fully nonlinear results with those of the weakly nonlinear model. This solution is not physically relevant, as discussed in more detail in section 2.3, but they [41] later gave a physically relevant form of this new solution in a regime involving two obstructions on the bottom of the channel, and justified it using the sfKdV analysis.

Binder, Dias and Vanden-Broeck [18, 16, 17] contrasted the weakly nonlinear sfKdV

model with a fully numerical scheme in order to determine the free surface profile subjected to various forcings, including; two different sized submerged triangular obstructions, a semi-infinite step on the bottom of the channel, and a sluice gate.

Bernard, Grimshaw, Zhang and Chow [14] used the sfKdV equation to examine the case of a forcing with negative polarity; a hole. They investigated the effects of changing the width of the hole and obtained solutions with a wave train trapped solely in the region of the hole.

Chardard, Dias, Nguyen and Vanden-Broeck [27] and Donahue and Shen [45] studied the stability of solutions to the fKdV equation. Chardard *et al.* focused on the case of a free surface flow over two submerged obstructions, and found that solutions with two localised bumps over the obstacles are stable whilst table-top solutions are unstable. Furthermore, they viewed this table-top solution as the superposition of two conjugate flows and postulated that the trapped wave solutions obtained by Dias and Vanden-Broeck [41] are unstable. Donahue and Shen perturbed their initial solutions with white noise, and then evolved the free surface profile in time. They found that the white noise in the pure gravity hydraulic fall solution dissipates, and concluded that the free surface therefore appears to be stable.

2.2 Numerical Methods

The Korteweg-de Vries and Nonlinear Schrodinger (discussed in section 2.4) model equations only provide an approximation to the solution to the problem. Therefore, numerical methods have also been developed to provide solutions of the fully nonlinear equations. A boundary integral equation method is commonly used. The idea behind such a method is to calculate the unknowns at just the boundaries of the problem, in order to determine the behaviour of the fluid as a whole. This reduces the dimension of the problem by one, and so the two-dimensional problem becomes one-dimensional; it is only necessary to consider what happens at the free surface. Fewer calculations are therefore required to solve the problem. Using a conformal mapping, the problem is mapped into an inverse (hodograph) plane where the velocity potential and the stream function are independent variables. The free surface and channel bottom are then represented by constant streamlines, and so the geometry of the problem is greatly simplified. The evident advantage of this is that the previously unknown free surface is now a known streamline. Integro-differential equations can then be derived by applying Green's theorem or Cauchy's integral formula to a function in this new region. Mesh points are placed on the free surface, and a system of nonlinear equations is then obtained by discretising the integro-differential equations. The system of equations can then be solved iteratively to find the free surface profile, using Newton's method.

This numerical scheme is widely utilised. King and Bloor [73] used such a scheme to find the free surface of a flow over a semi-infinite step and Forbes and Schwartz [54] and Grandison and Vanden-Broeck [59] used it to find the free surface over a semi-circular obstruction. However, in order to remove the singularities on the bottom where the semi-circle meets the undisturbed channel bottom, they used the Joukowski transformation to first map the problem into a plane in which the semi-circular obstacle becomes part of a constant streamline. The scheme has been adapted to allow for arbitrarily shaped obstacles on the channel bottom, see for example Belward [11] and Dias and Vanden-Broeck [41].

Other numerical schemes such as those using a series truncation technique have also been utilised for this problem, for example, see Vanden-Broeck and Dias [37] who used a series truncation technique to study the free surface flow over a submerged triangular obstacle.

Both steady and unsteady free surface solution profiles which are subjected to some form of forcing, are known to exist. Grimshaw and Smyth [65] studied an unsteady stratified flow over some underlying topography, and obtained both supercritical and subcritical solutions (defined in section 2.3).

The content of this research is restricted to the steady case in chapters 3-6 however, and so unless otherwise stated, the free surface is taken to be dependent on position only. In chapter 7 the time evolution of some of the steady solutions presented in chapter 4 is examined, so here the free surface depends on position and time.

2.3 Pure gravity waves

We restrict the work in this thesis to the study of ideal fluids- incompressible, inviscid fluids with irrotational flow. In the case where there exists a single disturbance in the channel (here, without loss of generality, we assume that the disturbance takes the form of a submerged obstruction), when the effects of surface tension are neglected so that the waves on the free surface are pure gravity waves, four different types of basic solution are known to exist. The solutions depend on the Froude number F defined in equation (2.1.6). When $F > 1$ the flow is said to be supercritical, and when $F < 1$ it is said to be subcritical. It is also necessary to introduce the upstream Froude number F_{up};

$$F_{up} = \frac{V}{\sqrt{gh}}, \tag{2.3.1}$$

where V is the upstream velocity of the fluid, and h is the upstream fluid depth.

The first type of basic solution is sketched in figure 2.1(a) and is classified as having uniform supercritical flow both up and downstream ($F > 1$, $F_{\rm up} > 1$). A forced solitary

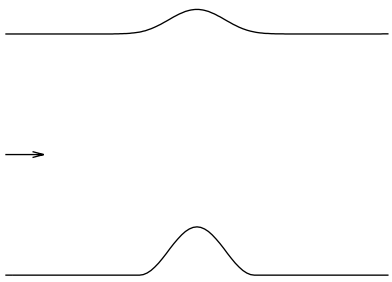

(a) Type 1 basic solution; $F > 1$. A forced solitary wave is found over the obstacle

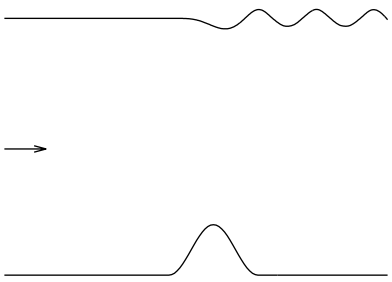

(b) Type 2 basic solution; $F < 1$. A train of gravity waves appears downstream of the obstacle

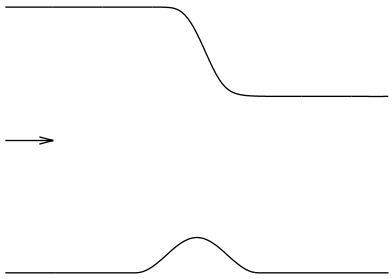

(c) Type 3 basic solution; $F_{up} < 1$ and $F > 1$. A hydraulic fall is found over the obstacle

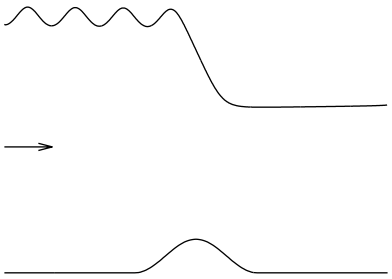

(d) Type 4 basic solution; $F_{up} < 1$ and $F > 1$. A generalised hydraulic fall is found over the obstacle.

Figure 2.1: The four types of basic pure gravity wave solutions for flow over an obstacle in a channel.

wave exists over the obstruction. If the obstacle has vertical symmetry about its centre, the free surface will then also be symmetrical about the obstacle.

The second type of basic classical flow, sketched in figure 2.1(b), is subcritical both up and downstream ($F < 1$, $F_{\rm up} < 1$). A train of waves is found downstream of the obstacle, whilst the flow upstream is uniform. In order for the flow to be physically realistic the radiation condition, which requires that there is no energy coming from infinity, must be satisfied. This means that any waves must appear behind the obstacle (downstream), so that the free surface remains flat upstream, as $x \to -\infty$. Or equivalently, the energy in the wave train must be travelling to the right if the waves appear downstream as $x \to \infty$, and to the left if the waves are upstream as $x \to -\infty$. More details regarding this concept can be found in chapter 4.

For both these first two types of classical solution the mean depth of the fluid in the linearised theory is uniform up and downstream. (Although, the nonlinearity of the waves in the second type of solution would actually cause a change in the mean depth of the flow.) Forbes and Schwartz [54] used a boundary integral technique to obtain both types of solution for flow over a semi-circular obstruction. Vanden-Broeck [122] then found

that flows of type one are not unique. There exist two solutions for particular values of the Froude number; a perturbation from a pure solitary wave, and a perturbation from the uniform stream.

The last two types of flow; the hydraulic fall and the generalised hydraulic fall, are critical. They are forced conjugate flows, which means that the depth of the fluid differs up and downstream. Sketches of their flow configurations are given in figures 2.1(c) and 2.1(d) respectively. The hydraulic fall has a subcritical uniform flow upstream. The Froude number gradually increases over the obstacle, resulting in supercritical uniform flow downstream. The change in the Froude number from subcritical to supercritical means that the depth of the fluid decreases over the obstacle. Forbes [51] computed a hydraulic fall over a semi-circular obstacle using boundary integral equation techniques, and Dias and Vanden-Broeck [37] used a series truncation method to obtain solutions over a triangular obstacle. It was shown that as the size of the obstacle increases, the downstream Froude number increases whilst the upstream Froude number tends to zero.

Generalised hydraulic falls were first computed numerically by Dias and Vanden-Broeck [38] in 2002. The generalised hydraulic fall is similar to the hydraulic fall but has the addition of a train of waves upstream of the disturbance, as $x \to -\infty$. However, as the the wave train, which is formed of pure gravity waves, occurs upstream of the obstruction, the radiation condition is violated. So, this fourth type of basic solution is unphysical when considered as the free surface flowing over a single obstruction. Hydraulic falls have only been observed with subcritical flow upstream, see for example Viollet *et al.* [127]. Therefore, it is not possible to simply change the direction of the flow, so that the wave train occurs in the subcritical regime downstream with the flow upstream being uniform and supercritical, in order to satisfy the radiation condition. In a regime in which just one locally applied forcing is present, the generalised hydraulic fall therefore has limited physical validity.

However, Dias and Vanden-Broeck [41] have shown that this flow can become physically relevant when it is considered as the localised flow over an obstacle, in a configuration which involves at least one other disturbance further upstream. They used an argument based on the weakly nonlinear theory to show that, in the limit, as the distance between the two obstacles approaches infinity, the flow local to the disturbance furthest downstream approaches a generalised hydraulic fall, whilst the flow local to the upstream disturbance approaches the second type of basic subcritical solution which has waves behind the obstacle. Thus, one can think of this free surface solution as a 'hybrid' flow. It is the superposition of the type two and type four basic flows. The 'hybrid' flow has a uniform flow upstream, and so satisfies the radiation condition; thus, it has more physical relevance than the type four basic flow. In fact, such flows over multiple submerged obstructions have been observed experimentally, for example see Pratt [95].

Pratt considered the flow regime over two submerged obstructions where the flow upstream of the first obstacle was subcritical and uniform, and the flow downstream of the second obstacle was supercritical and uniform. He observed different types of steady solutions including hydraulic falls and the solutions obtained by Dias and Vanden-Broeck [41], with a train of waves trapped solely between the two obstacles. By varying the height and position of the obstruction furthest upstream in this trapped wave configuration, he found that increasing the distance between the obstructions only changed the number of trapped waves, and not their actual form (i.e. the amplitude and length). Furthermore, varying the shape of the obstacles did not change the character of the flow. Only the amplitude and length of the resulting waves changed. Dias and Vanden-Broeck [41] similarly found that increasing the distance between the obstructions in their numerical analysis, only changed the number of trapped waves- the amplitude and wavelength of the waves remained the same.

Bernard *et al.* [14] used a stationary fKdV equation to contrast the flow over two submerged obstructions in the channel, with that of a single depression in the bed of 'sufficiently' large width. They obtained solutions with a train of trapped waves over the depression. In their stability analysis, Chardard *et al.* [27], whilst not actually computing trapped wave solutions, suggested that this type of solution is unstable.

In these multi-disturbance configurations, when the hydraulic fall occurs over the first obstruction, so that the flow local to the second obstruction is supercritical, there are no trapped waves between the obstacles. Instead, Belward [11] has shown that a solitary type wave, locally similar to the type one solution, appears downstream of the hydraulic fall over the second obstruction.

2.4 Gravity-capillary waves

In 1883, Rayleigh [102] studied the problem of a free surface flow past a disturbance in a channel. He considered the waves generated by a fishing line in water.

> "When a small obstacle, such as a fishing line, is moved forward slowly through still water, or (which of course comes to the same thing) is held stationary in moving water, the surface is covered with a beautiful wave-pattern, fixed relatively to the obstacle. On the up-stream side, the wave-length is short, and [...] the force governing the vibrations is principally cohesion. On the down-stream side the waves are longer, and are governed principally by gravity."

The effects of surface tension were thus included in his workings through the cohesive force. He describes the waves observed upstream of the disturbance as capillary waves

and those observed downstream, as gravity waves. He simplified this scenario to the application of a localised pressure on the free surface, and then, using a linearised theory, sought solutions with a train of waves both up and downstream of the forcing. He discovered some important results regarding the relationship between the Froude number and the surface tension; the linear dispersion relation determines the connection between the angular frequency and the wavenumber (or wavelength) of the waves, and thus describes the effects of dispersion on the waves. The dimensionless linear dispersion relation for gravity-capillary waves is now well known, and is given by

$$F^2 = \left(\frac{1}{k} + \tau k\right) \tanh(k), \tag{2.4.1}$$

where F is the Froude number, k is the wavenumber of the waves non-dimensionalised with respect to the fluid depth H, and τ is the Bond number defined in (2.1.2). Writing $\tanh(k)$ in terms of its Taylor series, (2.4.1) becomes

$$F^2 = \left(\frac{1}{k} + \tau k\right)\left(k - \frac{1}{3}k^3 + \mathcal{O}(k^4)\right) \tag{2.4.2}$$

$$= 1 + k^2\left(\tau - \frac{1}{3}\right) + \mathcal{O}(k^4) \tag{2.4.3}$$

At order one we see that $F^2 = 1$, giving the critical Froude number that solutions bifurcate from. At $\mathcal{O}(k^2)$ we have that $\tau - 1/3 = 0$. Therefore, the linear theory shows that there also exists a critical value of the Bond number, $\tau = 1/3$.

If $\tau < \frac{1}{3}$, Rayleigh showed that there exists a critical value of the Froude number, F_c, satisfying $dF_c/dk = 0$. At $F = F_c$ the dispersion curve possesses a minimum. If the flow is subcritical with $F > F_c$ (so that $1 < F < F_c$), there exist two trains of waves: a gravity wave train with wavenumber k_1, where $dF/dk_1 < 0$, and a capillary wave train with wavenumber k_2, satisfying $dF/dk_2 > 0$. An example linear dispersion relation for weak surface tension, $\tau < \frac{1}{3}$, is sketched in figure 2.2(a), where the wavenumbers k_1 and k_2 are indicated for a particular value of the Froude number. These solutions to the linearised theory are not unique as another wave train can simply be added to an existing solution. However, Rayleigh noted that a unique solution can be obtained by satisfying the radiation condition. This means that the gravity wave train must occur downstream of the disturbance with wavenumber k_1, whilst the capillary wave train can be found upstream with wavenumber k_2. The wavenumbers satisfy $k_1 < k_2$ and so the wavelength of the capillary waves is smaller than that of the gravity waves, as described in Rayleigh's observations of the fishing line problem.

If the Froude number is less than F_c, the linear theory does not predict a wave train. Instead, subcritical localised disturbances which decay in the far field both up and downstream are predicted e.g. solitary waves.

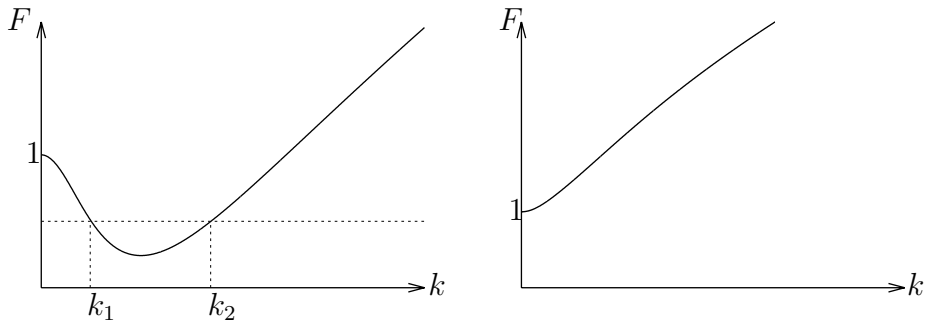

(a) $\tau < \frac{1}{3}$ **(b)** $\tau > \frac{1}{3}$

Figure 2.2: Gravity-capillary linear dispersion relations for strong and weak capillarity.

If $\tau > \frac{1}{3}$, the linear dispersion curve increases monotonically, as can be seen in the sketch in figure 2.2(b). The linear theory then predicts that solitary wave solutions exist for subcritical flows ($F < 1$).

However, the linear theory starts to fail when $F \to F_c$ or when $F \to 1$, and so a weakly nonlinear or fully nonlinear scheme is required. There are fewer studies of nonlinear gravity-capillary than pure gravity waves. This may be partly due to the difficulty in dealing with the potential resonant wave interactions caused when gravity and capillary wave trains of the same wavenumber and angular frequency interact.

In 1915, Wilton [129] conducted a pioneering study on nonlinear gravity-capillary waves and found that waves with particular critical wavelengths may possess small dimples in either the crests or the troughs of a downstream wave train. These waves differ from the linear solutions found by Rayleigh [102]. They have become known as Wilton ripples and are thought to be due resonant interactions. Vanden-Broeck [123] used a boundary-integral equation method to solve the fully nonlinear problem and investigate Wilton ripples in the presence of a localised pressure distribution, in water of infinite depth. He obtained Wilton ripples for particular values of the Bond number, and contrasted these results with the linear wave trains predicted by Rayleigh.

Forbes [49] calculated fully numerical gravity-capillary solutions for flow over a semi-circular obstacle. He classified his solutions into three different types. The first type consists of subcritical solutions with a train of waves both up and downstream, i.e. the solutions predicted by Rayleigh's linear theory with $F_c < F < 1$. However, due to having to truncate the flow domain both up and downstream at $x = -B$ and $x = A$ respectively (for positive constants A, B) in the numerical scheme, the mean-depth of the downstream waves decreases in his solutions as one travels further downstream. Grandison and Vanden-Broeck [59] addressed this problem, and were able to remove the inaccuracies in the solutions. They approximated the upstream wave train, for $-\infty < x < -B$,

by a linear train of waves and the downstream wave train, for $A < x < \infty$, by a periodic train of waves, obtained by repeating the waves for $0 < x < A$. The second type of Forbes' solutions are subcritical forced solitary depression waves, perturbed from the uniform stream. These correspond to the localised disturbances predicted by the linear theory for values of the Froude number satisfying $F < F_c$. Finally, the third type of solution is a supercritical ($F > 1$) forced elevation solitary wave. Forbes compared these solutions with the pure gravity supercritical solitary wave solutions. As $F > 1$, the linear dispersion relation predicts the presence of a capillary wave train upstream of the disturbance in the gravity-capillary case. However, the solutions obtained by Forbes showed no evidence of this.

The effects of surface tension can be included in the derivation of the stationary fKdV equation, to give a weakly nonlinear model for the gravity-capillary problem of a free surface flowing over a disturbance. It can be written in the form

$$(F-1)\eta_x - \frac{3}{2}\eta\eta_x + \frac{1}{2}(\tau - \frac{1}{3})\eta_{xxx} = \frac{1}{2}b_x(x). \tag{2.4.4}$$

Korteweg and de Vries [74] showed that the solitary waves admitted by the sKdV equation ((2.4.4) with $b(x) = 0$) are of elevation if $\tau < \frac{1}{3}$ and $F > 1$, and of depression if $\tau > \frac{1}{3}$ and $F < 1$. They are of the form

$$\eta = A\,\mathrm{sech}^2\left(\left(\frac{3A}{4h^2(1-3\tau)}\right)^{1/2} x\right), \tag{2.4.5}$$

where $A > 0$, and are thus unbounded as $\tau \to \frac{1}{3}$ and undefined at $\tau = \frac{1}{3}$. The KdV solitary wave solution is therefore invalid in the neighbourhood of $\tau = \frac{1}{3}$. This is because the dispersive effects (from the η_{xxx} term) in the KdV equation (2.4.4) disappear when $\tau = \frac{1}{3}$, and so the equation fails to maintain the balance between dispersion and nonlinearity. Hunter and Vanden-Broeck [70] addressed this problem in their research, and derived a new equation;

$$2(F-1)\eta_x - 3\eta\eta_x + (\tau - \frac{1}{3})\eta_{xxx} - \frac{1}{45}\eta_{xxxxx} = 0. \tag{2.4.6}$$

The equation is known as the fifth-order Korteweg-de Vries equation. It is valid near $\tau = \frac{1}{3}$, and includes a higher-order dispersive effect. The unsteady form of the equation was later derived by Hunter and Scheurle [69].

Hunter and Vanden-Broeck [70] also compared the solutions of the sKdV equation with those of a fully nonlinear scheme, and found that the sKdV equation is not valid in the region $0 < \tau < \frac{1}{3}$. The fully nonlinear solutions in this regime were found to have a train of periodic ripples in the far field both up and downstream. They are called

generalised solitary waves, and are thus distinguishable from solitary waves which are flat as $x \to \pm\infty$. The sfKdV equation does not describe these ripples, and therefore only provides an accurate model for the free surface flowing over a disturbance when $\tau = 0$ (as described in section 2.1), or when $\tau > \frac{1}{3}$.

Maleewong, Asavanant and Grimshaw [77] added a localised applied pressure distribution to the free surface and studied steady gravity-capillary solitary wave solutions to the sfKdV equation with $\tau > \frac{1}{3}$. They compared their results with both the linear solutions, and those of a fully nonlinear scheme. As previously discussed, if $\tau > \frac{1}{3}$, the flow must be subcritical ($F < 1$), in order to obtain solitary wave solutions. In this case, when the forcing is positive, Maleewong *et al.* showed that there exist three different cases. First, there are two families of solutions if the Froude number F lies between two critical values of the Froude number, F^* and F^{**}, which are dependent on the size of the forcing. Secondly, when $0 < F < F^*$ there exists a unique solution: a depression solitary wave bifurcating from the uniform stream. Finally, if $F^{**} < F < 1$, then there is no solution. In the critical region $F^* < F < F^{**}$, a depression wave bifurcating from the uniform stream is found, but as F increases towards the critical value F^{**}, which represents a turning point in the $F - y(0)$ plane (where $y(0)$ is the amplitude of the solitary wave), the solution changes from being a bifurcation from the uniform stream, to being a bifurcation from a pure solitary wave (a solitary wave sustained in the absence of forcing). The Froude number then begins to decrease, whilst the amplitude of the depression solitary wave continues to increase. Thus, there exist two possible depression solitary waves over the site of forcing, for the same value of the Froude number and the same Bond number.

When the forcing is of negative polarity, Maleewong *et al.* [77] showed that the bifurcation from the uniform stream is an elevation wave, and suggested that the solution is obtainable for the whole range $0 < F < 1$. Furthermore, they obtained a branch of forced depression solitary waves bifurcating from a pure depression solitary wave. At a critical value of the Froude number, $F^{***} < 1$, they showed that there exists a turning point in the $F - y(0)$ plane, after which, the forced depression solitary wave begins to develop a dimple in the trough. Thus, it is possible to obtain three different solutions with the same values of the Froude and Bond numbers and the same pressure forcing: an elevation wave bifurcating from the uniform stream, a forced depression solitary wave bifurcating from a pure solitary wave, and a forced depression solitary wave with a dimple in its trough, also bifurcating from the pure solitary wave.

Grimshaw, Maleewong and Asavanant [62] studied the stability of these solutions using both the fully nonlinear unsteady equations and the unsteady fKdV equation. They found that the positively forced depression wave bifurcating from the uniform stream is stable, but the second family of forced depression solitary wave solutions bifurcating from the solitary wave, are unstable. Similarly, the negatively forced elevation waves

bifurcating from the uniform stream were found to be stable, but the negatively forced depression waves bifurcating from the pure solitary wave, were unstable.

When the effects of surface tension are weak ($\tau < \frac{1}{3}$), the behaviour of the flow is more complex. Solutions take the form of envelope solitary waves, and the appropriate model for the weakly nonlinear analysis is no longer the KdV equation, as shown for example, by Hunter and Vanden-Broeck [70].

In 1968, Zakharov [132] showed that the nonlinear Schrödinger (NLS) equation,

$$iA_t + \gamma|A|^2A + \beta A_{xx} = 0, \tag{2.4.7}$$

can approximately model pure gravity two-dimensional waves in deep water. The equation describes wave packets on the free surface where a wave envelope encases damped decaying oscillating waves. Here, A is the envelope function describing the evolution of the wave packet with wavenumber k, and γ and β are defined parameters. Solitary wave solutions of the form

$$A = a\,\mathrm{sech}(\alpha(x - vt))e^{i(kx-\omega t)} \tag{2.4.8}$$

are admitted in the focusing case; $\gamma\beta > 0$. In 1972, Zakharov and Shabat [133] showed that the NLS equation is integrable via the inverse scattering transform method, and twelve years later Akylas [2] added the effects of forcing due to an applied pressure distribution to obtain the forced nonlinear Schrödinger (fNLS) equation. Kawahara [72] included the effects of surface tension in the NLS equation, and several authors, including for example Părău and Dias [96], Calvo and Akylas [23] and Maleewong, Grimshaw and Asavanant [78], combined the ideas of Kawahara and Akylas and considered the focusing fNLS equation. It can be written in the form

$$-iA_T + k_m\xi A + \lambda A_{XX} + \gamma|A|^2A = \frac{\omega_m p_m}{2g}\delta(X), \tag{2.4.9}$$

where the effects of surface tension have been included. Here, the forcing takes the form of the δ-function, where p_m is the Fourier transform of the pressure function at wavenumber k_m. Părău and Dias showed that the unsteady version of this equation can be used to model the problem of a free surface flow subjected to a localised pressure distribution, when the effects of surface tension are small and such that $\tau < \frac{1}{3}$. Calvo and Akylas [23] and Maleewong *et al.* [78] considered the unsteady case, and showed that there was generally good agreement between the fNLS model solutions and the fully nonlinear results.

In contrast to the strong surface tension case with $\tau > \frac{1}{3}$, Maleewong *et al.* [78] showed that in the weak surface tension case with $\tau < \frac{1}{3}$, both elevation and depression forced solitary waves exist for both positive and negative polarity pressure forcings. When the forcing is negatively orientated, critical Froude numbers F_2^* and F_2^{**} exist in

the same manner as for the strong surface tension solutions; so that there are no solutions for $F_2^{**} < F_2 < 1$, two families of depression wave solutions for $F_2^* < F_2 < F_2^{**}$, and a unique depression wave solution for $0 < F_2 < F_2^*$. However, the small amplitude waves here resemble wave packets so there exist small decaying oscillations in the tails of the forced depression envelope solitary waves. Forced elevation solitary waves also exist, and these waves bifurcate from a pure solitary wave.

When the forcing is negatively orientated, a forced depression (envelope) solitary wave bifurcates from the pure (envelope) depression solitary wave, as in the case with $\tau > \frac{1}{3}$. Again, elevation waves bifurcating from the uniform stream exist, but here, unlike in the stronger surface tension case where it was conjectured that solutions exist for the entire range $0 < F < 1$, there exists a turning point in the $F - y(0)$ plane. Therefore, a branch of forced elevation envelope solitary waves bifurcating from a pure solitary wave is also obtained in this weaker surface tension case. Therefore, whatever the orientation of the disturbance, in the weak surface tension case there exist two families of solutions for some critical region of the Froude number. When the Froude number is greater than this critical region, there are no solutions and when the Froude number is below the region, there is a single unique solution.

Maleewong *et al.* [78] also discovered new 'two-hump' solutions. These solutions have a two-peaked trough, and as the Froude number increases, the distance between the undisturbed stream and the peak in the trough increases. The weaker surface tension case is therefore richer than the stronger tension case, having more potential solutions.

Guayjarernpanishk and Asavanant [66] considered the problem of a free surface flow over an isosceles triangular obstacle, using both a fully numerical method based on Cauchy integral formula, and a weakly numerical analysis using the sfKdV equation. They obtained critical gravity-capillary hydraulic fall solutions, with subcritical flow upstream of the obstacle and supercritical flow downstream. They found that there exists a critical obstacle height, such that, for obstacles below this height, no hydraulic fall solution can be found. If the obstacle height is decreased towards the critical height, with the upstream surface tension held fixed, the free surface immediately before the hydraulic fall develops a slight elevation. Similarly, for an obstacle of fixed height, as the Bond number is decreased towards some critical value, the slight elevation immediately before the hydraulic fall increases. Furthermore, they showed that if the obstacle is of negative orientation, so that it is a dip in the channel, an elevation wave appears over the disturbance before the uniform depth of the flow decreases downstream.

The solutions can be summarised in the parameter space (F,τ) shown in figure 2.3 (see for example Dias and Iooss [36] and Trinh and Chapman [118]). The curve Γ represents the points at which the linear dispersion curve has a minimum, so that the two roots of the linear dispersion relation (2.4.1) merge into one double root. This means that, on

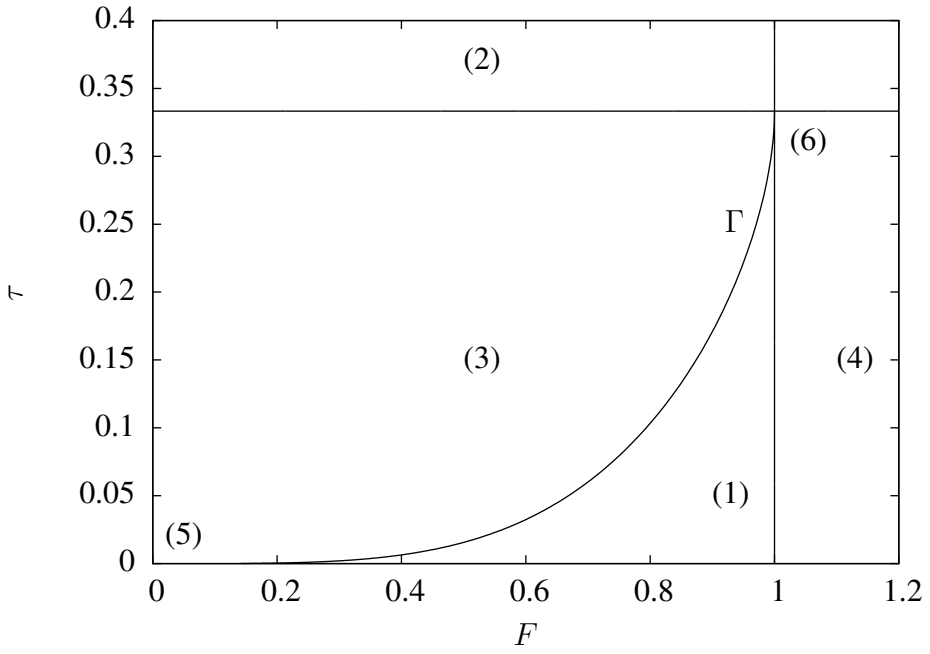

Figure 2.3: Parameter space (F,τ) showing the regions where different forced gravity-capillary solutions exist. The regions are separated by the vertical and horizontal lines $F = 1$, $\tau = \frac{1}{3}$ and the curve Γ of points on the minimum of the linear dispersion relation. Note that only the lines given by $F = 1$ and $\tau = \frac{1}{3}$ and the curve Γ are boundaries of classification. Furthermore note that region (4) extends beyond the $\tau = \frac{1}{3}$ boundary.

the curve, the phase velocity c must equal the group velocity c_g. We know that $\omega = ck$ and

$$c_g = \frac{d\omega}{dk} = \frac{d(ck)}{dk} = \frac{dc}{dk} + c. \tag{2.4.10}$$

So, $c = c_g$ requires that $dc/dk = 0$. Following Dias and Iooss [36], the linear dispersion relation can be written in the form

$$G(k) \equiv \left(\frac{1}{F^2} + Tk^2\right)\tanh(k) - k = 0, \tag{2.4.11}$$

where T is the Weber number defined by

$$T = \frac{\sigma}{\rho h c^2}. \tag{2.4.12}$$

Rearranging (2.4.11) for F^2 we obtain

$$\frac{1}{F^2} = k\frac{\cosh(k)}{\sinh(k)} - Tk^2. \tag{2.4.13}$$

We require $dG(k)/dk = 0$ in order to obtain the double roots of $G(k)$, corresponding to the minimum of the linear dispersion relation. Thus,

$$2Tk\frac{\sinh(k)}{\cosh(k)} + \left(\frac{1}{F^2} + Tk^2\right)\operatorname{sech}^2 k - 1 = 0. \tag{2.4.14}$$

Substituting (2.4.13) into (2.4.14) we obtain

$$2Tk\frac{\sinh(k)}{\cosh(k)} + \left(k\frac{\cosh(k)}{\sinh(k)} - Tk^2 + Tk^2\right)\operatorname{sech}^2 k - 1 = 0, \tag{2.4.15}$$

and so the Weber number T can be written in terms of k by

$$T = \frac{\cosh(k)\sinh(k) - k}{2k\sinh^2(k)}. \tag{2.4.16}$$

Substituting (2.4.16) into (2.4.13) we obtain F in terms of k:

$$F^2 = \frac{2\sinh^2(k)}{k\cosh(k)\sinh(k) + k^2}. \tag{2.4.17}$$

We plot the curve Γ in the $F - \tau$ plane, so we use the relationship

$$T = \frac{\sigma}{\rho h c^2} = \frac{\sigma}{\rho g h^2}\frac{gh}{c^2} = \frac{\tau}{F^2}, \tag{2.4.18}$$

between the Weber number and the Bond number, in order to write the Bond number in terms of k as

$$\tau = \frac{\cosh(k)\sinh(k) - k}{k^2\cosh(k)\sinh(k) + k^3}. \tag{2.4.19}$$

Equations (2.4.17) and (2.4.19) now describe the Γ curve parametrically. However, in the long ($k \to 0$) and short ($k \to \infty$) wave limits we approximate F and τ analytically. It is easier to do this by considering the long wave limit of $1/F^2$ and T. Using the Taylor expansions

$$\coth(k) = \frac{1}{k} + \frac{k}{3} - \frac{k^3}{45} + \frac{2k^5}{945} + ..., \tag{2.4.20}$$

$$\operatorname{cosech}^2(k) = \frac{1}{k} - \frac{k}{6} + \frac{7k^3}{360} - \frac{31k^5}{15120} + ..., \tag{2.4.21}$$

we see that in the long wave limit the inverse of (2.4.17) becomes

$$\frac{1}{F^2} = \frac{k}{2}\left(\frac{1}{k} + \frac{k}{3} - \frac{k^3}{45} + ...\right) + \frac{k^2}{2}\left(\frac{1}{k} - \frac{k}{6} + \frac{7k^3}{360} - \frac{31k^5}{15120} + ...\right)^2 \tag{2.4.22}$$

$$= 1 + \left(\frac{1}{6} - \frac{1}{6}\right)k^2 + \left(-\frac{1}{90} + \frac{1}{72} + \frac{7}{360}\right)k^4 + ... \tag{2.4.23}$$

$$= 1 + \frac{1}{45}k^4 + ... \tag{2.4.24}$$

and (2.4.16) becomes

$$T^2 = \frac{1}{2k}\left(\frac{1}{k} + \frac{k}{3} - \frac{k^3}{45}\right) - \frac{1}{2}\left(\frac{1}{k} - \frac{k}{6} + \frac{7k^3}{360}\right)^2 \tag{2.4.25}$$

$$= \frac{1}{3} - \frac{2k^2}{45} + ... \tag{2.4.26}$$

The long wave limits of F and τ are therefore $F \to 1$ and $\tau \to 1/3$ as $k \to 0$. In the short wave limit, $F^2 \to 2/k$ and $\tau \to (k-1)/(k^3+k^2) \to 1/k^2$ as $k \to \infty$. We now summarise the solutions in the (F, τ) parameter space.

- In region (1) the flow is subcritical ($F < 1$) and the surface tension is weak ($\tau < \frac{1}{3}$). The solutions are below the curve Γ, and take the form of the two wave trains (a train of capillary waves upstream of the disturbance, and a train of gravity waves downstream), observed by Rayleigh [102] and studied for example by Forbes [49] and Grandison and Vanden-Broeck [59]. Vanden-Broeck [123] has shown that solutions where the downstream gravity wave train takes the form of Wilton ripples, are also found in this region.

- In region (2) the flow is subcritical with strong surface tension ($\tau > \frac{1}{3}$). The solutions correspond to the solitary wave solutions with sech^2 type profiles, studied for example by Maleewong, Asavanant and Grimshaw [77]. As the Froude number is decreased towards $F = 0$, the trapped bubble limiting configuration, as first discovered by Crapper [33], is found.

- In region (3) the flow is subcritical and the surface tension is weak. The solutions are above the curve Γ and as the curve is approached, they correspond to the solutions which take the form of wave packets. Decaying oscillations therefore appear in the tails of the envelope solitary waves. Solutions in this regime were studied by Forbes [49] (away from the Γ-curve), and by Maleewong, Asavanant and Grimshaw [78].

- In region (4) the flow is supercritical ($F > 1$) with either $\tau < \frac{1}{3}$ or $\tau > \frac{1}{3}$. Forbes [49] found elevation solitary type wave solutions here, but remarked that the linearised theory predicts a train of capillary waves upstream, and indeed, as region

(6) is approached (where the flow is supercritical and surface tension is weak but in the neighbourhood of $\tau = \frac{1}{3}$), the unforced generalised solitary waves obtained by Hunter and Vanden-Broeck [70] using a fifth-order KdV equation are found.

- Finally, in region (5), Trinh and Chapman [118, 119] have recently conjectured the possibility of six different families of wavy solutions. The waves here are exponentially small and thus invisible to regular asymptotics. So, following the method used by Chapman and Vanden-Broeck ([25] in the capillary case and [26] in the pure gravity case), they used exponential asymptotics to justify these solutions. They found their six regions of different solutions by examining the Stokes lines associated with the singularities in the underlying geometry of the problem. These singularities cause a divergence in the asymptotic expansion, and thus Stokes' Phenomenon occurs whereby the asymptotic solution can cross one of the critical Stokes lines. This causes the switching on of a small exponential, resulting in gravity or capillary waves.

2.5 Flexural-gravity waves

In the colder regions of the world, such as the Arctic and Antarctic regions, the ocean, rivers and lakes are frozen over during the winter. This results in vast continuous ice plates that cover the water, the study of which is very important as the plates of ice make a platform for many human activities. For example, they are used as transportation links in the form of railway lines for trains in permanent areas of ice, as well as airline runways and roads. For communities relying on ferries across the water most of the year, without these alternative means of transportation in the remainder of the year, communications and the quality of life would be significantly affected. The safety of the ice crossing is therefore of concern. Crucially, the interaction of the deformable ice plate and the underlying water can lead to fatal results. In their book concerning moving loads on ice plates, Squire *et al.* [111] describe numerous ice crossings that have taken place throughout history. Methods to break the ice are also of concern, for example, in order to keep harbours clear, and to initiate the breakup of river ice. Air cushioned vehicles are often used to break the ice (see chapter 9 Ashton 1986 [7]).

The study of this hydroelastic problem has recently been receiving renewed interest. This is partially because the effects of global warming are having a significant effect on sea-ice conditions. In some regions warmer summers cause faster melting of the ice, and thus rougher sea conditions. In other areas ice is being found in increasingly wider regions. The desire for more renewable sources of energy also means that the practicalities of floating wind turbine farms in these colder regions is a current area of research (see Barker *et al.* 2005 [10], Gravesen *et al.* 2005 [60]). Similarly the feasibility

of oil rigs is of interest.

A moving load on an ice plate forces waves to propagate through the fluid. The ice plates have large area and are thin compared to the depth of the water below them, so the wavelength of the waves is much greater than the thickness of the plate. The flexural vibrations within the ice are therefore significant. The deformations in the ice are thus determined by the elasticity of the ice, rather than rigid body motions. The study of a floating ice plate is therefore a hydroelastic problem. It concerns the interaction between a deformable body and a moving fluid. The waves are known as flexural-gravity waves as the two restoring forces present are the flexural elasticity of the ice sheet, and gravitational acceleration acting on the fluid.

A number of experiments have been done concerning a moving load on an ice plate floating on top of a river or lake. Eyre [48] performed experiments in the freshwater lake Diefenbaker in Southern Saskatchewan in Canada. A variety of vehicles, moving at different speeds, were used as the moving load. The response of the ice plate was investigated, and ultimately, propositions were made regarding the safety of vehicles on ice. Eyre's experiments promoted further investigations and experiments into the effects of a moving load on an ice plate. For example, Takizawa [115, 116] used a snowmobile as the moving load in Lake Saroma in Hokkaid in Japan.

Modelling the ice is not easy. Linear theories, such as the Euler-Bernoulli model, have been used to study flexural-gravity waves when the amplitude of the water wave and the deformations in the ice are small (see Squire [111]). However, the linear theory fails when the load speed is near critical. Furthermore, the rougher sea conditions resulting from climate change (see Squire [110]) mean that nonlinear theories are becoming increasingly important.

Previously, many nonlinear studies used Kirchoff-Love plate theory to formulate the problem. For example, Forbes [50, 52] used the Kirchoff-Love model to study periodic waves. Părău and Dias [98] found flexural-gravity solitary waves with decaying oscillations in their tails, when the wave speed is near critical. They compared their results with those of a forced nonlinear Schrödinger equation. Vanden-Broeck and Părău [125] obtained generalised solitary waves, and Milewski et al. [82] obtained pure hydroelastic solitary waves in deep water. These solitary waves become generalised solitary waves if the speed of the forcing becomes greater than the minimum of the linear dispersion relation.

The nonlinearity in the Kirchoff-Love model is included in the elastic term, by defining the pressure of the ice at the free surface as

$$P = \mathcal{D}\frac{d^2\kappa}{dx^2}. \tag{2.5.1}$$

Here, κ is the curvature of the free surface, and D is the flexural rigidity of the ice. The

latter comes from thin plate theory (see Fung [55] pages 456-463) and is defined by

$$\mathcal{D} = \frac{Eh^3}{12(1-\nu^2)}, \tag{2.5.2}$$

where E is Young's modulus, ν is Poisson's ratio, and h is the thickness of the ice. The dynamic condition on the ice plate then becomes

$$\frac{1}{2}\rho(\phi_x^2 + \phi_y^2) + \rho g\eta + \mathcal{D}\partial_{xx}^2\left(\frac{\eta_{xx}}{(1+\eta_x^2)^{\frac{3}{2}}}\right) = 0 \tag{2.5.3}$$

where ρ is the density of the fluid, g is gravitational acceleration, $\eta(x)$ is the deformation of the ice sheet, and ϕ_x and ϕ_y are the horizontal and vertical components of the fluid velocity respectively.

However, the Kirchoff-Love model does not have a conservative form; elastic potential energy is not conserved. Plotnikov and Toland [93] have therefore recently considered the ice plate as a thin elastic shell. Using the special Cosserat theory of hyperelastic shells, satisfying Kirchoff's hypothesis, they were able to study the interactions between the ice plate and an infinite ocean. Guyenne and Părău [67] have used the Cosserat formulation to look for pure solitary wave solutions for near critical wave speeds (i.e. for speeds near the minimum of the phase velocity) in both infinite and finite depth. They compared their results with weakly nonlinear solutions of a forced Nonlinear Schrödinger equation.

As the special Cosserat theory is conservative, we use this model for the ice plate in the work presented in this thesis. This means that we describe the position of the elastic shell using Lagrangian coordinates, along with a single directional vector field on the surface, in order to satisfy Kirchoff's hypothesis. The directional vector field is taken to be the unit vector normal to the surface. This means that the thickness of the ice plate will remain constant. Furthermore, we assume that the plate does not shear.

The thin elastic shell supports the external load or disturbance, and deforms from its stable state due to stresses on the shell. If the bending and twisting moments of the shell are negligible, the membrane theory of shells can be applied. The theory neglects all moments. This state of stress is then known as the membrane state of stress. One way to justify this is to assume that the curvature and twisting at the centre of the free surface are small. It can therefore be assumed that the moments can be neglected, although a load could still be supported in bending.

A completely flexible shell cannot support stresses as a compressive force will cause a loss of stability of the equilibrium state. So, any load or disturbance in the shell must be sustained by tensions. Therefore, we can replace the stresses on the elastic plate with tensions. See Ventsel and Krauthammer [126] for more details.

We consider the deformed segment of length δs shown in figure 2.4. The deformation

is sustained by the tangential tensions $\tau(s)$ and the shear tensions $q(s)$ shown in the figure, along with the bending moments which we denote by $m(s)$. Here, s is the arclength along the shell segment, and p in the figure represents the forcing term on the shell. The force is due to gravity and the pressure jump across the shell.

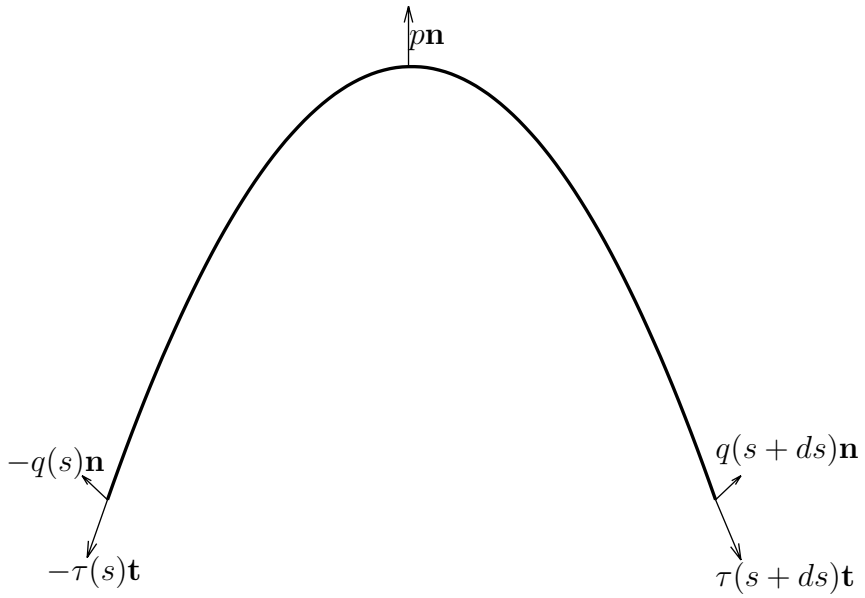

Figure 2.4: Elastic shell segment

The total tension exerted on the shell segment is then

$$\mathbf{T} = \tau(s)\mathbf{t} + q(s)\mathbf{n}, \tag{2.5.4}$$

where $\mathbf{t}$ is the tangential unit vector and $\mathbf{n}$ is the outward unit normal. Then balancing the forces across the segment gives

$$-q(s)\mathbf{n}(s)+q(s+\delta s)\mathbf{n}(s+\delta s)-\tau(s)\mathbf{t}(s)+\tau(s+\delta s)\mathbf{t}(s+\delta s)+p\delta s\mathbf{n}(s)=0. \tag{2.5.5}$$

Dividing by δs we can rewrite (2.5.5) as

$$\begin{aligned}&\frac{q(s+\delta s)\mathbf{n}(s+\delta s)-q(s)\mathbf{n}(s+\delta s)}{\delta s}+\frac{q(s)\mathbf{n}(s+\delta s)-q(s)\mathbf{n}(s)}{\delta s}\\&+\frac{\tau(s+\delta s)\mathbf{t}(s+\delta s)-\tau(s)\mathbf{t}(s+\delta s)}{\delta s}+\frac{\tau(s)\mathbf{t}(s+\delta s)-\tau(s)\mathbf{t}(s)}{\delta s}\\&+p\mathbf{n}(s)=0.\end{aligned} \tag{2.5.6}$$

Taking the limit as $\delta s \to 0$ this becomes

$$\frac{dq}{ds}\mathbf{n}(s) + q\frac{d\mathbf{n}}{ds} + \frac{d\tau}{ds}\mathbf{t} + \tau\frac{d\mathbf{t}}{ds} + p\mathbf{n} = 0. \tag{2.5.7}$$

Now we need to find $d\mathbf{t}/ds$ and $d\mathbf{n}/ds$. In Cartesian coordinates we define a point parametrically by $x(s)\mathbf{i} + y(s)\mathbf{j}$. The tangent to a small segment of the shell is then given by

$$\mathbf{t} = \frac{dx}{ds}\mathbf{i} + \frac{dy}{ds}\mathbf{j}, \tag{2.5.8}$$

and the normal component by

$$\mathbf{n} = -\frac{dy}{ds}\mathbf{i} + \frac{dx}{ds}\mathbf{j}. \tag{2.5.9}$$

Differentiating with respect to s gives

$$\frac{d\mathbf{t}}{ds} = \frac{d^2x}{ds^2}\mathbf{i} + \frac{d^2y}{ds^2}\mathbf{j}, \tag{2.5.10}$$

$$\frac{d\mathbf{n}}{ds} = -\frac{d^2y}{ds^2}\mathbf{i} + \frac{d^2x}{ds^2}\mathbf{j}. \tag{2.5.11}$$

We can now find $\mathbf{i}$ by multiplying (2.5.8) by dx/ds and (2.5.9) by $-dy/ds$. Adding the results gives

$$\begin{aligned}\frac{dx}{ds}\mathbf{t} - \frac{dy}{ds}\mathbf{n} &= \frac{dx}{ds}\left(\frac{dx}{ds}\mathbf{i} + \frac{dy}{ds}\mathbf{j}\right) - \frac{dy}{ds}\left(-\frac{dy}{ds}\mathbf{i} + \frac{dx}{ds}\mathbf{j}\right) \\ &= \left(\frac{dx}{ds}\right)^2\mathbf{i} + \frac{dx}{ds}\frac{dy}{ds}\mathbf{j} + \left(\frac{dy}{ds}\right)^2\mathbf{i} - \frac{dx}{ds}\frac{dy}{ds}\mathbf{j} \\ &= \mathbf{i}.\end{aligned} \tag{2.5.12}$$

Similarly, we obtain $\mathbf{j}$ by multiplying (2.5.8) by dy/ds and (2.5.9) by dx/ds, and adding the results. We find that

$$\mathbf{t}\frac{dy}{ds} + \mathbf{n}\frac{dx}{ds} = \mathbf{j}. \tag{2.5.13}$$

Now, substituting $\mathbf{i}$ and $\mathbf{j}$ from (2.5.12) and (2.5.13) into (2.5.10) and (2.5.11), we obtain

$$\frac{d\mathbf{t}}{ds} = \frac{d^2x}{ds^2}\left(\frac{dx}{ds}\mathbf{t} - \frac{dy}{ds}\mathbf{n}\right) + \frac{d^2y}{ds^2}\left(\frac{dy}{ds}\mathbf{t} + \frac{dx}{ds}\mathbf{n}\right), \tag{2.5.14}$$

$$\frac{d\mathbf{n}}{ds} = -\frac{d^2y}{ds^2}\left(\frac{dx}{ds}\mathbf{t} - \frac{dy}{ds}\mathbf{n}\right) + \frac{d^2x}{ds^2}\left(\frac{dy}{ds}\mathbf{t} + \frac{dx}{ds}\mathbf{n}\right). \tag{2.5.15}$$

Next, we rewrite these as

$$\frac{d\mathbf{t}}{ds} = \left(\frac{d^2x}{ds^2}\frac{dx}{ds} + \frac{d^2y}{ds^2}\frac{dy}{ds}\right)\mathbf{t} + \left(\frac{d^2y}{ds^2}\frac{dx}{ds} - \frac{d^2x}{ds^2}\frac{dy}{ds}\right)\mathbf{n}, \tag{2.5.16}$$

$$\frac{d\mathbf{n}}{ds} = \left(-\frac{d^2y}{ds^2}\frac{dx}{ds} + \frac{d^2x}{ds^2}\frac{dy}{ds}\right)\mathbf{t} + \left(\frac{d^2y}{ds^2}\frac{dy}{ds} + \frac{d^2x}{ds^2}\frac{dx}{ds}\right)\mathbf{n}. \tag{2.5.17}$$

We know that

$$\frac{d^2x}{ds^2}\frac{dx}{ds} + \frac{d^2y}{ds^2}\frac{dy}{ds} = 0 \tag{2.5.18}$$

because parameterising x and y with the arclength s means that the parametric equation

$$\left(\frac{dx}{ds}\right)^2 + \left(\frac{dy}{ds}\right)^2 = 1 \tag{2.5.19}$$

must be satisfied. Differentiating with respect to s then gives

$$2\left(\frac{d^2x}{ds^2}\frac{dx}{ds} + \frac{d^2y}{ds^2}\frac{dy}{ds}\right) = 0. \tag{2.5.20}$$

We also know that

$$\frac{d^2x}{ds^2}\frac{dy}{ds} - \frac{d^2y}{ds^2}\frac{dx}{ds} = \kappa. \tag{2.5.21}$$

because the curvature of the shell $\kappa = |d\mathbf{t}/ds|$ by definition. Therefore, (2.5.16) and (2.5.17) become

$$\frac{d\mathbf{t}}{ds} = -\kappa\mathbf{n}, \tag{2.5.22}$$

$$\frac{d\mathbf{n}}{ds} = \kappa\mathbf{t}. \tag{2.5.23}$$

Here, κ may also be defined by $\kappa = d\alpha/ds$, where α is the angle between the horizontal and the tangent to the shell segment. Substituting (2.5.23) and (2.5.22) into (2.5.7) gives

$$\frac{dq}{ds}\mathbf{n}(s) + q\kappa\mathbf{t}(s) + \frac{d\tau}{ds}\mathbf{t}(s) - \tau\kappa\mathbf{n}(s) + p\mathbf{n}(s) = 0. \tag{2.5.24}$$

The tangential and normal components are thus given by

$$\frac{d\tau}{ds} + q\kappa = 0, \tag{2.5.25}$$

$$\frac{dq}{ds} - \kappa\tau = -p, \tag{2.5.26}$$

respectively. Then rearranging (2.5.26) for τ and substituting this into (2.5.25) gives

$$\frac{d}{ds}\left[\frac{1}{\kappa}\left(\frac{dq}{ds} + p\right)\right] + \kappa q = 0. \tag{2.5.27}$$

Now we consider the shear stress moment on the small segment of the elastic shell. We balance the momentum over the small shell segment so that the rate of momentum entering and exiting the shell plus the total shear stress on the shell (given by $q\delta s$) is zero. Thus,

$$-m(s) - q(s)\delta s + m(s + \delta s) = 0. \tag{2.5.28}$$

Dividing by δs and taking the limit as $\delta s \to 0$ gives

$$q = \frac{dm}{ds}. \tag{2.5.29}$$

We introduce the linear constitutive equation

$$m = \mathcal{D}\kappa, \tag{2.5.30}$$

where $\mathcal{D}$ is defined by (2.5.2). A justification for using this equation is given in [94]. Eliminating m using (2.5.29) and (2.5.30) we obtain

$$q = \frac{d}{ds}(\mathcal{D}\kappa). \tag{2.5.31}$$

Then substituting into (2.5.27) and assuming that $\mathcal{D}$ is constant, gives

$$\frac{d}{ds}\left[\frac{1}{\kappa}\left(\frac{d^2\kappa}{ds^2} + \frac{p}{\mathcal{D}}\right)\right] + \kappa\frac{d\kappa}{ds} = 0 \tag{2.5.32}$$

$$\Rightarrow \frac{d}{ds}\left[\frac{1}{\kappa}\left(\frac{d^2\kappa}{ds^2} + \frac{p}{\mathcal{D}} + \frac{1}{2}\kappa^3\right)\right] = 0. \tag{2.5.33}$$

Finally, integrating with respect to s gives

$$\frac{1}{\kappa}\left(\frac{d^2\kappa}{ds^2} + \frac{p}{\mathcal{D}} + \frac{1}{2}\kappa^3\right) + C = 0 \tag{2.5.34}$$

$$\Rightarrow \qquad \kappa'' + \frac{p}{\mathcal{D}} + \frac{1}{2}\kappa^3 + C\kappa = 0 \tag{2.5.35}$$

$$\Rightarrow \qquad p = -\mathcal{D}(\kappa'' + \frac{1}{2}\kappa^3 + C\kappa), \tag{2.5.36}$$

where the prime denotes a derivative with respect to s, and C is the constant of integration. Blyth, Părău and Vanden-Broeck [20] explain that one can think of the constant of integration as a form of pre-stressing on the elastic shell, before any deformation. Therefore, if we assume that there is no tension in the ice plate, so that it is not pre-stressed, we can take $C = 0$.

In Cartesian coordinates

$$\frac{d\kappa}{ds} = \frac{d\kappa}{dx}\frac{dx}{ds}, \tag{2.5.37}$$

where dx/ds can be obtained by considering a small shell segment of length ds. Using Pythagoras' theorem we obtain $ds^2 = dx^2 + dy^2$, and thus

$$\frac{ds}{dx} = \sqrt{1 + \left(\frac{dy}{dx}\right)^2} \qquad \Rightarrow \qquad \frac{dx}{ds} = \frac{1}{\sqrt{1+\eta_x^2}}. \tag{2.5.38}$$

Then,

$$\frac{d\kappa}{ds} = \frac{d\kappa}{dx}\frac{dx}{ds} = \frac{d\kappa}{dx}\left(\frac{1}{\sqrt{1+\eta_x^2}}\right). \tag{2.5.39}$$

Differentiating again with respect to s gives

$$\frac{d^2\kappa}{ds^2} = \frac{d}{ds}\left(\frac{d\kappa}{dx}\frac{1}{\sqrt{1+\eta_x^2}}\right) = \frac{d}{dx}\left(\frac{d\kappa}{dx}\frac{1}{\sqrt{1+\eta_x^2}}\right)\frac{dx}{ds} \tag{2.5.40}$$

$$= \frac{1}{\sqrt{1+\eta_x^2}}\frac{d}{dx}\left(\frac{1}{\sqrt{1+\eta_x^2}}\frac{d}{dx}\left(\frac{\eta_{xx}}{(1+\eta_x^2)^{\frac{3}{2}}}\right)\right), \tag{2.5.41}$$

so (2.5.36) becomes

$$p = -\mathcal{D}\left(\frac{1}{\sqrt{1+\eta_x^2}}\frac{d}{dx}\left(\frac{1}{\sqrt{1+\eta_x^2}}\frac{d}{dx}\left(\frac{\eta_{xx}}{(1+\eta_x^2)^{\frac{3}{2}}}\right)\right) + \frac{1}{2}\left(\frac{\eta_{xx}}{(1+\eta_x^2)^{\frac{3}{2}}}\right)^3\right). \tag{2.5.42}$$

The dynamic condition on the ice plate then becomes

$$\frac{1}{2}\rho(\phi_x^2+\phi_y^2) + \rho g\eta + \mathcal{D}(\kappa_{ss} + \frac{1}{2}\kappa^3) = 0, \tag{2.5.43}$$

for example, see Plotnikov and Toland [93], and Blyth and Pozrikidis [19].

2.6 Two-layer flows

The study of free surface flows past disturbances in a two-layer channel configuration of finite depth is also of interest. In order to model flows over an obstacle (such as a mountain) in an atmospheric or oceanographic situation, a multi-layered flow configuration is required as the densities of the ocean and the atmosphere are each continuously stratified. The density distribution can be approximated by the simpler situation of two fluids of different but constant densities, flowing one on top of the other. The same simplifying assumptions as in the single layer model are made; the fluids in the two layers are assumed to be inviscid and incompressible, and the flows irrotational. The key differences between the fluids is in their densities and depths. When two fluids of different densities lie one on top of the other, an instability may occur on the interface. If the denser fluid lies on top of the less dense fluid (e.g. water on top of oil), the instability is known as the Rayleigh-Taylor instability. However, we assume that the density in the top-layer fluid is less than (or equal to) the density of the bottom-layer fluid. The potential instability in this case is the Kelvin-Helmholtz instability. It is more well-known than the Rayleigh-Taylor instability as it can be seen in clouds and the ocean. Vincent van Gogh even captured the instability in his painting 'La Nuit Étoilée'. The instability occurs when there exists a

velocity shear between the two fluids of different densities. This leads to vorticity at the interface and thus results in a transition to turbulent flow, with a rolling up of the interface and a mixing of the fluids.

Both the upper surface and the interface between the two-fluids are 'free surfaces' and must be found as part of the solution. Therefore, as one might expect, the two-layer flow configuration allows for a much wider variety of flows than the single-layer case. Therefore, there is extra complexity in this problem due to the fact there are now two modes: an external (fast) mode and an internal (slow) mode. Furthermore, there is also additional complexity due to the existence of a critical thickness ratio:

$$D = \sqrt{R}, \tag{2.6.1}$$

where D is the depth ratio given by $D = h_2/h_1$ and R is the density ratio given by $R = \rho_2/\rho_1$. Here, h_i and ρ_i for $i = 1, 2$, are the depths and densities of the lower and upper fluids, respectively.

The importance of understanding two-layer fluid flows is also demonstrated by the dead-water phenomenon. The phenomenon was observed in 1893 by Norwegian explorer Fridtjof Nansen [85] who was on an expedition to the North Pole in his ship '*Fram*';

> " When caught in dead water, *Fram* appeared to be held back, as if by some mysterious force [...] *Fram* was capable of 6 to 7 knots. When in dead water she was unable to make 1.5 knots. We made loops in our course, turned sometimes right around, tried all sorts of antics to get clear of it, but to very little purpose. "

The phenomenon occurs when a layer of fresh water lies on-top of a layer of (much denser) salt water. The propeller, or some other form of underwater thrust used to move a ship forward, may start to generate internal waves (or turbulence) on the interface between the two fluids of different densities, instead of using the energy created to move forward. The upper surface does not change form, and so a ship travelling in such water meets some resistance and slows down, for no apparent reason. This can be a big problem for ships and occurs for example, near melting glaciers. Ekman [46] reported Nansen's observations in 1904, and conducted further experiments in order to try and explain the phenomenon. Mercier, Vasseur and Dauxois [79] have also recently reproduced and generalised (including considering the case of a three-layer fluid) these effects in laboratory studies. Woolfenden and Părău [130] noted that the effects of both interfacial and surface tensions play a major role in the experiments by Mercier *et al.* [79] due to the shallow depths they used. This therefore helps to demonstrate the importance of understanding the influence of both surface and interfacial tensions, in two-layer flow configurations.

2.6.1 Rigid-lid approximation

The problem of interfacial waves in a two-fluid regime, where the upper and lower fluids are bounded above and below by a rigid surface respectively, has received extensive study. This case is known as the rigid-lid approximation, and as there is just a single free surface here, the complexities in dealing with the nonlinear effects of an upper free surface on the interfacial waves are absent.

Baines [8] conducted experiments where an obstacle was towed along the upper free surface of a two-layer fluid configuration consisting of a thin layer of kerosene on top of a layer of water. The towing speed and fluid depths were chosen in order to model the rigid-lid approximation, and then particular attention paid to the interfacial free surface (the internal mode). Baines found that when the upper-layer is thin (so that $D << 1$), the interfacial flow is very similar to the free surface flow in the single-layer configuration. However, when the fluids are of more comparable depths ($D \approx \frac{1}{2}$), different behaviour is seen. Both supercritical and subcritical interfacial solitary waves were observed, and in addition, hydraulic falls, bores (moving hydraulic falls), and rarefactions were found.

In the absence of any forcing, interfacial solitary waves have been studied, for example, by Amick and Turner [4, 5] and Laget and Dias [75]. In the rigid-lid approximation, gravity solitary wave solutions bifurcate from a uniform stream at the critical Froude number

$$F_{bif} = \sqrt{\frac{D(1-R)}{D+R}}. \tag{2.6.2}$$

In this two-layer configuration, a flow is said to be subcritical if $F < F_{bif}$ and supercritical if $F > F_{bif}$. The nature of the solitary waves depends on the critical depth ratio (2.6.1). If $D > \sqrt{R}$, the solitary waves are pure elevation solitary waves, and if $D < \sqrt{R}$, they are pure depression solitary waves. The solution branches of these solitary waves have been followed in order to find their limiting configurations. Both infinite broadening of the solitary waves (e.g. see Turner and Vanden-Broeck [120]), and overhanging waves (e.g. see Grimshaw and Pullin [64]) have been seen. (Overhanging waves can be identified as waves with a mushroom-shaped structure.)

Sha and Vanden-Broeck [104] included the effects of forcing and used an integro-differential equation formulation to study symmetric interfacial gravity solitary waves over a semi-circular obstruction on the bottom of the channel. The rigid-lid approximation was assumed, and waves perturbating from both the uniform stream, and the branches of the pure solitary waves were obtained. Both the infinite broadening and the overhanging limiting configurations were found here, but in the case of the broadening of the forced solitary waves, a small bump was found to exist at the centre of the broad wave. This bump was shown to be a perturbation from the uniform stream if it occurred on the forced elevation solitary wave. If it was on the forced depression solitary wave, it could

either be a small bump perturbing a uniform stream, or a much larger bump perturbing a pure solitary wave.

Belward and Forbes [12] used a two-layer flow theory to model the atmospheric situation associated with a thunderstorm, where cool dense air is expelled under warmer less dense air. In most studies previously considered, the exact geometry of the topography was used to simplify the problem. However, Belward and Forbes developed a boundary integral formulation in which the channel bottom can be an arbitrary function of position. They used this fully numerical method to model lee waves (atmospheric standing waves) over a mountain range. They obtained solutions with a waveless uniform region upstream of the mountain, and periodic waves downstream. Belward and Forbes [13] later modified this numerical method to look for critical interfacial flow solutions, where the mean depth of the interface decreases over the mountain, i.e. hydraulic fall solutions.

The effects of interfacial tension in the rigid-lid case in the absence of any forcing has been studied, for example, by Laget and Dias [75]. Pure solitary waves bifurcating from the uniform stream at critical Froude number F_{bif}, given by (2.6.2), can be found, as in the pure gravity case. However, if the Bond number is less than some critical value, these solitary waves become generalised solitary waves and possess ripples in their tails. As in the pure gravity case, the orientation of these solitary waves depends on the critical depth ratio. The orientation of the gravity-capillary interfacial solitary waves is the exact opposite to that of the pure gravity waves: if $D > \sqrt{R}$, the waves are pure depression solitary waves, and if $D < \sqrt{R}$, they are pure elevation solitary waves.

When the depth ratio is near critical, (i.e. $D^2 \approx R$), small amplitude fronts have been found to exist (e.g. see Amick and Turner [5]). A front describes the unforced hydraulic fall, i.e. it is a conjugate flow which connects two uniform flows of different heights.

The sfKdV equation has been used to model waves on the interface of a two-layer fluid. However, when the ratio of layer depths is near critical, the coefficient of the nonlinear term in the sfKdV equation vanishes, so that the effects of nonlinearity vanish and the sfKdV ceases to provide an accurate model for the flow. Instead, by changing the order of the scaling in the long-wave analysis, a stationary forced modified KdV (sfmKdV) equation is derived. The sfmKdV equation includes an additional cubic term, $\eta^2\eta_x$, and has been derived, for example, by Choi, Sun and Shen [29] using a unified asymptotic method. It can be written in the form

$$A_1\eta_x + A_2\eta^2\eta_x + A_3\eta_{xxx} = b_x(x), \tag{2.6.3}$$

where A_i, $_{i=1,2,3}$ are constant coefficients. Choi *et al.* studied solutions to the sfmKdV equation for a two-layer flow in the rigid-lid approximation. An obstruction was placed on each horizontal rigid boundary, and gravity-capillary solutions were obtained for two different regimes; $\tau > \tau_c$ and $\tau < \tau_c$, where τ_c is the critical value of the Bond number at

which the coefficient of the dispersive term in the sfmKdV equation vanishes:

$$\tau_c = \frac{1 - RD}{3}. \tag{2.6.4}$$

For strong tension, $\tau > \tau_c$, Choi *et al.* found three different types of solutions: (i) four symmetric solitary wave solutions, of which three are single peaked waves, and one is two-crested, (ii) a non-symmetric solution consisting of part of a solitary wave behind the obstacle, with a periodic wave train ahead of the obstacle, (iii) a uniform stream upstream of the obstacle, with a periodic wave train downstream. For weaker surface tension, $\tau < \tau_c$, hydraulic fall solutions and multi-crest solutions were obtained for particular values of the Froude number in the subcritical regime.

Dias and Vanden-Broeck [39] also used a weakly nonlinear analysis for the rigid-lid approximation problem in the Boussinesq limit (where the two fluids have almost identical density) with $R \approx 1$. They used the sfKdV equation in the absence of interfacial tension in the form

$$\frac{1}{6}\eta_{xxx} \pm \frac{3}{2}\eta\eta_x - \mu\eta_x = -\frac{1}{2}b_x, \tag{2.6.5}$$

where $\mu = F - F_{bif}$ (F_{bif} is the critical value of the Froude number, from which the solitary waves bifurcate, defined by (2.6.2)). The plus sign is chosen in the case of a 'thick upper layer' ($D > \sqrt{R}$), and the minus sign for the 'thick bottom layer' ($D < \sqrt{R}$). They examined the noncritical case, i.e. where the ratio of layer depths is far from critical, and considered four different cases: subcritical flows with a thick upper layer, subcritical flows with a thick bottom layer, supercritical flows with a thick upper layer, and supercritical flows with a thick bottom layer. Using a phase-plane analysis they showed that the thick upper layer cases are just an extension of the single-layer flows. Hydraulic falls which are subcritical upstream and supercritical downstream are found, as well as the two classical forced supercritical solitary wave solutions and the subcritical solutions with a wave train downstream of the obstacle. In addition, generalised hydraulic falls with supercritical flow upstream and subcritical flow downstream were obtained.

In the case of the thick bottom layer, solutions in the absence of forcing have been shown to be qualitatively similar to those for the case of a thick upper layer, and thus, the single-layer flow configuration. However, when forcing is introduced to the problem, this is not so. The depth of the lower fluid in the subcritical hydraulic fall solution decreases directly over the obstacle as predicted by the single-fluid configuration, but it then increases to a larger depth downstream. The main difference for this case however, is with the supercritical forced solitary wave solutions. Three symmetric solitary wave solutions exist here; two of which are depression waves (as obtained by Sha and Vanden-Broeck [104]), and the third is an elevation wave. The elevation wave can be found at values of the Froude number for which no solution existed in the thick upper layer case; it exists

for all $F > F_{bif}$. The generalised hydraulic fall solution found in the thick upper layer case also exists here, but now the depth of the lower fluid decreases downstream of the obstacle. Dias and Vanden-Broeck confirmed their solutions with the results obtained when solving the full nonlinear equations.

Dias and Vanden-Broeck [42] then extended their phase plane analysis to study the critical case where $D \approx \sqrt{R}$, using a stationary forced extended KdV (sfeKdV) equation of the form

$$\frac{1}{6}\eta_{xxx} + \frac{3}{2}A\eta\eta_x - \frac{3}{4}\eta^2\eta_x - \mu\eta_x = -b_x, \tag{2.6.6}$$

where $\mu = F - F_{bif}$ and A is a constant measuring the distance from the critical thickness. This differs from the sfmKdV equation obtained by Choi *et al.* [29] due to the inclusion of the nonlinear $\eta\eta_x$ term. This enables solutions close to the critical thickness to be examined. The constant A vanishes at the point $D = \sqrt{R}$. In this work, Dias and Vanden-Broeck found a third critical value of the Froude number, F_{max}, representing the maximum Froude number for hydraulic falls. They used this Froude number alongside the critical values F_{bif} (defined in (2.6.2)) and F_{front} (defined below in (2.6.7)), to provide a full picture of pure gravity hydraulic falls in the two-layer rigid-lid approximation.

The branches of subcritical hydraulic falls obtained in the 'far from critical' case extend into the critical case. However, in the 'near critical' and thick bottom layer case, a new subcritical hydraulic fall is found due to the cubic nonlinearity in the sfeKdV equation. The 'near critical' thick upper layer supercritical case is also more complex. The hydraulic fall solution branch in the 'far from critical' case stops at the new critical value of the Froude number F_{max}. New types of hydraulic fall, requiring four independent parameters to characterise them (rather than the usual three), are also found in the range $F_{front} < F < F_{max}$. Vanden-Broeck and Dias showed that there can be as many as three different falls for the same values of these four parameters. Similarly, in the 'near critical' thick bottom layer supercritical case, the hydraulic fall solution branch in the 'far from critical' case stops at the critical value of the Froude number F_{front}. New hydraulic fall solutions in the region $F_{bif} < F < F_{front}$ again requiring four independent parameters to characterise them, may be found.

The critical Froude number F_{front} is the value of the Froude number at which a front exists. It is given by

$$F_{front} = \sqrt{\frac{(1+D)(1-\sqrt{R})}{1+\sqrt{R}}}, \tag{2.6.7}$$

see for example Laget and Dias [75] and Dias and Vanden-Broeck [40]. The front conserves the mass, the total momentum and the total energy in both fluid layers. When $D = \sqrt{R}$ we see that $F_{bif} = F_{front}$, so no front exists. Much of the evidence for fronts has already been discussed because the broad solitary wave, introduced with respect to the limiting configuration of pure solitary waves, can be viewed as a superposition of

two fronts. In a similar manner to the pure solitary waves, the orientation of a front is therefore also determined by the critical thickness ratio i.e. if $D < \sqrt{R}$, the front is a 'depression', and if $D > \sqrt{R}$, it is an 'elevation'. Dias and Vanden-Broeck [40] have shown that depression fronts exist for all $0 < D < \sqrt{R}$. They obtained a limiting configuration wherein the interfacial surface touches the fixed horizontal rigid-lid. Elevation fronts on the other hand exist only in the range $\sqrt{R} < D < D_{max}$, and overhanging develops as one approaches the limiting configuration.

The linear dispersion relation for gravity-capillary interfacial waves, in the rigid lid approximation with finite depth, can be written in the form

$$F^2(k) = \frac{(1 - R + \tau_I k^2)\tanh\left(\frac{k}{D}\right)\tanh\left(k\right)}{k(R\tanh\left(\frac{k}{D}\right) + \tanh\left(k\right))}, \tag{2.6.8}$$

where τ_I is the interfacial Bond number (see for example Laget and Dias [75] and Părău and Woolfenden [100]).

2.6.2 Free surface boundary conditions

When the upper fluid is not bounded above, so instead it is governed by a free surface, the situation is far more complex. The presence of two modes (a fast 'external' mode and a slow 'internal' mode, both of which are governed by two distinct linear dispersion relations), and the potential nonlinear interactions between them, make the problem much more difficult than its rigid-lid approximation counterpart. Peters and Stoker [92] and Kakutani and Yamasaki [71] modelled pure gravity solitary waves on both the free surface and the interface, using coupled KdV equations. They showed that whilst the fast mode can always be modelled with the KdV equation itself, the slow mode needs cubic nonlinearity when the depth of the fluids are such that one is near the critical depth ratio. Modified and extended KdV equations are therefore required. Peters and Stoker, and Kakutani and Yamasaki showed that the free surface and interfacial waves are in-phase in the case of the fast mode, and 180° out-of-phase for the slow mode. Moni and King [84] used a fully nonlinear technique, involving a generalised Schwartz-Christoffel transformation, to provide fully nonlinear external pure gravity solitary wave solutions in this two-layer flow configuration.

In the single layer configuration, generalised solitary waves are only obtainable using the fifth order KdV equation (2.4.6) in the neighbourhood of $\tau = \frac{1}{3}$; so only in the gravity-capillary configuration. In contrast, in the two-layer configuration, generalised solitary waves can also be obtained in the pure gravity case. They can be caused by the resonant interactions between the two modes of the dispersion curve. Michallet and Dias [80], and Părău and Dias [97] studied the resonant interactions between the two modes in order to calculate periodic interfacial waves of permanent form. The resonance can be explained

in terms of the linear dispersion relation. When a periodic wave with wavenumber $k \neq 0$, has the same linear phase velocity $c(k)$ as the long-wave with wavenumber $k = 0$, a resonance occurs between the periodic wave train and the solitary long-wave. Therefore, when a long internal mode interacts with a short external mode, solitary waves (long waves) which have periodic ripples (short waves) in their tails, are obtained on both the interface and the free surface. These waves are called generalised solitary waves, and whilst the solitary pulses are out-of-phase, the short-wave ripples are in-phase. This type of resonance is known as $1 : M$ resonance, where $M \in \mathbb{N}$ is large.

These generalised solitary waves were not obtained by Kakutani and Yamasaki [71] as they cannot be modelled by the classical KdV equation. Dias and Il'ichev [35] used coupled extended KdV equations to derive a weakly nonlinear model capable of including resonant effects. They were able to obtain generalised solitary waves. Furthermore, they modified their model so that it was valid when the fluid depths are at the critical thickness ratio, by including cubic nonlinearity. They then obtained fronts with ripples in their tails- generalised fronts.

There have been far fewer studies into this two-layer configuration, when the effects of surface tension are included either on the free surface, on the interface, or even on both. Woolfenden and Părău [130] studied gravity-capillary solitary waves in the two-fluid system using a fully nonlinear boundary integral equation method. They explained their results in terms of the linear dispersion relation, given by

$$F_{\pm}(k)^2 = \frac{b(k) \pm \sqrt{b^2(k) - 4a(k)c(k)}}{2ka(k)}, \tag{2.6.9}$$

where $a(k), b(k)$ and $c(k)$ are functions of the wavenumber k;

$$\begin{cases} a(k) = 1 + R\tanh(\frac{k}{D})\tanh(k), \\ b(k) = \tanh(\frac{k}{D}) + \tanh(k) + k^2\left(\tau_I\tanh(\frac{k}{D}) + \tau_F\left(R\tanh(\frac{k}{D}) + \tanh(k)\right)\right), \\ c(k) = (1 - R + \tau_I k^2)(1 + \tau_F k^2)\tanh(\frac{k}{D})\tanh(k). \end{cases} \tag{2.6.10}$$

Here, τ_I and τ_F are the Bond numbers on the interface and the free surface respectively. The fast mode takes the positive root of (2.6.9) and is defined by $F_+(k)$, and the slow mode the negative root, defined by $F_-(k)$.

Woolfenden and Părău showed that in this two-layer configuration there exist two critical values of both the free surface and interfacial Bond numbers, $\tau_F = \tau^*_{F_\pm}$ and $\tau_I = \tau^*_{I_\pm}$, which determine the behaviour of the dispersion relations. They included surface tension either on the upper free surface, on the interface (Părău and Woolfenden [100]), or on both the free surfaces, to look for pure solitary waves. These waves occur at values of the Froude number in the spectral gap between the two dispersion curves (if

such a gap exists), i.e. for values of the Froude number where resonant interactions with a linear wave train are not possible. Solitary wave solutions with sech^2 type profiles (similar to the KdV equation solutions) and solitary waves with damped decaying oscillations in their tails (similar to the NLS equation solutions), were obtained. Furthermore, as in the rigid-lid approximation, limiting configurations taking the form of either an increasingly sharp wave, or a broadening wave, were approached as F was increased towards F_{front}.

In the rigid-lid configuration, the orientation of the interfacial wave was shown to depend on the critical depth ratio (2.6.1). In the presence of an upper free surface, Woolfenden and Părău showed that when surface tension is included only on the upper free surface (i.e. $\tau_F \neq 0$, $\tau_I = 0$), solutions bifurcating from the critical value of the fast mode $F_+(0)$ are in-phase depression solitary waves, whereas those bifurcating from the critical value of the slow mode are out-of-phase waves which change their orientation dependent on the critical depth ratio. If $D > \sqrt{R}$, the surface wave is a depression, and the interfacial wave an elevation, and vice versa if $D < \sqrt{R}$. When surface tension is included on both the upper free surface and the interface, Woolfenden and Părău also showed that the solitary waves on the two free surfaces are of opposite orientation, but the exact orientation can be either way round for the same given parameters.

When only interfacial tension is considered, Părău and Woolfenden [100] showed that the slow mode possesses a maximum and the fast mode a minimum, so, the spectral gap between the two modes can be made very small. The waves in this regime have damped oscillations in their tails and are out-of-phase if they bifurcate from the critical value of the slow mode, and in-phase if bifurcating from the critical value of the fast mode. This is in agreement with the case where surface tension is only present on the upper free surface.

The forced problem in this two-layer flow configuration has also received attention. Forbes [53] extended his work on critical free surface flows over a semi-circular obstruction in a single-layer of fluid, to critical two-layer flows. He solved the fully nonlinear equations in both layers and looked for pure gravity hydraulic falls on both the interface and the free surface. The mean levels of the upper free surface and the interface therefore decrease over the obstruction. Forbes allowed for different flow velocities upstream, by introducing the parameter γ to define the ratio of the upstream flow velocities. Many of the results discussed here so far assumed that the upstream velocities were the same in both fluids. This reduced the number of independent variables, and is a required condition when dealing with wave trains of permanent form travelling through fluids at rest. In such solutions, a wave train could not appear stationary in both fluids if $\gamma \neq 1$. However, there is no such requirement when dealing with hydraulic falls and solitary waves. The flow speed is then such that the dispersion relation has no real k solution and thus, there can be no waves to govern the flow.

In the context of the shallow water approximation, the combination Froude number f_c, given by

$$f_c^2 = f_1^2 + f_2^2 - f_1^2 f_2^2 + R, \tag{2.6.11}$$

can be used to describe two-layer critical flows, and has been derived, for example, by Armi [6] and Forbes [53]. Here, f_1 and f_2 are the local Froude numbers in the lower and upper layers respectively, defined by $f_1^2 = u_1^2/g(\eta_1 - b(x))$ and $f_2^2 = u_2^2/g(\eta_2 - \eta_1)$, where u_i for $i = 1, 2$ and $\eta_1(x)$ and $\eta_2(x)$ define the horizontal velocity components and the surface of the lower and upper fluids, respectively. The local Froude numbers therefore vary along the channel (and approach their corresponding upstream Froude numbers as $x \to -\infty$). The combination Froude number will satisfy $f_c = 1$ over the obstacle where the flow is critical. Furthermore, it will satisfy $f_c > 1$ and $f_c < 1$ far up and downstream respectively. However, Forbes [53] showed that the combination Froude number ceases to describe the flow when the obstacle size becomes large.

Furthermore, Forbes showed that when the density ratio R is reduced to zero, the lower fluid and its free surface behave like the single layer flow. In this situation, the upper layer has zero weight and so does not influence the lower fluid. However, the free surface solution for the upper-layer is not unique: first, there exists a solution in which the Froude number in the upper layer is supercritical throughout the flow (the Froude number increases to a greater supercritical flow downstream of the obstruction). Secondly, there is a solution in which the Froude number is subcritical upstream of the obstruction and supercritical downstream. Forbes attempted to obtain this second type of solution for different values of the density ratio, but was only able to continue the solutions into some small neighbourhood of $R = 0$.

Forbes conjectured the possibility of far more complex solutions to this problem, such as critical flow in the lower-layer with downstream waves in the upper-layer. However, Shen [107] derived decoupled pure gravity fKdV equations to model the interface and free surface far from the critical depth ratio. He found a linear relationship between the first order elevations of the upper free surface and the interface (and indicated that the fast mode is in-phase, whilst the slow mode is out-of-phase). Consequently, this suggests that critical flow in one-layer with wavy flow in the other, as conjectured by Forbes [53], is not possible. Shen [107] also showed that the hydraulic fall solutions obtained by Forbes [53], were valid only for the fast mode. Furthermore, he found that there are twice as many solitary wave and hydraulic fall solutions in the two-layer case, than in the single-layer case. However, as in the rigid-lid approximation, the sfKdV equation does not adequately describe the nonlinearity in the neighbourhood of the critical thickness ratio, so sfmKdV equations are required for the weakly nonlinear analysis.

When both capillarity and an underlying forcing are considered, the published record of research again grows thin. Woolfenden and Părău [130] obtained their gravity-capillary

pure solitary wave solutions by including a pressure forcing on the interface. Then, using parameter continuation on the amplitude of the resulting forced solitary wave, they obtained forced solitary waves bifurcating from a pure solitary wave. They then simply removed the forcing to obtain the pure solitary wave. This shows that multiple forced solitary wave solutions exist, with the same parameters, on both the upper free surface and the interfacial surface, in a similar manner to the multiple solutions in the single layer case, as shown for example by Maleewong *et al.* [77].

The problem has also been studied using a weakly nonlinear analysis. Choi, Sun and Shen [30] derived a sfeKdV equation to model interfacial waves of near critical speed over a small obstruction. As in the rigid-lid case, they found a relationship between the upper free surface and the interfacial surface. Four supercritical solitary type waves were also found to exist. Furthermore, solutions were seen which are flat upstream, or form part of a solitary wave upstream, with a periodic wave train ahead of the obstacle. It was shown that a hydraulic fall is also obtained as the limiting configuration of the flat upstream-wavy downstream subcritical solution.

2.7 Stability

The stability discussed in this work refers to the time evolution of the numerical solution to an initial value problem. Stability or lack of stability is deduced according to the change in shape of the free surface as an initially steady solution evolves in time. Stability here therefore does not refer to the more rigorous case involving solving the eigenvalue problem to determine the attracting or repelling nature of the equilibrium points.

There are many numerical methods which use boundary integral equation techniques to determine the motion of pure gravity water waves. As in the steady case, this has the advantage of reducing the dimension, and thus the number of unknowns, of the problem. The kinematic and dynamic boundary conditions are computed as before, but this time in their unsteady form. They are then expressed in terms of the rate of change of the velocity potential ϕ and the coordinates of the free surface following a fluid particle. The derivative of the velocity potential with respect to time, ϕ_t, can then be obtained from the dynamic condition, once ϕ_x and ϕ_y are known. These velocity components are obtained after determining the tangential and normal components of velocity. The tangential component is obtainable simply by differentiating ϕ with respect to arclength, using adjacent fluid particles, but the normal component can only be obtained using, for example, a Cauchy integral equation. Longuet-Higgins and Cokelet [76] developed a numerical method to compute periodic gravity waves and steep and overturning waves, in deep water. They transformed the coordinates of their flow configuration so that the fluid

was contained within a simple closed contour. The boundary of the contour then represented the free surface of the fluid. Adams-Bashforth-Moulton scheme was then used for the time stepping. Dold and Peregrine [44] developed a different method to compute unsteady pure gravity free surface flows. They explicitly calculated the time derivatives of ϕ and the free surface using Laplace's equation along with the dynamic boundary condition and the knowledge that the derivatives of ϕ must also satisfy Laplace's equation. Truncated Taylor series were then used to perform the time stepping explicitly.

Cooker, Peregrine, Vidal and Dold [32] followed the method developed by Dold and Peregrine [44] to study a pure gravity solitary wave propagating over a submerged semi-circular obstruction. They noted that this configuration may be used to model ocean waves causing damage to coastal structures. Using a conformal map, they mapped the submerged obstruction into a flat-bedded plane, and then showed that when the obstacle is relatively small, the solitary wave is not perturbed much with time, but small dispersive waves appear behind the solitary wave, along with a train of reflected waves. When the obstacle is larger however, they found that there exist a few different flow possibilities, dependent on the exact size of the obstruction. The free surface may develop another crest which propagates away from the obstruction or different forms of wave breaking may occur. They supported these findings with experimental results.

Dold [43] also applied the method developed by Dold and Peregrine [44] to unsteady pure gravity waves. He commented that using conformal mapping techniques, such as those used by Cooker *et al.*, limits the ability of the scheme to obtain steep free surface profiles, without having many extra free surface mesh points. He also investigated the stability of the method using test runs and a model stability analysis, and noted that three instabilities exist:

1. A strong instability appears if the time step is excessively large,

2. A weak instability appears if quadratic or cubic backward differencing is used in the time stepping,

3. A steep-wave, sawtooth instability appears for any size time step. The steeper the wave, the smaller the time-scale over which the instability grows.

He therefore modified the numerical method to remove the instabilities by resolving the issues generating them. He noted that an appropriately small time step and higher order backward differencing are needed to resolve the first two issues, and smoothing techniques are required to remove the third instability.

Much of the previous work on the stability of gravity and gravity-capillary waves past some form of disturbance in the channel has focused on the cases where the flow is uniform, with the same constant mean depth up and downstream. For example, as previously discussed, Grimshaw, Maleewong and Asavanant [62] considered the stability

of gravity-capillary solitary waves. Grimshaw and Maleewong [61] also showed that in the pure gravity case the subcritical flow solutions, which have a train of waves downstream of the disturbance, are stable. They also showed that the supercritical solitary wave solutions were stable if they bifurcated from the uniform stream and unstable if they bifurcated from a pure solitary wave. Milewski and Vanden-Broeck [81] computed unsteady gravity-capillary solutions where the effects of gravity and surface tension were equally important, i.e. $\tau \approx 1/3$, using a fifth order fKdV equation. They obtained Wilton ripples and solitary waves with decaying and non-decaying oscillations in their tails.

Fewer studies have considered the stability of conjugate flow solutions i.e. hydraulic falls and generalised hydraulic falls. The work that has been done on the stability of hydraulic falls has used a weakly nonlinear analysis to investigate just the pure gravity case. Chardard *et al.* [27] showed that the fKdV equation suggests that the pure gravity hydraulic fall generated over a moving obstacle is stable. Furthermore, they showed that if one did consider a reversed hydraulic 'fall', i.e. with supercritical flow upstream and subcritical flow downstream, so that the free surface rises over the disturbance, the weakly nonlinear analysis suggests that it is unstable. This would explain why such hydraulic 'rises' are not observed in nature (see Viollet *et al.* [127]).

Chardard *et al.* also considered the stability of supercritical pure gravity solitary wave solutions past two disturbances. Starting with a steady wave solution, they perturbed the solution slightly and then followed it in time to assess the stability. They showed that, as in the case of a single disturbance in the channel, unless the disturbances were too close together, bifurcations from the uniform stream are stable whereas bifurcations from a pure elevation solitary wave are unstable. However, they showed that the solution with a solitary wave bifurcating from the uniform stream followed by a solitary wave bifurcating from a pure solitary wave, is unstable. In fact they showed that if these waves were perturbed so that they were larger than the original steady state, the two solitary waves would interact and generate a new solitary type wave.

Donahue and Shen [45] also showed that the fKdV equation suggests that the pure gravity hydraulic fall is stable. They considered a submerged obstacle flowing through a fluid at rest. They perturbed an initial stationary hydraulic fall solution with white noise and then demonstrated that as time evolves the white noise dissipates and the solution returns to the shape of the initial hydraulic fall. Physically, when a submerged obstruction moves through a fluid at rest, one would require that any disturbances should decay to zero far up and downstream. However, a hydraulic fall is a conjugate flow solution, and so requires that the fluid depth far up and downstream of the moving obstruction should be of different. Therefore, this creates a discontinuity in the flow in the numerical scheme, either far up or far downstream. However, Donahue and Shen simulated the effect of the upstream discontinuity and showed that, provided the domain was large enough, the

discontinuity did not locally affect the results.

2.8 Research rationale

There is scope for further work in this vast area, particularly into the effects of surface tension in both the single and multi-layered fluid flow configurations of finite depth, over one or more disturbances in the channel. Certainly, following the work of Binder *et al.* [18] on single layer pure gravity flows over two triangular obstructions for example, one would expect to be able to find many more types of flow over multiple submerged obstructions, both in a single layered configuration, which includes capillarity, and in the two-layer configuration.

In this research, the papers of Maleewong *et al.* [77] and Binder *et al.* [18] are followed and extended in order to find gravity-capillary solutions in a single-layered ideal fluid, subjected to multiple localised pressure distributions. A fully nonlinear boundary integral equation method is utilised to obtain solutions to the full Euler equations, and the solutions are then explained in the context of the linear dispersion relation. Furthermore, the pure gravity critical flow solutions obtained by Forbes [51] in the case of a single disturbance in the channel, and by Belward [11] in the presence of an additional disturbance further downstream, are considered. The effects of capillarity are then included in the formulation, and the resulting solutions examined. The 'trapped wave' solutions discovered by Dias and Vanden-Broeck [41] consisting of critical flow over a central disturbance, with a train of waves trapped between the central obstruction and a second submerged obstruction further upstream, are obtained. The effects of surface tension on these trapped waves is then investigated, and further critical gravity-capillary solutions are sought. Again, solutions are explained in the context of the gravity-capillary linear dispersion relation.

A thin ice plate floating on top of a fluid of constant density is then examined, and the current research on flexural-gravity waves under an ice plate is extended by considering the critical regime, where the depth of the fluid under the ice sheet changes. The existing research on flexural-gravity periodic waves (Forbes [50]), elevation and depression solitary waves with decaying oscillations in their tails (Părău and Dias [98]), generalised solitary waves (Vanden-Broeck and Părău [125]), and solitary waves in infinite depth (Guyenne and Părău [67]) for example, is thus extended to include flexural-gravity hydraulic fall solutions. Furthermore, 'trapped wave' solutions, similar to the pure gravity solutions obtained by Dias and Vanden-Broeck [41], are sought in this flexural-gravity regime. Solutions in this case are explained in the context of the flexural-gravity linear dispersion relation, and comparisons between the gravity-capillary and flexural-gravity critical flow solutions are drawn.

The research then goes on to model two-layer flow in a channel of finite depth in the rigid-lid configuration. In contrast to much of the previous work on two-layer flows discussed in this chapter, both the effects of gravity and capillarity are included in our formulation, so that gravity-capillary interfacial waves are sought. By manipulating the shape and positions of the submerged obstructions or pressure forcing, it is anticipated that one should be able to obtain the solutions obtained in the case of a single layer (see for example Binder *et al.*), with the addition of several new flows. Here, critical flows are focused on, where the depth of the fluid in both layers changes as one travels past a disturbance. The pure gravity interfacial hydraulic fall solutions obtained by Dias and Vanden-Broeck [39, 42] are obtained and analysed, and then the effects of capillarity added. Again, solutions with a train of waves trapped between two disturbances are sought. A second submerged obstruction is therefore added to the pure gravity formulation presented by Dias and Vanden-Broeck, and also to the gravity-capillary case presented here for the first time.

Finally, we examine the issue of the stability of the hydraulic fall. We have discussed how the pure gravity hydraulic fall has been shown to be stable using a weakly nonlinear analysis, by Chardard *et al.* [27] and Donahue and Shen [45]. We confirm these findings using a fully nonlinear scheme, and then extend this work on stability by considering the conjugate solution profiles over two obstructions, and the stability of gravity-capillary hydraulic falls.

CHAPTER THREE

FREE SURFACE FLOWS GENERATED BY AN APPLIED PRESSURE DISTRIBUTION

3.1 Introduction

We consider the problem of a single-layer fluid, flowing in a channel of finite depth, which is subjected to localised applied pressure distributions on the free surface. Both the effects of gravity and surface tension are included, and the steady flow problem is solved using the boundary integral equation techniques discussed in chapter 2. The aim in this chapter is to extend and combine the work of Maleewong *et al.* [77], who included the effects of capillarity and considered a single disturbance in the channel, with the work of Binder *et al.* [18], who considered pure gravity waves with two disturbances in the channel. Therefore, in this chapter we seek gravity-capillary solitary wave solutions where two localised pressure distributions are applied to the free surface.

The fully numerical problem is formulated in section 3.2, the numerical method is described in full in section 3.3 and the numerical results are presented and discussed in section 3.4. Finally, in section 3.5 we conclude with a summary of our results.

3.2 Formulation

We consider the steady two-dimensional flow of an incompressible, inviscid fluid of constant density ρ, bounded below by a horizontal impermeable bed at $y^* = -H$. We introduce dimensional Cartesian coordinates (x^*, y^*) such that the x^*-axis is aligned on the undisturbed free surface, parallel to the bottom of the channel. The influences of both gravity and surface tension are taken into account, where g is gravitational acceleration acting in the negative y^*-direction, and σ is the constant coefficient of surface tension on

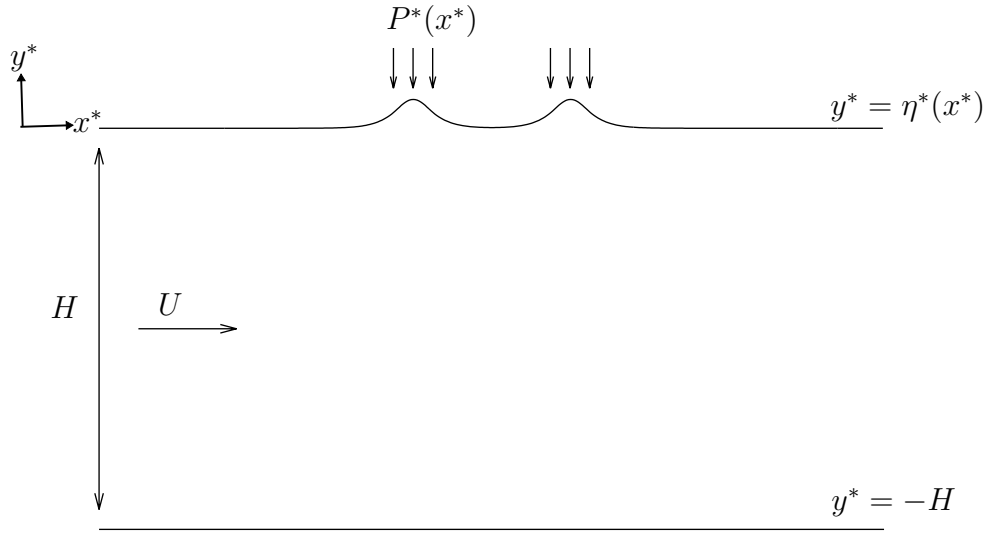

Figure 3.1: Physical flow domain showing the pressure distribution $P^*(x^*)$ applied to the uniform stream of constant depth H and constant velocity U.

the free surface. We then define the free surface by $y^* = \eta^*(x^*)$ and subject it to two localised applied pressure distributions, given by the function $P^*(x^*)$. The flow is assumed steady, so that $\eta^*(x^*)$ is independent of time. We choose a frame of reference travelling with the pressure distributions, and far from the pressure distributions (as $x^* \to \pm\infty$) we assume that the flow becomes a uniform stream with constant velocity U and constant depth H. A sketch of the flow configuration can be seen in figure 3.1.

The fluid is assumed to be incompressible so that $\nabla \cdot \mathbf{u}^* = 0$, i.e.

$$\frac{\partial u^*}{\partial x^*} + \frac{\partial v^*}{\partial y^*} = 0, \tag{3.2.1}$$

where $\mathbf{u}^* = (u^*, v^*)$. The velocity field $\mathbf{u}^*(\mathbf{x}^*, \mathbf{y}^*)$ is assumed to be irrotational so that $\nabla \times \mathbf{u}^* = \mathbf{0}$, i.e.

$$\frac{\partial u^*}{\partial y^*} - \frac{\partial v^*}{\partial x^*} = 0. \tag{3.2.2}$$

This means that we can introduce the velocity potential function $\phi^*(x^*, y^*)$, such that

$$\mathbf{u}^* = \nabla\phi^* = \left(\frac{\partial \phi^*}{\partial x^*}, \frac{\partial \phi^*}{\partial y^*}\right), \tag{3.2.3}$$

where $\phi^*(x^*, y^*)$ satisfies Laplace's equation;

$$\nabla^2\phi^* = 0. \tag{3.2.4}$$

Next, we impose two boundary conditions on the free surface. First, the kinematic condition, which ensures that a particle that starts on the free surface remains on the free surface. This means that if the free surface is given by $f(x^*, y^*) = y^* - \eta^*(x^*) = 0$, we

require that the material derivative Df/Dt vanishes at the free surface:

$$\begin{aligned} \frac{Df}{Dt} &= \frac{\partial f}{\partial t} + \mathbf{u}^*.\nabla f = 0, \\ \Rightarrow \qquad & -u^*\frac{\partial \eta^*}{\partial x^*} + v^* = 0, \end{aligned} \tag{3.2.5}$$

on $y^* = \eta^*(x^*)$. We also apply a kinematic condition on the bottom of the channel, meaning we require

$$\frac{\partial \phi^*}{\partial y^*} = 0, \tag{3.2.6}$$

on $y^* = -H$.

Secondly, we impose the dynamic boundary condition, which ensures the continuity of the pressure across the fluid-air interface in the absence of surface tension. When surface tension is present this condition relates the pressure jump across the interface between the two fluid. As we have assumed that the flow is steady and irrotational, the steady Bernoulli equation must be satisfied everywhere in the fluid:

$$\frac{1}{2}\rho(u^{*2} + v^{*2}) + p^* + \rho g y^* = \mathcal{B}, \tag{3.2.7}$$

where $p^*(x^*, y^*)$ is the pressure on the liquid side of the free surface and $\mathcal{B}$ is the Bernoulli constant at the free surface streamline, obtained by examining the flow far downstream. As $x^* \to \infty$ we know that $\mathbf{u}^*(x^*, y^*) \to (U, 0)$, $\eta^* \to 0$, and at the free surface, $p^* \to P_\infty$; the constant pressure at the free surface far downstream. Then substituting the variables far downstream into (3.2.7), gives

$$\mathcal{B} = \frac{1}{2}\rho U^2 + P_\infty, \tag{3.2.8}$$

and thus, at the free surface, (3.2.7) becomes

$$\begin{aligned} & P_a + P^*(x^*) + \frac{1}{2}\rho(u^{*^2} + v^{*^2}) + \rho g y^* = P_\infty + \frac{1}{2}\rho U^2, \\ \Rightarrow & \frac{P^*(x^*)}{\rho} - \frac{P_\infty - P_a}{\rho} + \frac{1}{2}(u^{*^2} + v^{*^2} - U^2) + g y^* = 0, \\ \Rightarrow \quad & \frac{P^*(x^*)}{\rho} + \frac{\sigma}{\rho}\nabla \cdot \mathbf{n} + \frac{1}{2}(u^{*^2} + v^{*^2} - U^2) + g y^* = 0, \end{aligned} \tag{3.2.9}$$

on $y^* = \eta^*(x^*)$. Here, $p^*(x^*, \eta^*) = P_a + P^*(x^*)$, where P_a denotes the atmospheric pressure, and $\mathbf{n}$ denotes the unit normal pointing out of the fluid. We have utilised the Young-Laplace equation (1.2.19) in the form $P_\infty - P_a = -\sigma\nabla \cdot \mathbf{n}$. In the absence of any curvature of the free surface, $P_a = P_\infty$ and the second term in (3.2.9) disappears.

If the free surface is given by $y^* = \eta^*(x^*)$, then the unit outward normal is given by

$$\mathbf{n} = \frac{\nabla(\eta^* - y^*)}{|\nabla(\eta^* - y^*)|} = \left(\frac{-\eta^*_{x^*}}{(\eta^{*2}_{x^*} + 1)^{\frac{1}{2}}}, \frac{1}{(\eta^{*2}_{x^*} + 1)^{\frac{1}{2}}} \right), \tag{3.2.10}$$

and in section 1.2 we showed that

$$\nabla \cdot \mathbf{n} = \frac{-\eta^*_{x^*x^*}}{(\eta^{*2}_{x^*} + 1)^{\frac{1}{2}}} + \frac{\eta^{*2}_{x^*}\eta^*_{x^*x^*}}{(\eta^{*2}_{x^*} + 1)^{\frac{3}{2}}} = \frac{-\eta^*_{x^*x^*}}{(\eta^{*2}_{x^*} + 1)^{\frac{3}{2}}}. \tag{3.2.11}$$

Substituting into (3.2.9) we obtain:

$$\frac{P^*(x^*)}{\rho} - \frac{\sigma}{\rho} \frac{\eta^*_{x^*x^*}}{(\eta^{*2}_{x^*} + 1)^{\frac{3}{2}}} + \frac{1}{2}(u^{*^2} + v^{*^2} - U^2) + gy^* = 0. \tag{3.2.12}$$

This is the dynamic condition on the free surface $y^* = \eta^*(x^*)$.

The problem is now simplified by non-dimensionalising the variables using H and U as unit length and unit velocity respectively. We introduce the scalings

$$\begin{aligned} u = \frac{u^*}{U}, \quad v = \frac{v^*}{U}, \\ x = \frac{x^*}{H}, \quad y = \frac{y^*}{H}, \quad \eta = \frac{\eta^*}{H}, \end{aligned} \tag{3.2.13}$$

and on substituting them into Laplace's equation (3.2.4) and the boundary conditions (3.2.5), (3.2.6) and (3.2.12), we obtain the dimensionless form of the problem:

$$\nabla^2 \phi = 0, \tag{3.2.14}$$

in the fluid,

$$\phi_y = \phi_x \eta_x, \tag{3.2.15}$$

$$\frac{1}{2}(\phi_x^2 + \phi_y^2 - 1) + \frac{1}{F^2}\eta = \beta \frac{\eta_{xx}}{(\eta_x^2 + 1)^{\frac{3}{2}}} - P(x), \tag{3.2.16}$$

on the free surface $y = \eta(x)$, and

$$\phi_y = 0, \tag{3.2.17}$$

on the channel bottom $y = -1$. Here $\beta = \tau/F^2$ where F and τ are the dimensionless Froude and Bond numbers defined by equations (2.1.6) and (2.1.2) respectively. The pressure is scaled so that $P^*(x^*) = \rho U^2 P(x)$.

In the far field, as $x \to \pm\infty$, away from the pressure disturbances, the flow is required

to become that of a uniform stream. Therefore, we impose the conditions

$$\phi_x \to 1,\ \eta \to 0 \quad \text{as} \quad |x| \to \infty. \tag{3.2.18}$$

The problem is now fully defined. We must find the unknown functions $\phi(x, y)$ and $\eta(x)$ which satisfy the Laplace equation (3.2.14) in the fluid, the kinematic (3.2.15) and dynamic (3.2.16) boundary conditions on the free surface $y = \eta(x)$, the kinematic condition (3.2.17) on the channel bottom $y = -1$, and the far-field uniform flow conditions (3.2.18).

3.3 Numerical Scheme

In order to solve the problem numerically we reformulate it as a system of integro-differential equations, using the method briefly outlined in section 2.2.

First, it is necessary to introduce the stream function $\psi(x, y)$, see for example Naylor [87]. We know that $P(x, y)dx + Q(x, y)dy$ is a perfect differential if and only if

$$\frac{\partial P}{\partial y} = \frac{\partial Q}{\partial x}. \tag{3.3.1}$$

Due to the incompressibility of the fluid we know that

$$\frac{\partial(-v)}{\partial y} = \frac{\partial u}{\partial x}, \tag{3.3.2}$$

and so, $udy - vdx- = d\psi$ is a perfect differential. Therefore, as $d\psi$ is perfect, it must satisfy

$$d\psi = \frac{\partial \psi}{\partial x}\delta x + \frac{\partial \psi}{\partial y}\delta y. \tag{3.3.3}$$

Then we can easily see that

$$\frac{\partial \psi}{\partial x} = -v, \qquad \frac{\partial \psi}{\partial y} = u. \tag{3.3.4}$$

So, we can define the stream function by writing $\mathbf{u} = \nabla \times \boldsymbol{\psi}$, where $\mathbf{u} = (u, v, 0)$ and $\boldsymbol{\psi} = (0, 0, \psi)$. This then ensures the incompressibility of the fluid and so significantly simplifies the problem. Instead of having the two dependent variables; u and v, just one

dependent variable is now required; ψ. As the flow is irrotational (3.2.2) implies that

$$\frac{\partial}{\partial y}\left(\frac{\partial \psi}{\partial y}\right) - \frac{\partial}{\partial x}\left(-\frac{\partial \psi}{\partial x}\right) = 0, \tag{3.3.5}$$

$$\Rightarrow \qquad \frac{\partial^2 \psi}{\partial x^2} + \frac{\partial^2 \psi}{\partial y^2} = 0\ , \tag{3.3.6}$$

so provided that the flow is incompressible and irrotational, the stream function also satisfies the Laplace equation.

A relationship between the stream function ψ and the velocity potential ϕ can now be established by combining equation (3.3.4) with equation (3.2.3). It follows that

$$u = \frac{\partial \phi}{\partial x} = \frac{\partial \psi}{\partial y}, \qquad v = \frac{\partial \phi}{\partial y} = -\frac{\partial \psi}{\partial x}. \tag{3.3.7}$$

These are the Cauchy-Riemann equations. They imply that we can introduce an analytic function,

$$w(z) = \phi(x, y) + i\psi(x, y), \tag{3.3.8}$$

of $z = x + iy$ in the flow domain, where $i = \sqrt{-1}$. This function is known as the complex potential function.

The problem can now be mapped into the inverse (hodograph) plane so that ϕ and ψ become the independent variables. The stream function $\psi(x, y)$ possesses the property that it is constant along the streamlines. This provides the convenient simplification in mapping the flow into the inverse plane, as both the free surface and the channel bottom are then described by given, straight, streamlines. The unknown free surface is therefore mapped to a known boundary. Without loss of generality, we can choose $\phi = 0$ at $x = 0$, as upon integrating (3.3.4) and (3.2.3), both ϕ and ψ are defined only up to some constant. The fluid may then be mapped into the infinite strip $-\infty < \phi < \infty$, $-1 < \psi < 0$ in the complex ω-plane, shown in figure 3.2. The streamline $\psi = 0$ describes the free surface, whilst $\psi = -1$ describes the channel bottom.

We introduce the conjugate complex velocity, given by

$$\frac{dw}{dz} = \phi_x - i\phi_y, \tag{3.3.9}$$

and because w is an analytic function of z, its derivative, the conjugate complex velocity, is also an analytic function of z. Furthermore, the function

$$g(w) = x_\phi - iy_\phi \tag{3.3.10}$$

is analytic in our flow domain if we assume that there is no stagnation point within the

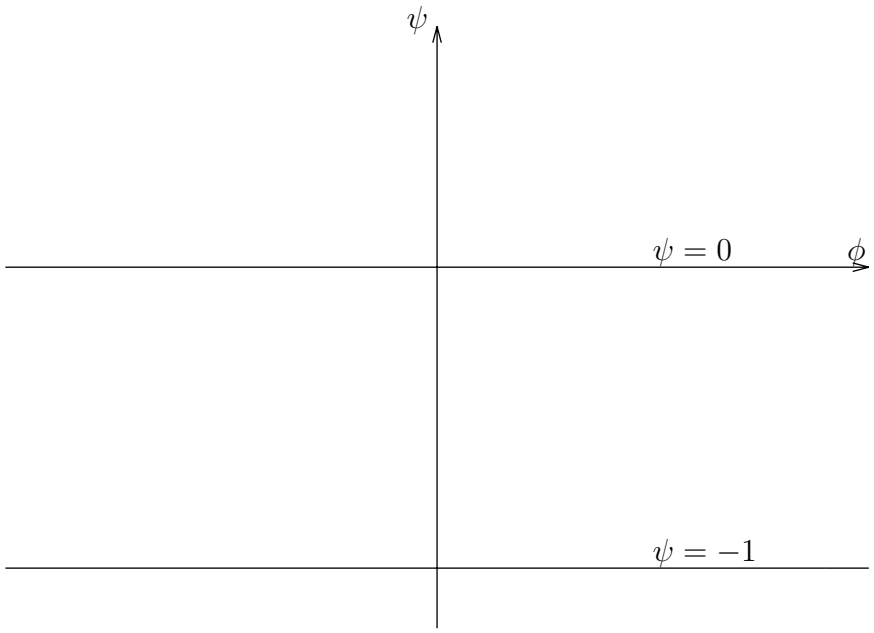

Figure 3.2: Flow configuration in the complex w-plane.

domain, i.e. that there is no point at which $\mathbf{u} = \mathbf{0}$. Therefore, under the same assumption,

$$h(w) = x_\phi - 1 + iy_\phi \tag{3.3.11}$$

is an analytic function of w.

The kinematic condition (3.2.17), requiring that there is zero velocity component normal to the impermeable bottom, can be satisfied by using the method of images. This method involves adding an image of the flow to the opposite side of the rigid bottom boundary. The resulting flow is then symmetric about the boundary, and thus satisfies $\mathbf{u} \cdot \mathbf{n} = 0$ on the boundary. Therefore, the flow domain here is reflected in the streamline $\psi = -1$, in order to satisfy the kinematic condition.

The problem can now be reformulated as a system of integro-differential equations by applying Cauchy's integral formula in principal value form to the complex analytic function $h(w)$ given by (3.3.11), around the contour $\mathcal{C}$ shown in figure 3.3. The contour consists of the free surface, its reflection in the channel bottom, and vertical lines joining them at $\phi = \pm L$, in the limit as $L \to \infty$. The contour is transversed in the anti-clockwise direction. Letting w_o represent the evaluation point on the free surface, we obtain

$$\frac{1}{2\pi i} \oint_c \frac{h(w)}{w - w_o} dw = \frac{1}{2} h(w_o). \tag{3.3.12}$$

We know that $\psi = 0$ on the free surface, and denote $\phi = \phi_o$ on the free surface so that

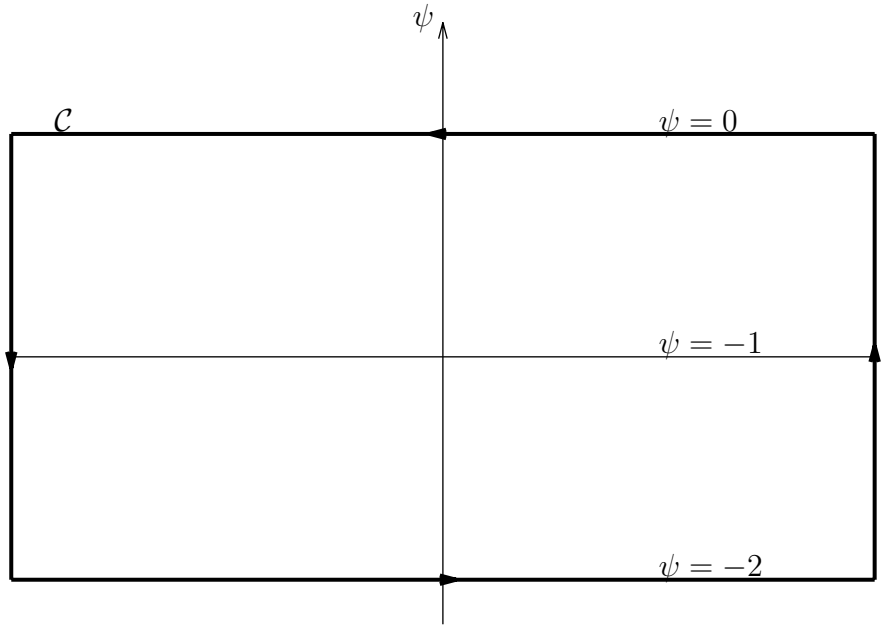

Figure 3.3: The path of integration around the contour $\mathcal{C}$.

(3.3.12) becomes

$$\begin{aligned} \pi i h(w_o) &= \oint_c \frac{h(w)}{w - w_o} dw, \\ &= \oint_c \frac{h(w)}{(\phi + i\psi) - \phi_o} d(\phi + i\psi), \\ \Rightarrow \pi h(w_o) &= \oint_c \frac{h(w)(-\psi - i(\phi - \phi_o))}{(\phi - \phi_o)^2 + \psi^2} d(\phi + i\psi). \end{aligned} \tag{3.3.13}$$

The contribution to the integral from the vertical lines becomes zero because $h(w) \to 0$ as $\phi \to \pm\infty$. Thus, on taking the real part of the equation and noting that on the image of the free surface $\psi = -2$ and $h(w) = h(\phi - i\psi) = x_\phi - 1 - iy_\phi$, due to the symmetry implying that $h(w)$ is an odd function, one obtains

$$x_\phi(\phi_o) - 1 = -\frac{1}{\pi} \int_{-\infty}^{+\infty} \frac{y_\phi}{\phi - \phi_o} d\phi + \frac{1}{\pi} \int_{-\infty}^{+\infty} \frac{2(x_\phi - 1) - (\phi - \phi_o) y_\phi}{(\phi - \phi_o)^2 + 4} d\phi, \tag{3.3.14}$$

where the contour $\mathcal{C}$ has been traversed in the positive (anti-clockwise) sense as indicated in figure 3.3 with $L \to \infty$. The first integral in (3.3.14) is evaluated as a Cauchy Principal Value. The integral equation therefore satisfies the kinematic condition (3.2.17) on the bottom of the channel, and provides a relationship between x_ϕ and y_ϕ on the free surface.

The dynamic boundary condition (3.2.16) must also be mapped into the complex plane. The velocity components u and v are thus written in terms of x_ϕ and y_ϕ. We

differentiate

$$x = x(\phi(x,y),\psi(x,y)), \tag{3.3.15}$$

$$y = y(\phi(x,y),\psi(x,y)), \tag{3.3.16}$$

with respect to both x and y, to obtain

$$1 = x_\phi\phi_x + x_\psi\psi_x, \tag{3.3.17}$$

$$0 = x_\phi\phi_y + x_\psi\psi_y, \tag{3.3.18}$$

$$1 = y_\phi\phi_y + y_\psi\psi_y, \tag{3.3.19}$$

$$0 = y_\phi\phi_x + y_\psi\psi_x, \tag{3.3.20}$$

respectively. Using the Cauchy-Riemann equations (3.3.7) in (3.3.18) and (3.3.20) one obtains

$$x_\psi = -x_\phi\frac{v}{u} \qquad \text{and} \qquad y_\psi = y_\phi\frac{u}{v}, \tag{3.3.21}$$

and substituting into (3.3.17) and (3.3.19),

$$x_\phi = \frac{u}{u^2+v^2} \qquad \text{and} \qquad y_\phi = \frac{v}{u^2+v^2}. \tag{3.3.22}$$

Hence,

$$\frac{1}{x_\phi + iy_\phi} = u - iv, \tag{3.3.23}$$

and so

$$u = \frac{x_\phi}{x_\phi^2+y_\phi^2} \qquad \text{and} \qquad v = \frac{y_\phi}{x_\phi^2+y_\phi^2}. \tag{3.3.24}$$

The curvature in the dynamic condition must also be mapped into the (ϕ,ψ) plane, so η_{xx} must be found in terms of y_ϕ and x_ϕ. Using the kinematic boundary condition on the free surface (3.2.15), one obtains

$$\eta_x = \frac{\phi_y}{\phi_x} = \frac{y_\phi}{x_\phi}, \tag{3.3.25}$$

having substituted ϕ_y and ϕ_x from (3.3.24). Then, η_{xx} on the free surface is

$$\eta_{xx} = \frac{\partial}{\partial x}\left(\frac{y_\phi}{x_\phi}\right) = \frac{y_{\phi\phi}x_\phi - x_{\phi\phi}y_\phi}{x_\phi^3}, \tag{3.3.26}$$

having used (3.3.17) with $\psi = 0$.

Using (3.3.24), (3.3.25) and (3.3.26), the dynamic boundary condition (3.2.16) on the

free surface becomes

$$\frac{1}{2}\left(\frac{1}{(x_\phi^2+y_\phi^2)}-1\right)+\frac{1}{F^2}\eta=\beta\frac{y_{\phi\phi}x_\phi-x_{\phi\phi}y_\phi}{(x_\phi^2+y_\phi^2)^{\frac{3}{2}}}-P. \tag{3.3.27}$$

The reformulation of the problem as a system of integro-differential equations is now complete. Equations (3.3.14) and (3.3.27) must be solved iteratively using Newton's method, to find x_ϕ and y_ϕ on the free surface, subject to the far-field uniform conditions (3.2.18).

Next, to solve the problem numerically, the potential function ϕ is discretised by introducing N equally spaced mesh points on the free surface, separated by a constant interval e;

$$\phi_i=-\frac{N}{2}e+(i-1)e, \quad i=1,...,N. \tag{3.3.28}$$

Then, ϕ_1 and ϕ_N correspond to ϕ at $-\infty$ and ∞. The variables x_ϕ and y_ϕ can be evaluated at each mesh point, and thus, the system of integro-differential equations can be solved at each point. However, the first integral in the integral equation (3.3.14) is a Cauchy Principal Value. If one were to evaluate the integral at each mesh point, a singularity would occur whenever $\phi_i=\phi_o$. Therefore, the $N-1$ mesh midpoints,

$$\phi_i^m=\phi_i+\frac{e}{2}, \quad i=1,...,N-1, \tag{3.3.29}$$

are introduced. The integrals are then truncated at ϕ_1 and ϕ_N, and evaluated at the mesh midpoints using the trapezoidal rule, with summation over the mesh points. Due to the symmetry in the way in which the singularity now occurs (i.e. directly between two mesh points), the singularity in the Cauchy Principal Value can be ignored and the integral evaluated as if it were a non-singular integral (see for example Monacella [83] and Vanden-Broeck [124]).

The integral equation (3.3.14) can now be written in matrix form (see for example Woolfenden and Părău [130]);

$$\mathbf{Qx}=\mathbf{b}. \tag{3.3.30}$$

Here, $\mathbf{x}$ and $\mathbf{b}$ are $(N-1)\times 1$ column vectors with entries

$$x(i)=x_\phi(\phi_i^m)-1, \tag{3.3.31}$$

$$b(i)=\sum_{j=2}^{N}\frac{1}{\pi}\left(\frac{-y_\phi(j)}{\phi_j-\phi_i^m}-\frac{y_\phi(j)(\phi_j-\phi_i^m)}{(\phi_j-\phi_i^m)^2+4}\right), \tag{3.3.32}$$

respectively ($i=1,...N-1$), where the notation $y_\phi(j)=y_\phi(\phi_j)$ has been employed. The $(N-1)\times(N-1)$ matrix $\mathbf{Q}$ is the matrix $(\mathbf{I}-\mathbf{M})$, where $\mathbf{I}$ is the $(N-1)\times(N-1)$

identity matrix, and **M** is a $(N-1)\times(N-1)$ matrix with elements

$$M_{ij} = \frac{1}{\pi}\frac{2}{(\phi_j - \phi_i^m)+4}, \qquad i,j = 1,...,N-1. \tag{3.3.33}$$

The elements of the matrix **M** are constant coefficients which can be computed directly from the discretisation of ϕ. Given an initial set of values for y_ϕ, the column vector **b** can also be computed. Using LU decomposition one can then solve this system to obtain the vector **x**, and thus, the values of x_ϕ at the mesh midpoints.

A four-point dyadic interpolation scheme (where points half-way between two existing points are sought) is employed to obtain the values of x_ϕ at the mesh points. As the points in the neighbourhood of the sought after mesh point are always in the same place (the midpoints), a Deslauriers-Dubuc interpolation is used. The four-point scheme is given by

$$x_\phi(i) = \frac{9}{16}(x_\phi(\phi_i^m) + x_\phi(\phi_{i-1}^m)) - \frac{1}{16}(x_\phi(\phi_{i-2}^m) + x_\phi(\phi_{i+1}^m)). \tag{3.3.34}$$

The values of x at the free surface are obtained by numerically integrating x_ϕ using the midpoint rule

$$x(i) = x(i-1) + \int_{\phi_{i-1}^m}^{\phi_i^m} x_\phi^m d\phi = x(i-1) + x_\phi(\phi_{i-1}^m)e. \tag{3.3.35}$$

The remaining unknowns in the problem are the values of y_ϕ at the N mesh points. We therefore require N equations to solve the problem, of which, $N-2$ are obtained by satisfying the dynamic condition (3.3.27) at the mesh points (3.3.28) for $i = 2,...,n-1$. So, we must first obtain the derivatives $y_{\phi\phi}$ and $x_{\phi\phi}$ by numerically differentiating x_ϕ and y_ϕ, using two-point centred finite differences of the form

$$y_{\phi\phi}(i) = \frac{y_\phi(i+1) - y_\phi(i-1)}{2e}, \tag{3.3.36}$$

$$x_{\phi\phi}(i) = \frac{x_\phi(\phi_i^m) - x_\phi(\phi_{i-1}^m)}{e}. \tag{3.3.37}$$

Here, the second equation is obtained by combining the finite difference with the two point interpolation

$$x_\phi^{m_i} = \frac{x_\phi(i+1) - x_\phi(i)}{e}, \tag{3.3.38}$$

in order to obtain $x_{\phi\phi}$ at the mesh points from x_ϕ at the mesh midpoints. The values of y are obtained from y_ϕ by setting $y(1) = 0$ and evaluating the integral

$$\int_{\phi_i}^{\phi_{i+1}} y_\phi d\phi, \tag{3.3.39}$$

numerically using the trapezoidal rule. We obtain

$$y(i+1) = y(i) + \frac{y_\phi(i) + y_\phi(i+1)}{2} e. \tag{3.3.40}$$

All the variables required to satisfy the dynamic boundary condition (3.3.27) have thus been obtained. The remaining two equations come from enforcing

$$y_\phi(1) = y(N) = 0, \tag{3.3.41}$$

which forces the free surface to become flat and settle to a uniform stream as $x \to \pm\infty$, i.e. it enforces a zero mean level, and satisfies the far-field conditions (3.2.18). The system of N equations (3.3.27) and (3.3.41) is then solved iteratively using Newton's method to find the N unknowns; $y_\phi(i)$, for $i = 1, ..., N$.

Newton's method is used to solve a system of equations of the form $\mathbf{F}(\mathbf{x}) = \mathbf{0}$, where $\mathbf{F}$ is a column vector of the N equations to be solved and $\mathbf{x}$ is the column vector of N unknowns upon which the equations in $\mathbf{F}$ depend. Denoting $y'_i = y_\phi(i)$ for $i = 1, ..., N$, the vector $\mathbf{x}$ becomes $\mathbf{x} = (y'_1, y'_2, ..., y'_N)^T$, and the problem is thus written in the form $\mathbf{F}(y'_1, y'_2, ..., y'_N)^T = \mathbf{0}$, where $\mathbf{F}$ is the vector of functions obtained from the dynamic boundary condition (3.3.27) at the $N-2$ mesh points (3.3.28) for $i = 2, ..N-1$, and the equations (3.3.41). An initial guess for the vector, $\mathbf{x}$, of unknowns is required. The idea of Newton's method is then to update this initial guess, moving closer to a solution on each iteration. A correction vector $\Delta\mathbf{x}$ must therefore be obtained.

If f were a single variable function, on applying Newton's method one would obtain the next estimate x_{n+1} to the root of the function f by

$$x_{n+1} = x_n - \frac{f(x_n)}{f'(x_n)}, \tag{3.3.42}$$

where n is the number of iterations. When $\mathbf{F}$ is multi-variable the derivative of every function with respect to every unknown variable is required. This produces the Jacobian matrix

$$\mathbf{J}(\mathbf{x}) = \left(\frac{\partial F_i}{\partial x_j} \right), \tag{3.3.43}$$

and thus Newton's method becomes

$$\mathbf{x}_{n+1} = \mathbf{x}_n - \mathbf{J}(\mathbf{x}_n)^{-1}\mathbf{F}(\mathbf{x}_n). \tag{3.3.44}$$

The correction vector $\Delta\mathbf{x}$ is thus defined by $-\mathbf{J}(\mathbf{x}_n)^{-1}\mathbf{F}(\mathbf{x}_n)$ and is found by solving the linear system of equations

$$\mathbf{J}\Delta\mathbf{x} = -\mathbf{F}(\mathbf{x}_n). \tag{3.3.45}$$

The derivatives in the Jacobian matrix are obtained numerically using forward finite differences in the form

$$\frac{\partial F_i}{\partial x_j} = \frac{\mathbf{F}_i(y(\phi_j) + h) - \mathbf{F}_i(y(\phi_j))}{h}. \tag{3.3.46}$$

The linear system of equations (3.3.45) is then solved using LU-decomposition. Finally, the now known correction vector $\Delta\mathbf{x}$ is added to the initial guess

$$\mathbf{x}_{n+1} = \mathbf{x}_n + \Delta\mathbf{x}, \tag{3.3.47}$$

to produce a new improved estimate to the solution. At each stage the error in the solution is also calculated. The system being solved is of the form $\mathbf{F}(\mathbf{x}) = \mathbf{0}$, and so summing the squares of each entity in $\mathbf{F}$ provides a good estimation to the error. The Newton method is then continued iteratively until the error is less than some pre-defined value; 1×10^{-15}.

However, in order to decrease the computing time required to obtain the solutions, a modified Newton's method is used here. The Jacobian matrix is only calculated once at the start of the iterative scheme, and this single calculated matrix is then used in every subsequent iteration as well.

To obtain solitary type wave perturbations from the uniform stream an initial guess of $y_\phi(i) = 0$ for $i = 1, ..., N$ is sufficient. However, to obtain the perturbations from pure solitary waves one must first obtain a wave profile perturbating from the uniform stream, using the scheme as described above. Then, by using parameter continuation on the amplitude of the peak of one of the waves (increasing the amplitude of the wave, whilst allowing the value of F to become part of the solution), one can follow the solution branch in the $F - y_{max}$ plane (where y_{max} is the amplitude of the peak of the wave). A critical value of the Froude number is eventually reached where the branch possesses a turning point. At this point, the perturbations from the uniform stream become perturbations from a pure solitary wave. Indeed, by decreasing the pressure forcing to zero beyond the turning point, pure solitary waves are obtained.

In some cases, when considering symmetric solutions, we can improve the computational efficiency of our code by modifying it to specifically look for symmetric solutions. Only half the number of mesh points are then required on the free surface, and the discretisation of ϕ for the N equally spaced mesh points (3.3.28), becomes

$$\phi_i = (i-1)e, \qquad i = 1, ..., N. \tag{3.3.48}$$

The integral equation (3.3.14) also changes as the contour $\mathcal{C}$ now only includes the free surface and channel bottom when $\phi \geq 0$. Therefore, on the symmetric domain (3.3.14)

becomes

$$x_\phi(\phi_o) - 1 = -\frac{1}{\pi}\int_0^\infty \left(\frac{y_\phi}{\phi-\phi_o} + \frac{y_\phi}{\phi+\phi_o}\right) d\phi + \frac{1}{\pi}\int_0^\infty \left(\frac{2(x_\phi-1)-(\phi-\phi_o)y_\phi}{(\phi-\phi_o)^2+4} + \frac{2(x_\phi-1)-(\phi+\phi_o)y_\phi}{(\phi+\phi_o)^2+4}\right) d\phi, \tag{3.3.49}$$

which we evaluate where ϕ_o is at the mesh midpoints, with summation over the mesh points. The problem is then solved in the same manner as above, with the variables coming from numerical integration using the trapezoidal rule, numerical differentiation using finite centred differences and from a dyadic interpolation. When integrating y_ϕ to obtain y however, we must set $y(1) = y_0$, where y_0 is the amplitude of the free surface at $x = 0$, rather than $y(1) = 0$. At the point of symmetry we will have that $y_\phi = 0$ which we can then use to solve the dynamic boundary condition at $x = 0$.

3.4 Results

The results in this section are computed using the method described in section 3.3, with a pressure distribution of the form

$$P(x) = \begin{cases} \epsilon_1 \exp\left(\frac{1}{(\phi-a)^2-1}\right) & -1 < |\phi - a| < 1, \\ \epsilon_2 \exp\left(\frac{1}{(\phi-b)^2-1}\right) & -1 < |\phi - b| < 1, \\ 0 & \text{otherwise.} \end{cases} \tag{3.4.1}$$

Here, $\phi = a$ and $\phi = b$ are the centres of the forcings on the ϕ-axis, and ϵ_1 and ϵ_2 describe the strength of the forcings. In the modified symmetric code, we take $\epsilon_2 = 0$ so that $p(x)$ describes two pressure distributions symmetric about $x = 0$, centred at $x = a$ and $x = -a$.

To ensure that the results obtained are numerically accurate we computed the same solutions on meshes of different densities and lengths L. We varied the number of mesh points on the free surface between $N = 400$ and $N = 801$ for a given fixed domain. The mesh spacing was also varied between $e = 0.05$ and $e = 0.1$. To aid in the computation on meshes of different densities, we use a numerical scheme which reads the values of y_ϕ from a mesh of lower density. These values of y_ϕ at each mesh point are stored in alternative spaces in an array of twice the length. Using Deslauriers-Dubuc interpolation, values of y_ϕ at the remaining array spaces are computed. This then gives a likely result for y_ϕ on a domain that is twice as dense. Using this set of values for y_ϕ as the initial guess in our numerical scheme defined in section 3.3, provided that the scheme converges, we

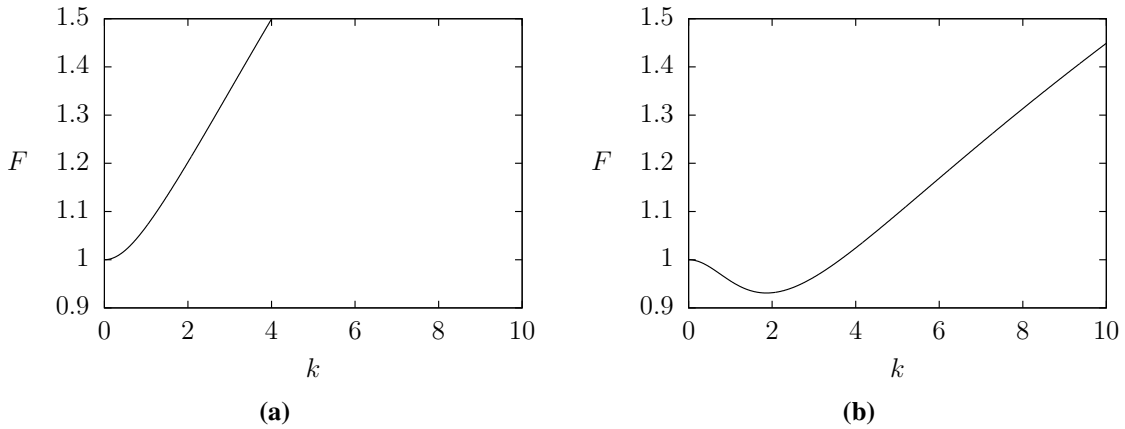

Figure 3.4: Linear dispersion relations in the cases of (a) strong surface tension and (b) weak surface tension.

can compare the results on this mesh with the results on the initial mesh to ensure that the density of the mesh does not affect the result. Similarly, we check that solutions on domains of different length also agree.

The solutions are restricted to the case of subcritical flow ($F < 1$). Sketches of typical linear dispersion relations in both the strong surface tension and weak surface tension regimes are shown in figure 3.4. The solitary waves that we seek bifurcate from the long wave limit ($k = 0$) when the surface tension is strong, and from the minimum of the linear dispersion relation, when the surface tension is weak. Values for the parameters ϵ_1, ϵ_2, β and F are set, and the distance $x_d = |b - a|$ between the pressure distributions is fixed.

When $\epsilon_1 = \epsilon_2 = 0.05$, $x_d = 6$, $\beta = 0.49$, and $F = 0.92$, $\tau = 0.414$ and a typical forced solitary type wave free surface profile is shown in figure 3.5(a). This result is similar to the wave profile found by Binder, Vanden-Broeck and Dias [18] for supercritical flow in the absence of surface tension, over two submerged triangular obstructions. The gravity-capillary waves obtained here are depression waves however, whereas the gravity waves obtained by Binder *et al.* were elevation waves. The result is also similar to the classical gravity-capillary solitary wave profile over a single disturbance in the flow. As $\epsilon_1 \to 0, \epsilon_2 \to 0$ the broken curve solution in 3.5(b) reduces to a uniform stream.

Only depression waves are found when the pressure forcings are positive ($\epsilon_1 > 0$, $\epsilon_2 > 0$). By gradually increasing the amplitude of one of the troughs in such solutions, and allowing the Froude number to be found as part of the solution, we are able to follow the solution branch in the $y(0) - F$ plane, see figure 3.7(a). At some critical value of the Froude number F^*, a turning point is obtained. When $F > F^*$, no solitary wave solutions are found, and if $F < F^{**}$, where F^{**} is some other critical value of the Froude number, just one family of solutions is found; perturbations from a uniform stream. However, if

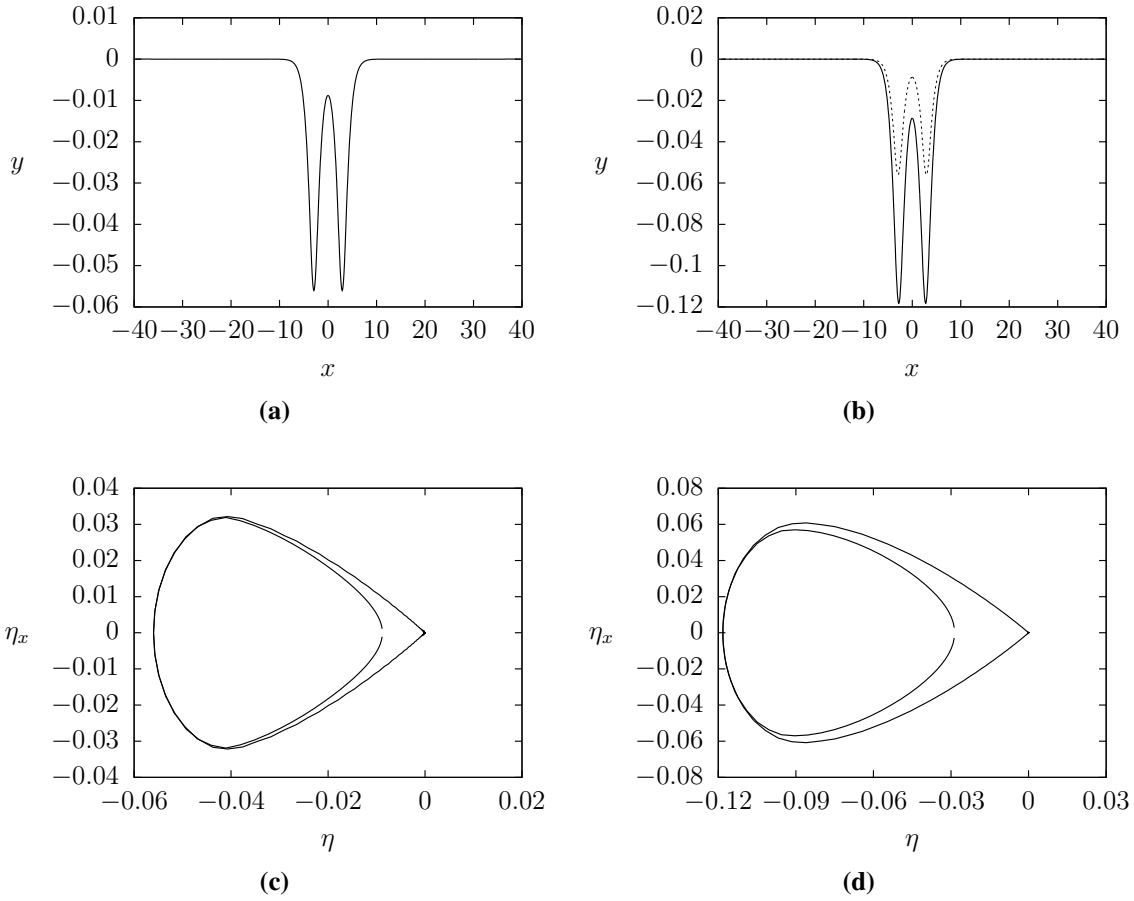

Figure 3.5: Typical fully nonlinear free surface profiles for $\epsilon_1 = \epsilon_2 = 0.05$, $x_d = 6$, $\beta = 0.49$, and $F = 0.92$. The pressures are centred at $a = 3$ and $b = -3$. (a) A perturbation from a uniform stream with maximum depression -0.056. (b) The solid curve is a perturbation from a depression solitary wave solution, and has maximum amplitude -0.118. The dashed curve is the solution shown in (a). The phase portraits for the solid line solutions in (a) and (b) are shown in (c) and (d) respectively. It should be noted that the phase curves are actually continuous. The discontinuity present in the figures is an artefact of the numerical scheme.

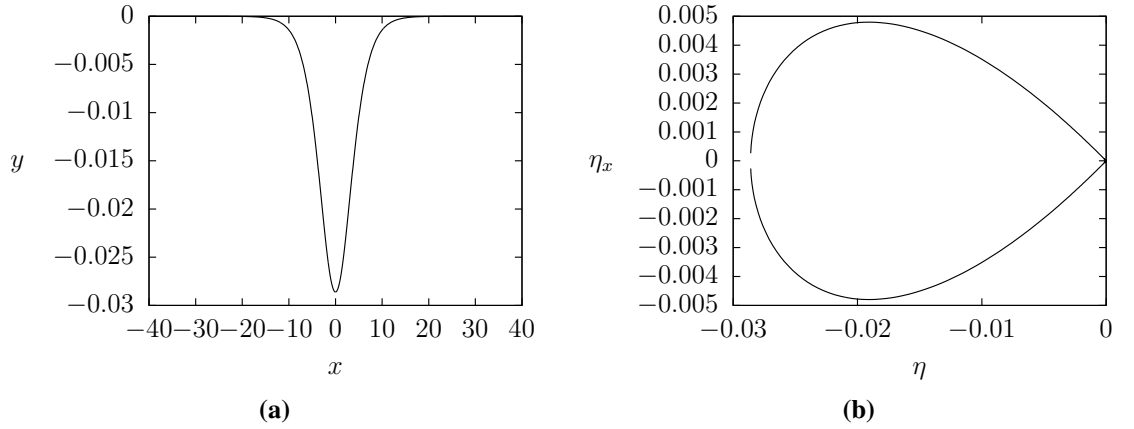

Figure 3.6: (a) Pure depression solitary wave solution profile with $F = 0.99$ and $\beta = 0.49$. The phase portrait of the solution given in (a) is shown in (b).

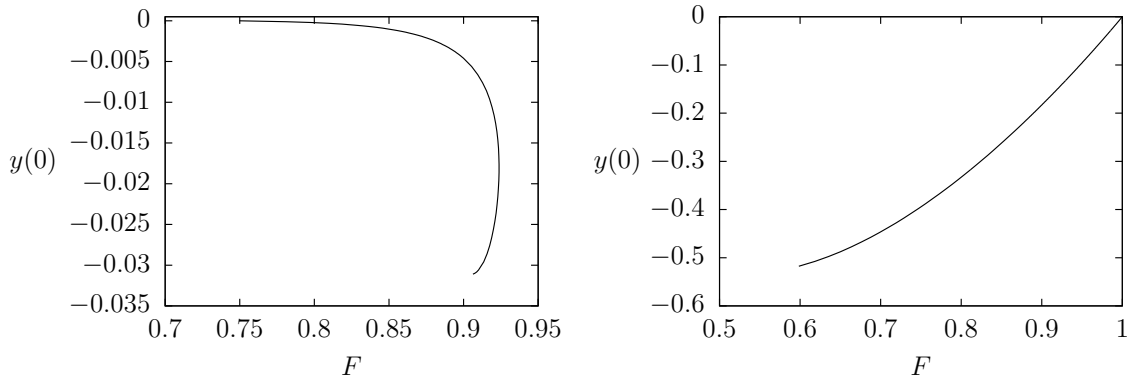

Figure 3.7: Solution branches in the $F - y(0)$ plane for (a) a forced solitary type wave solution profile with $\epsilon_1 = \epsilon_2 = 0.05$, and (b) the pure solitary wave solution shown in figure 3.6. In (a), $y(0)$ is the amplitude of the free surface between the two depressions, whereas in (b), $y(0)$ is the amplitude of the pure solitary wave.

$F^{**} < F < F^*$, two families of solitary wave solutions may be found; perturbations from the uniform stream, and perturbations from a pure solitary wave. Both solution branches determine depression waves. These three regions in the $y(0) - F$ plane are in agreement with the findings of Maleewong, Asavanant and Grimshaw [77] for flow disturbed by a single localised pressure distribution, as discussed in section 2.4. The solid curve solution in figure 3.5(b) is a perturbation from a pure solitary wave. As $\epsilon_1 \to 0$ and $\epsilon_2 \to 0$, the free surface profile tends to the pure solitary wave solution shown in figure 3.6. So the two-wave forced depression solitary wave bifurcates from a single pure solitary wave. In figure 3.7(b) we plot part of the pure solitary wave solution branch, from which our forced two-trough solution bifurcates, in the $F - y(0)$ plane.

Next, we look for negatively forced profiles, where $\epsilon_1 < 0$ and $\epsilon_2 < 0$. The associated depression waves are obtained by firstly using parameter continuation on the amplitude of a positively forced depression wave perturbating from the uniform stream, as discussed previously. After the turning point in the $F - y_{max}$ plane, the coefficients ϵ_1 and ϵ_2 on the pressure distributions are gradually decreased to zero to give a pure depression solitary wave. The coefficients can then be reduced further to obtain another depression wave bifurcating from the pure solitary wave solution, but with $\epsilon_1 < 0$ and $\epsilon_2 < 0$. Parameter continuation can then be used on the amplitude of one of the troughs in this solution, to move along the negatively forced solution branch. In figure 3.8(a) we show a typical solution profile with pressures determined by $\epsilon_1 = \epsilon_2 = \epsilon = -0.05$, centred at $\phi = \pm 3$. The corresponding phase portrait is shown in figure 3.8(b). Despite the presence of two separate localised pressures, the solution profile here consists of a single large trough, with slight elevations just before the depression. Negatively forced elevation waves can also be obtained. They are bifurcations from the uniform stream, so are of much smaller

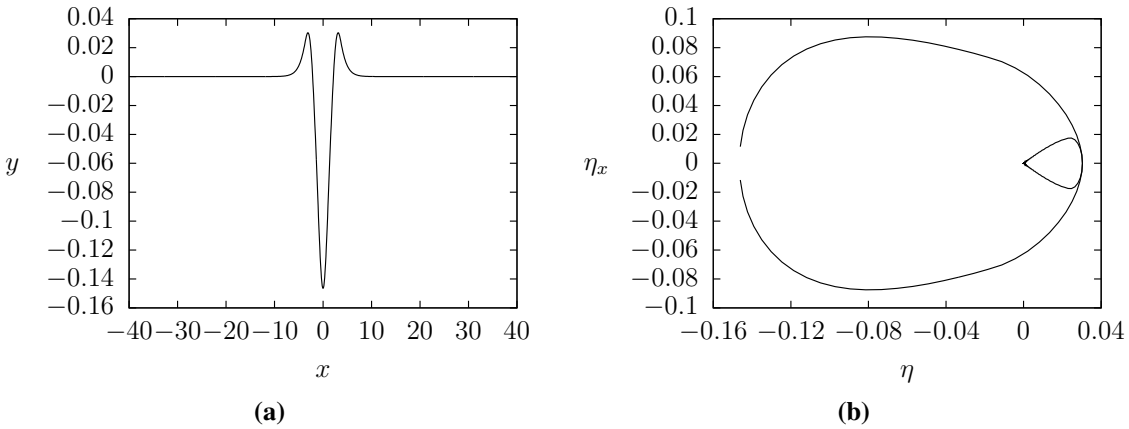

Figure 3.8: (a) Typical solitary wave solution profile with $\epsilon_1 = \epsilon_2 = -0.05$, bifurcating from a pure depression solitary wave. The two pressures are centred at $a = 3$, $b = -3$. The corresponding phase portrait is shown in (b).

amplitude than the associated depression waves. A typical solution profile is shown in figure 3.9.

As the distance x_d between the obstacles decreases, the wave (with either $\epsilon > 0$ or $\epsilon < 0$) bifurcating from the pure depression solitary waves reduces to the classical free surface profile obtained for flow over a single disturbance; see the solid curve in figure 3.10 and the broken curve in figure 3.9(a). These solution profiles bifurcate from a single pure solitary wave. Conversely, as the distance x_d increases, the wave profile becomes that of two classical solutions over two separate disturbances; the depression waves made by the localised pressure distributions do not appear to influence one another. So next we ask the question, how far apart must we move the two pressure distributions in order for the larger amplitude solution to bifurcate from two pure solitary waves rather than just the one? In answer to this question, we keep β fixed, and find that we can actually obtain solutions bifurcating from two solitary waves when $x_d = 6$, where the pressures are located at $\phi = \pm 3$. However, previously we showed a solution with pressures at $\phi = \pm 3$, where the larger solution bifurcated from a single pure solitary wave. The difference is in the parameter continuation. We find that in order to obtain a solution bifurcating from a two-peaked solitary wave, one must manipulate the amplitude of one (or both) of the troughs, rather than $y(0)$. A typical solution profile bifurcating from a two-troughed wave is shown in figure 3.11. Here, the localised pressures are centred at $\phi = \pm 5$ and one can see that the minimum of the troughs does not occur exactly under the pressure distribution. This phenomenon is similar to that seen by Binder *et al.* [18] for pure gravity flow past two submerged obstructions. When x_d is reduced so that the pressures are located at $\phi = \pm 2.5$ the solutions in both cases, whether we perform parameter continuation on the amplitude of the troughs or on $y(0)$, bifurcate from just a single solitary wave. The critical value of x_d therefore appears to be between $x_d = 5$ and

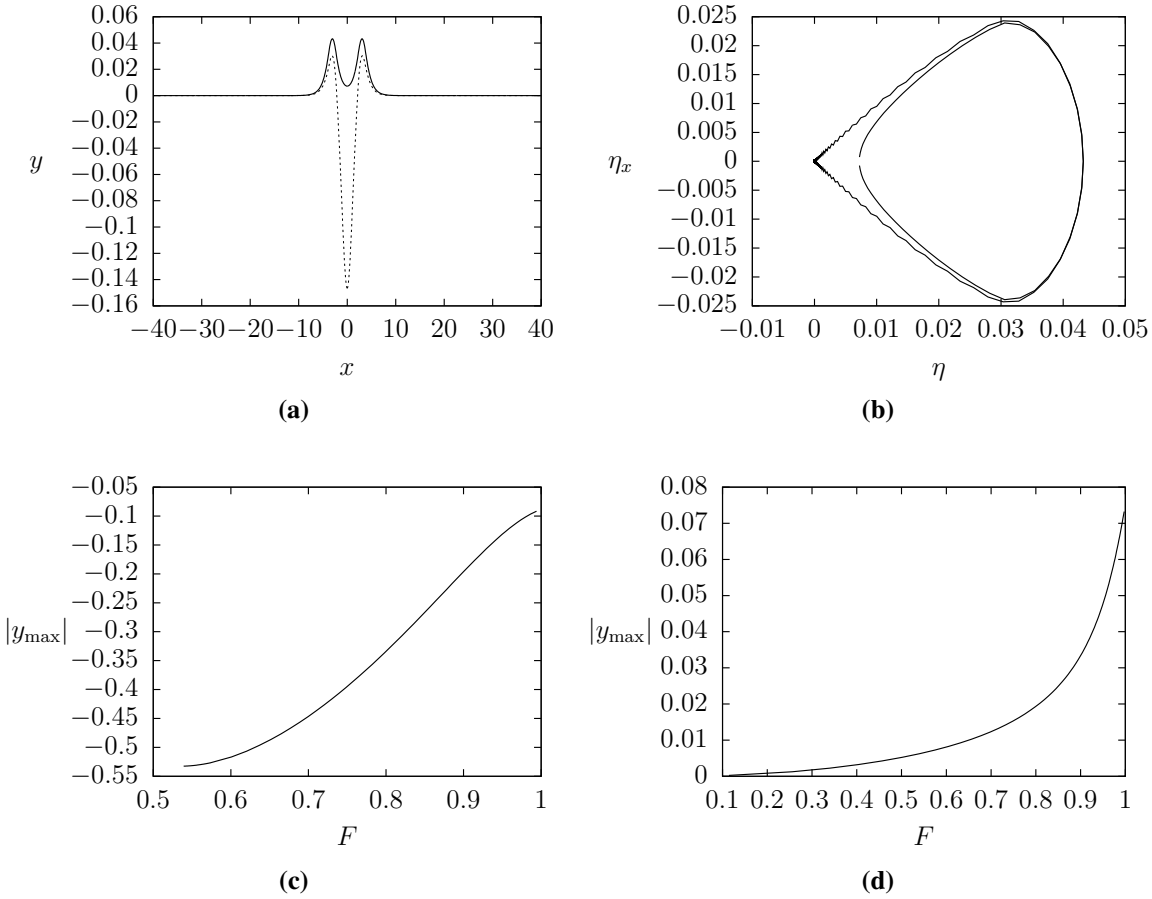

Figure 3.9: (a) Solution profiles past two negatively orientated pressure distributions ($\epsilon_1 = \epsilon_2 = -0.05$) with $F = 0.94$ and $\beta = 0.49$. The solid profile is a solution bifurcating from the uniform stream, and the dashed profile is the solution bifurcating from a pure solitary wave, shown in figure 3.8. The phase portrait corresponding to the bifurcation from the uniform stream is shown in (b). The solution branches in the $F - |y_{max}|$ for the depression and elevation waves are shown in figures (c) and (d) respectively.

$x_d = 6$.

When $\epsilon_1 < 0$ and $\epsilon_2 < 0$, as $F \to 1$ the amplitude of the peak between the two troughs increases, and a flat region between the troughs can be approached. This is illustrated by the solution profiles in figure 3.12, and the solution branches in figure 3.13. If we gradually increase the distance x_d between the two pressure distributions, the free surface between the two troughs steepens and eventually approaches the level of the undisturbed flat stream far upstream. Conversely, as we gradually decrease x_d, the region between the troughs flattens more quickly, and the amplitude of the region gradually increases.

We also obtain solutions with $\epsilon_1 = \epsilon_2 < 0$, which, when $F \to 1$, have a dimple on the region of the free surface between two troughs. A typical solution profile can be seen in figure 3.14(a), where the pressures are centred at $\phi = \pm 3$. If we continue to decrease the amplitude of one of the troughs, the Froude number increases further towards one, and the amplitude of the 'dimple' becomes of similar amplitude to the two troughs. The

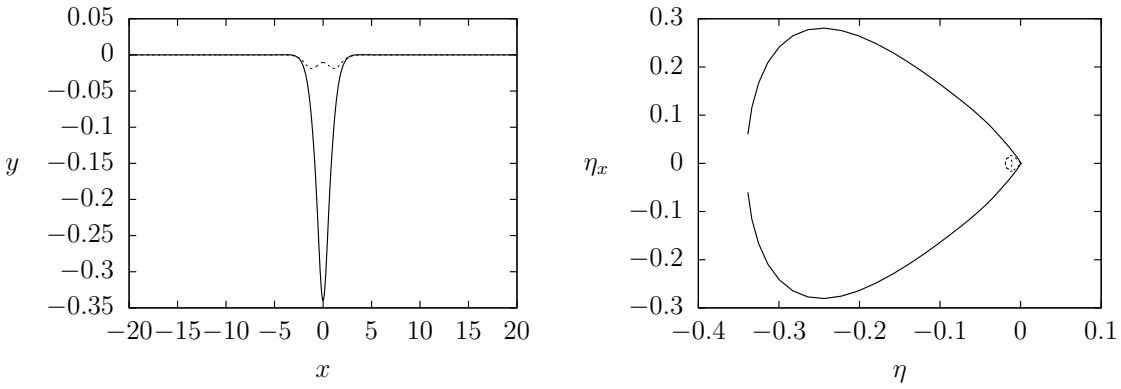

Figure 3.10: Fully nonlinear wave profiles for $\epsilon_1 = \epsilon_2 = 0.05$, $x_d = 2.4$, $\beta = 0.49$, and $F = 0.78$. The pressures are centred at $a = 1.2$ and $b = -1.2$. The broken curve is a perturbation from a uniform stream and the solid curve a perturbation from a pure depression solitary wave. The respective phase portraits are shown in (b).

solution therefore takes the form of one large depression wave, with smaller waves in its trough, as can be seen in figure 3.14(c). In figure 3.15 we show the branch of solutions with $\epsilon_1 = \epsilon_2 = -0.01$ and $\beta = 0.49$, with pressure distributions centred at $\phi = \pm 3$.

We can obtain an interesting result now by starting with the solution shown in figure 3.14(c), and increasing the amplitude of the dimple; $y(0)$. This results in the amplitude of the middle wave increasing beyond the amplitude of the two original troughs, as shown in figure 3.16(a). It may be possible to continue increasing this amplitude much further so that we obtain three distinct depression waves. When attempting this, we see that the location of the two original troughs changes; they move away from the third trough centred at $y(0)$. However, the distance they move appears to change with grids of different densities, and so we are unable to confirm that such a solution really does exist.

So far, all the results presented, whether computed using a symmetric version of the numerical method or not, have been symmetric about $x = 0$. A nonsymmetric solution can be found by taking $\epsilon_1 \neq \epsilon_2$. By setting $\epsilon_1 > 0$ and $\epsilon_2 < 0$ we obtain a depression wave near the positively forced pressure distribution, and an elevation wave near the negatively forced distribution, see figure 3.17. This solution is similar, but of opposite orientation, to the solution obtained by Binder *et al.* [18] for pure gravity flow over a triangular dip and a triangular obstruction at the bottom of the channel. Using parameter continuation on the amplitude of the depression wave, we find a turning point in the $y_{\max} - F$ plane. Figure 3.18(a) shows such a typical solution branch in the $F - y_{\max}$ plane, where $y_{\max}$ is the maximum amplitude of the depression wave. The amplitude of the elevation wave is found as part of the solution, and in figure 3.18(b) we plot the maximum of this elevation, against the Froude number, to see how it changes with the change in the depression wave. Next, we use parameter continuation on the amplitude of the elevation wave, but find that

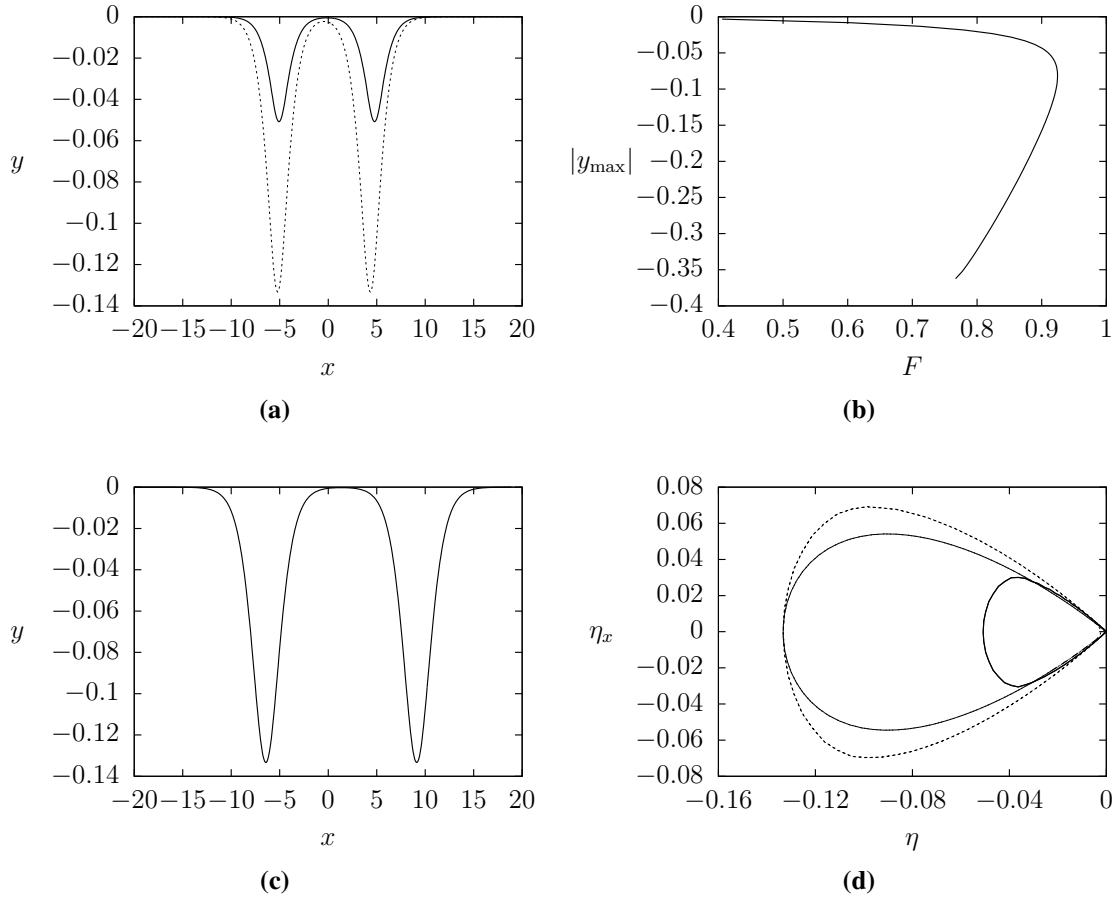

Figure 3.11: (a) Typical solution profiles for flow past two localised pressure distributions centred at $a = 5$, $b = -5$ for the parameters $F = 0.91$ and $\beta = 0.49$. The solid line solution is a bifurcation from the uniform stream, whereas the dashed line solution bifurcates from the pure solitary wave solution shown in (c). The branch of solutions in the $F - y_{max}$ plane for the pressure distributions used in (a), β fixed, is shown in (b). In (d) we plot the phase portraits of the solution bifurcating from the uniform stream in (a) (the thick solid line), the solution bifurcating from a pure solitary wave solution in (a) (the broken line), and the pure wave solution in (c) (the thin solid line).

we simply obtain the same solution branches as those obtained when using the depression wave; i.e. the branches in figure 3.18.

These nonsymmetric solution profiles are therefore also multivalued for some particular values of the Froude number. The wave profile given by the broken curve in figure 3.17(b) is a perturbation from the uniform stream. The solid curve solution in figure 3.17(b) is more complex. After the turning point on the solution branch is reached, decreasing/increasing the pressure forcings to zero reduces the amplitude of the elevation to zero, but the depression wave reduces to a pure depression solitary wave. The elevation is therefore a perturbation from the uniform stream, but the depression is a perturbation from a pure depression solitary wave. This is in agreement with the gravity-capillary results obtained by Maleewong *et al.* [77] in the case of flow past a single forcing; any

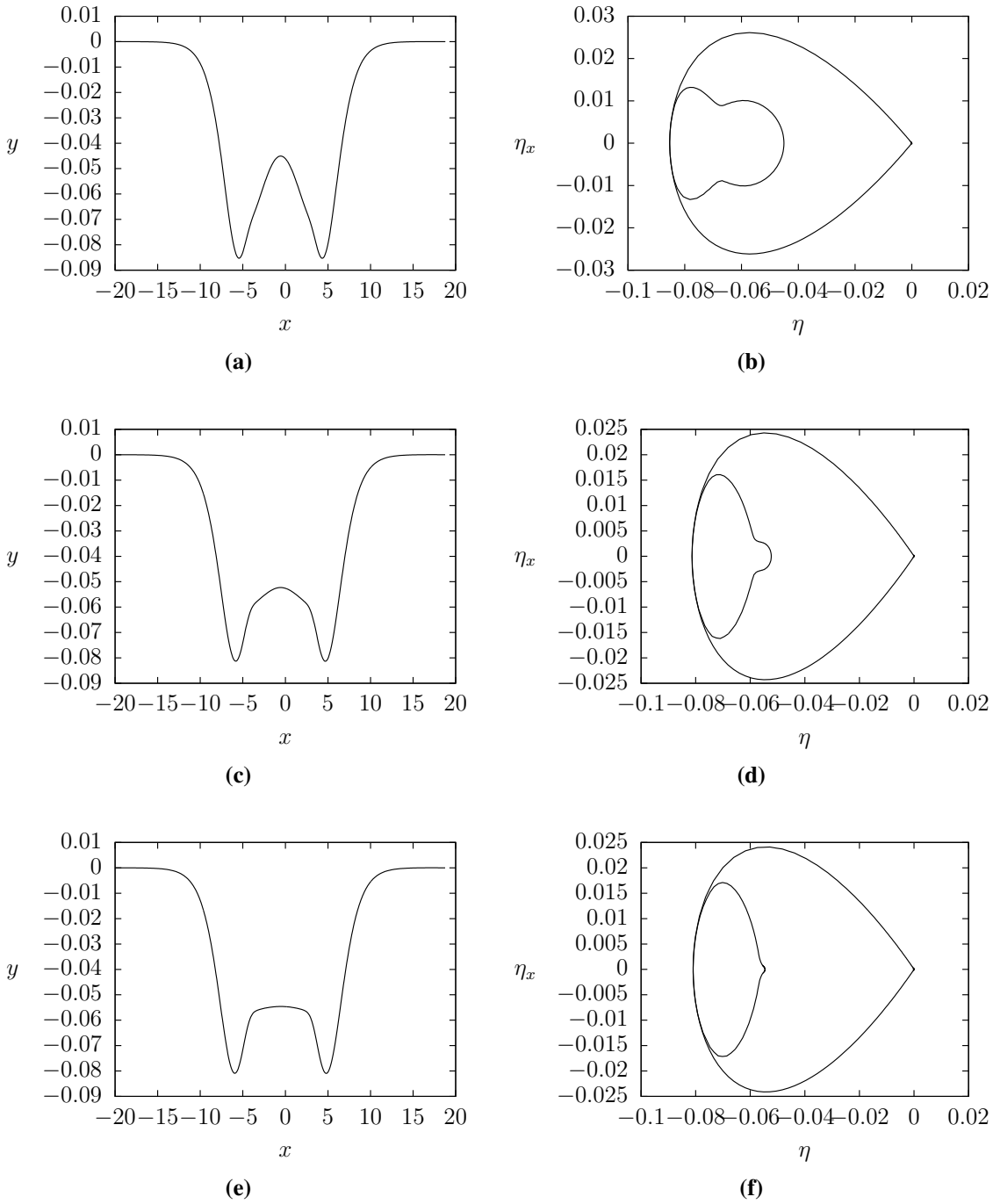

Figure 3.12: Negatively forced fully nonlinear free surface profiles bifurcating from a pure solitary wave. Here, $\epsilon_1 = \epsilon_2 = -0.01$, $x_d = 8$ and $\beta = 0.49$. The pressures are centred at $a = 4$ and $b = -4$. The Froude number is given by (a) $F = 0.9558$, (c) $F = 0.9579$ and (e) $F = 0.9581$. Figures (b), (d) and (f) show the phase portraits of the solutions in (a), (c) and (e) respectively.

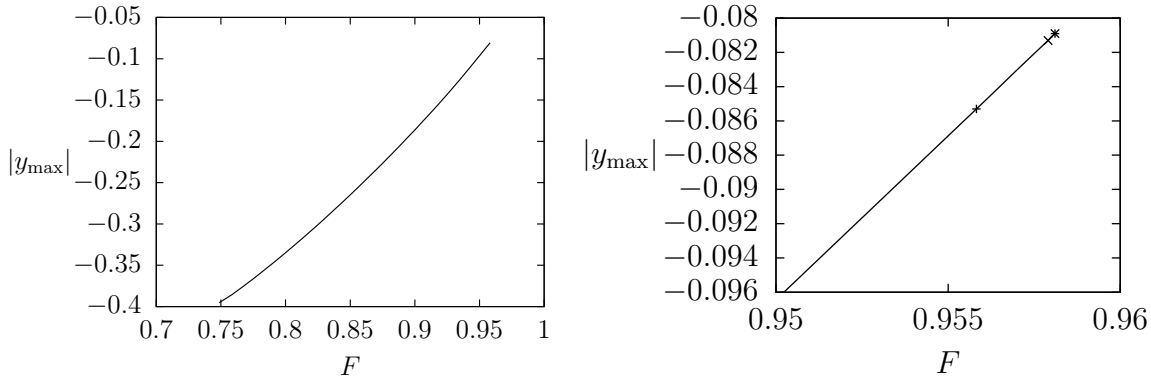

(a) **(b)**

Figure 3.13: Negatively forced solution branches in the $F - y_{max}$ plane. The pressures are centred at $a = 4$, $b = -4$ where $\epsilon_1 = \epsilon_2 = -0.01$ and $\beta = 0.49$ are fixed. (b) shows a close up of (a). The points marked by the $+$, $\times$ and $*$ symbols represent where figures 3.12(a), 3.12(c) and 3.12(e) respectively, appear on the solution branch.

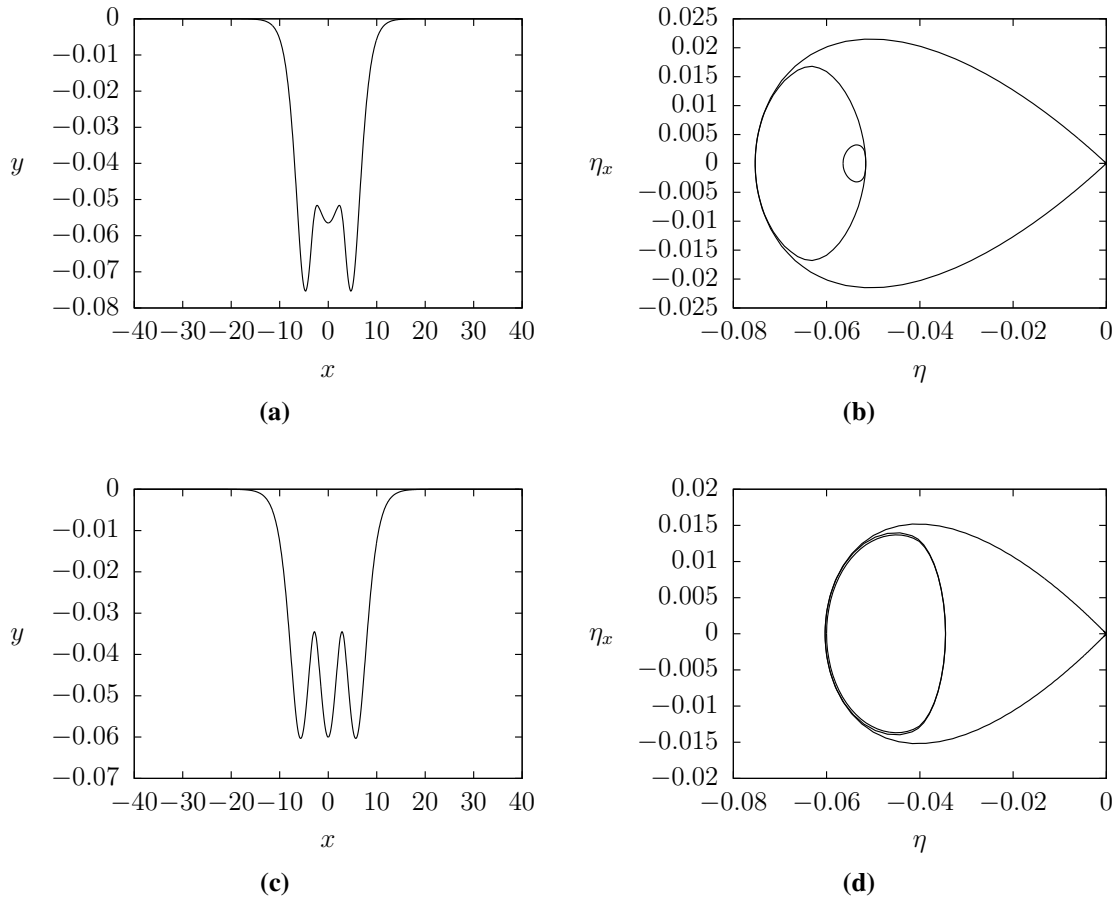

(a) **(b)**

(c) **(d)**

Figure 3.14: Free surface solution profiles subject to two localised negatively orientated pressures with $\epsilon_1 = \epsilon_2 = -0.01$. The Froude number is given by (a) $F = 0.961$, (c) $F = 0.969$, and in each case $\beta = 0.49$. The phase portraits for figures (a) and (c) are shown in (b) and (d) respectively.

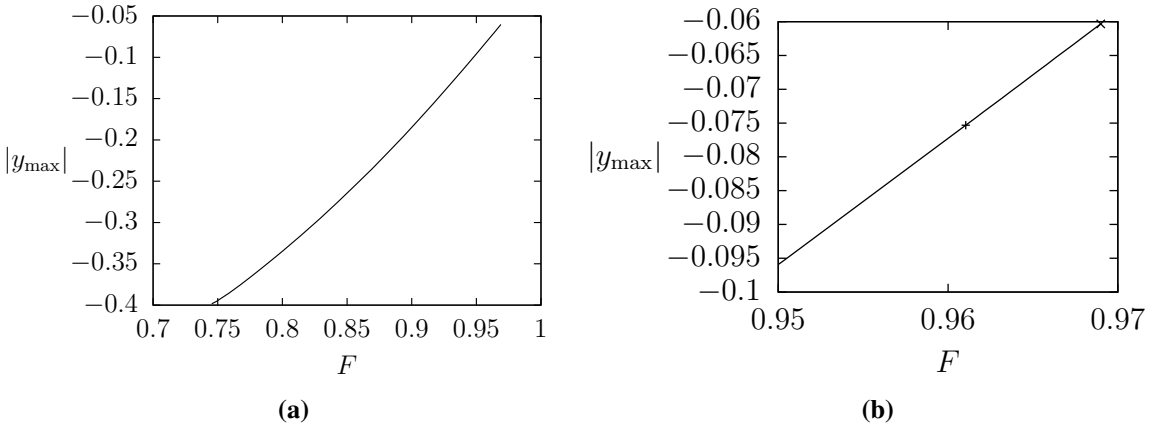

Figure 3.15: Negatively forced solution branches in the $F - y_{max}$ plane. The pressures are centred at $a = 3$, $b = -3$, where $\epsilon_1 = \epsilon_2 = -0.01$ and $\beta = 0.49$ are fixed. (b) shows a close up of (a). The points marked by the $+$ and $\times$ symbols represent where figures 3.14(a) and 3.14(c) respectively, appear on the solution branch.

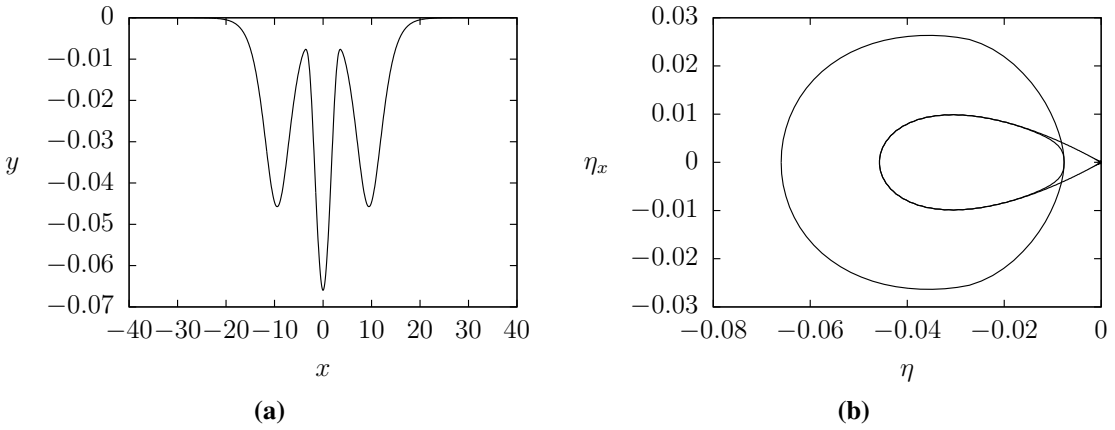

Figure 3.16: Free surface solution profiles subject to two localised negatively orientated pressures with $\epsilon_1 = \epsilon_2 = -0.01$. The Froude number is given by $F = 0.977$ and $\beta = 0.49$.

elevation solitary wave in a flow configuration where $F < 1$ and $\tau > \frac{1}{3}$ must be a perturbation from the uniform stream and not a pure solitary elevation wave.

So far, in all the results presented, the Weber number has been fixed at $\beta = 0.49$. We now investigate the effects of changing β. So we modify the numerical scheme to fix the Froude number and the amplitude of the waves, and allow β to come as part of the solution. Using parameter continuation on the amplitude of one of the troughs, we can then obtain a solution branch in the $\beta - |y_{max}|$ plane to see how the Weber number changes with the amplitude of the waves. We fix the Froude number F, and consider both the solutions with $\epsilon_1 = \epsilon_2 > 0$, and those with $\epsilon_1 = \epsilon_2 < 0$, and sketch the solution branches in figure 3.19. In figure 3.19(a) we see that a turning point exists on the solution branch for $\epsilon_1 = \epsilon_2 > 0$, at some small value of β. When the maximum amplitude

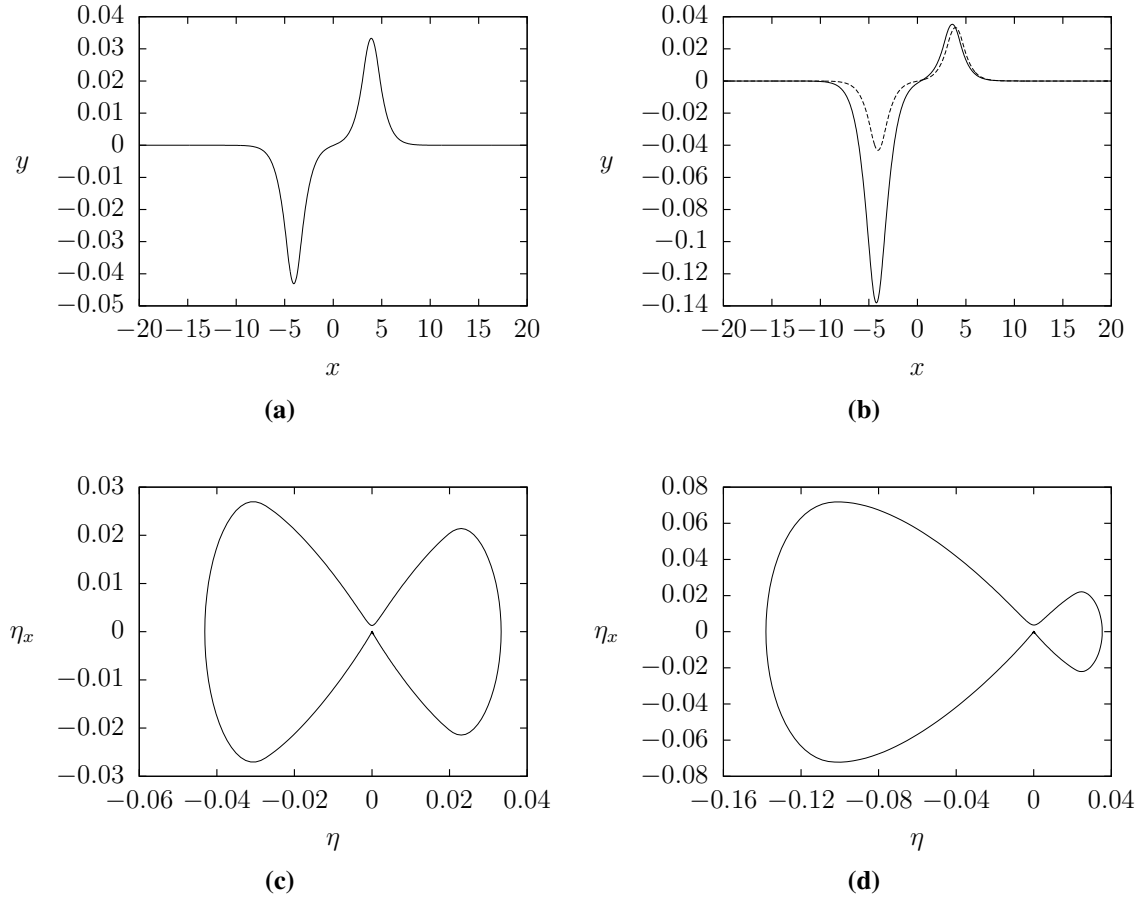

Figure 3.17: Fully nonlinear wave profiles for $\epsilon_1 = 0.05, \epsilon_2 = -0.05$, $x_d = 8$, $\beta = 0.49$, and $F = 0.91$. The pressures are centred at $a = 4$ and $b = -4$. (a) shows the solution perturbating from a uniform stream and has maximum depression amplitude -0.043 and maximum elevation 0.033. (b) shows the solution where the depression wave on the solid curve is a perturbation from a pure depression solitary wave and has maximum amplitude -0.14. The elevation wave is a perturbation from the uniform stream, with maximum elevation 0.035. The dashed curve is the solution perturbating from the uniform stream, shown in (a). The phase portraits for the dashed and solid line solutions shown in (b) are shown in figures (c) and (d) respectively.

of the solution is small, we see that if we decrease the surface tension, the maximum amplitude will increase. After the turning point however, decreasing the surface tension will cause the maximum amplitude to decrease. As in the case of the solution branches in the $F - y_{max}$ plane, the turning point represents the point at which the solutions cease to bifurcate from the uniform stream, and instead bifurcate from a pure depression solitary wave. In figure 3.19(b) we see that when $\epsilon_1 = \epsilon_2 < 0$, decreasing the surface tension will increase the amplitude of the elevation bifurcating from the uniform stream, but will decrease the amplitude of the depression wave bifurcating from a pure solitary wave.

Sketches of solutions with different values of β are shown in figures 3.20 and 3.21. One can see that as the surface tension decreases, decaying oscillations begin to appear in the tails of the forced solitary waves. Similar behaviour is seen in the case of flow

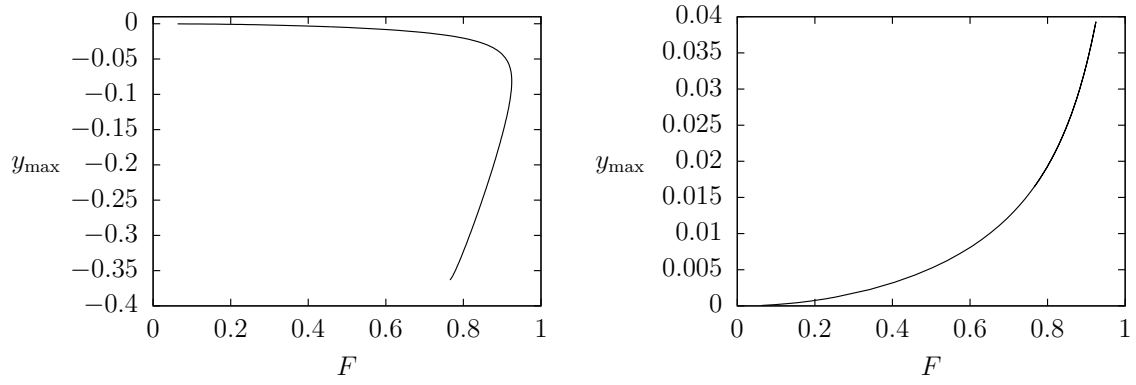

Figure 3.18: Solitary wave solution branches for flow past two localised pressure distributions of different orientations ($\epsilon_1 = 0.05$, $\epsilon_2 = -0.05$ and $x_d = 8$), in the $F - y_{\max}$ plane, where $y_{\max}$ is the maximum amplitude of (a) the depression wave and (b) the elevation wave.

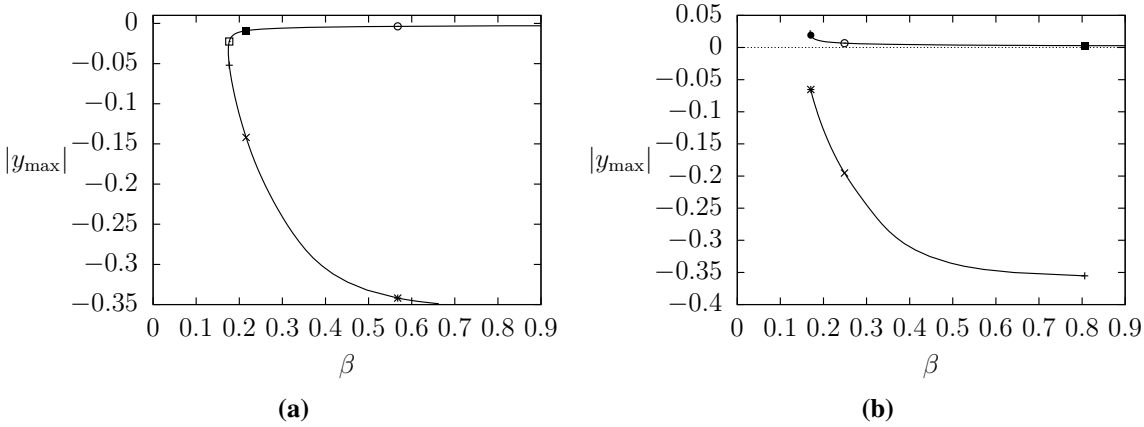

Figure 3.19: Solution branches in the $\beta - |y_{max}|$ plane. In (a) $\epsilon_1 = \epsilon_2 > 0$ and the points marked by $\circ$, $\blacksquare$, $\square$, $+$, $\times$ and $*$ represent the points at which the sketches in figures 3.20(a), 3.20(c) and 3.20(e) occur respectively, bifurcating from both the uniform flow and the pure solitary wave accordingly. In (b) $\epsilon_1 = \epsilon_2 < 0$ and the points marked by $\blacksquare$, $\circ$, $\bullet$, $+$, $\times$ and $*$ represent the points at which the sketches in figures 3.21(a), 3.21(c) and 3.21(e) occur respectively, bifurcating from both the uniform flow and the pure solitary wave accordingly.

past a single disturbance with weak surface tension, studied for example by Maleewong *et al.* [78]. When $\beta < 1/3$, the linear dispersion relation possesses a minimum, see for example Dias and Iooss [36], and so there exists a minimum Froude number $F_{\min}$ and a corresponding minimum wavenumber $k_{\min}$. Solitary wave solutions are computed in the region in which the Froude number does not intersect the linear dispersion relation. Therefore, when there exists a minimum $F_{\min} < 1$, the solitary waves can only exist for a smaller range of Froude numbers $F < F_{\min} < 1$. In chapter 2 we discussed how in this region of weak surface tension, the solitary wave solutions take the form of envelope solitary waves. There exist more points of inflection in the solution as one approaches

the minimum of the linear dispersion relation, resulting in more decaying oscillations appearing on the free surface. So, the smaller the value of β, the more oscillations that appear on the free surface. This is clearly shown in figures 3.20 and 3.21. The increasing number of inflection points on the free surface makes the solutions harder and harder to compute as one approaches the minimum Froude number, with the calculations becoming formidable when F is near $F_{\min}$. More and more mesh points are therefore required on the free surface in order to produce accurate solutions.

3.5 Conclusions

We have examined the free surface of a fluid subjected to two distinct localised pressure distributions, in the subcritical flow regime. Fully nonlinear numerical results, calculated using a boundary integral equation method based on Cauchy's integral formula, have been presented. We have shown that, as in the case of gravity-capillary solitary waves subject to a single disturbance in the channel (Maleewong *et al.* [77]), multiple families of solutions exist for particular values of the Froude number. In the case of positively orientated pressure distributions, depression solitary waves bifurcate from the uniform stream or from either one or two pure depression solitary waves, depending on the distance between the two pressure distributions. We have shown that elevation waves only exist when the pressure distribution is negatively forced. They are always perturbations from the uniform stream. Our findings are thus in agreement with those of Maleewong *et al.* [77].

Following the ideas of Binder *et al.* [18] in the pure gravity case, we went on to show that other, new types of solution can be obtained in the gravity-capillary regime by the inclusion of a second pressure distribution. These solutions included, for example, one large depression wave with additional waves in its trough, and a nonsymmetric profile with a depression wave bifurcating from a pure depression solitary wave upstream and an elevation wave bifurcating from the uniform stream downstream.

Finally, we presented solution profiles with weaker surface tension, which take the form of wave packets; solitary waves with decaying oscillations in their tails.

We also briefly examined the effects of restricting the scope of the surface tension acting on the free surface. The aim was to restrict the surface tension to just the central part of the domain, local to a single pressure distribution. To achieve this, we used two different methods. Firstly, we, somewhat naively, introduced an additional parameter to the numerical scheme which was set to one if the surface tension was present and zero otherwise. This parameter then allowed us to turn on and off the influence of surface tension at different points, simply by multiplying it by the Weber number. Secondly, we removed the abrupt changes from full surface tension to no surface tension, by writing

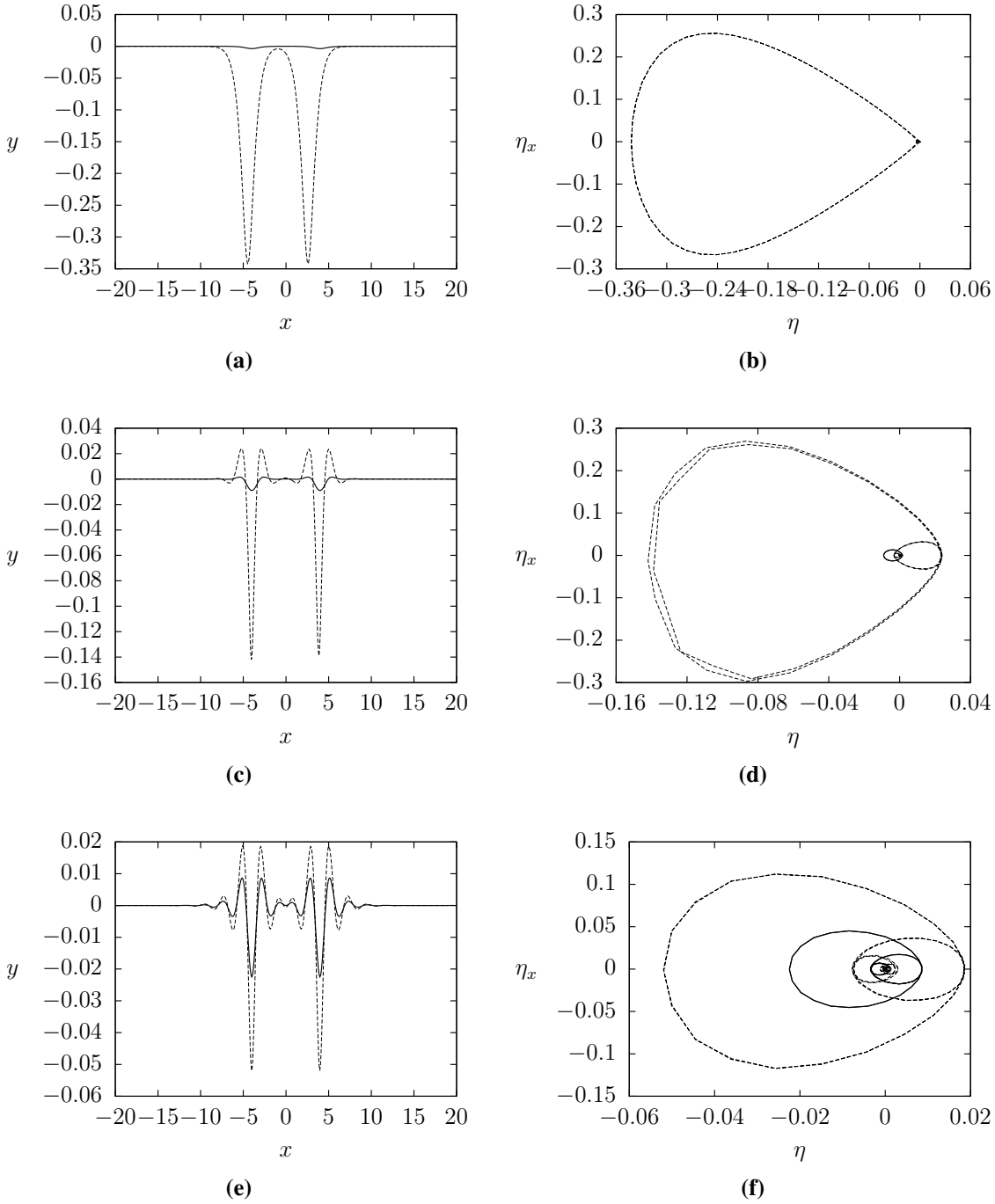

Figure 3.20: Sketches of typical solution profiles with corresponding phase portraits, for $\epsilon_1 = \epsilon_2 > 0$. The value of F is fixed in each figure, and β is given by (a) $\beta \approx 0.57$, (c) $\beta \approx 0.22$, (e) $\beta \approx 0.18$. In each figure the solid curve is a sketch of a solution bifurcating from the uniform stream and the broken curve, a solution bifurcating from a pure depression solitary wave.

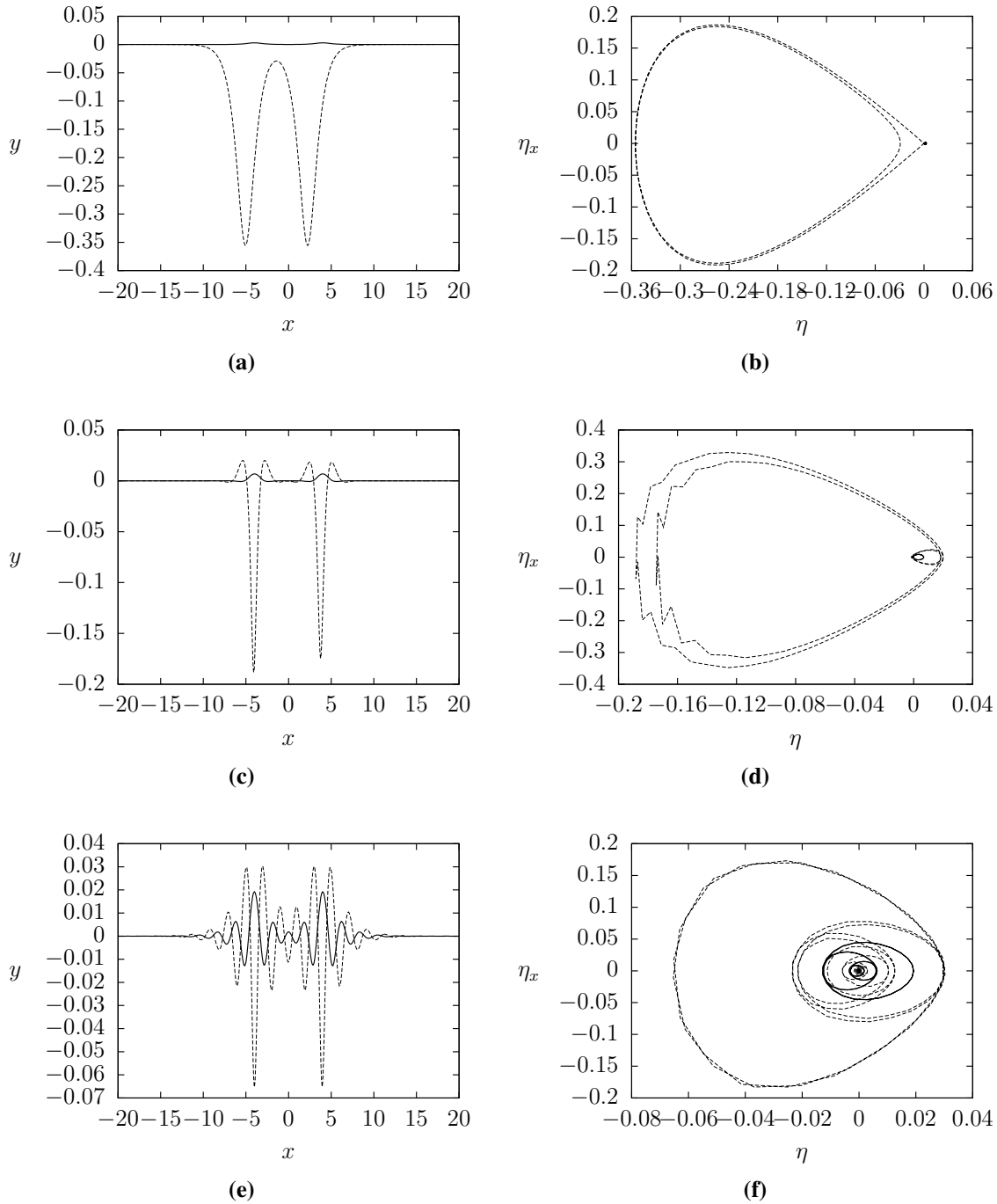

Figure 3.21: Sketches of typical solution profiles with corresponding phase portraits, for $\epsilon_1 = \epsilon_2 < 0$. The value of F is fixed in each figure, and β is given by (a) $\beta \approx 0.81$, (c) $\beta \approx 0.25$, (e) $\beta \approx 0.17$. In each figure the solid curve is a sketch of a solution bifurcating from the uniform stream and the broken curve, a solution bifurcating from a pure depression solitary wave.

the surface tension as a smooth function of position.

After restricting the surface tension, the force of gravity alone is present far up and downstream, so we continue to require $y(1) = y(2) = 0$ to satisfy the radiation condition. However, we are no longer looking for a solitary wave in the pure gravity regime, so we can relax the condition which ensures that the free surface is flat downstream. We found that this resulted in a subcritical gravity-capillary orientated solitary wave local to the disturbance (as in Maleewong *et al.* [77]), but with wave trains of different amplitudes up and downstream in the pure gravity regime. We know that for a subcritical pure gravity flow, gravity waves occur downstream of a forcing (see the second classical type of solution). The turning off of the surface tension may act as such a forcing, so waves may indeed be predicted downstream here. The upstream waves are clearly unphysical however, as they violate the radiation condition. It also appears that many more mesh points are required on the free surface to accurately describe the existence of any gravity waves. On some meshes of the free surface for example, we were able to remove the gravity waves completely, so the existence of such waves is even questionable. However, this may be due to the lack of a condition that $\eta_{xx} = 0$ at the point at which the surface tension disappears. At this point, we have that $\eta(x) = 0$ from the solitary wave upstream, and we must have that $\eta_{xx} = 0$ to satisfy the Bernoulli condition (3.3.27) continuously. In order to obtain waves after the surface tension is switched off we would therefore require that $\eta_x \neq 0$ at this point. Theoretically this is possible (e.g. $\eta = \sin(x)$ at $x = \pi$), but as the free surface is flat upstream of this point due to the solitary wave, it may not be possible, and is certainly not easy, to obtain a match between a wavy solution downstream and the solitary wave.

To improve the accuracy of our solutions with waves, we briefly examined the use of a variable mesh on the free surface. We concentrate the mesh points around the area of interest by changing e, the distance between the mesh points, so that it is no longer constant. As well as the obvious changes in the numerical scheme requiring that we replace e with $\phi_{i+1} - \phi_i$, we also have to recompute the finite differences. Therefore we consider the Taylor series expansion of ϕ about the i_{th} mesh point:

$$\phi_{i+1} = \phi_i + h_{i+1}\phi_i' + \frac{h_{i+1}^2}{2}\phi_i'' + ..., \tag{3.5.1}$$

$$\phi_{i-1} = \phi_i - h_{i-1}\phi_i' + \frac{h_{i-1}^2}{2}\phi_i'' + ..., \tag{3.5.2}$$

where h_{i+1} and h_{i-1} represent the two different mesh spacings and the prime here denotes the derivative, with respect to x for example. Multiplying (3.5.1) by h_{i-1}^2 and (3.5.2) by

$-h_{i+1}^2$ and adding the result gives

$$h_{i-1}^2\phi_{i+1} - h_{i+1}^2\phi_{i-1} = h_{i-1}^2\phi_i + h_{i+1}h_{i-1}^2\phi_i' - h_{i+1}^2\phi_i + h_{i+1}^2h_{i-1}\phi_i' + ... \tag{3.5.3}$$

$$\Rightarrow \phi_i' \approx \frac{h_{i-1}^2\phi_{i+1} + (h_{i+1}^2 - h_{i-1}^2)\phi_i - h_{i+1}^2\phi_{i-1}}{h_{i+1}h_{i-1}(h_{i-1} + h_{i+1})}. \tag{3.5.4}$$

Letting $\alpha = h_{i+1}/h_{i-1}$ and dividing through by h_{i-1}^2, we obtain

$$\phi_i' \approx \frac{\phi_{i+1} + (\alpha^2 - 1)\phi_i - \alpha^2\phi_{i-1}}{h_{i+1}(1 + \alpha)}, \tag{3.5.5}$$

(see Sundqvist and Veronis [114] for more details). These ideas, whilst not used to obtain the results presented in this thesis, provide possible means for computing further solution profiles in future work.

CHAPTER FOUR

CRITICAL FREE SURFACE FLOWS AND TRAPPED WAVE SOLUTIONS

4.1 Introduction

A single layer of fluid flowing in a channel of finite depth is considered as in chapter 3, but this time the disturbances are in the form of submerged obstructions on the bottom of the channel. Both the effects of gravity and surface tension are included, and the problem is solved using a modified version of the boundary integral equation method discussed in section 2.2. Critical flow solutions, where the flow is subcritical upstream and supercritical downstream, are sought. Multiple disturbances on the bottom of the channel are utilized to look for 'trapped wave' solutions. In the case of pure gravity flows, the addition of a second obstacle further upstream results in trapped waves appearing between the two obstacles. The wavetrain is thus found in the subcritical regime upstream of a hydraulic fall. Further upstream of the additional obstruction, as $x \to -\infty$, the flow is uniform. Such solutions were found by Dias and Vanden-Broeck [41]. The aim in this chapter is to extend this work by considering the effects of surface tension on the solutions. Critical flows over a single submerged obstruction are studied, and then trapped waves are sought by including an additional obstruction further up or downstream of the hydraulic fall.

The fully nonlinear problem is formulated in section 4.2. Section 4.3 then describes the numerical scheme, and the results are presented in section 4.4. Finally, in section 4.5 a summary of the results is provided, and conclusions are drawn.

4.2 Formulation

The two-dimensional free surface of an inviscid fluid flowing along a channel of finite depth is considered. The flow is assumed to be steady and is subjected to multiple disturbances in the form of obstructions on the bottom of the channel. Cartesian coordinates (x^*, y^*) are introduced and the x^*-axis is aligned so that it is parallel to the channel bottom in the absence of an obstruction. The y^*-axis is directed vertically upwards through one of the obstructions. Both the effects of gravitational acceleration g in the negative y^* direction and capillarity are included, where σ is the coefficient of surface tension on the free surface. The fluid is assumed to be incompressible with constant density ρ, and the flow irrotational. Equations (3.2.1) and (3.2.2) defined in section 3.2 are therefore satisfied. Thus, there exists a velocity potential $\phi^*(x^*, y^*)$ and a stream function $\psi^*(x^*, y^*)$ satisfying (3.2.3) and (3.3.4), such that

$$\nabla^2 \phi^* = 0, \tag{4.2.1}$$

is satisfied in the fluid domain.

We denote the free surface by $y^*(x^*) = H + \eta^*(x^*)$, and the function describing the bottom of the channel by $y^* = B^*(x^*)$. The flow is assumed to be uniform in the far field as $x^* \to \pm\infty$, with constant depth H and constant velocity U downstream, and constant depth h and constant velocity V upstream.

The dimensionless downstream Froude and Bond numbers are given by equations (2.1.6) and (2.1.2) respectively. The upstream Froude number is given by equation (2.3.1), and here it is also necessary to introduce the upstream Bond number which, we define as

$$\tau_{\rm up} = \frac{\sigma}{\rho g h^2}. \tag{4.2.2}$$

Hydraulic fall solutions are sought, which are critical flow solutions where the flow upstream of an obstacle is subcritical and uniform, and downstream of the obstacle is supercritical and uniform. The change in the Froude number from subcritical ($F_{\rm up} < 1$) to supercritical ($F > 1$) implies that the depth of the fluid must decrease as one travels downstream past the obstruction (i.e. we require $h > H$).

The kinematic boundary conditions on the free surface $y^*(x^*) = H + \eta^*(x^*)$ and the channel bottom $y^* = B^*(x^*)$ are given by

$$-\frac{\partial \phi^*}{\partial x^*}\frac{\partial \eta^*}{\partial x^*} + \frac{\partial \phi^*}{\partial y^*} = 0, \tag{4.2.3}$$

$$-\frac{\partial \phi^*}{\partial x^*}\frac{\partial B^*}{\partial x^*} + \frac{\partial \phi^*}{\partial y^*} = 0, \tag{4.2.4}$$

respectively.

The dynamic boundary condition on the free surface comes from satisfying Bernoulli's equation (3.2.7) everywhere in the fluid. As $x^* \to \infty$ we require that $\mathbf{u}^*(x^*, y^*) \to (U, 0)$ and $y^* \to H$. The Bernoulli constant $\mathcal{B}$ is therefore defined by

$$\mathcal{B} = \frac{1}{2}\rho U^2 + P + \rho g H, \tag{4.2.5}$$

where P is the pressure in the fluid at the free surface. Substituting B into the Bernoulli equation at the free surface, we obtain

$$\begin{aligned} P_a + \frac{1}{2}\rho(u^{*2} + v^{*2}) + \rho g y^* &= \frac{1}{2}\rho U^2 + P + \rho g H, \\ \Rightarrow \frac{1}{\rho}(P_a - P) + \frac{1}{2}(u^{*2} + v^{*2} - U^2) + g(y^* - H) &= 0, \\ \Rightarrow \quad \frac{-\sigma}{\rho}\nabla \cdot \mathbf{n} + \frac{1}{2}(u^{*2} + v^{*2} - U^2) + g(y^* - H) &= 0, \end{aligned} \tag{4.2.6}$$

where we have used the Young Laplace equation (1.2.19) in the form $P - P_a = \sigma \nabla \cdot \mathbf{n}$.

The mass of the fluid must be conserved up and downstream, so we obtain

$$UH = Vh. \tag{4.2.7}$$

Next, we non-dimensionalise the problem by taking U as the unit velocity scale and H as the unit height. Then, we define the the upstream non-dimensional flow velocity γ by $\gamma = V/U$. From (4.2.7) we can then obtain the non-dimensional upstream depth, $1/\gamma$. A sketch of the dimensionless flow configuration is shown in figure 4.1.

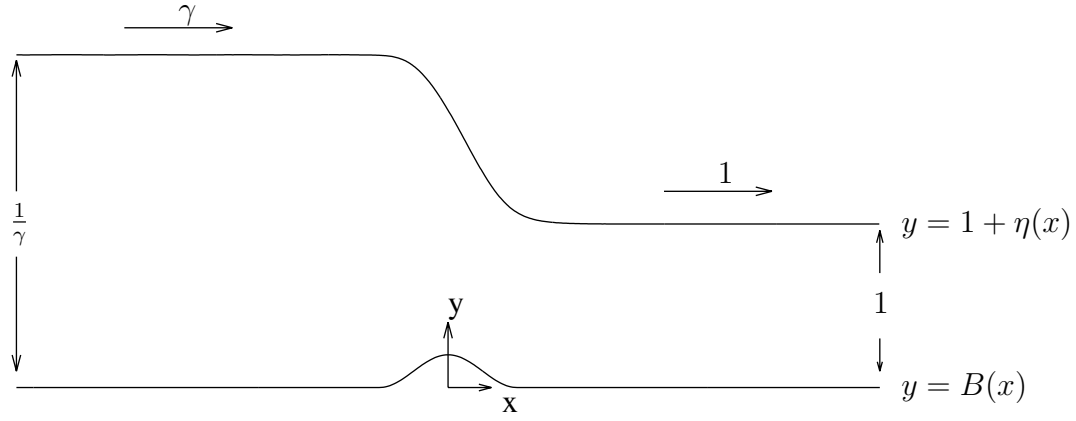

Figure 4.1: Dimensionless flow configuration over an arbitrary obstacle on the bottom of the channel.

Non-starred variables are now understood to be dimensionless. The Laplace equation (4.2.1) and the boundary conditions (4.2.3), (4.2.6) and (4.2.4) then become

$$\nabla^2\phi = 0 \qquad B(x) < y < 1+\eta(x), \tag{4.2.8}$$

$$\phi_y - \phi_x\eta_x = 0 \qquad \text{on } y = 1+\eta(x), \tag{4.2.9}$$

$$\phi_x^2 + \phi_y^2 + \frac{2}{F^2}y = \frac{2}{F^2}\tau\kappa + 1 + \frac{2}{F^2} \qquad \text{on } y = 1+\eta(x), \tag{4.2.10}$$

$$\phi_y - \phi_x B_x = 0 \qquad \text{on } y = B(x), \tag{4.2.11}$$

respectively, where $\kappa = \eta_{xx}/(1+\eta_x^2)^{\frac{3}{2}}$ is the curvature of the free surface $y = 1+\eta(x)$.

In the far field away from the disturbance the flow must be uniform. We therefore impose the conditions

$$\phi_x \to 1, \;\; y(x) \to 1 \quad \text{as} \;\; x \to \infty, \tag{4.2.12}$$

$$\phi_x \to \gamma, \;\; y(x) \to \frac{1}{\gamma} \;\; \text{as} \;\; x \to -\infty. \tag{4.2.13}$$

A further condition relating the Froude number F to the upstream flow velocity γ is obtained by applying Bernoulli's equation in the far field both up and downstream. In dimensional form we obtain

$$\frac{1}{2}V^2 + gh = \frac{1}{2}U^2 + gH. \tag{4.2.14}$$

Non-dimensionalising (4.2.14) and using the non-dimensionalised conservation of mass (4.2.7), we can rewrite (4.2.14) as

$$\frac{1}{2} - \frac{1}{2}\gamma^2 + \frac{1}{F^2} - \frac{1}{F^2\gamma} = 0. \tag{4.2.15}$$

Following Forbes [51], the Froude number F can be written in the form

$$F^2 = \frac{2}{\gamma(\gamma+1)}, \tag{4.2.16}$$

and a relationship between the upstream and downstream Froude numbers, in terms of the non-dimensionalised upstream velocity, can be found;

$$F_{\text{up}} = F\gamma^{\frac{3}{2}} = \sqrt{\frac{2\gamma^2}{(\gamma+1)}}. \tag{4.2.17}$$

A relationship between the upstream and downstream Bond numbers is similarly given by

$$\tau_{\text{up}} = \tau\gamma^2. \tag{4.2.18}$$

The relation (4.2.15) is a cubic equation in γ so there exist three possible flows. Solutions with $\gamma = 1$ have the same constant mean depth up and downstream. These are non-critical flow solutions, and include for example the solitary wave profiles discussed in chapter 3. Solutions with a drop in the mean depth of the flow are critical. They correspond to solutions with $\gamma = (-1 \pm \sqrt{1 + \frac{8}{F^2}})/2$. Here, hydraulic falls flowing from left to right are considered, and so the positive root for γ must be taken.

The problem is now fully defined; we seek $\phi(x, y)$ and $\eta(x)$ satisfying Laplace's equation (4.2.8), and the kinematic and dynamic boundary conditions (4.2.9) - (4.2.11), subject to the far-field flow conditions (4.2.12) and (4.2.13), and the relation (4.2.15).

4.3 Numerical Scheme

Following Belward and Forbes [12, 13], Belward [11], and Dias and Vanden-Broeck [41], we reformulate the problem as a system of integro-differential equations. The system can then be solved for the unknown free surface $y = 1 + \eta(x)$, over arbitrarily shaped obstructions of finite support on the bottom of the channel.

One method to solve the problem is to use a a potentially complicated conformal map to map the exact geometry of an arbitrarily shaped underlying channel bottom to the complex plane. Instead, we choose to simplify the boundary conditions by parameterising the free surface. We therefore introduce an arclength s, and write $x = X(s)$, $y = Y(s)$.

We must then satisfy the parametric equation

$$\left(\frac{dX(s)}{ds}\right)^2 + \left(\frac{dY(s)}{ds}\right)^2 = 1. \tag{4.3.1}$$

In order to satisfy the dynamic boundary condition (4.2.10), we must first rewrite the velocity components in parametric form. Using the chain rule to differentiate $\tilde{\phi}(x) = \phi(x, \eta(x))$ on the free surface, the velocity component u can be written as

$$\frac{d\tilde{\phi}}{dx} = \frac{\partial \phi}{\partial x} + \frac{\partial \phi}{\partial y}\frac{\partial \eta}{\partial x}. \tag{4.3.2}$$

We can then eliminate ϕ_y using the kinematic condition (4.2.9) on the free surface. Substituting ϕ_y into (4.3.2) we obtain

$$\frac{d\tilde{\phi}}{dx} = \frac{\partial \phi}{\partial x} + \frac{\partial \phi}{\partial x}\frac{\partial \eta}{\partial x}\frac{\partial \eta}{\partial x}. \tag{4.3.3}$$

The chain rule is similarly used to parametrise $u = \frac{d\tilde{\phi}}{dx}$, where $\tilde{\phi}(x) = \phi(x, \eta(x)) =$

$\phi(X(s), Y(s)) = \tilde{\phi}(s)$, giving

$$\frac{d\tilde{\phi}}{dx} = \frac{d\tilde{\phi}}{ds}\frac{ds}{dX}\frac{dX}{dx} = \frac{d\tilde{\phi}}{ds}\frac{ds}{dX}. \tag{4.3.4}$$

By equating equations (4.3.3) and (4.3.4) we obtain

$$\begin{aligned}
\frac{\partial\phi}{\partial x} + \frac{\partial\phi}{\partial x}\frac{\partial\eta}{\partial x}\frac{\partial\eta}{\partial x} &= \frac{d\tilde{\phi}}{ds}\frac{ds}{dX}, \\
\Rightarrow \frac{\partial\phi}{\partial x} &= \frac{d\tilde{\phi}}{ds}\frac{ds}{dX}\frac{1}{1+\left(\frac{d\eta}{dx}\right)^2}, \\
&= \frac{d\tilde{\phi}}{ds}\frac{X'}{X'^2+Y'^2} \qquad \text{having used } \frac{d\eta}{dx} = \frac{Y'}{X'}, \\
&= \frac{d\tilde{\phi}}{ds}\frac{dX}{ds} \qquad \text{having used (4.3.1).}
\end{aligned}$$

Here, we differentiated $Y(s) = \eta(X(s)) + 1$ using the chain rule, to obtain $Y' = \frac{d\eta}{dx}X'$. The prime denotes the derivative with respect to s. We now drop the ˜ and similarly parametrise v so that the velocity components on the free surface in parametric form can be written as:

$$u = \frac{d\phi}{ds}\frac{dX}{ds}, \qquad v = \frac{d\phi}{ds}\frac{dY}{ds}. \tag{4.3.5}$$

To parametrise η_{xx} we first obtain

$$Y' = \frac{d\eta}{dx}X', \tag{4.3.6}$$

by differentiating $Y(s)$ as above. Differentiating again gives

$$\begin{aligned}
Y'' &= \left(\frac{d\eta}{dx}X'\right)' \\
&= \frac{d\eta}{dx}X'' + X'\left(\frac{d\eta}{dx}\right)' \\
&= \frac{d\eta}{dx}X'' + X'\frac{d^2\eta}{dx^2}X' \\
&= \frac{Y'}{X'}X'' + X'^2\frac{d^2\eta}{dx^2} \\
\Rightarrow \eta_{xx} &= \frac{Y''X' - X''Y'}{X'^3}.
\end{aligned} \tag{4.3.7}$$

The dynamic condition is now easily parameterised by substituting (4.3.5) and (4.3.7)

into (4.2.10) to obtain;

$$(\phi' X')^2 + (\phi' Y')^2 + \frac{2}{F^2} Y(s) = \frac{2\tau}{F^2} \frac{Y'' X' - X'' Y'}{X'^3 (1 + \frac{Y'^2}{X'^2})^{\frac{3}{2}}} + 1 + \frac{2}{F^2},$$

$$\Rightarrow \qquad \phi'^2 + \frac{2}{F^2}(Y(s) - 1) = \frac{2\tau}{F^2}(Y'' X' - X'' Y') + 1, \tag{4.3.8}$$

where the parametric equation (4.3.1) has been used to simplify the condition.

The problem is now reformulated as a system of integro-differential equations by using Cauchy's integral formula. The complex variable $z = x + iy$ and the complex potential $w(z) = \phi(x, y) + i\psi(x, y)$ are introduced, where $\psi(x, y)$ is the stream function satisfying (3.3.4). Cauchy's integral formula is applied to the analytic, complex function

$$h(z) = \frac{dw}{dz} - \gamma = \phi_x - \gamma - i\phi_y, \tag{4.3.9}$$

around a contour $\mathcal{C}$. The method of images used in chapter 3 cannot be used in this case because of the obstruction on the channel bottom. So instead, the contour $\mathcal{C}$ is taken to consist of the free surface, the channel bottom itself and two vertical lines $x = \pm L$ in the limit as $L \to \pm\infty$, and is shown in figure 4.2. Now, letting s represent the evaluation point on the contour $\mathcal{C}$, we obtain

$$\frac{1}{2\pi i} \oint_c \frac{h(z)}{z - Z(s)} dz = \frac{1}{2} h(Z(s)). \tag{4.3.10}$$

Letting $\hat{\sigma}$ be the arclength in the integrand: $z(\hat{\sigma}) = x(\hat{\sigma}) + iy(\hat{\sigma})$ on the contour, and

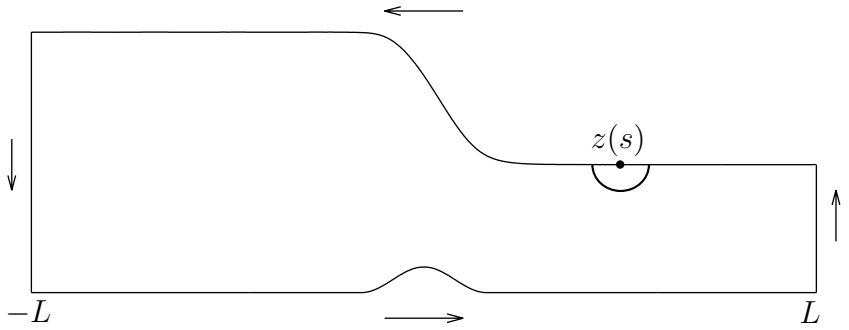

Figure 4.2: The contour $\mathcal{C}$ of integration. When the evaluation point s is on the free surface, a semicircle of infinitesimally small radius is added to the contour, around the point $z(s)$, as depicted in the figure.

placing $z(s)$ on the free surface, (4.3.10) becomes

$$\oint_c \frac{h(z(\hat{\sigma}))}{z(\hat{\sigma}) - Z(s)} z'(\hat{\sigma}) d\hat{\sigma} = \pi i h(Z(s)) = \pi i(\phi_x(s) - \gamma - i\phi_y(s)), \tag{4.3.11}$$

where $\phi_x(s) = \frac{\partial \phi}{\partial x}(X(s), Y(s))$. Thus,

$$\begin{aligned}\pi i(\phi'(s)X'(s) - \gamma - i\phi'(s)Y'(s)) &= \oint_c \frac{(\phi_x(\hat{\sigma}) - \gamma - i\phi_y(\hat{\sigma}))(x'(\hat{\sigma}) + iy'(\hat{\sigma}))}{(x(\hat{\sigma}) + iy(\hat{\sigma})) - (X(s) + iY(s))} d\hat{\sigma}, \\ &= \oint_c \frac{(\phi_x(\hat{\sigma}) - \gamma)x'(\hat{\sigma}) + \phi_y(\hat{\sigma})y'(\hat{\sigma}) + i(-\phi_y(\hat{\sigma})x'(\hat{\sigma}) + (\phi_x(\hat{\sigma}) - \gamma)y'(\hat{\sigma}))}{(x(\hat{\sigma}) - X(s)) + i(y(\hat{\sigma}) - Y(s))} d\hat{\sigma}, \\ &= \oint_c \frac{A(\hat{\sigma})((x(\hat{\sigma}) - X(s) - i(y(\hat{\sigma}) - Y(s))}{(x(\hat{\sigma}) - X(s))^2 + (y(\hat{\sigma}) - Y(s))^2} d\hat{\sigma}, \end{aligned} \tag{4.3.12}$$

having used (4.3.5) and set $A(\hat{\sigma}) = (\phi_x(\hat{\sigma}) - \gamma)x'(\hat{\sigma}) + \phi_y(\hat{\sigma})y'(\hat{\sigma}) + i(-\phi_y(\hat{\sigma})x'(\hat{\sigma}) + (\phi_x(\hat{\sigma}) - \gamma)y'(\hat{\sigma}))$. When $z(\hat{\sigma})$ is on the free surface we see that

$$A(\hat{\sigma}) = A_1(\hat{\sigma}) = \phi'(\hat{\sigma})(X'(\hat{\sigma})^2 + Y'(\hat{\sigma})^2) - \gamma X'(\hat{\sigma}) - i\gamma Y'(\hat{\sigma}). \tag{4.3.13}$$

When $\hat{\sigma}$ is on the channel bottom $x'(\hat{\sigma}) = 1$ and $y'(\hat{\sigma}) = B_x(\hat{\sigma})$, so

$$A(\hat{\sigma}) = A_2(\hat{\sigma}) = \phi_x(\hat{\sigma}) - \gamma + \phi_y(\hat{\sigma})B_x(\hat{\sigma}) + i(-\phi_y(\hat{\sigma}) + (\phi_x(\hat{\sigma}) - \gamma)B_x(\hat{\sigma})). \tag{4.3.14}$$

Using the kinematic condition (4.2.11) on the channel bottom, we can eliminate ϕ_y to obtain

$$A_2(\hat{\sigma}) = \phi_x(\hat{\sigma})(1 + B_x(\hat{\sigma})^2) - \gamma - i\gamma B_x(\hat{\sigma}). \tag{4.3.15}$$

We are now able to ignore the contributions to the integrals on the lines $y = \pm L$. Upstream, this is simply because as $L \to -\infty$ we have that $h(z) \to \gamma - \gamma = 0$. However, downstream $h(z)$ does not vanish, as $\phi_x \to 1$. Instead, we show that this contribution from the integrals with $L \to \infty$ is bounded. Then, using the estimation lemma, we see that the integral over $x = L$ goes to zero. Our integrals over $x = L$ are of the form

$$\int_0^1 \frac{h(z)}{(x(\hat{\sigma}) - X(s)) + i(y(\hat{\sigma}) - Y(s))} dz, \tag{4.3.16}$$

which we can approximate by

$$\int_0^1 \frac{M}{L + iQ} dQ. \tag{4.3.17}$$

where M is the bound of $h(z)$ given by

$$M = \max_{z \in \mathcal{C}} |\phi_x(z) - \gamma - i\phi_y(z)|. \tag{4.3.18}$$

Then,

$$\left|\int_0^1 \frac{M}{L+iQ}dQ\right| \leq \int_0^1 \left|\frac{M}{L+iQ}\right| dQ, \tag{4.3.19}$$

by the absolute value inequality for integrals, and

$$\int_0^1 \left|\frac{M}{L+iQ}\right| dQ \leq \int_0^1 \frac{M}{||L|-|Q||}dQ \leq \frac{M}{|L|-1}, \tag{4.3.20}$$

by the estimation lemma. As $|L| \to \infty$ we have that $M/(|L|-1) \to 0$, and thus, the contribution to the integral goes to zero. We therefore obtain

$$\begin{aligned}\pi i(\phi'(s)X'(s) - \gamma - i\phi'(s)Y'(s)) = &-\int_{-\infty}^{\infty} \frac{A_1(\hat{\sigma})(X(\hat{\sigma}) - X(s) - i(Y(\hat{\sigma}) - Y(s)))}{(X(\hat{\sigma}) - X(s))^2 + (Y(\hat{\sigma}) - Y(s))^2}d\hat{\sigma} \\ &+ \int_{-\infty}^{\infty} \frac{A_2(\hat{\sigma})(\hat{\sigma} - X(s) - i(B(\hat{\sigma}) - Y(s)))}{(\hat{\sigma} - X(s))^2 + (B(\hat{\sigma}) - Y(s))^2}d\hat{\sigma}.\end{aligned} \tag{4.3.21}$$

Then, taking the imaginary part of (4.3.21), we obtain the integro-differential equation

$$\begin{aligned}&\pi(\phi'(s)X'(s) - \gamma) \\ &= -\int_{-\infty}^{\infty} \frac{(\phi'(\hat{\sigma}) - \gamma X'(\hat{\sigma}))(Y(s) - Y(\hat{\sigma})) - \gamma Y'(\hat{\sigma})(X(\hat{\sigma}) - X(s))}{(X(\hat{\sigma}) - X(s))^2 + (Y(\hat{\sigma}) - Y(s))^2}d\hat{\sigma} \\ &+ \int_{-\infty}^{\infty} \frac{(\hat{u}(\hat{\sigma})(1 + B_x(\hat{\sigma})^2) - \gamma)(Y(s) - B(\hat{\sigma})) - \gamma B_x(\hat{\sigma})(\hat{\sigma} - X(s))}{(\hat{\sigma} - X(s))^2 + (B(\hat{\sigma}) - Y(s))^2}d\hat{\sigma},\end{aligned} \tag{4.3.22}$$

where the horizontal velocity of the fluid on the bottom of the channel, which depends on the arclength, is given by $u(\hat{\sigma}, B(\hat{\sigma})) = \hat{u}(\hat{\sigma})$.

Similarly, by placing the evaluation point x on the channel bottom, we obtain the integro-differential equation

$$\begin{aligned}\pi(\hat{u}(x) - \gamma) = &-\int_{-\infty}^{\infty} \frac{(\phi'(\hat{\sigma}) - \gamma X'(\hat{\sigma}))(B(x) - Y(\hat{\sigma})) - \gamma Y'(\hat{\sigma})(X(\hat{\sigma}) - x)}{(X(\hat{\sigma}) - x)^2 + (Y(\hat{\sigma}) - B(x))^2}d\hat{\sigma} \\ &+ \int_{-\infty}^{\infty} \frac{(-B(\hat{\sigma}) + B(x))(\hat{u}(\hat{\sigma})(1 + B_x(\hat{\sigma})^2) - \gamma) - \gamma B_x(\hat{\sigma})(\hat{\sigma} - x)}{(\hat{\sigma} - x)^2 + (B(\hat{\sigma}) - B(x))^2}d\hat{\sigma}.\end{aligned} \tag{4.3.23}$$

Equations (4.3.22) and (4.3.23) have Cauchy principal value singularities at $\hat{\sigma} = s$ and $\hat{\sigma} = x$ in the first and second integrals respectively, but their net contributions to the integrals are both zero. By performing the integrations numerically using the trapezoidal rule as in chapter 3, these singularities can be ignored and the integrals treated as non-singular integrals (see Monacella [83]).

The two integral equations (4.3.22) and (4.3.23), together with the dynamic condition (4.3.8), and the parametric equation (4.3.1), complete the reformulation of the problem and provide the system of integro-differential equations to be solved via Newton's method.

To solve the system of equations numerically, the work of Dias and Vanden-Broeck [41] is followed. We introduce N equally spaced mesh points, separated by an interval e, on the free surface;

$$s_i = -\frac{N-1}{2}e + e(i-1), \quad i = 1, ..., N, \tag{4.3.24}$$

together with the $N-1$ mesh midpoints $s_i^m = \frac{1}{2}(s_i + s_{i+1})$, for $i = 1, ..., N-1$. Similarly, M equally spaced mesh points

$$x_i = -\frac{M-1}{2}h + h(i-1), \quad i = 1, ..., M \tag{4.3.25}$$

separated by the interval h, are introduced on the channel bottom with their corresponding mesh midpoints $x_i^m = \frac{1}{2}(x_i + x_{i+1})$, for $i = 1, ..., M-1$.

To obtain a critical flow, just two independent dimensionless parameters are needed to uniquely determine a solution. These are taken to be the obstacle size and the downstream Bond number τ. Therefore, the downstream Froude number F and the depth of the channel upstream, are found as part of the solution. Thus, $3N + M + 2$ unknowns; $Y'(i) = Y'(s_i), X'(i) = X'(s_i), \phi'(i) = \phi'(s_i)$, for $i = 1, ..., N, \hat{u}(i) = \hat{u}(x_i)$, for $i = 1, ..., M, \gamma$ and F are sought.

However, given a set of values for $Y'(i)$, we can reduce the number of unknowns in the problem by obtaining $X'(i)$ from the parametric equation (4.3.1). We then use the upstream condition $X(1) = s_1$ and the downstream condition $Y(N) = 1$ to integrate $Y'(i)$ and $X'(i)$ numerically, using the trapezoidal rule. So we now know $Y(i)$ and $X(i)$ at the free surface mesh points, s_i for $i = 1, ..., N$. Next, centred finite differences are used to differentiate $X'(i)$ and $Y'(i)$ numerically. A further reduction in the number of unknowns is then possible by rearranging the dynamic condition (4.3.8) to find $\phi'(i)$ on the free surface. This leaves a set of $N + M + 2$ unknowns; $Y'(i) = Y'(s_i)$, for $i = 1, ..., N$, $\hat{u}(i) = \hat{u}(x_i)$ for $i = 1, ..., M$, γ and F.

The initial set of values for $Y'(i)$, where $i = 1, ..., N$, come from approximating the free surface by an initial guess in the form of a hydraulic fall, with heights $y = 1/\gamma$ upstream, and $y = 1$ downstream. This form is given by

$$Y(i) = \frac{1}{2\gamma}(1-\gamma)\tanh\left(\frac{s_i}{2}\right) + \frac{1}{2\gamma}(\gamma+1), \tag{4.3.26}$$

and we then differentiate (4.3.26) numerically to find $Y'(i)$.

The two integro-differential equations (4.3.22) and (4.3.23) are evaluated at the mesh midpoints s_i^m and x_i^m respectively. The integrals from $-\infty$ to ∞ are truncated at $-\bar{A}$ and $\bar{B}$, where $\bar{A}$ and $\bar{B}$ are large positive constants. They are then approximated numerically using the trapezoidal rule, with summation over the mesh points s_i and x_i respectively. Solutions in which the depth of the channel changes up and downstream are sought, and so it is necessary to consider the integrals from $-\infty$ to $-\bar{A}$, and $\bar{B}$ to ∞, in order to minimise the truncation error and thus improve the accuracy of the solutions. Following Dias and Vanden-Broeck [41] this is done by approximating the integrals analytically. As $\hat{\sigma} \to -\infty$, we require that $\phi'(\hat{\sigma}) \to \gamma, Y(\hat{\sigma}) \to \frac{1}{\gamma}, Y'(\hat{\sigma}) \to 0, X'(\hat{\sigma}) \to 1, B(\hat{\sigma}) \to 0$ and $\hat{u}(\hat{\sigma}) \to \gamma$. The integrals from $-\infty$ to $-\bar{A}$ therefore approximate to zero and thus, the contributions from these integrals can be neglected. As $\hat{\sigma} \to \infty$, the integrals are non-zero and so are determined analytically by approximating the unknowns $\phi'(\hat{\sigma}), X'(\hat{\sigma}), Y(\hat{\sigma})$ and $B(\hat{\sigma})$ by their values at the last mesh point on the free surface and channel bottom respectively. We must also set $\hat{u}(\hat{\sigma}) = 1, Y'(\hat{\sigma}) = 0$ and $B_x(\hat{\sigma}) = 0$. Far upstream, for $x > \bar{B}$, the first integral equation (4.3.22) becomes

$$\begin{aligned} T_1 = &- \int_{\bar{B}}^{\infty} \frac{(\phi'(N) - \gamma X'(N))(Y(s) - Y(N))}{(X(\hat{\sigma}) - X(s))^2 + (Y(N) - Y(s))^2} d\hat{\sigma} \\ &+ \int_{\bar{B}}^{\infty} \frac{(\hat{u}(M) - \gamma)(Y(s) - B(M))}{(\hat{\sigma} - X(s))^2 + (B(M) - Y(s))^2} d\hat{\sigma}. \end{aligned} \tag{4.3.27}$$

The truncation correction T_1 to the integral equation (4.3.22) is then found to be

$$\begin{aligned} T_1 = &- \left(\frac{\phi'(N) - \gamma X'(N)}{X'(N)} \right) \left(\pm \frac{\pi}{2} - \arctan \left(\frac{X(N) - X(s_i^m)}{Y(N) - Y(s_i^m)} \right) \right) \\ &+ (1 - \gamma) \left(-\frac{\pi}{2} - \arctan \left(\frac{x_M - X(s_i^m)}{B(M) - Y(s_i^m)} \right) \right). \end{aligned} \tag{4.3.28}$$

The choice of $\pm$ in the first term is the same as the sign of $(Y(N) - Y(s_i^m))$. If $Y(N) = Y(s_i^m)$ the first term is neglected completely. Similarly, the correction term T_2 to the second integral equation (4.3.23), is found to be

$$\begin{aligned} T_2 = &- \left(\frac{\phi'(N) - \gamma X'(N)}{X'(N)} \right) \left(\frac{\pi}{2} - \arctan \left(\frac{X(N) - x_i^m}{Y(N) - B(x_i^m)} \right) \right) \\ &+ (1 - \gamma) \left(\pm \frac{\pi}{2} - \arctan \left(\frac{x_M - x_i^m}{B(M) - B(x_i^m)} \right) \right). \end{aligned} \tag{4.3.29}$$

The sign in the second term is the same as the sign of $(B(M) - B(x_i^m))$. If $B(M) = B(x_i^m)$ the second term is neglected completely.

So we now have $N - 1$ equations from the first integral equation (4.3.22) together with its truncation correction T_1, and $M - 1$ equations from the second integral equation (4.3.23) together with its truncation correction T_2. A further four equations are required.

These equations come from defining the flow in the far field. Therefore, we impose

$$Y'(1) = Y'(2) = 0, \tag{4.3.30}$$

to ensure that the free surface is flat far upstream as $x \to -\infty$ and to satisfy the radiation condition. Furthermore, we fix

$$\hat{u}(M) = 1 \tag{4.3.31}$$

to ensure that the flow is uniform downstream as $x \to \infty$. We must also satisfy the relation between the Froude number and γ (the undisturbed velocity upstream), given by equation (4.2.15). This gives a system of $N + M + 2$ equations for the $N + M + 2$ unknowns, to be solved iteratively using Newton iterations, as described in section 3.3.

To ensure that the results obtained are numerically accurate, the same solutions are computed on meshes of different densities and sizes. We vary the number of mesh points on the free surface between $N = 401, 601, 801$ and 1601, and on the channel bottom, between $M = 201, 301$, and 401 for a given fixed domain. The mesh spacings e and h are also varied between $e = 0.025, 0.05$, and 0.1 and $h = 0.05, 0.1$, and 0.2, respectively. We are then able to ascertain that the solutions are independent of the mesh for small enough e and h. Fewer points are needed to describe the channel bottom accurately than required on the free surface. Furthermore, results are computed for different length domains of the same mesh density, to ensure that any errors caused by truncating the integrals, do not impact on the solution.

4.4 Results

The results in this section were computed using the method described in section 4.3. Following Dias and Vanden-Broeck [41] we use a cosine squared profile for the submerged obstructions, of the form

$$B(x) = \begin{cases} 2A_1 \cos^2\left(\frac{\pi(x-x_d)}{2L_1}\right) & -L_1 < x - x_d < L_1, \\ 2A_2 \cos^2\left(\frac{\pi x}{2L_2}\right) & -L_2 < x < L_2, \\ 0 & \text{otherwise.} \end{cases} \tag{4.4.1}$$

The heights of the obstacles are therefore given by $2A_1$ and $2A_2$, and the half-lengths of the two obstacles, by L_1 and L_2 respectively. The obstacle of height A_2 has been chosen so that it is centred at the origin and is a distance x_d from the other obstacle. We take A_1 to be zero when considering a flow over just a single submerged obstruction.

4.4.1 Hydraulic Falls

Firstly, we consider the case where $y = B(x)$ describes a uniform channel bottom with a single obstruction. Therefore, we set $A_1 = 0$, $A_2 > 0$ and fix L_2. Pure gravity ($\tau = 0$) hydraulic fall solutions where the flow upstream is subcritical and uniform, and the flow downstream is supercritical and uniform, were previously computed by Dias and Vanden-Broeck [41]. We compute these solutions and show a typical hydraulic fall profile in figure 4.3. Forbes [51] showed that as the height of the obstacle is increased, the speed of the flow downstream increases and thus, the height of the channel upstream increases. We obtain similar results here; we are able to obtain solutions over very tall obstructions, which allows for very fast flows downstream. The relationship between the Froude number and the height of an obstruction with half-width $L_2 = 3.2$ is shown by the solid line in figure 4.4. Very small amplitude waves begin to appear upstream on the free surface as the obstacle height is increased. Such waves have previously been discussed by Forbes and Schwartz [54]. They claim that the waves are a result of the numerical scheme requiring the flow to be uniform at the first mesh point upstream, rather than at $x = -\infty$.

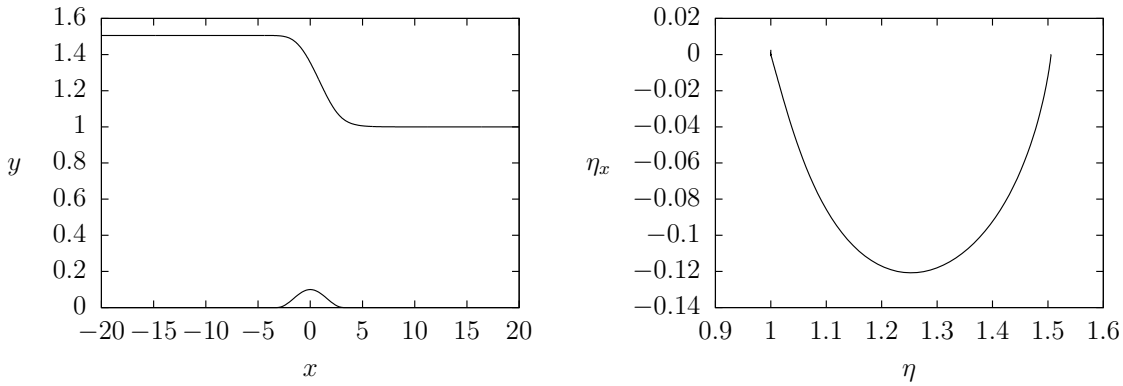

Figure 4.3: (a) Hydraulic fall solution, in the absence of surface tension, $\tau = 0$, over a single submerged obstruction of height $2A_2 = 0.1$ and half-width $L_2 = 3.2$. The Froude number, $F = 1.345$, is found as part of the solution. The phase portrait of the solution profile is shown in (b).

Next, we include the effects of surface tension, and find similar hydraulic fall profiles with subcritical uniform flow upstream and supercritical uniform flow downstream. Figure 4.5 shows typical solution profiles for an obstruction with $A_2 = 0.05$ and $L_2 = 3.2$, and three different values of the Bond number; weak surface tension both up and downstream ($\tau = 0.32$), strong surface tension downstream with weak surface tension upstream ($\tau = 0.6$), and strong surface tension both up and downstream ($\tau = 0.9$).

For $0 < \tau < \tau^*$, where τ^* is some critical value of the Bond number, increasing

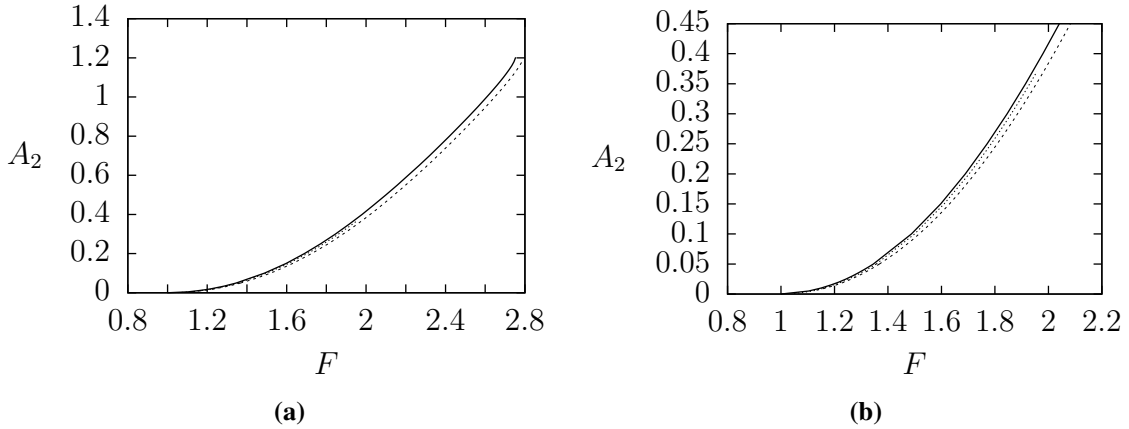

Figure 4.4: Relationship between the downstream Froude number F, and the half-height A_2 of the submerged obstacle of half-width $L_2 = 3.2$. The solid curve represents the relationship for $\tau = 0$, the dotted curve is the relationship for $\tau = 0.2$, and the dashed broken curve is the relationship for $\tau = 0.5$. In (b) we show a close-up of (a).

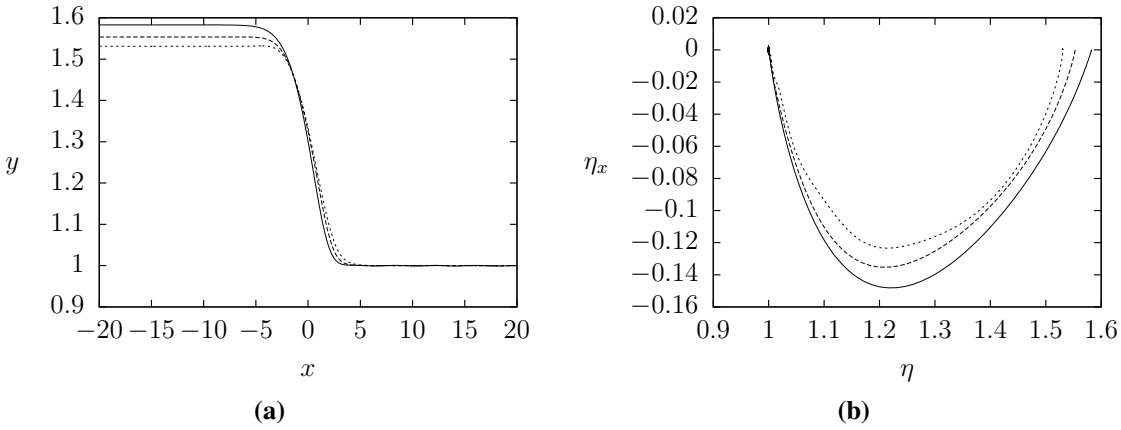

Figure 4.5: (a) Gravity-capillary hydraulic fall solution profiles. The single submerged obstruction is characterised by $A_2 = 0.05$ and $L_2 = 3.2$. The solid line is the solution with $\tau = 0.9$ and $F = 1.393$, the dashed line the solution with $\tau = 0.6$ and $F = 1.375$ and the dotted line the solution with $\tau = 0.32$ and $F = 1.361$. In each case the Froude number was found as part of the solution. The respective phase portraits of the solution profiles are shown in (b).

the strength of the surface tension increases the Froude number F and thus, increases the height of the channel upstream. We see that the gradient of the hydraulic fall also increases with the surface tension. The relationship between the downstream Froude number and the downstream Bond number, for $0.175 < \tau < 5$, where $A_2 = 0.05$ and $L_2 = 3.2$, can be seen in figure 4.6. At the critical Bond number $F^* \approx 1.403$, with corresponding $\tau^* \approx 1.397$, there exists a turning point in the $F - \tau$ plane, and thus, it is possible to obtain more than one solution with the same value of the Froude number F, over the same obstruction, but with different values of the Bond number. Figure 4.7 shows an example of this. We plot two hydraulic fall solution profiles which have

the same underlying obstruction and the same Froude number $F = 1.398$, but different values of the Bond number; $\tau = 1.024$ and $\tau = 2$. Furthermore, we find that there exists a gravity-capillary hydraulic fall which has the same Froude number as the pure gravity case and the same upstream depth, but a steeper fall.

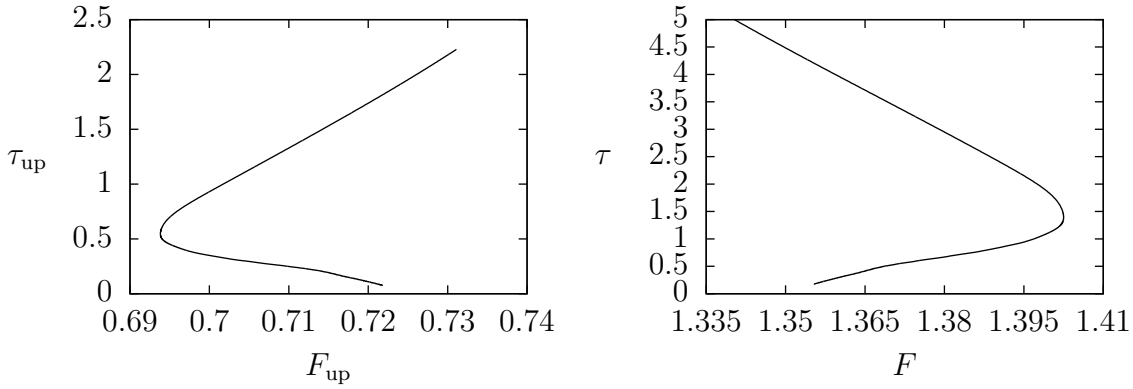

(a) Upstream **(b)** Downstream

Figure 4.6: Relationship between the Bond and Froude numbers both up and downstream for a single submerged obstacle characterised by $A_2 = 0.05, L_2 = 3.2$.

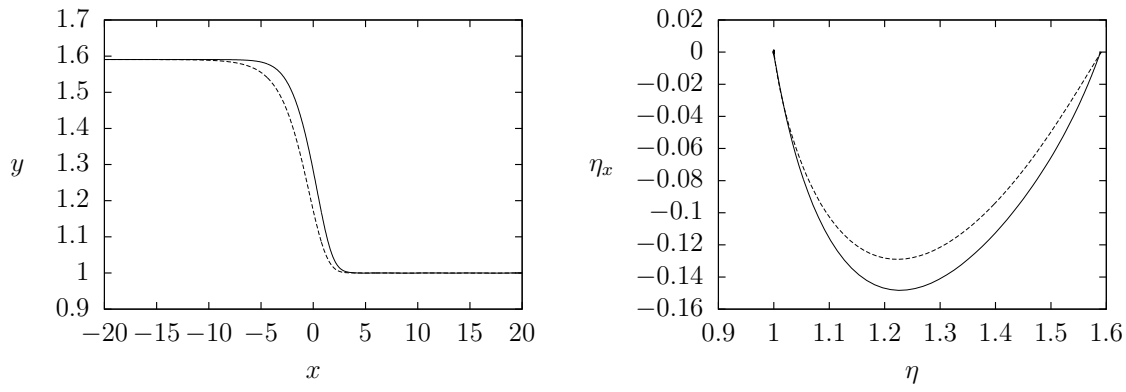

(a) **(b)**

Figure 4.7: (a) Gravity-capillary hydraulic fall solution profiles over a single submerged obstruction characterised by $A_2 = 0.05$ and $L_2 = 3.2$, with Froude number $F = 1.398$. The solid line is the solution with $\tau = 1.024$, and the broken line is the solution with $\tau = 2$. In both cases the Froude number was found as part of the solution. The respective phase portraits of the solution profiles are shown in (b).

These multiple solutions for a particular value of the Froude number can be explained by considering the linear theory. By substituting a linear periodic wave function of the form $\phi(x, y) = E(y)e^{i(Kx-\omega t)}$ and $\eta(x) = Ge^{i(Kx-\omega t)}$; where G is constant, K is the wavenumber of the waves and ω the angular frequency, into the governing equations

(4.2.8), (4.2.9), (4.2.10), and (4.2.11) (with $B(x) = 0$), we obtain the dispersion relations

$$F_{\text{up}}^2 = \left(\frac{\gamma}{k} + \frac{\tau_{\text{up}}}{\gamma}k\right)\tanh\left(\frac{k}{\gamma}\right), \tag{4.4.2}$$

$$F^2 = \left(\frac{1}{k} + \tau k\right)\tanh(k), \tag{4.4.3}$$

upstream and downstream respectively, where $k = KH$. For a particular value of the Froude number F, there is one corresponding dispersion curve in the pure gravity case, given by equation (4.4.3) with $\tau = 0$. However, when surface tension is included we are free to change the value of the Bond number for any given Froude number. This means that multiple dispersion curves can exist for the same fixed value of F, but with different values of τ and k. This can therefore explain the existence of more than one solution for a give Froude number.

When τ is small, small numerical oscillations appear on the solution branch in the $F - \tau$ plane. More mesh points are then needed on the free surface to obtain the required degree of accuracy. However, the computational cost then starts to become prohibitive. When τ is chosen such that $\tau_{\text{up}} < 1/3$, there exists a minimum in the upstream linear dispersion relation. As τ is decreased, the upstream Froude number F_{up} approaches this minimum. In figure 4.6 the branch in the $F-\tau$ plane ends at $\tau = 0.175$, where F_{up} is just above the minimum. Below the minimum the linear theory suggests the presence of some capillary waves upstream. However, in the numerical scheme we imposed the condition that the flow upstream is uniform. This therefore eliminates the possibility of capillary waves upstream. Unfortunately, we have to impose such a condition to prevent gravity waves occurring upstream, which would violate the radiation condition. It is not known what condition could be imposed to prevent gravity waves upstream whilst allowing for capillary waves.

Similar solution branches can be obtained in the $F - \tau$ plane for different sized obstacles. Figure 4.8 shows the solution branches for underlying obstacles with $A_2 = 0.01$, $A_2 = 0.05$ and $A_2 = 0.1$, and $L_2 = 3.2$, for $\tau^{**} < \tau < 10$. The value of the critical Bond number τ^* increases with A_2, so that, for an obstacle of height $A_2 = 0.1$ for example, $\tau^{**} \approx 2.894$ and the corresponding value of the downstream Froude number is $F^* \approx 1.606$.

When τ is increased enough, small numerical oscillations begin to appear on the solution branch. Such oscillations can be seen on the $A_2 = 0.01$ branch in figure 4.8. Here, more points on both the free surface and the channel bottom would be needed to obtain an improved degree of accuracy, but again the computational costs start to become prohibitive.

As we increase the height of the obstacle for a given flow, the downstream Froude number increases, whilst the upstream Froude number decreases. This is comparable to

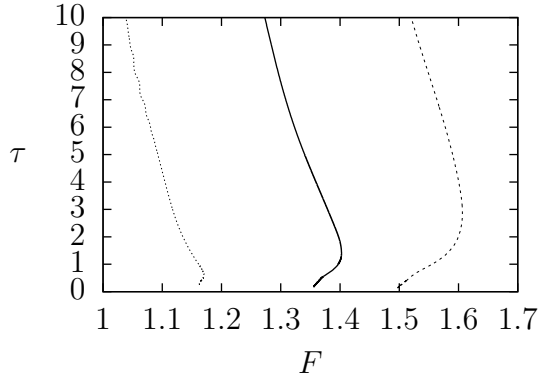

Figure 4.8: Relationship between the downstream Bond and Froude numbers for a single submerged obstacle with $L_2 = 3.2$. The dotted line shows the branch with $A_2 = 0.01$, the solid line the branch with $A_2 = 0.05$ and the dashed line the branch with $A_2 = 0.1$.

the findings of Forbes [51] for the pure gravity case. The relationship between F and A_2, for $\tau = 0.2$ and $\tau = 0.5$, can be seen in figure 4.4.

Guayjarernpanishk and Asavanant [66] found that for obstacles below some critical height, gravity-capillary critical flow solutions do not exist. Furthermore, they found that as the height of the obstacle decreases towards the critical height for some fixed τ_{up}, the free surface develops a slight elevation immediately in front of the hydraulic fall. Similarly, for an obstacle of fixed height, as the Bond number is decreased towards some critical value, the slight elevation immediately in front of the hydraulic fall, increases in amplitude.

When τ_{up} is weak ($\tau_{\text{up}} < \frac{1}{3}$), the upstream dispersion curve possesses a minimum $F_{\text{up}_{\text{min}}} < 1$. As we decrease A_2, the upstream Froude number F_{up} increases towards $F = 1$, and thus approaches the minimum of the dispersion curve. We obtain similar results to Guayjarernpanishk and Asavanant and find that for F_{up} near $F_{\text{up}_{\text{min}}}$, the free surface immediately in front of the hydraulic fall develops a slight elevation. As A_2 is decreased further, the amplitude of the slight elevation increases, and solutions where the elevation becomes part of a small train of decaying waves immediately in front of the hydraulic fall are found. An example free surface profile is shown in figure 4.9 with $\tau = 0.2$ and $F = 1.198$. At some critical value of A_2, the Froude number intersects the dispersion curve and the numerical method ceases to provide accurate solutions. Numerically generated waves start to appear on the free surface. For stronger surface tension, $\tau_{\text{up}} > \frac{1}{3}$, the upstream dispersion curve increases monotonically. As we decrease A_2, F_{up} increases towards $F = 1$, and the depth of the fluid upstream decreases. We continue to obtain hydraulic fall solutions until the upstream depth reduces to the same depth as downstream, resulting in a uniform stream. This is in conflict with the findings of Guayjarernpanishk and Asavanant [66].

The maximum height of the obstacle for which we find solutions is also determined by

τ. In the pure gravity case ($\tau = 0$) the maximum height is quite large, but on introducing a little surface tension it reduces rapidly. As τ increases the maximum obstacle height increases.

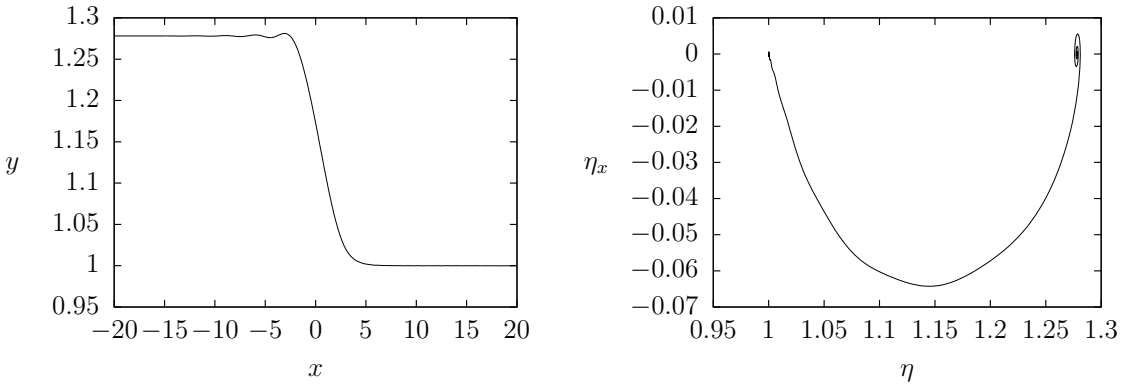

Figure 4.9: (a) Hydraulic fall solution over a single submerged obstruction characterised by $A_2 = 0.015$, $L_2 = 3.2$. Weak surface tension acts on the free surface; $\tau = 0.2$. A small train of decaying waves immediately before the hydraulic fall can be seen. The Froude number $F = 1.198$ is found as part of the solution. The phase portrait of the solution profile is shown in (b).

4.4.2 Generalised Hydraulic Falls

Following the work of Dias and Vanden-Broeck [41], the scheme in section 4.3 is modified to look for generalised hydraulic falls. In the pure gravity case such a flow requires three independent parameters to uniquely define a solution. These parameters are taken to be the Froude number F, the obstacle size (A_2 and L_2), and for convenience, the height of the channel at the first mesh point. Equations (4.3.30) (which ensure that the free surface is flat far upstream), are relaxed to allow for a wave train upstream, with the condition

$$Y(1) = \delta \tag{4.4.4}$$

is imposed, for some given constant δ. We then fix the value of F. By varying δ different pure gravity generalised hydraulic falls can be computed, as in [41]. Typical generalised hydraulic fall profiles with $A_2 = 0.05$ and $L_2 = 3.2$ are shown in figure 4.10 for three different values of δ. However, following this scheme we were only able to obtain gravity-capillary generalised hydraulic falls when the surface tension was very weak.

This result can be explained in the context of the linear dispersion relations both up and downstream, given by equations (4.4.2) and (4.4.3). In figure 4.11 we plot the upstream and downstream linear dispersion relations in the pure gravity case 4.11(a) and a gravity-capillary case 4.11(b). We also mark the up and downstream Froude numbers

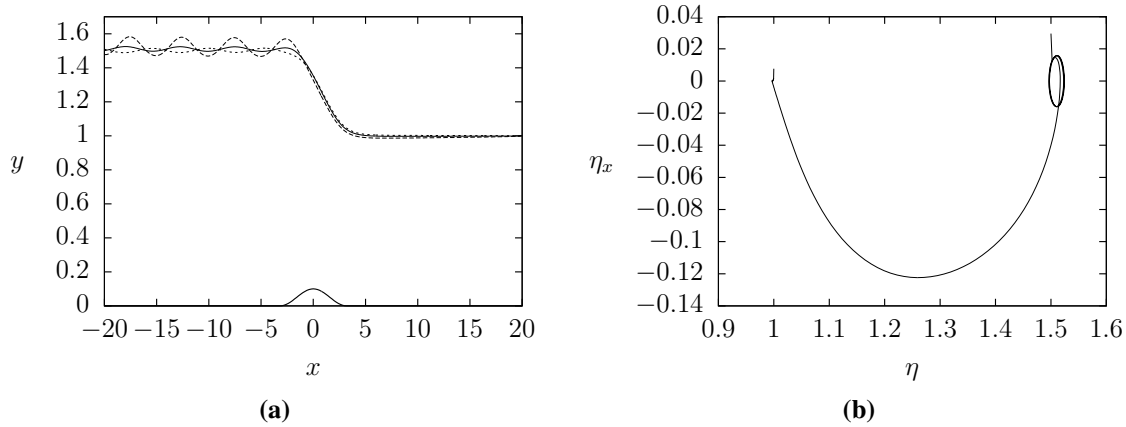

Figure 4.10: (a) Generalised hydraulic fall solutions, over a single submerged obstruction, in the absence of surface tension. The obstacle is of height $2A_2 = 0.1$, and width $2L_2 = 6.4$. The Froude number $F = 1.345$ is fixed. The phase portrait of the solution profile given by the solid line in (a) is shown in (b).

for the given solution with $2A_2 = 0.1$ and $2L_2 = 6.4$ with horizontal lines. In the pure gravity case we see that the upstream linear dispersion relation (dashed curve) intersects the horizontal dashed line marking the upstream Froude number. The downstream linear dispersion relation (solid curve) does not intersect the downstream Froude number (horizontal solid line). This means that the linear theory predicts a train of waves upstream of the obstruction, with wavenumber $k_{intersect}$, and a uniform stream downstream. When surface tension is included in the configuration, unless it is very small (as discussed below), the downstream Froude number intersects the downstream linear dispersion relation and figure 4.11(b) shows that the situation is reversed. The linear theory now predicts a train of waves downstream of the fall, with the flow remaining uniform upstream.

Motivated by this prediction, we modified the scheme in section 4.3 to look for a train of waves downstream of the hydraulic fall. We still require that the flow is uniform upstream, so we need to keep the equations (4.3.30). We want to manipulate any waves downstream, so instead of satisfying the downstream condition $Y(N) = 1$ in the numerical integration of Y_s, we impose the condition $Y(N) = \delta$, for some given constant δ. We can then compute different solutions for a particular obstacle by varying δ. Solutions with subcritical uniform flow upstream and a supercritical wave train downstream are obtained and we show a typical solution profile in figure 4.12. The wavelength of the downstream waves appears to be roughly in agreement with the linear theory. In figure 4.12 the wavelengths appear to have length $\lambda \approx 13.73 - 11.35 = 2.38$. The Froude number intersects the linear dispersion curve at $k \approx 2.43$ implying that $\lambda = 2\pi/k \approx 2.59$. However, the free surface in such solutions appears to be subject to some form of numerical error as the supercritical mean level flow is not constant. The depth of the fluid appears to decrease as we travel downstream. Furthermore, the profile is found to be influenced by the

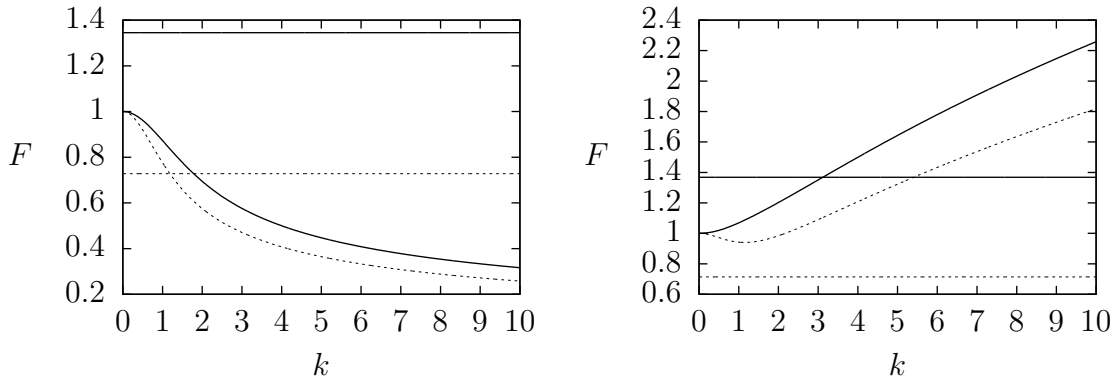

(a) Pure gravity case, $\tau = 0$.

(b) Gravity-capillary case, $\tau = 0.5$.

Figure 4.11: Linear dispersion relations. The solid curves represent the dispersion relation downstream, and the solid horizontal lines give the downstream value of the Froude number F for a submerged obstacle classified by $A_2 = 0.05, L_2 = 3.2$. The broken curves represent the dispersion relation upstream, and the broken horizontal lines give the upstream value of the Froude number $F_{\rm up}$ for the same obstacle.

truncation of the flow domain up and downstream. If we vary the length of the channel in the numerical scheme, the mean level of the flow changes, and so the position of the downstream wave train is altered.

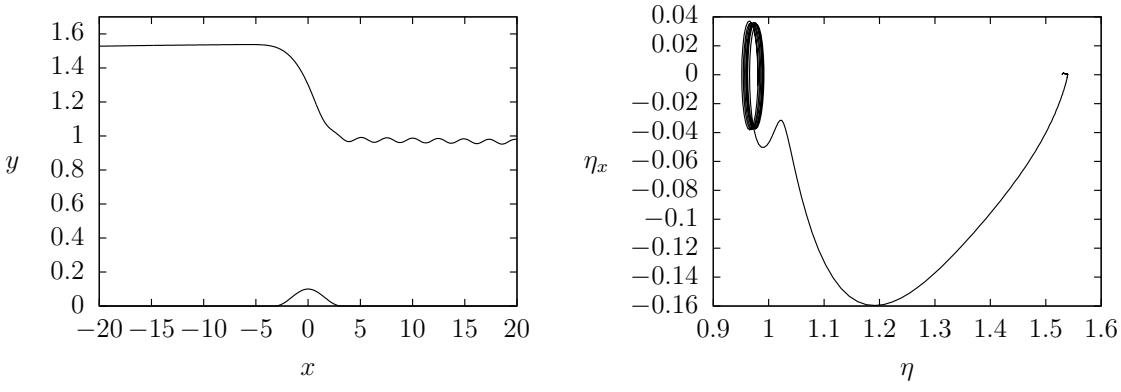

(a) **(b)**

Figure 4.12: Computed solution over a single submerged obstruction of height $2A_2 = 0.1$ and half-width $L_2 = 3.2$, with surface tension $\tau = 0.6$. The Froude number $F = 1.358$ is found as part of the solution. The phase portrait of the solution profile in (a) is shown in (b).

Therefore, we also sought these solutions by changing the numerical scheme in section 4.3 so that the upstream depth is fixed at $y = 1$, i.e. we non-dimensionalised the governing equations with respect to the upstream variables V and h instead of the downstream variables U and H. The downstream depth is then sought as part of the solution. However, we found that we could not obtain these generalised type hydraulic fall solutions, where the wave train occurs downstream, at all in this manner.

Regardless of whether this type of solution does actually exist numerically, in the absence of a further obstacle downstream, the physical relevance of any such solution is questionable. Any waves downstream of the hydraulic fall would correspond to the waves predicted by the linear theory on the increasing part of the linear dispersion relation, i.e. where $dF/dk > 0$, see figure 4.11(b). This means that the group velocity c_g (the velocity at which the energy of linear waves travels) is greater than the phase velocity c (the velocity at which the waves travel) because $\omega = ck$,

$$c_g = \frac{d\omega(k)}{dk} = \frac{dc}{dk} + c, \tag{4.4.5}$$

and $dF/dk > 0 \iff dc/dk > 0$. However, we have selected a frame of reference which moves with the submerged obstructions. This means that the waves in our case do not move and the energy in the waves instead travels upstream with velocity $c_g - c$. Furthermore, we know that in order to satisfy the radiation condition we cannot have energy coming from infinity. This means that the energy in any wave train that exists upstream of an obstacle (as $x \to -\infty$), must be travelling upstream. The obstacle is then responsible for the waves. Thus, $c_g - c > 0$ so $c_g > c$. Similarly, the energy in any wave train that exists downstream of an obstacle (as $x \to \infty$), must be travelling downstream. Thus, $c_g - c < 0$ so $c_g < c$. (See Vanden-Broeck [124] for more details). However, this contradicts our earlier observations that we must have $c_g > c$ in the case of the downstream wave train for the gravity-capillary generalised hydraulic fall. We would expect the waves that appear to be in front of, rather than behind the obstacle. So the generalised type gravity-capillary hydraulic fall appears to lack physical relevance in a configuration involving just a single obstacle.

When the surface tension is such that $\tau_{\text{up}} < \frac{1}{3}$, the upstream dispersion curve possesses a minimum. We define $F_{\text{up}_{\text{min}}}$ to be the critical value of the Froude number corresponding to this minimum. The Froude number F_{up} may intersect the dispersion curve if it is such that $F_{\text{up}_{\text{min}}} < F_{\text{up}} < 1$. This means that a train of upstream capillary dominated waves of wavelength $k_{\text{up}_{\text{intersect}}}$ exist for a critical range of Froude numbers. Generalised gravity-capillary hydraulic falls therefore do exist when the upstream surface tension is small. We find that the actual values of τ_{up} for which we obtain solutions are actually much less than one third. This is because these solutions also require that $\tau < 1/3$, but the upstream Bond number τ_{up} is much smaller than the downstream Bond number τ because $\tau_{\text{up}} = \tau\gamma^2$ (see equation (4.2.18)) and $\gamma < 1$. In figure 4.13 we show such a solution profile with $\tau = 0.01$. This corresponds to $\tau_{\text{up}} = 3.34 \times 10^{-3}$. Again, by varying δ, upstream wave trains of different amplitudes may be obtained.

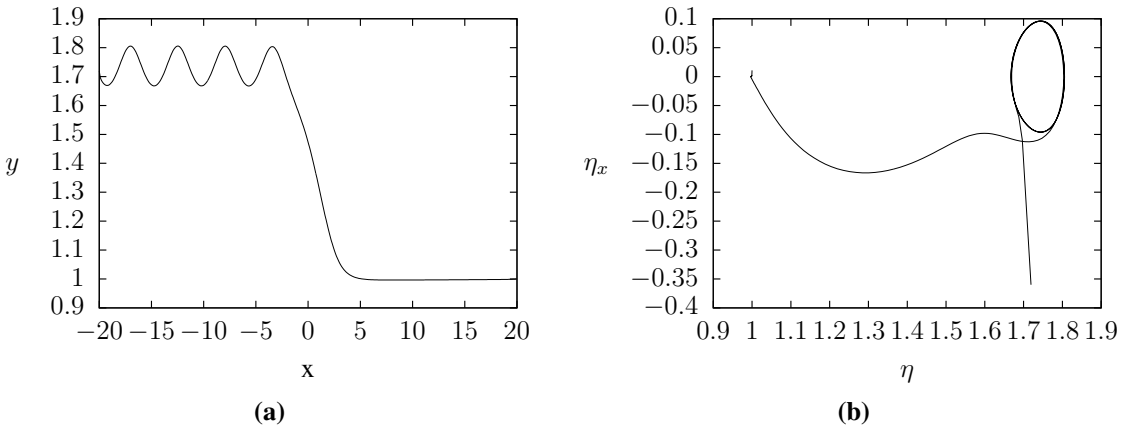

Figure 4.13: Gravity-capillary generalised hydraulic fall solution over a single submerged obstruction of height $2A_2 = 0.2$ and half-width $L_2 = 3$. The downstream Froude and Bond numbers are given by $F = 1.358$ and $\tau = 0.01$ respectively. The phase portrait of the solution profile in (a) is shown in (b).

4.4.3 Trapped Waves

When surface tension is neglected ($\tau = 0$) and a second positively orientated obstruction is included further upstream ($x_d < 0$ with $A_1 > 0$), a train of waves appears between the two obstacles. The flow is uniform upstream of the first obstacle (as $x \to -\infty$) and downstream after the fall (as $x \to \infty$). Figure 4.14 shows a typical free surface profile, with trapped waves between two obstructions characterised by $A_1 = 0.04$, $L_1 = 3.2$ and $A_2 = 0.05$, $L_2 = 3.2$. We can see in the figure that the waves have slightly broader troughs than crests meaning that the only restoring force on the particles in the flow is gravity (see Stokes [112, 113]). Such solutions were found by Dias and Vanden-Broeck [41]. They used an argument based on weakly nonlinear theory to show that as the distance between the two obstructions increases, the flow over the obstacle centred at $x = 0$ approaches that of a generalised hydraulic fall past a single disturbance. As there are no waves in the far field the radiation condition is satisfied. Thus, the unphysical generalised hydraulic fall becomes physically relevant when it is considered as the localised flow over an obstacle in a configuration which involves a second obstruction further upstream.

When $A_1 < 0$, the hydraulic fall is preceded by a dip in the channel. We find that a train of trapped waves also exists between the obstacles here. However, the behaviour of the free surface above the upstream, negatively orientated disturbance is different to that over the positively orientated one. We see an elevation over the negatively orientated obstruction, before the train of waves. For a wide enough obstruction we find that this elevation wave can be multi-peaked. We show typical free surface profiles with single and multi-peaked elevations over the obstruction in figure 4.15.

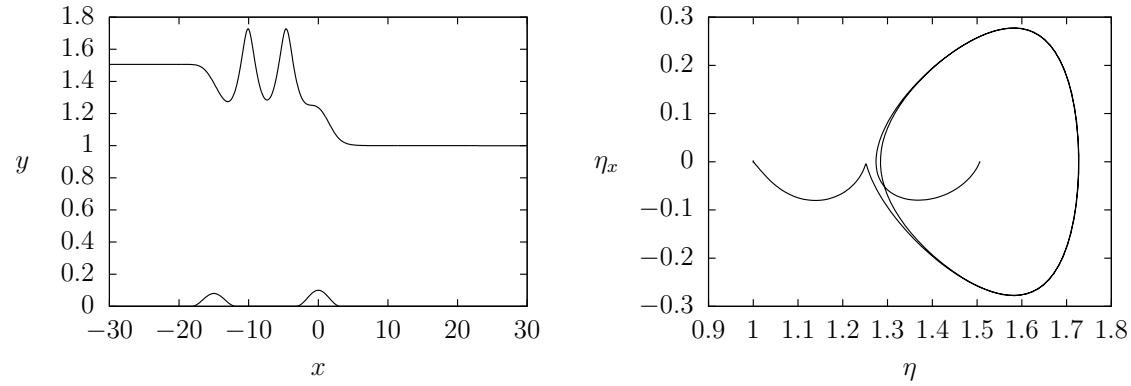

(a) **(b)**

Figure 4.14: (a) Free surface profile past two obstacles on the bottom of the channel. The first of which is characterised by $A_1 = 0.04, L_1 = 3.2$ and is centred upstream at $x = -15$, and the second by $A_2 = 0.05, L_2 = 3.2$. Waves appear trapped between the obstacles. The Froude number $F = 1.345$ is found as part of the solution. The phase portrait of the solution profile in (a) is shown in (b).

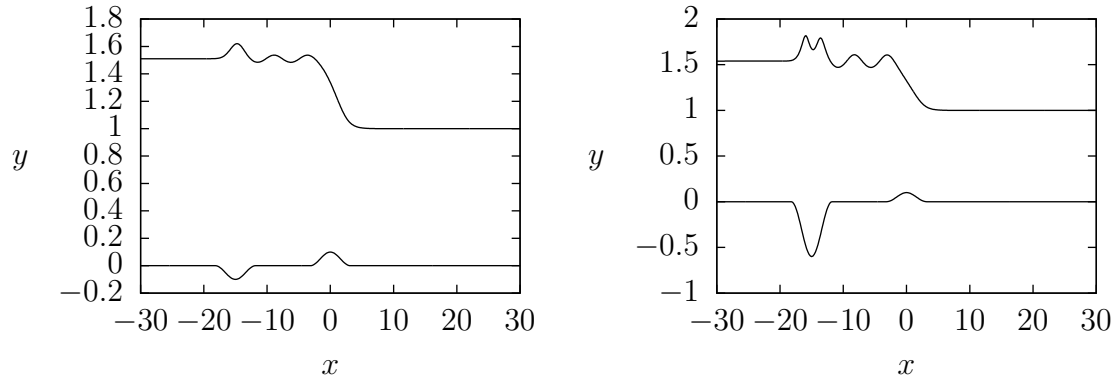

(a) **(b)**

Figure 4.15: Free surface profile past two disturbances on the bottom of the channel. The first disturbance represents a dip in the channel, and is given by (a) $A_1 = -0.05, L_1 = 3.2$, (b) $A_1 = -0.3, L_1 = 3.2$, centred upstream at $x = -15$, and the second is an obstacle characterised by $A_2 = 0.05, L_2 = 3.2$. Waves appear trapped between the obstacles. In (a) $F = 1.348$ and an elevation wave is found over the dip. In (b) $F = 1.364$ and a two-peaked elevation wave is found over the dip. In both cases, the Froude number was found as part of the solution.

Next, we add the effects of surface tension to the flow configuration over two obstructions. We find that including a second obstacle further upstream does not result in trapped waves between the obstacles, unless the upstream Bond number is very small. Dias and Vanden-Broeck [41] have shown that upstream trapped wave solutions are hybrid solutions between a generalised hydraulic fall, which, as discussed in section 4.4.2, are not obtained in the gravity-capillary case unless τ is very small, and type two basic solution discussed in chapter 3. It is therefore no surprise that we do not obtain solutions with trapped waves upstream for most gravity-capillary flows.

When the surface tension is very weak so that $\tau_{\rm up} < 1/3$ and the upstream dispersion curve possesses a minimum, if the upstream Froude number $F_{\rm up}$ intersects the upstream linear dispersion curve (i.e. $F_{\rm up_{min}} < F_{\rm up}$, where $F_{\rm up_{min}}$ is the value of the Froude number corresponding to the minimum of the dispersion curve), trapped wave solutions are obtainable. Figure 4.16 shows a typical free surface profile, with trapped waves between the hydraulic fall and an obstacle further upstream. The Bond number used in the figure is $\tau = 0.1$, and the Froude number is found to be $F = 1.497$. The upstream Bond number is thus extremely small, and is given by $\tau_{\rm up} \approx 0.032$. The linear theory now predicts a train of gravity dominated waves trapped between the obstacles and a train of capillary dominated waves upstream as $x \to -\infty$. The capillary wave train is not captured by our numerical scheme, as the scheme ensures that the free surface is flat upstream in order to satisfy the radiation condition. A train of very small amplitude spurious waves with the same wavelength as the downstream wave train is sometimes found though.

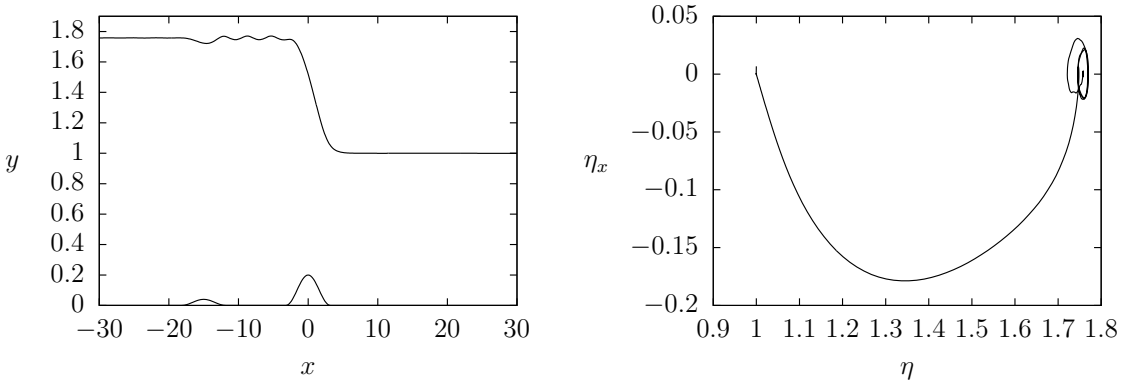

Figure 4.16: (a) Free surface profile past two obstacles on the bottom of the channel, with weak surface tension $\tau = 0.1$. The first obstacle is characterised by $A_1 = 0.02, L_1 = 3.2$ and is centred upstream at $x = -15$, and the second by $A_2 = 0.1, L_2 = 3.2$. Small amplitude waves appear trapped between the obstacles. The Froude number $F = 1.497$ is found as part of the solution. The phase portrait of the solution profile in (a) is shown in (b).

In terms of the upstream linear dispersion relation, if we gradually increase the surface tension, $F_{\rm up_{min}}$ approaches one. This means that the Froude number for the given

fixed submerged obstruction approaches the minimum; $F_{\mathrm{up}_{\mathrm{min}}}$. At some point near the minimum, the calculations fail to provide solutions with the required degree of accuracy. If we increase $F_{\mathrm{up}_{\mathrm{min}}}$ further, so that $F_{\mathrm{up}} < F_{\mathrm{up}_{\mathrm{min}}} < 1$, the Froude number ceases to intersect the dispersion curve, so the trapped waves disappear. The solutions obtained in this case are discussed in section 4.4.4.

Figure 4.17 shows upstream trapped wave solutions for the gravity wave case $\tau_{\mathrm{up}} = 0$ and for the gravity-capillary case with $\tau_{\mathrm{up}} = 0.04$ (corresponding to $\tau = 0.1$). We see that the wavelength of the trapped waves in the gravity-capillary solution is smaller than the wavelength of the pure gravity waves. The linear dispersion relations for both the pure gravity case and the gravity-capillary case, with $\tau_{\mathrm{up}} = 0.04$, are shown in figure 4.18. From the figure, we see that the gravity dispersion curve intersects the Froude number at a smaller value of k than the decreasing part of the gravity-capillary curve. This means the wavenumber of the gravity-capillary waves is greater than that of the pure gravity waves, and so this is in agreement with our fully nonlinear results.

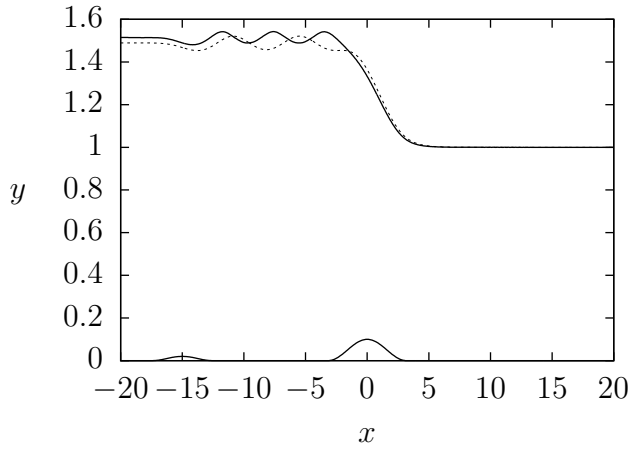

Figure 4.17: Free surface profile past two obstacles on the bottom of the channel, characterised by $A_2 = 0.05, L_2 = 3.2$ and $A_1 = 0.01, L_1 = 3.2$. The solid curve represents the solution with $\tau = 0.1$ and $F = 1.350$. The broken curve represents the pure gravity solution with $\tau = 0$ and $F = 1.334$.

In the case of stronger surface tension, we place the second obstacle downstream of the hydraulic fall where the flow is supercritical. As might be expected from the linear theory, we find a train of waves trapped between the obstacles. Further downstream in the far field beyond the obstacles, the flow is uniform and supercritical. Upstream of the first obstacle the flow is uniform and subcritical. We find that unlike the other trapped wave free surface profiles, an elevation wave appears over the downstream obstruction. We show a typical solution profile with $\tau = 0.6$ with $A_2 = 0.05, L_2 = 3.2$ in figure 4.19.

The number of waves trapped between the two submerged obstructions increases as

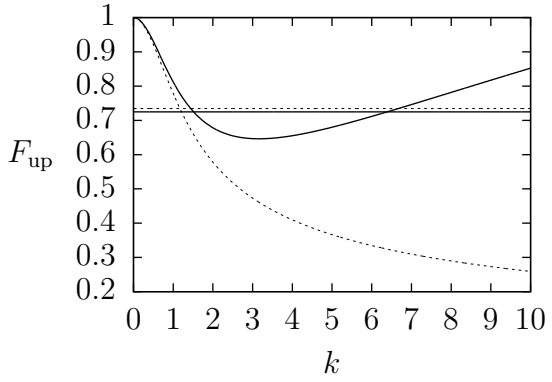

Figure 4.18: Upstream linear dispersion relations. The solid curves represent the dispersion relation with $\tau = 0.1$ and the upstream value of the Froude number $F_{\rm up}$ for submerged obstacles characterised by $A_2 = 0.05, L_2 = 3.2$ and $A_1 = 0.01, L_1 = 3.2$. The broken curves are the dispersion relation with $\tau = 0$ and the upstream value of the Froude number for the same channel bottom configuration.

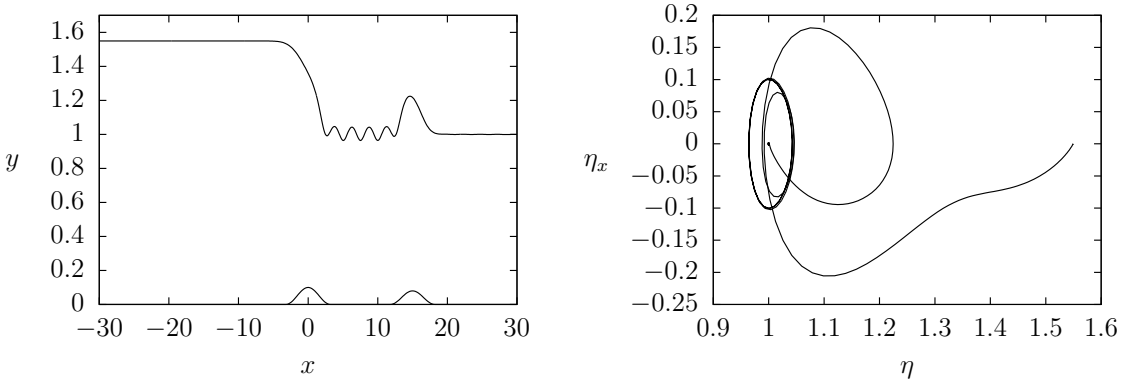

Figure 4.19: (a) Free surface profile past two obstacles on the bottom of the channel, with surface tension $\tau = 0.6$. The first obstacle is characterised by $A_2 = 0.05, L_2 = 3.2$ and the second by $A_1 = 0.04, L_1 = 3.2$, centred downstream at $x = 15$. Trapped waves appear between the two obstacles. The Froude number $F = 1.372$ is found as part of the solution. The phase portrait of the solution profile in (a) is shown in (b).

we increase the distance x_d between the obstructions. However, the amplitude and wavelength of the waves remains roughly constant. This is similar to the results of the experiments by Pratt [95], where pure gravity trapped waves were obtained upstream between two submerged obstacles. Pratt found that the amplitude and wavelength of the waves remained the same when the position of the obstacles was altered, but the number of trapped waves changed.

We investigate the effects of the downstream obstruction on the free surface by changing the height A_1, whilst keeping L_1, τ, A_2 and L_2 fixed. We find that decreasing the obstacle height decreases the amplitude of the trapped waves. When A_1 is small compared to A_2, the amplitude of the waves becomes so small that the trapped waves cease

to be visible between the obstructions. The free surface profile thus appears to take the form of a hydraulic fall with an elevation solitary type wave over the downstream obstruction. Figure 4.20 shows a typical solution profile over obstacles characterised by $A_2 = 0.1, L_2 = 3.2$, and $A_1 = 0.02, L_1 = 3.2$. This type of solution is similar to the pure gravity wave solution obtained by Belward [11] for flow over two successive obstacles. Belward found a hydraulic fall over the first obstacle and a near symmetric elevation wave, in the supercritical flow regime, over the second. He found that by increasing the height of the first obstacle, the maximum possible height of the second obstacle for which solutions exist, increases. Furthermore, he showed that the value of the Froude number for hydraulic falls is almost entirely determined by the height of the first obstacle. Increasing the height of this obstacle increases the Froude number. In the gravity-capillary case we find similar relationships between the Froude number and the obstacle heights A_2 and A_1. The difference between the pure gravity and the gravity-capillary cases is that in the gravity-capillary case very small amplitude trapped waves still exist between the obstructions, with the waves becoming visible upon much closer examination of the free surface.

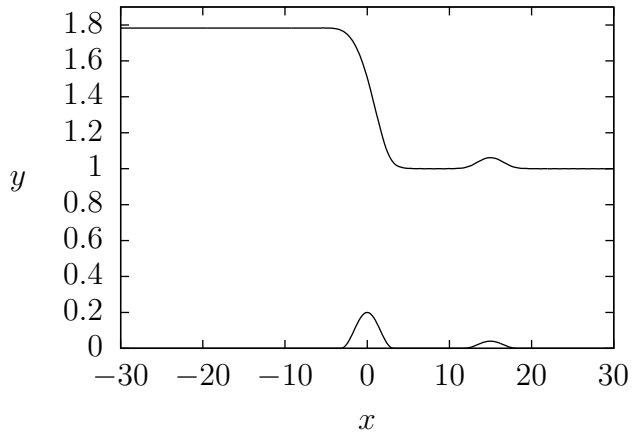

Figure 4.20: Free surface profile past two obstacles on the bottom of the channel, with surface tension $\tau = 0.4$. The first obstacle is characterised by $A_2 = 0.1, L_2 = 3.2$, and the second by $A_1 = 0.02, L_1 = 3.2$, centred downstream at $x = 15$. The free surface appears to be uniform between the obstacles. The Froude number $F = 1.512$ is found as part of the solution.

We find that the gravity-capillary trapped wave solutions are much richer than the pure gravity solutions. Not only is it possible to obtain trapped wave solutions both up and downstream as shown, but most importantly, the downstream trapped wave solutions are not unique. For a given channel bottom configuration, multiple families of trapped wave solutions, which all have the same value of the Froude number, exist. In figure 4.21 we show the solution branches in the $F-\tau$ and $F_{\rm up}-\tau_{\rm up}$ planes for the flow configuration classified by $A_2 = 0.1$, $A_1 = 0.05$ and $L_1 = L_2 = 3.2$. One can easily see that there are several different turning points on the branches, resulting in the multiple solution families

for particular values of the Froude number.

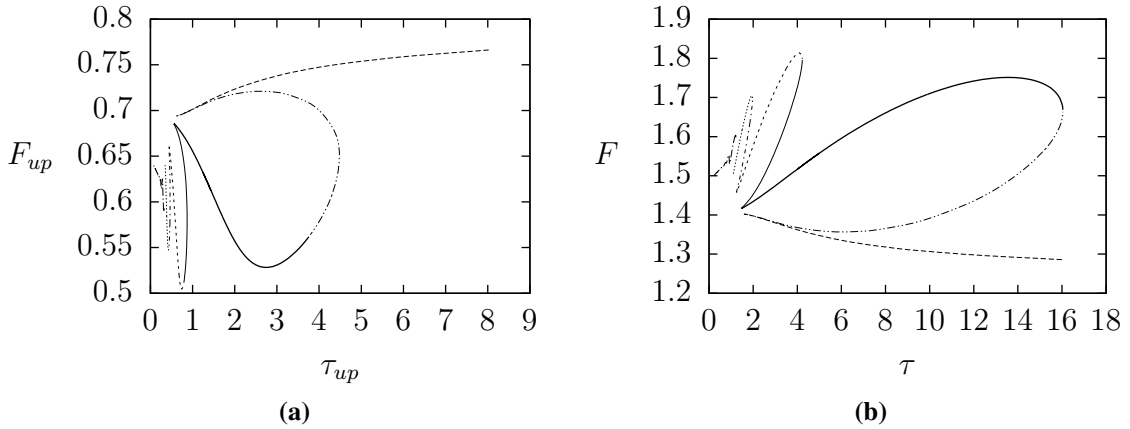

Figure 4.21: Trapped wave solution branches in the $F - \tau$ and $F_{\rm up} - \tau_{\rm up}$ plane for flow past two submerged obstacles classified by $A_2 = 0.1$, $A_1 = 0.05$ and $L_1 = L_2 = 3.2$.

To give an example of the multiple solutions that can be obtained, we fix the Froude number $F = 1.535$ and see that seven different solutions can be obtained for the different values $\tau = 0.8, 1.21, 1.54, 1.74, 2.97, 4.45$ and 14.65 of the Bond number. In figures 4.22 and 4.23 we plot six of these solutions. One can see that as τ increases, with F fixed, the wavelength and amplitude of the trapped waves increases. We also conclude that the gradient of the hydraulic fall is determined by the Bond number. The smaller the Bond number, the steeper the fall. As we increase the Bond number, the gradient of the associated gravity-capillary linear dispersion relation increases (i.e. the Froude number increases more quickly with the wavenumber k). This means that for some given Froude number, the linear dispersion relation will intersect the Froude number for smaller and smaller values of the wavenumber, as τ increases. Therefore, the linear theory predicts that the wavelength of the trapped waves should increase as the surface tension increases. This is in agreement with our observations, and the results shown in figures 4.22 and 4.23, and thus helps to validate our results.

The effects of capillarity on the waves appear to be more important than the effects of gravity. The nonlinearity can be seen in the waves as the wavetrain is not sinusoidal; the waves have slightly more rounded crests than troughs. This means that the waves are dominated by the effects of capillarity. We show this clearly in figure 4.24. The wavelength of the trapped waves is close to the wavelength predicted by the linear theory for such gravity-capillary waves. The downstream dispersion relation with $\tau = 0.9$, shown in figure 4.24(b), predicts waves with a wavenumber of $k \approx 1.68$ for $F = 1.4$. The waves seen in figure 4.24 are thus expected to have wavelength $\lambda \approx 3.74$. We find that the numerical results are in good agreement with this. Between obstacles centred at $x = 0$ and $x = 15$, both of half-width 3.2, the numerical method finds approximately 2.3

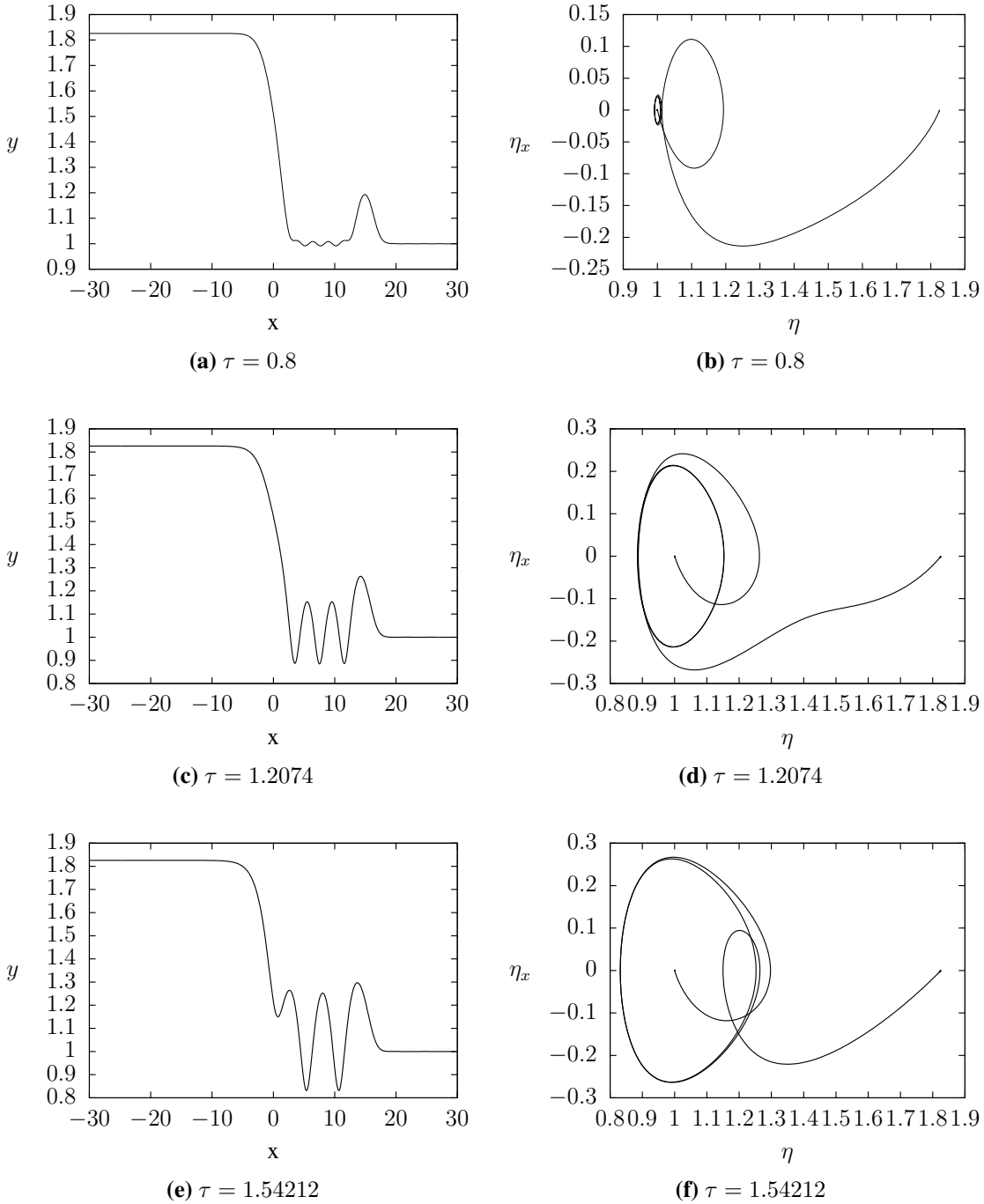

(a) $\tau = 0.8$ **(b)** $\tau = 0.8$

(c) $\tau = 1.2074$ **(d)** $\tau = 1.2074$

(e) $\tau = 1.54212$ **(f)** $\tau = 1.54212$

Figure 4.22: Free surface profiles past two obstacles on the bottom of the channel, characterised by $A_2 = 0.1, L_2 = 3.2$, centred at $x = 0$ and $A_1 = 0.02, L_1 = 3.2$, centred downstream at $x = 15$. All the solutions have the same value of the Froude number: $F = 1.535$. On the right, the phase portraits of the associated solution profile is plotted.

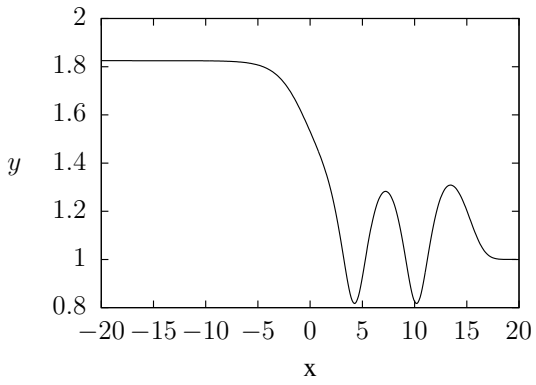

(a) $\tau = 1.74$

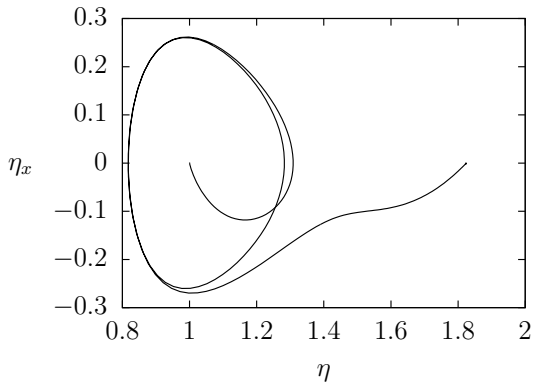

(b) $\tau = 1.74$

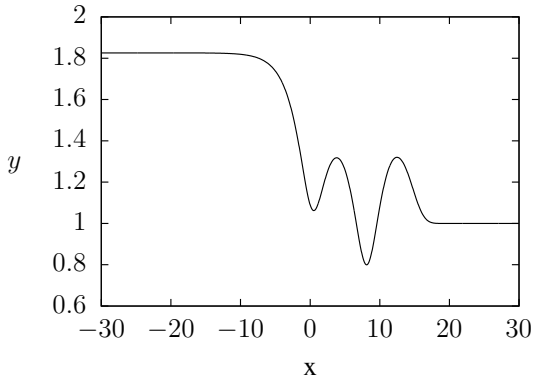

(c) $\tau = 2.973$

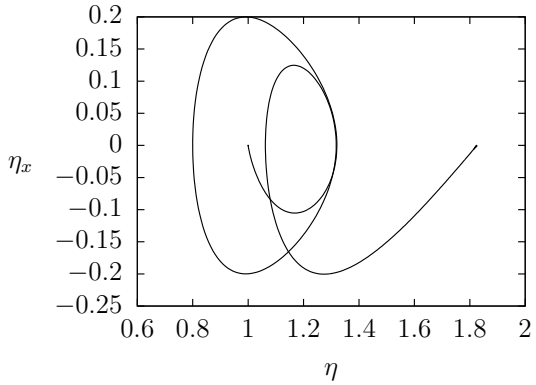

(d) $\tau = 2.973$

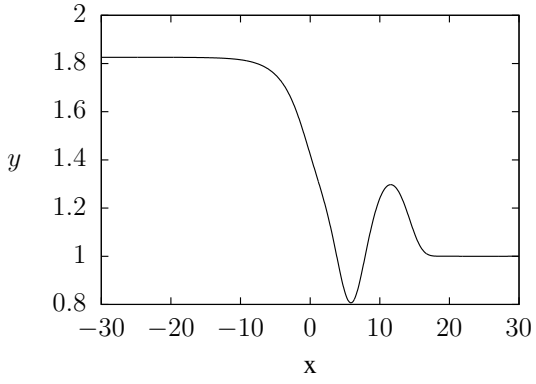

(e) $\tau = 4.451$

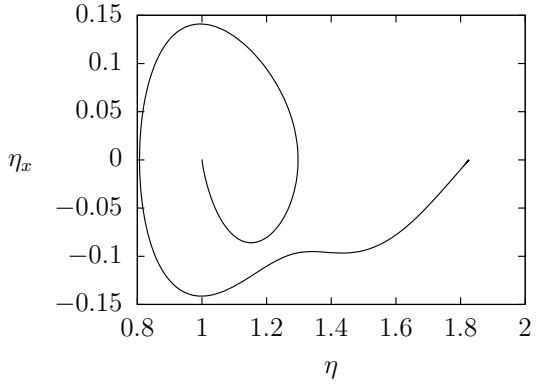

(f) $\tau = 4.451$

Figure 4.23: Free surface profiles past two obstacles on the bottom of the channel, characterised by $A_2 = 0.1, L_2 = 3.2$, centred at $x = 0$ and $A_1 = 0.02, L_1 = 3.2$, centred downstream at $x = 15$. As in figure 4.22 the solutions all have the same value of the Froude number: $F = 1.5345$. On the right, the phase portraits of the associated solution profile is plotted.

waves of wavelength $\lambda \approx 3.74$, as predicted.

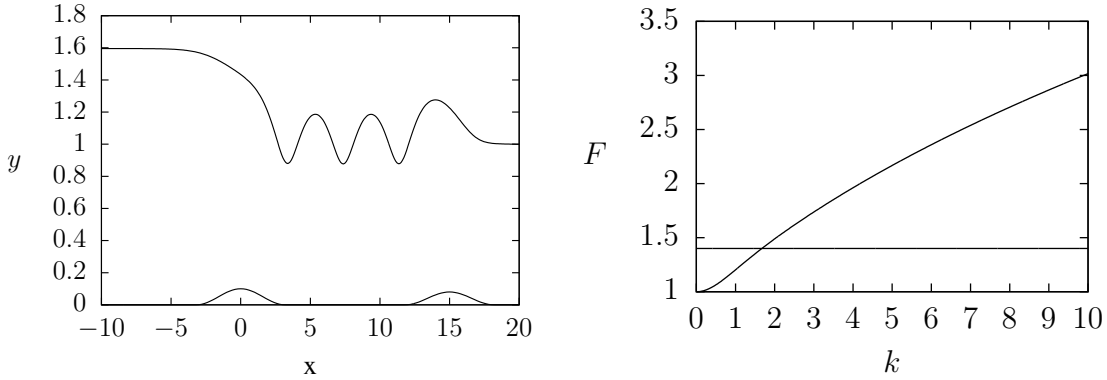

Figure 4.24: Free surface profile past two submerged obstructions on the bottom of the channel, with surface tension $\tau = 0.9$. High amplitude trapped waves are found between the obstacles characterised by $A_2 = 0.05, A_1 = 0.04$ and $L_1 = L_2 = 3.2$ with $x_d = 15$. The Froude number $F = 1.4$ is found as part of the solution. One can see that the crests of the waves are slightly more rounded than the troughs. (b) Linear downstream dispersion relation with $\tau = 0.9$. The horizontal line $F = 1.4$ intersects the dispersion curve at $k \approx 1.68$.

Next, hydraulic fall profiles with an additional downstream disturbance of negative orientation ($A_1 < 0$) are considered. Again, waves are trapped between the two disturbances. Their wavelength is approximately that predicted by linear theory. Instead of an elevation wave over the second obstruction, a near symmetric depression wave is found. The trapped waves have smaller amplitude when $A_1 < 0$ than when $A_1 > 0$. For relatively weak surface tension, or when the height of the first obstacle is large (so that the downstream Froude number F is also large), the free surface resembles a hydraulic fall over the first obstacle, with a depression wave over the downstream obstacle. The amplitude of any trapped waves is so small that the free surface between the hydraulic fall and the depression wave appears to be uniform. Figure 4.25 shows the trapped waves when $A_2 = 0.05, A_1 = -0.09, L_1 = L_2 = 3.2, F = 1.368$ and $\tau = 0.6$. Solutions can be computed for much greater $|A_1|$ when $A_1 < 0$, than for the positive case $A_1 > 0$. However, when the amplitude of the downstream obstacle becomes large, very small amplitude numerically generated waves appear downstream of the second disturbance.

4.4.4 Hydraulic falls with a solitary type wave

If we neglect the effects of surface tension and set $x_d > 0$ and $A_1 > 0$, then we obtain solutions with a hydraulic fall over the obstacle, centred at $x = 0$, and a supercritical solitary type elevation wave over the second obstacle further downstream. Such solutions have previously been studied by Belward [11], and were discussed briefly in section 4.4.3. We showed that in a comparable flow configuration in which the effects of surface tension

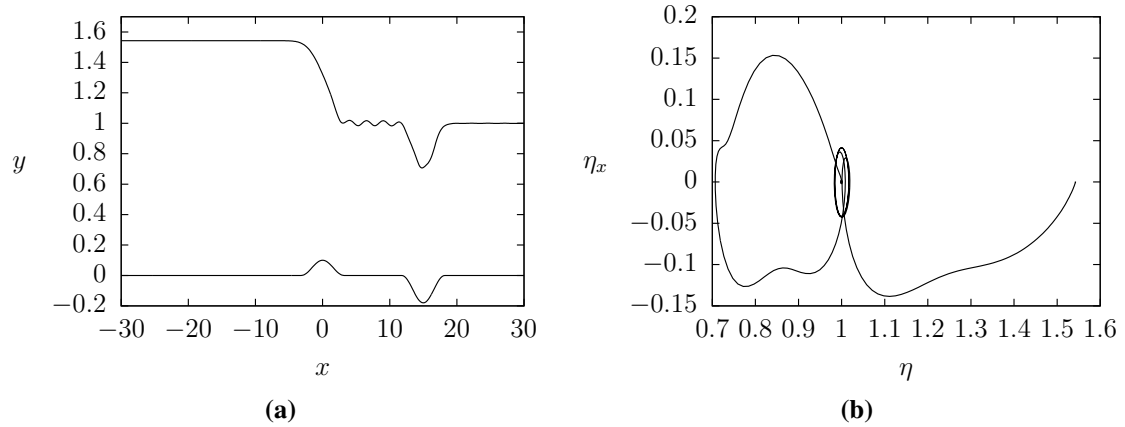

Figure 4.25: (a) Free surface profile past two submerged obstructions on the bottom of the channel, with surface tension $\tau = 0.6$. Trapped waves are found between the obstacles characterised by $A_2 = 0.05, A_1 = -0.09$ and $L_1 = L_2 = 3.2$ with $x_d = 15$. The Froude number $F = 1.368$ is found as part of the solution. The phase portrait of the solution profile in (a) is shown in (b).

are included, so long as the tension is strong enough, and the obstacle height A_1 not too small, a train of trapped waves is visible between the obstacles. However, in the pure gravity case (as with the weaker surface tension cases discussed in section 4.4.3), the flow between the obstacles appears to be uniform. Figure 4.26 shows a typical pure gravity free surface profile (dashed curve) alongside the corresponding gravity-capillary free surface profile (solid curve), with $\tau = 0.6$.

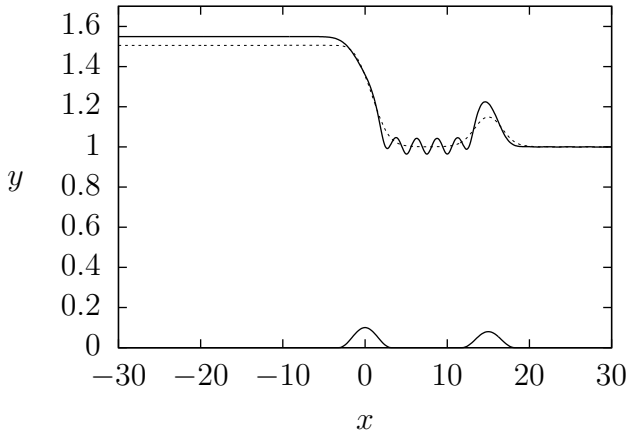

Figure 4.26: Free surface profile past two submerged obstructions on the bottom of the channel, characterised by $A_2 = 0.05, A_1 = 0.04$ and $L_1 = L_2 = 3.2$ with $x_d = 15$. The solid line is the solution with $\tau = 0.6$ and $F = 1.372$. Trapped waves are found between the obstacles. The broken curve is the gravity solution with $\tau = 0$ and $F = 1.345$. The flow appears uniform between the obstacles.

We find that in a gravity-capillary configuration, solutions with uniform flow between a solitary type wave and a hydraulic fall can be obtained by setting $x_d < 0$, so that the second obstacle occurs upstream where the flow is subcritical. If the surface tension is

so small that $F_{\mathrm{up}_{\mathrm{min}}} > F_{\mathrm{up}}$, solitary type waves exist upstream before the hydraulic fall. Solutions with $F_{\mathrm{up}_{\mathrm{min}}} < F_{\mathrm{up}} < 1$ have trapped waves between the obstacles, and were discussed in section 4.4.3.

We find a depression solitary type wave over the upstream obstacle when $A_1 > 0$ and an elevation solitary type wave when $A_1 < 0$. Typical free surface profiles are shown in figure 4.27. The flow near the upstream obstruction is subcritical and is comparable to subcritical gravity-capillary solutions over a single obstacle. See for example Forbes [49] and Maleewong, Asavanant and Grimshaw [77, 78]. When the surface tension is strong ($\tau > \frac{1}{3}$), Maleewong *et al.* [77] obtained a depression solitary wave on a free surface which was subjected to a single positively orientated localised pressure distribution, and an elevation solitary wave for a negatively orientated distribution. As $F \to 1$, they found that the amplitude of the elevation wave increases. Here, the upstream Froude number is determined predominantly by the height of the obstacle centred at $x = 0$. By decreasing the obstacle height, with $\tau_{\mathrm{up}} > \frac{1}{3}$, the upstream Froude number is increased, and we see that the amplitude of the elevation increases. So this appears to be in agreement with Maleewong *et al*'s results. Similarly, Maleewong *et al*. found that as F is increased from zero up to some critical value of $F = F^*$, the amplitude of the depression solitary wave increases. At $F = F^*$ their solution branch in the $F - y(0)$ plane, where $y(0)$ is the amplitude of the solitary wave, possesses a turning point and the solutions change from perturbations of a uniform stream to perturbations of a pure solitary wave. Here, we obtain similar results to the results corresponding to perturbations from the uniform stream; by increasing F_{up}, we increase the amplitude of the depression solitary type wave. The hydraulic fall requires an extra independent parameter than the solitary wave solutions, and so we found obtaining an upstream solitary type wave perturbating from a pure solitary wave much harder. In chapter 3 we discussed how we obtained solitary waves bifurcating from a pure solitary wave. We used parameter continuation on the amplitude of the solitary wave, and let the Froude number come as part of the solution. In the critical flow solutions, the Froude number already comes as part of the solution and is determined predominantly by the hydraulic fall over the first obstruction. Therefore, although we could in theory force the amplitude of the upstream wave to increase, the Froude number cannot change. In fact, the only parameters that may change in the solution are A_1 and L_1, but this just changes the solution branch we are on, as opposed to moving along it.

When the surface tension is weak, the situation is more complicated because, when the wave amplitude is small, the forced solitary type wave solutions resemble envelope solitary waves. Maleewong *et al*. [78] found turning points in the $F - y(0)$ plane for both the elevation and depression solitary waves when $\tau < \frac{1}{3}$. They showed that if the forcing is positive and the Froude number is increased from zero such that $F < F^*$, the

amplitude of the depression solitary wave increases, as in the case with $\tau > \frac{1}{3}$. If the forcing is negative and the Froude number is increased from zero with $F < F^{**}$, where F^{**} is the turning point in the $F - y(0)$ plane, the amplitude of the elevation solitary waves increases. The solutions in these cases are perturbations from a uniform stream. In our results, if we decrease the height of the obstacle centred at $x = 0$, the upstream Froude number $F_{\rm up}$ increases, and the amplitude of the elevation wave when $A_1 < 0$, or the depression wave when $A_1 > 0$, increases. Again, this appears to be in agreement with Maleewong *et al*'s results. Figure 4.28 shows a typical free surface profile with the solitary type wave appearing upstream before a hydraulic fall. Small oscillations can be seen in the tails of the upstream solitary type waves. As $F_{\rm up}$ increases and as τ decreases, $F_{\rm up}$ approaches the minimum of the upstream linear dispersion curve, and the amplitude and number of waves in the oscillatory tail increases. Immediately before the hydraulic fall in figure 4.28, we see a slight elevation in the free surface. This is in agreement with the findings of Guayjarernpanishk and Asavanant [66], discussed in section 4.4.1.

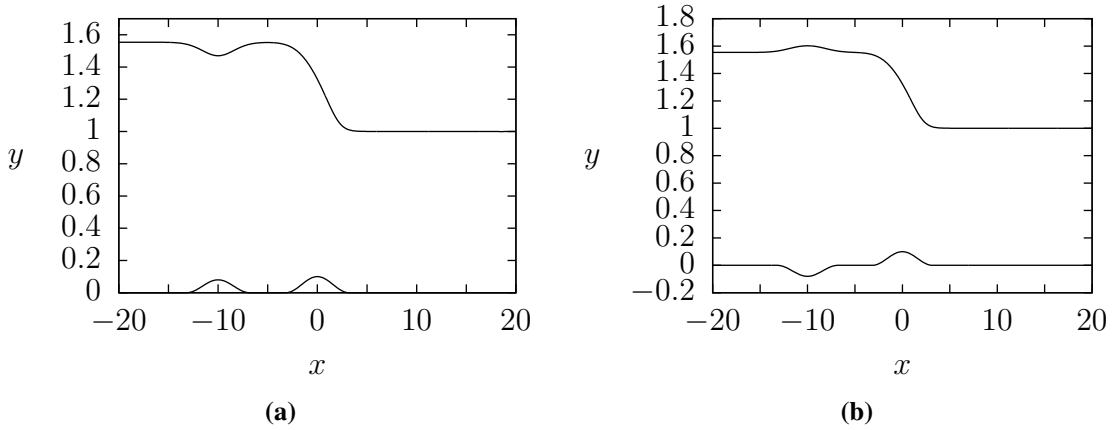

Figure 4.27: Free surface profile past two submerged obstructions on the bottom of the channel, with $\tau = 0.6$. An elevation wave appears over the upstream obstacle characterised by $A_1 = \pm 0.04, L_1 = 3.2$ and $x_d = -10$. The hydraulic fall occurs further downstream over the obstacle characterised by $A_2 = 0.05, L_2 = 3.2$. The value of the Froude number $F = 1.375$ is found as part of the solution.

4.5 Conclusions

We have computed critical flow, gravity-capillary solutions past a single submerged obstruction on the bottom of a channel, using a fully nonlinear boundary integral equation method. We have shown that multiple families of hydraulic fall solutions exist for particular values of the Froude number. Furthermore, we have presented new hydraulic fall solutions which possess a small train of decaying oscillations upstream of the submerged obstruction. Using an argument based on the linear theory we showed that gravity-capillary

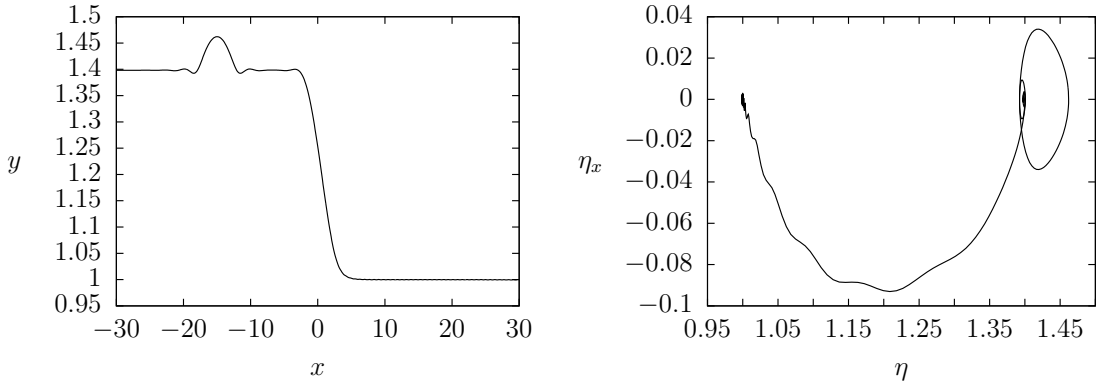

Figure 4.28: (a) Free surface profile past two submerged obstructions on the bottom of the channel, with $\tau = 0.19$. The obstacles are characterised by $A_1 = -0.03$, $A_2 = 0.03$ and $L_1 = L_2 = 3.2$. An elevation solitary wave with damped oscillations appears over the dip before the hydraulic fall. The Froude number $F = 1.277$ is found as part of the solution. The phase portrait of the solution profile in (a) is shown in (b).

generalised hydraulic falls can only be obtained when the surface tension is very small. However, we have investigated the possibility of a different type of generalised hydraulic fall solution for gravity-capillary flows, where the wavetrain occurs downstream of the hydraulic fall, in the supercritical regime. Again, such solutions violate the radiation condition so lack physical relevance in a flow configuration involving just one obstacle. However, we speculate that such a solution is physically relevant when it is considered as the localised flow over an obstacle in a flow configuration involving another submerged obstruction further downstream.

We therefore considered the case of two submerged obstructions and showed that the pure gravity trapped wave solutions found upstream of the hydraulic fall cease to exist in the gravity-capillary case, unless the surface tension is very small. Instead, in order to obtain trapped wave solutions in this case we showed that (as speculated from looking at the generalised hydraulic fall analysis), the second obstacle must be placed downstream of the hydraulic fall. As in the pure gravity case studied by Dias and Vanden-Broeck [41] we therefore postulate that this gravity-capillary solution with trapped waves downstream can be viewed as some sort of hybrid solution. The solution would then have to be the composition of the gravity-capillary generalised hydraulic fall, which has a wavetrain downstream, and a supercritical solution consisting of a wavetrain upstream with an elevation solitary type wave over the submerged obstruction and a uniform stream downstream of the obstruction.

In the pure gravity case, Dias and Vanden-Broeck [41] used a weakly nonlinear analysis to show that the flow near the central obstruction at $x = 0$ approaches that of the generalised hydraulic fall. They observed that the fKdV equation can describe such a flow

in the long wave/small amplitude limit (see for example Dias and Vanden-Broeck [38]). The presence of the two underlying forcings/obstructions then means that there must be two jumps in η in the $\eta - \eta_x$ plane. The solution must then satisfy the unforced KdV equation away from the obstructions and a jump condition at each obstruction. Bounded, continuous solutions of the KdV equation correspond to cnoidal wave solutions and solitary waves. The type-two basic solution, which is uniform upstream and has a wavetrain downstream (see figure 2.1(b)), corresponds to a solution which starts at the origin $\eta = \eta_x = 0$ of the phase plane, and then jumps to a cnoidal wave solution at the obstruction. The generalised hydraulic fall corresponds to the solution starting on a cnoidal wave orbit and then jumping to the solitary wave homoclinic orbit at the obstruction. Dias and Vanden-Broeck showed that when there are two obstructions, the solution starts at the origin $\eta = \eta_x = 0$ then jumps to the cnoidal wave solution at the first obstruction (so locally over the first obstruction is a type-two basic solution) and then at the second obstruction, jumps to the solitary wave homoclinic orbit, giving a generalised hydraulic fall above the second obstruction.

We use a similar argument in the gravity-capillary case. The fKdV equation can again be used to describe the flow in the gravity-capillary case. The unsteady fKdV equation can be written as

$$\frac{1}{2}\left(\frac{1}{3} - \tau\right)\eta_{xxx} + \frac{3}{2}\eta\eta_x - (F_{\text{up}} - 1)\eta_x = -\frac{1}{2}B_x. \tag{4.5.1}$$

A Dirac delta function can then be used to approximate the channel bottom, so that the unsteady KdV equation

$$\left(\frac{1}{3} - \tau\right)\eta_{xx} + \frac{3}{2}\eta^2 - 2(F_{\text{up}} - 1)\eta = 0 \tag{4.5.2}$$

must be satisfied away from the obstructions, alongside a jump condition at each submerged obstruction. More details on the derivation of the jump condition are given in chapter 6. The subcritical gravity-capillary phase portrait of the unforced KdV equation is sketched in figure 4.29(a). In the case of a single obstruction for the new gravity-capillary type of generalised hydraulic fall, the solution starts at the equilibrium point on the homoclinic orbit and then follows the solitary wave trajectory before jumping upwards onto a cnoidal wave trajectory at the obstruction. Figure 4.12(b) shows a fully nonlinear version of this phase portrait. The second type of solution needed to form our hybrid solution is the supercritical solution described above. The supercritical gravity-capillary phase portrait of the unforced KdV equation is sketched in figure 4.29(b). The solution must start on a cnoidal wave trajectory around the origin, and then jump upwards onto the equilibrium point at the origin. However, this solution does not display the elevation directly over the obstruction. It is thought that this is due to using the Dirac delta

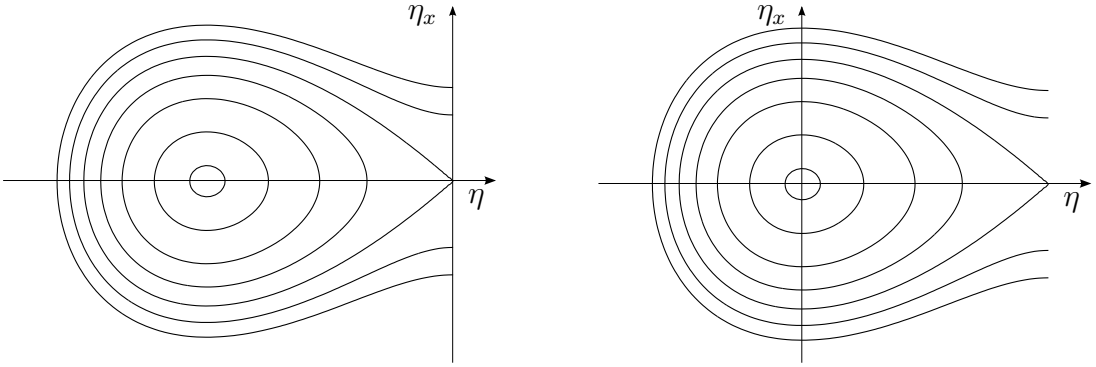

(a) Subcritical flow **(b)** Supercritical flow

Figure 4.29: Sketches of the phase portraits of the gravity-capillary KdV equation.

function to approximate the obstruction on the channel bottom.

As in the pure gravity case, we expect two jumps in η to appear in the two-obstruction configuration. Therefore, we speculate that the solution will start at the equilibrium point on the homoclinic orbit and then follow the solitary wave trajectory. At the first submerged obstruction the solution will jump upwards onto a cnoidal wave trajectory (so, locally over the first obstruction is the new type of gravity-capillary generalised hydraulic fall). Then, at the second submerged obstruction, the solution will jump upwards onto the equilibrium point at the origin, meaning that a solution which has waves upstream but is uniform downstream, occurs locally over the second obstruction.

In section 4.4.3 we showed the existence of multiple families of these gravity-capillary trapped wave solutions, where a wavetrain occurs between the two submerged obstructions.

We have therefore shown that, although unphysical, generalised hydraulic falls can be obtained in the traditional sense, i.e. with waves occurring upstream, when there is very weak surface tension. We have also shown that when surface tension is present, a new type of generalised hydraulic fall exists where the wavetrain occurs downstream, straight after the change of depth. We can thus speculate that there may exist gravity-capillary solutions which have a train of waves both up and downstream of the change in depth. As the surface tension is required to be so small however, the downstream waves may not be easily visible. This leads onto another question: what happens to the flow if we add a third or fourth obstacle to the channel bottom? In the same manner as the generalised hydraulic falls, can we place one obstruction upstream of the hydraulic fall and one downstream, and then obtain two trains of trapped waves (one upstream and one downstream) between the obstacles? Again, we would require that the surface tension be very small, and so careful manipulation of the central and downstream obstruction heights would be required to obtain visible waves downstream. Although no results are shown here, we also briefly investigated including two obstructions downstream of the

hydraulic fall. We saw that two trains of trapped waves then appeared between the first and second, and second and third obstructions. A solitary type elevation wave appeared over both the downstream obstructions.

The stability of pure gravity critical flows was considered by Chardard *et al.* [27] and Donahue and Shen [45]. It was suggested that the hydraulic fall is stable. However these studies used a weakly nonlinear analysis, in the form of a fKdV model. In chapter 7 we use a fully nonlinear scheme to investigate the stability of the gravity and gravity-capillary solutions presented in this chapter.

CHAPTER FIVE

HYDROELASTIC CRITICAL FLOWS AND TRAPPED WAVE SOLUTIONS

5.1 Introduction

As in the previous two chapters, a single layer of fluid flowing in a channel of finite depth is considered. Here however, a thin sheet of ice is assumed to cover the fluid. The restoring forces in this case are therefore the gravitational acceleration on the fluid, and the flexural elasticity of the ice sheet. Critical flexural-gravity solutions, where the flow is subcritical upstream and supercritical downstream, over an obstacle are sought using a similar numerical scheme to that described in chapter 4. The ice plate is first modelled using Cosserat theory and then the boundary integral equation techniques are employed to solve the problem. If the gradient of the hydraulic fall is very steep, the model becomes unphysical as one would then expect the ice to break. This issue of wave breaking is examined, and thus the relevant physical applications of our findings are addressed.

As in the gravity-capillary case in section 4, an additional obstacle is utilised to obtain flexural-gravity trapped waves between two obstacles. The similarities between the gravity-capillary case and the flexural-gravity case are highlighted.

The fully nonlinear problem is formulated in sections 5.2 and 5.3, the results are then presented in section 5.4 along with a discussion concerning the physical relevance of the results. Finally, in section 5.5, we conclude with a summary of the findings.

5.2 Formulation

The steady two-dimensional flow of an inviscid, incompressible fluid is considered. The flow is assumed to be irrotational, and flows along a channel, in which, one or multiple

submerged obstructions lie on the bottom. The Laplace equation,

$$\nabla^2\phi^* = 0, \tag{5.2.1}$$

must therefore be satisfied in the fluid domain, as in the previous two chapters. The fluid is covered by a thin continuous sheet of ice. It is assumed that there are no cavities in the ice so that the entire surface of the fluid coincides with the ice plate. Hydroelastic problems, in contrast to pure gravity and gravity-capillary problems which are geometrically invariant, require a particular parametrisation of the free surface. However, by neglecting any inertia in the ice and assuming that the deformation of the free surface is smooth, the hydroelastic system also becomes geometrically invariant. The inertia in the ice can be neglected as it is much smaller than the inertia of the fluid, see Squire *et al.* [111]. It can further be assumed that the ice is not pre-stressed. Any stretching in the plate is also neglected, as one can assume that the ice sheet floats freely, so that the bending moment is zero. Cartesian coordinates x^*, y^* are introduced, such that the x^*-axis is aligned along the undisturbed channel bottom as $x^* \to \pm\infty$. The y^*-axis is directed vertically upwards through an obstacle, so that gravitational acceleration g acts in the negative y^* direction. The density of the fluid is denoted by ρ.

The flow is assumed to be uniform in the far field as $x^* \to \pm\infty$ with constant depth H, and constant velocity U downstream, and constant depth h and constant velocity V upstream. The deformation of the ice plate is defined by $y^* = H + \eta^*(x^*)$, and the rigid channel bed by $y^* = B^*(x^*)$. The dimensionless upstream and downstream Froude numbers are given by equations (2.3.1) and (2.1.6) respectively. Critical flow solutions are sought, and so it is required that $h > H$ and $V < U$ (see chapter 4).

The kinematic conditions of the free surface and the channel bottom are given by

$$-\frac{\partial\phi^*}{\partial x^*}\frac{\partial\eta^*}{\partial x^*} + \frac{\partial\phi^*}{\partial y^*} = 0 \qquad \text{and} \qquad -\frac{\partial\phi^*}{\partial x^*}\frac{\partial B^*}{\partial x^*} + \frac{\partial\phi^*}{\partial y^*} = 0, \tag{5.2.2}$$

respectively.

The dynamic condition on the free surface comes from satisfying Bernoulli's equation (3.2.7) everywhere in the fluid. The Bernoulli constant $\mathcal{B}$ is defined, as in chapter 4, by

$$\mathcal{B} = \frac{1}{2}\rho U^2 + P + \rho g H. \tag{5.2.3}$$

Thus, we obtain

$$P_a + \frac{1}{2}\rho\left(u^{*2} + v^{*2}\right) + \rho g y^* = \frac{1}{2}\rho U^2 + P + \rho g H, \tag{5.2.4}$$

$$\Rightarrow \frac{1}{\rho}\left(P_a - P\right) + \frac{1}{2}\left(u^{*2} + v^{*2} - U^2\right) + g\left(y^* - H\right) = 0, \tag{5.2.5}$$

$$\Rightarrow \quad -\frac{1}{\rho}P_\alpha + \frac{1}{2}\left(u^{*2} + v^{*2} - U^2\right) + g\left(y^* - H\right) = 0, \tag{5.2.6}$$

where P_α is given by (2.5.42).

Next, we non-dimensionalise the equations by taking U as unit velocity and H as unit length. Non-starred variables are thus now understood to be dimensionless. Furthermore, following the work in section 4.3, we introduce the arclength s to parametrise the free surface. This also has the advantage of simplifying P_α in (5.2.6). Then (5.2.6) becomes

$$\begin{aligned}
&\frac{\mathcal{D}}{\rho}\left(\frac{1}{H^3}\kappa_{ss} + \frac{1}{H^3}\kappa^3\right) + \frac{U^2}{2}\left(\phi'^2 - 1\right) + gH(y(s) - 1) = 0,\\
\Rightarrow\ &\frac{\mathcal{D}}{\rho H^3 U^2}\left(\kappa_{ss} + \frac{1}{2}\kappa^3\right) + \frac{1}{2}\left(\phi'^2 - 1\right) + \frac{gH}{U^2}\left(y(s) - 1\right) = 0,\\
\Rightarrow&\frac{\mathcal{D}}{\rho H^3 U^2}\frac{gH}{gH}\left(\kappa_{ss} + \frac{1}{2}\kappa^3\right) + \frac{1}{2}(\phi'^2 - 1) + \frac{1}{F^2}(y(s) - 1) = 0,\\
\Rightarrow\ &\frac{\mathcal{D}}{\rho H^4 g}\frac{gH}{U^2}\left(\kappa_{ss} + \frac{1}{2}\kappa^3\right) + \frac{1}{2}(\phi'^2 - 1) + \frac{1}{F^2}(y(s) - 1) = 0,
\end{aligned}$$

where we have used (2.5.36). Thus, the dynamic boundary condition is

$$\frac{2E_b}{F^2}\left(\kappa_{ss} + \frac{1}{2}\kappa^3\right) + \phi'^2 - 1 + \frac{2}{F^2}(y(s) - 1) = 0, \tag{5.2.7}$$

where we have introduced the parameter

$$E_b = \frac{\mathcal{D}}{\rho g H^4}, \tag{5.2.8}$$

with $\mathcal{D}$ given by (2.5.2). The system of equations to solve is therefore

$$\nabla^2\phi = 0 \qquad B(x) < y < 1 + \eta(x), \tag{5.2.9}$$

$$\phi_x\eta_x - \phi_y = 0 \qquad \text{on} \qquad y = 1 + \eta(x), \tag{5.2.10}$$

$$\frac{2E_b}{F^2}\left(\kappa_{ss} + \frac{1}{2}\kappa^3\right) + \phi'^2 - 1 + \frac{2}{F^2}\left(y(s) - 1\right) = 0 \qquad \text{on} \qquad y = 1 + \eta(x), \tag{5.2.11}$$

$$\phi_x B_x - \phi_y = 0 \qquad \text{on} \qquad y = B(x). \tag{5.2.12}$$

As in chapter 4, we define the dimensionless upstream flow velocity by γ so that by considering the conservation of the mass of the fluid, we see that the dimensionless

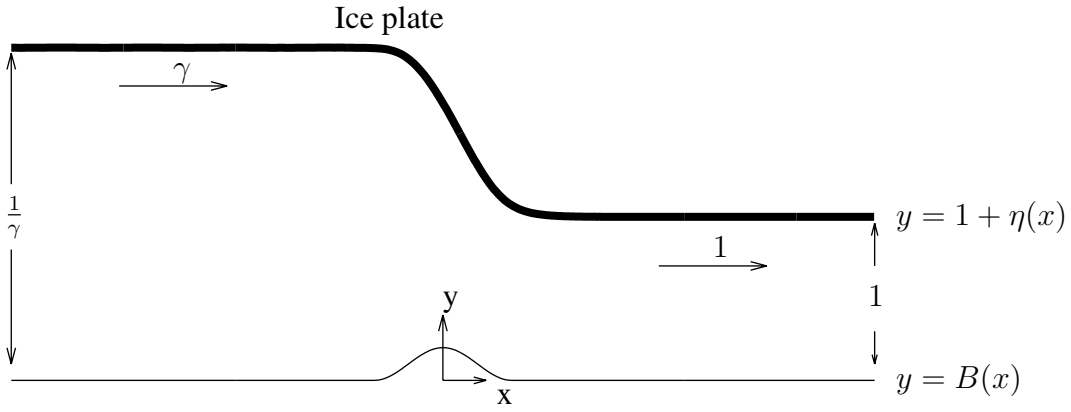

Figure 5.1: The dimensionless flow configuration over a single obstruction on the bottom of the channel.

upstream depth is given by $1/\gamma$. The dimensionless flow configuration is shown in figure 5.1. The far field conditions are thus written as

$$\phi_x \to 1, \;\; y(x) \to 1 \;\; \text{as} \;\; x \to \infty, \tag{5.2.13}$$

$$\phi_x \to \gamma, \;\; y(x) \to \frac{1}{\gamma} \;\; \text{as} \;\; x \to -\infty, \tag{5.2.14}$$

and following our work in chapter 4 we have one further equation which provides the relationship between the Froude number and the upstream flow velocity. Again, this equation is given by

$$\frac{1}{2} - \frac{1}{2}\gamma^2 + \frac{1}{F^2} - \frac{1}{F^2\gamma} = 0. \tag{5.2.15}$$

This then completes the reformulation of the problem; we need to find the unknown functions $\phi(x, y)$ and $\eta(x)$ satisfying the Laplace equation (5.2.9), and the kinematic and dynamic boundary conditions (5.2.10) - (5.2.12), subject to the far field flow conditions (5.2.13) and (5.2.14), and the relation (5.2.15). We can see that the problem formulation is similar to that for gravity-capillary waves, except for the pressure term in the dynamic boundary condition (5.2.11).

5.3 Numerical scheme

Following our work in chapter 4, we reformulate the problem as a system of integro-differential equations. The system can then be solved for the unknown free surface $y = 1 + \eta(x)$, over arbitrarily shaped obstructions on the bottom of the channel.

The dynamic boundary condition (5.2.11) has already been parametrised, so we just need to simplify the rest of the formulation by considering the parametrisation of the free surface with the arclength s; $x = X(s)$, $y = Y(s)$. We must then satisfy the parametric

equation

$$\left(\frac{dX(s)}{ds}\right)^2 + \left(\frac{dY(s)}{ds}\right)^2 = 1. \tag{5.3.1}$$

Using the kinematic boundary condition (5.2.10), we write the velocity components in parametric form, as in chapter 4, as

$$u = \frac{d\phi}{ds}\frac{dX}{ds}, \qquad v = \frac{d\phi}{ds}\frac{dY}{ds}. \tag{5.3.2}$$

The complex variable $z = x+iy$ and the complex potential $w(z) = \phi(x,y)+i\psi(x,y)$, where $\psi(x,y)$ is the stream function satisfying (3.3.4), are introduced. Cauchy's integral formula is then applied to the analytic, complex function

$$h(z) = \frac{dw}{dz} - \gamma = \phi_x - \gamma - i\phi_y \tag{5.3.3}$$

around a contour $\mathcal{C}$, consisting of the fluid surface, the channel bottom, and vertical lines joining them at $x = \pm L$, in the limit as $L \to \infty$. Now, letting s represent the evaluation point on the contour $\mathcal{C}$, and σ the value of the arclength at the varying point $z(\sigma) = x(\sigma) + iy(\sigma)$ on the contour, we obtain the same two integro-differential equations as in the gravity-capillary case in chapter 4;

$$\begin{aligned}
&\pi(\phi'(s)X'(s) - \gamma) = \\
&-\int_{-\infty}^{\infty} \frac{(\phi'(\sigma) - \gamma X'(\sigma))(Y(s) - Y(\sigma)) - \gamma Y'(\sigma)(X(\sigma) - X(s))}{(X(\sigma) - X(s))^2 + (Y(\sigma) - Y(s))^2} d\sigma \\
&+\int_{-\infty}^{\infty} \frac{(\hat{u}(\sigma)(1 + B_x(\sigma)^2) - \gamma)(Y(s) - B(\sigma)) - \gamma B_x(\sigma)(\sigma - X(s))}{(\sigma - X(s))^2 + (B(\sigma) - Y(s))^2} d\sigma,
\end{aligned} \tag{5.3.4}$$

and

$$\begin{aligned}
\pi(\hat{u}(x) - \gamma) = &-\int_{-\infty}^{\infty} \frac{(\phi'(\sigma) - \gamma X'(\sigma))(B(x) - Y(\sigma)) - \gamma Y'(\sigma)(X(\sigma) - x)}{(X(\sigma) - x)^2 + (Y(\sigma) - B(x))^2} d\sigma \\
&+\int_{-\infty}^{\infty} \frac{(-B(\sigma) + B(x))(\hat{u}(\sigma)(1 + B_x(\sigma)^2) - \gamma) - \gamma B_x(\sigma)(\sigma - x)}{(\sigma - x)^2 + (B(\sigma) - B(x))^2} d\sigma.
\end{aligned} \tag{5.3.5}$$

The horizontal fluid velocity component on the channel bottom is defined by $u(\sigma, B(\sigma)) = \hat{u}(\sigma)$.

The two integral equations (5.3.4) and (5.3.5), together with the parametrised dynamic condition (5.2.11) and the parametric equation (5.3.1) provide the system of integro-differential equations to be solved iteratively via Newton's method, for the unknown variables $Y'(s), X'(s), \phi'(s)$ on the fluid-ice interface, and $\hat{u}(x)$ on the channel bottom.

The free surface is discretised with N equally spaced mesh points, separated by an

interval e, on the free surface, and M equally spaced mesh points, separated by an interval h, on the channel bottom. This time, we choose the two independent parameters needed to uniquely determine a solution, as the obstacle size and the flexural rigidity of the ice, E_b. The Froude number and the upstream fluid depth are then found as part of the solution. We have $3N + M + 2$ unknowns; $Y'(i) = Y'(s_i), X'(i) = X'(s_i), \phi'(i) = \phi'(s_i)$, for $i = 1, ..., N, \hat{u}(i) = \hat{u}(x_i)$, for $i = 1, ..., M, \gamma$ and F. However, following our work in chapter 4, given an initial set of values for $Y'(i)$, we obtain $X'(i)$ from the parametric equation (5.3.1) and $\phi'(i)$ on the free surface from the dynamic condition (5.2.11). The number of unknowns is thus reduced by $2N$.

The two integro-differential equations (5.3.4) and (5.3.5) are evaluated at the mesh midpoints, using the trapezoidal rule with summation over the mesh points. Therefore, integro-differential equation (5.3.4) provides $N - 1$ equations and (5.3.5) provides $M - 1$ equations. The analytical truncation corrections T_1 and T_2, defined by (4.3.28) and (4.3.29) respectively, are added to the numerical solutions of the truncated versions of the integrals. So, we have $N+M-2$ equations for the $N+M+2$ unknowns. The remaining four equations are those imposed in the numerical scheme in chapter 4 to define the flow in the far field, as well as the relationship between the Froude number F and the upstream flow speed γ;

$$Y'(1) = Y'(2) = 0, \tag{5.3.6}$$

$$\hat{u}(M) = 1, \tag{5.3.7}$$

$$\frac{1}{2} - \frac{1}{2}\gamma^2 + \frac{1}{F^2} - \frac{1}{F^2\gamma} = 0. \tag{5.3.8}$$

5.4 Results

5.4.1 Linear theory

We linearise the time dependent dimensional form of the problem (5.2.9) - (5.2.12) in a fixed frame of reference, after considering the Taylor expansions about $y = H$. In the absence of forcing, and reverting to the original Cartesian variables, we obtain

$$\phi_{xx} + \phi_{yy} = 0 \qquad 0 < y < H, \tag{5.4.1}$$

$$\phi_y = \eta_t \qquad \text{on} \qquad y = H, \tag{5.4.2}$$

$$\phi_t + \frac{\mathcal{D}}{\rho}\eta_{xxxx} + g\eta = 0 \qquad \text{on} \qquad y = H, \tag{5.4.3}$$

$$\phi_y = 0 \qquad \text{on} \qquad y = 0. \tag{5.4.4}$$

We seek linear sinusoidal wave functions of the form

$$\phi(x,y) = \hat{a}(y)e^{i(kx-\omega t)}, \tag{5.4.5}$$

$$\eta(x) = ae^{i(kx-\omega t)}, \tag{5.4.6}$$

for some constant a. Substituting (5.4.5) into (5.4.1) gives

$$-\hat{a}(y)k^2 + \hat{a}''(y) = 0, \tag{5.4.7}$$

$$\Rightarrow \quad \hat{a}(y) = c_1 e^{ky} + c_2 e^{-ky}, \tag{5.4.8}$$

$$\Rightarrow \quad \phi = (c_1 e^{ky} + c_2 e^{-ky})e^{i(kx-\omega t)}, \tag{5.4.9}$$

where c_1 and c_2 are arbitrary constants. Then, substituting (5.4.9) into (5.4.4) we obtain

$$c_1 k - c_2 k = 0, \tag{5.4.10}$$

$$\Rightarrow \quad c_1 = c_2, \tag{5.4.11}$$

and thus,

$$\phi = 2c_1 \cosh(ky)e^{i(kx-\omega t)}. \tag{5.4.12}$$

Now substituting (5.4.12) and (5.4.6) into (5.4.2) gives

$$-ai\omega = 2c_1 k \sinh kH, \tag{5.4.13}$$

$$\Rightarrow \quad 2c_1 = \frac{-ai\omega}{k\sinh(kH)}. \tag{5.4.14}$$

Next, substituting (5.4.6) and (5.4.12) into (5.4.3) we obtain

$$-2c_1\omega i \cosh kH + \frac{\mathcal{D}}{\rho}k^4 a + ga = 0. \tag{5.4.15}$$

Finally, eliminating $2c_1$ from (5.4.15) using (5.4.14) gives

$$-a\omega^2 \frac{\cosh(kH)}{k\sinh(kH)} + \frac{\mathcal{D}}{\rho}k^4 a + ga = 0, \tag{5.4.16}$$

$$\Rightarrow \quad \frac{-\omega^2}{k}\tanh^{-1}(kH) + g + \frac{\mathcal{D}}{\rho}k^4 = 0\ . \tag{5.4.17}$$

Then, we know that $\omega = ck$, so the phase speed c is given by

$$k^2 c^2 = \left(gk + \frac{\mathcal{D}}{\rho}k^5\right)\tanh(kH), \tag{5.4.18}$$

or in dimensionless form;

$$F^2 = \left(\frac{1}{K} + E_b K^3\right)\tanh(K), \tag{5.4.19}$$

where $K = kH$ is the dimensionless wavenumber. One important property of the flexural-gravity linear dispersion relation, (5.4.19), is that we can show that there is always a point at which the phase velocity equals the group velocity, i.e. there is always a minimum wavenumber $k_{\min}$. Differentiating (5.4.19) we obtain

$$\begin{aligned} 2FF' =& (-K^{-2} + 3E_bK^2)\tanh(K) + (K^{-1} + E_bK^3)(1 - \tanh^2(K)), && (5.4.20)\\ \approx& (-K^{-2} + 3E_bK^2)\left(K - \frac{1}{3}K^3 + \frac{2}{15}K^5 + ...\right)\\ &+ (K^{-1} + E_bK^3)\left(1 - \left(K - \frac{1}{3}K^3 + \frac{2}{15}K^5 + ...\right)^2\right), && (5.4.21)\\ \approx& -\frac{2}{3}K + \left(\frac{8}{15} + 4E_b\right)K^3 + O(K^5), && (5.4.22) \end{aligned}$$

where we have approximated $\tanh(K)$ by its Taylor expansion $\tanh(K) \approx K - 1/3K^3 + \frac{2}{15}K^5 + ...$ Here, the prime denotes a derivative with respect to K. Assuming K is small, at first order we see that

$$F' < 0, \tag{5.4.23}$$

which is true for all values of E_b. We also know that as $K \to \infty$, $\lim_{K\to\infty}(\tanh(K)) \to 1$. Therefore, (5.4.19) tells us that as $K \to \infty$ we must have $F \to \infty$. So, there must exist a minimum in the linear dispersion relation in order for the gradient of the curve to start decreasing for small K, but then increase for larger K.

5.4.2 Physical validity of the fully nonlinear model

For the solutions found in this section, when the amplitude is large, it is possible that modelling the ice plate as a thin elastic shell becomes an unrealistic assumption. In order to ensure physical realism, Brocklehurst, Korobkin and Părău [22] describe how the strain of the ice plate needs to be less than the yield strain of ice. Otherwise, at such high strains, the behaviour of the plate becomes plastic and so one would expect the ice to fracture or break. The strain of the ice is proportional to the curvature of the free surface. It may be calculated by

$$\epsilon = \frac{\bar{h}}{2}\kappa^* \approx \frac{\bar{h}}{2}\eta^*_{x^*x^*}, \tag{5.4.24}$$

where $\bar{h}$ is the thickness of the ice, and κ^* is the dimensional curvature of the ice plate (see for example Ugural [121], Brocklehurst *et al.* [22] and Squire [109]). For short waves the increase of the curvature in the deformation of the ice plate therefore causes greater strain in the plate.

Goodman, Wadhams and Squire [58] describe how a swell-induced failure of the ice is a result of cracks propagating through the ice. They claim that a crack will propagate if the intensity of the stress near the crack reaches some critical value. Through experimental work, Goodman [57] determined that this critical stress in pure ice can be represented by the value $115\text{KN m}^{-3/2}$. The critical strain of the ice is then calculated by considering the length of the crack and this critical stress. Goodman found this critical strain to be $\epsilon_{cr} = 2.14 \times 10^{-4}$. However, in the ocean salt can creep into the cracks so that the critical stress near the crack reduces. It is therefore much easier for a crack to propagate in the ocean/salt water. Salt creeps into the crack so the crack is much less likely to refreeze. So, the critical strain is approximated by a smaller value, and Goodman estimated this to be $\epsilon_{cr} = 4.3 \times 10^{-5}$. Furthermore, Goodman *et al.* [58] went on to find a critical wave height which would cause cracks to propagate.

Both physically realistic results, where the ice is not expected to fracture, and less physical results are presented in this chapter. Whilst some results may be unphysical in ice (although there may be other applications), it is interesting to compare them to the gravity-capillary results in chapter 4. Furthermore, one can extrapolate the results to flows of different depths or flows over less steep obstructions, where the strain of the ice is much smaller. Plots of the strain given by (5.4.24) are therefore shown alongside the plots of the free surface profiles.

5.4.3 Previous experimental results

In order to help to determine the physical situations which the results presented in this chapter represent, we analyse the findings with respect to representative parameters found during experiments in Lake Diefenbaker in Canada (by Eyre [48]) and Lake Saroma in Japan (by Takizawa [115, 116]). The parameters we use are defined in table 5.1.

We classify our solutions according to the value of the dimensionless parameter E_b, defined by (5.2.8). This depends directly on the water depth H, gravitational acceleration (which we take to be $g = 9.8\text{ms}^{-2}$), the density of the water, and the flexural rigidity of the ice, $\mathcal{D}$ given by (2.5.2). We assume that the water density and gravitational acceleration are fixed for all water flows. The flexural rigidity depends on the Young's modulus and Poisson's ratio, which we assume are fixed, and on the thickness of the ice $\bar{h}$. Therefore, we can interpret our results in terms of E_b by determining either the value of H for which the flow must exist (given that $\bar{h}$ is fixed), or the value of $\bar{h}$ (given that H is fixed). In most of the results presented in the following sections we fix $\bar{h}$ and find H.

	Lake Diefenbaker	Lake Saroma
Water depth H	35m	6.8m
Ice thickness $\bar{h}$	0.73m	0.17m
Young's modulus E	13×10^9 Nms^{-2}	5.1×10^5 Nms^{-2}
Poisson's ratio ν	0.33	0.33
Flexural rigidity $\mathcal{D}$	4.73×10^8 Nm	2.34×10^5 Nm
Water density ρ	1026 kg m^{-3}	1026 kg m^{-3}

Table 5.1: Some of the physical parameters used in experiments performed in Lake Diefenbaker and Lake Saroma.

5.4.4 Hydraulic falls

We assume that $B(x)$ is given by (4.4.1) and then begin by considering the case where the function $y = B(x)$ describes a uniform channel bottom along which a single obstruction lies. Therefore, we set $A_1 = 0$, $A_2 > 0$, and fix the value of L_2. We seek hydraulic fall solutions with subcritical flow upstream ($F_{\text{up}} < 1$) and supercritical flow ($F > 1$) downstream. Typical hydraulic fall solution profiles obtained using the scheme described in section 5.3 are shown in figure 5.2(a), where three different values are used for the dimensionless parameter E_b; $E_b = 0.5$, $E_b = 0.2$ and $E_b = 0.1$. Immediately before the hydraulic fall, we see that there exists a slight elevation in the ice plate deformation. A similar phenomenon was observed in chapter 4 for weak gravity-capillary (i.e. $\tau < \frac{1}{3}$) hydraulic falls found in the neighbourhood of the minimum of the upstream gravity-capillary linear dispersion relation.

To calculate the strain on the ice plate in these solutions, we first obtain the physical depth of the fluid downstream using (5.2.8):

$$H = \left(\frac{\mathcal{D}}{\rho g E_b}\right)^{\frac{1}{4}}. \tag{5.4.25}$$

Then, using (5.4.24) and (4.3.7) we compute the strain ϵ on the free surface:

$$\epsilon(i) = \bar{h}\frac{(Y''X' - X''Y')}{2X'^3 H}. \tag{5.4.26}$$

Here we use $\bar{h} = 0.73$m, corresponding to the depth of the ice in Lake Diefenbaker. It should be noted that in Lake Saroma the depth of the ice and the flexural rigidity of the ice was slightly smaller, meaning that the strain in such solutions is slightly greater. The maximum strain in the hydraulic fall solutions occurs at the beginning and the end of the falls. As we decrease the value of E_b (corresponding to deeper water depths), the strain

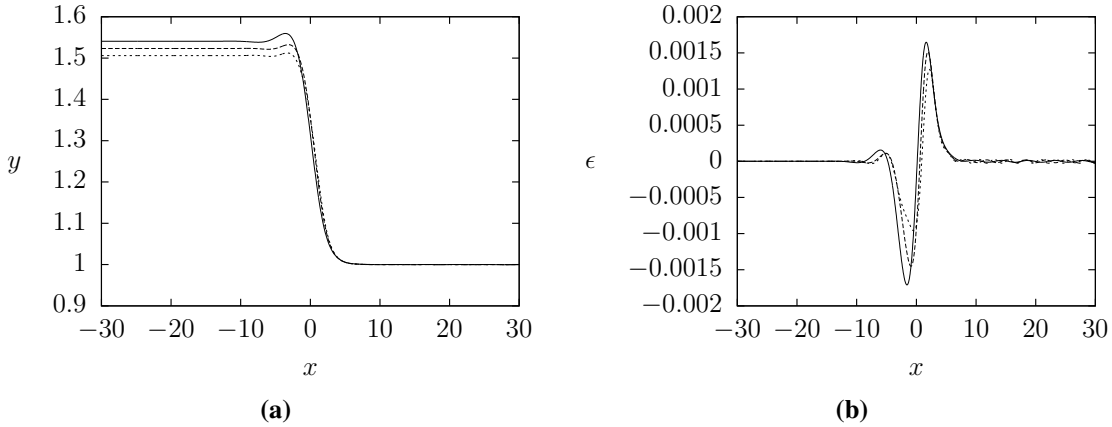

Figure 5.2: (a) Hydraulic fall profiles over a submerged obstruction of height $2A_2 = 0.1$ with lengths $2L_2 = 6$. An elevation appears immediately before the fall for the parameters $E_b = 0.5$, $F = 1.367$, $F_{\text{up}} = 0.715$ (solid line), $E_b = 0.2$, $F = 1.356$, $F_{\text{up}} = 0.721$ (dashed line), and $E_b = 0.1$, $F = 1.345$, $F_{\text{up}} = 0.728$ (dotted line). (b) Strain present in the profiles shown in (a), when considered with the parameters of Lake Diefenbaker.

in the solution decreases. Figure 5.2(b) shows the strains of the solutions given in figure 5.2(a). We see that the maximum strain is of order 1×10^{-3}, and so according to the analysis in section 5.4.2 we would expect the ice to break for an ice depth comparable to the Lake Diefenbaker experiments. For physically realistic solutions with these values of E_b, we would require a thicker ice plate with a higher flexural rigidity.

By decreasing either the value of the parameter E_b or the height of the obstruction, the upstream Froude number approaches the minimum of the upstream linear dispersion relation, and the small upstream elevation eventually becomes part of a train of decaying waves before the fall. A similar result has been seen in the critical solutions for the gravity-capillary case in chapter 4. However, the waves found here in the flexural-gravity cases are more pronounced and extend further upstream. In order to minimise any truncation problems, we had to use a longer domain, truncating at $x = \pm 60$. Figure 5.3(a) shows such a train of waves immediately before a fall when $E_b = 0.1$ and $F = 1.159$. The computed upstream Froude number is then $F_{\text{up}} = 0.858$, which is near the minimum of the upstream linear dispersion relation $F_{\text{up}_{\min}} \approx 0.86$, with corresponding wavenumber $k_{\min} \approx 1.2$. The strain of the ice is much smaller in this solution, being of the order 1×10^{-4}. This solution is therefore much more likely to be physically realistic for the ice plate experimented with in Lake Diefenbaker (although in Lake Saroma, we would still expect the ice to break).

Next we try to compute flows for smaller values of E_b, in order to obtain solutions valid in deeper fluids. This is difficult however, as such solutions occur close to the minimum of the upstream linear dispersion relation. Reducing E_b, with the size of the obstacle fixed, increases the upstream Froude number, so that it approaches $F_{\text{up}_{\min}}$. In

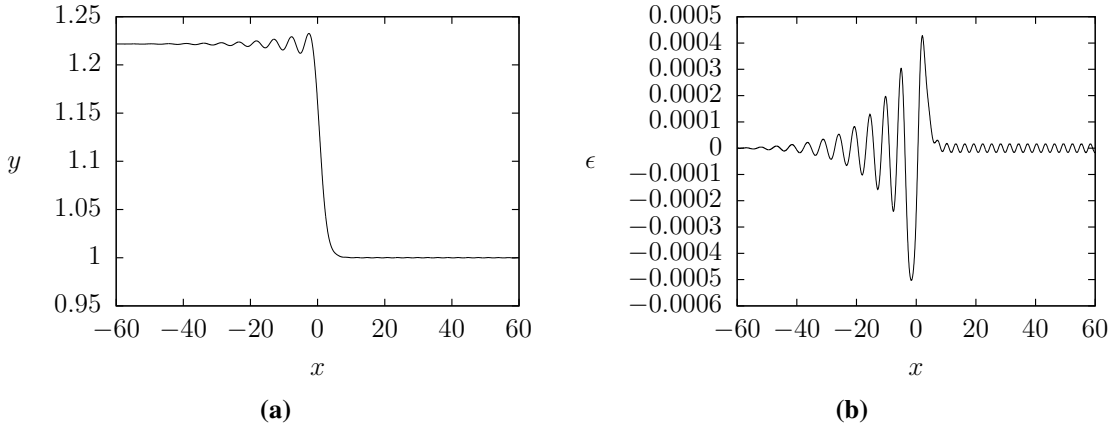

Figure 5.3: (a) Hydraulic fall profile over a submerged obstruction of height $2A_2 = 0.02$ with length $2L_2 = 6.4$. For the parameters $E_b = 0.1$, $F = 1.159$ and $F_{\text{up}} = 0.858$, upstream, a train of decaying waves before the fall can be seen. The Froude number was found as part of the solution. (b) The strain present in the solution profile shown in (a), when considered with the parameters of Lake Diefenbaker.

the pure gravity case we have seen that, when the upstream Froude number intersects the upstream linear dispersion relation, generalised hydraulic falls may be obtained (Dias and Vanden-Broeck [38]). When the Froude number intersects the upstream flexural-gravity linear dispersion relation, unless the Froude number is exactly at the minimum, it will intersect the dispersion relation twice. Therefore, we expect generalised hydroelastic hydraulic falls to exist in this regime. A resonance occurs between the two modes in a similar manner to the gravity-capillary case. So, waves of two different wavelengths travelling at the same speed can appear on the upstream part of the solution (see Vanden-Broeck and Părău [125]). Therefore, one might expect that some solutions, at greater depths in Lake Saroma and Lake Diefenbaker, over a fixed obstacle, will take the form of, for example, Wilton ripples upstream of the fall (see Vanden-Broeck [123]) whilst being uniform downstream, i.e. generalised type solutions. However, such solutions are of course unphysical as they violate the radiation condition, as discussed in the gravity-capillary case in chapter 4.

Alternatively, we find that if we increase the height and/or width of the underlying obstruction, the upstream Froude number F_{up} decreases so that, with E_b fixed, the difference between F_{up} and $F_{\text{up}_{\text{min}}}$ increases. Then, we see that E_b may be reduced further before F_{up} intersects the upstream linear dispersion relation. Therefore, for a 'large enough' obstacle, the hydraulic falls found in the deeper lakes Saroma and Diefenbaker may be uniform both up and downstream. A solution with $E_b = 0.02$ over an obstacle of height $2A_2 = 0.35$ and width $2L_2 = 35$ is shown in figure 5.4(a). The slope of the fall in this solution is clearly less steep than that for solutions over a narrower and smaller obstacle. Here we see that the strain of the solution is always less than 2.5×10^{-4}, which is much

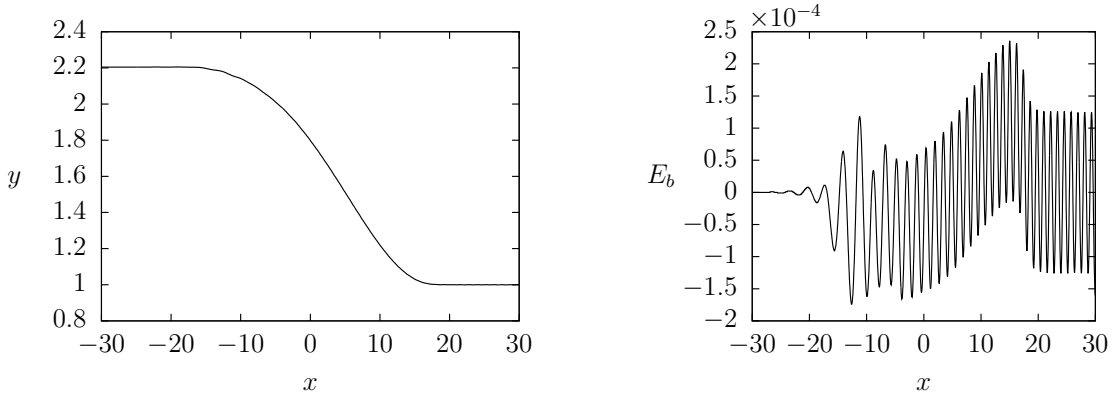

Figure 5.4: (a) Hydraulic fall profile over a submerged obstruction of height $2A_2 = 0.35$ with length $2L_2 = 35$. No elevation is seen before the fall. We set $E_b = 0.02$ and found the Froude number to be $F = 1.74$ (b) Strain present in the solution profile shown in (a), when considered with the parameters of Lake Diefenbaker.

smaller than in the solutions presented in figure 5.2(a). The ice is therefore much less likely to fracture in such flow configurations.

As in the gravity-capillary case, small amplitude spurious periodic waves are sometimes found downstream of the hydraulic fall, where the flow is supercritical. In this region the downstream Froude number intersects the downstream linear dispersion curve (see figure 5.5 for the linear dispersion relation corresponding to figure 5.3(a)), and so (short) flexural waves, ahead of the forcing, are indeed predicted by the linear theory. There is no obstacle to generate these waves in this downstream region, but the downstream truncation can act as a form of artificial forcing, ahead of which waves can form. However, by manipulating the far field conditions downstream it is possible to reduce the amplitude of the spurious waves so much that we obtain negligible waves downstream, and thus physically relevant solutions. In the gravity-capillary case examined in chapter 4, we discussed the possibility of a form of generalised hydraulic falls where the flow is uniform upstream, and has periodic waves downstream. Such solutions may also occur in the flexural-gravity case. However, without a second disturbance further downstream, such solutions would also lack physical relevance in this regime.

In figure 5.6(a) we plot the solution branch in the $F - E_b$ plane, for $0.08 < E_b < 5$, with a submerged obstacle for which $A_2 = 0.05$ and $L_2 = 3$. The figure shows that the Froude number increases with E_b up to some critical value, E_b^*. Conversely, as E_b decreases (towards $E_b = 0.08$), the minimum of the upstream linear dispersion relation is approached, and small amplitude numerical oscillations begin to appear on the branch. A longer domain, with more mesh points on the free surface, is required to produce accurate solutions. Due to computational limitations we therefore truncate the lower end of the branch at $E_b = 0.08$, before getting too close to the minimum. If we were able to

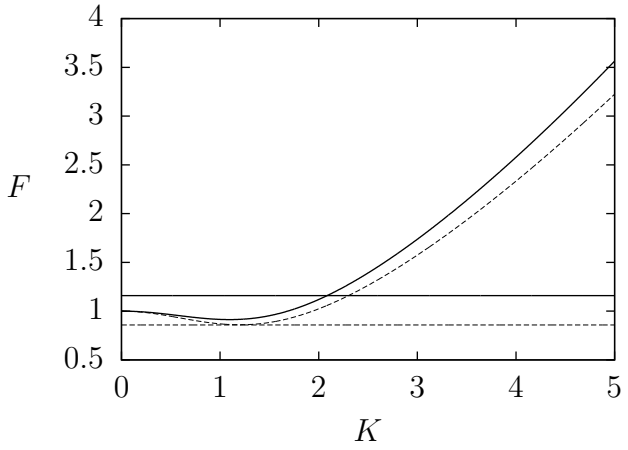

Figure 5.5: Linear dispersion relations downstream (solid line) and upstream (broken line) for figure 5.3(a). The constant solid/broken lines correspond to the downstream/upstream value of the Froude number found in figure 5.3(a) respectively.

reduce E_b further, then more turning points may be found on the branch.

At E_b^* a turning point exists in the $F - E_b$ plane, after which the Froude number decreases monotonically as E_b is increased. The existence of this turning point means that for a critical range of Froude numbers, there exist two solutions over the same underlying obstruction, with the same value of the Froude number, but with different values of E_b. Two such solutions are shown in figure 5.7 for $F = 1.36$. The two values of E_b are $E_b = 1.5$ and $E_b = 0.33$. It should be noted that for such solutions, the density ρ, the gravitational acceleration g, and the flexural rigidity of the ice $\mathcal{D}$ are fixed. Therefore, having different values of E_b must correspond to having different values of H, and thus different downstream fluid depths. However, the downstream Froude number is also fixed in both solutions. As the gravitational acceleration is fixed but the fluid depth differs, the downstream fluid speeds in the two solutions must also change in order to keep F fixed. The phenomenon here is therefore not bi-stability in the traditional sense; the flows are different.

Figure 5.6(b) shows the solution branches in the $F - E_b$ plane for three different underlying obstacles. We see that the downstream Froude number and the critical value E_b^* at which the turning point exists, increase with obstacle size. Similar behaviour was found for the $\tau - F$ branches in the gravity-capillary case. However, the critical range of Froude numbers for which there exist two solutions (with the same value of the Froude number, but different values of τ), is wider than the corresponding critical range in the flexural-gravity case for two different values of E_b. A rough sketch of the comparison between the flexural-gravity and the gravity-capillary cases is shown in figure 5.8.

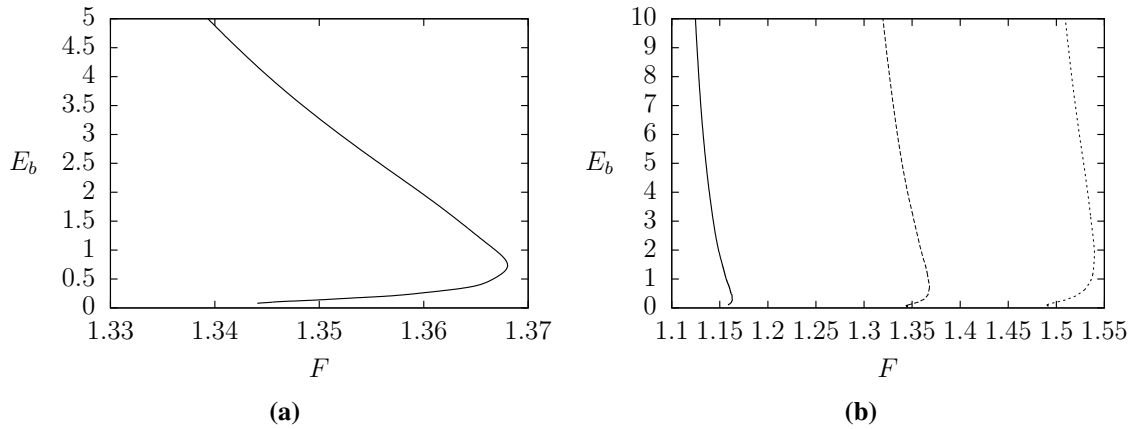

Figure 5.6: Solution branches in the $F - E_b$ plane downstream, for flow over a single submerged obstruction characterised by (a) $A_2 = 0.05$, $L_2 = 3$, and by (b) $A_2 = 0.01$, $L_2 = 3.2$ (solid line), $A_2 = 0.05$, $L_2 = 3$ (dashed line) and $A_2 = 0.1$, $L_2 = 3.2$ (dotted line).

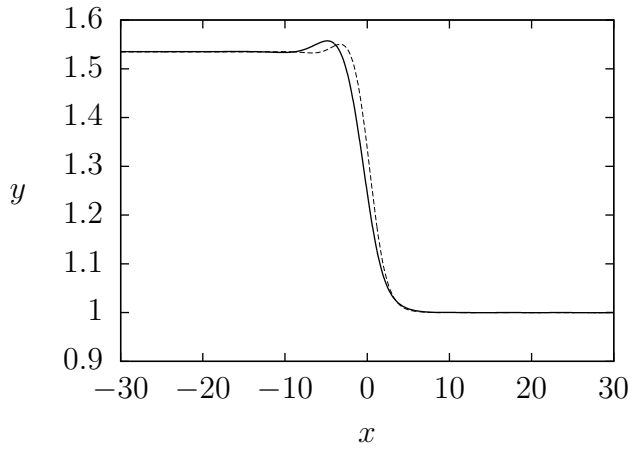

Figure 5.7: Hydraulic fall solution profiles over a submerged obstacle of height $2A_2 = 0.1$ and width $2L_2 = 6$. The Froude number in both cases is found to be $F = 1.36$. The solid curve is the solution with $E_b = 1.5$ and the broken curve is the solution with $E_b = 0.33$.

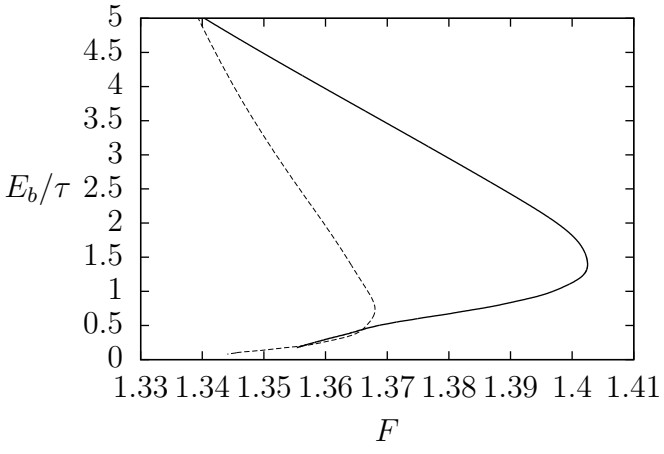

Figure 5.8: Rough sketch of solution branches in the $F - E_b$ plane (dashed line) and the $F - \tau$ plane (solid line) over an obstacle characterised by $A_2 \approx 0.05$ and $L_2 \approx 3$.

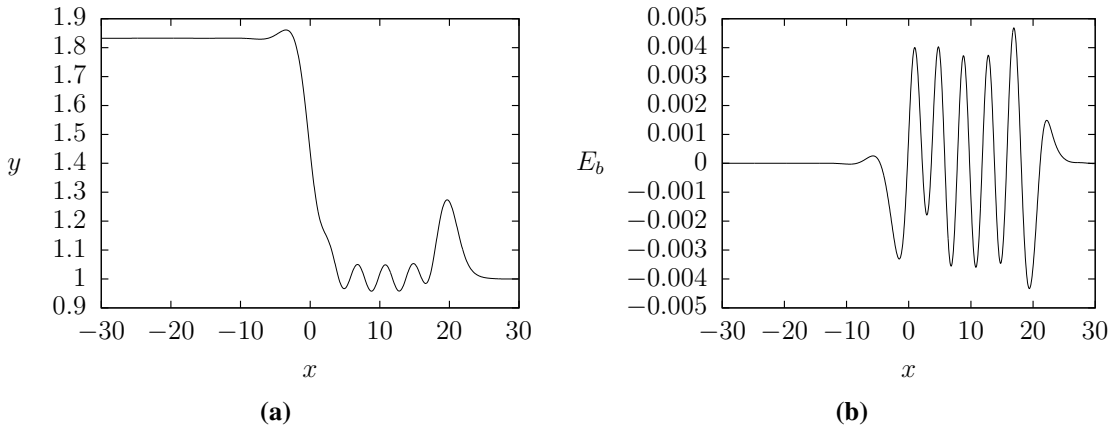

Figure 5.9: (a) Hydraulic fall profile over a submerged obstacle of height $2A_2 = 0.2$ and width $2L_2 = 6.4$, with an additional obstacle characterised by $2A_1 = 0.16$, $2L_1 = 6.4$ with $x_d = 20$, downstream. A train of trapped waves exists between the obstacles. The Froude number $F = 1.54$ is found as part of the solution, and $E_b = 0.5$ is given. (b) The strain of the free surface profile given in (a).

5.4.5 Trapped waves

In the absence of a thin ice sheet covering the fluid, in chapter 4, we discussed how placing an additional obstruction upstream of the hydraulic fall in the pure gravity case has the effect of producing a train of trapped waves between the two obstacles before the hydraulic fall (see Dias and Vanden-Broeck [41] for numerical solutions, and Pratt [95] for experimental results). Furthermore, we showed that in the gravity-capillary problem, unless the surface tension is very small (so that the upstream Froude number intersects the upstream gravity-capillary linear dispersion relation), the additional obstacle must be placed downstream of the hydraulic fall in order to obtain a train of trapped waves between the two obstacles.

We have seen that the flexural-gravity problem has similarities with the gravity-capillary problem. As the linear dispersion relation in the flexural-gravity case acts in a similar manner to the linear dispersion relation in the weak surface tension ($\tau < \frac{1}{3}$) case, i.e. they both have a minimum before the Froude number increases monotonically with the wavenumber K, unless E_b is very small so that the upstream Froude number intersects the upstream linear dispersion relation, we expect to place the additional obstruction downstream of the hydraulic fall, in order to obtain trapped wave solutions. A typical profile with the additional obstacle centred at $x = 20$ is shown in figure 5.9(a). A train of supercritical waves exists between the two underlying obstructions, with a higher amplitude elevation wave occurring over the second obstruction. A small elevation appears upstream immediately before the fall, over the first obstruction.

The wavelength of the trapped waves can be inferred from the linear theory. The downstream Froude number for the solution in figure 5.9(a) intersects the downstream

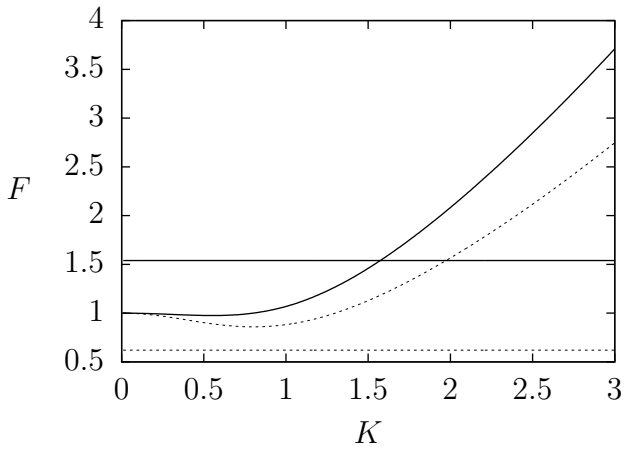

Figure 5.10: Linear dispersion relations for $E_b = 0.5$. The solid curve gives the downstream linear dispersion relation, and the solid line for constant F gives the downstream value of the Froude number for a channel bottom configuration classified by $A_2 = 0.1$, $A_1 = 0.08$, $L_1 = L_2 = 3.2$, and $x_d = 20$. The broken curve gives the upstream linear dispersion relation, and the upstream Froude number for the same configuration.

linear dispersion relation at wavenumber $K \approx 1.573$. The corresponding upstream and downstream linear dispersion relations are shown in figure 5.10. A wave train of wavelength $\lambda = 2\pi/1.573 \approx 4.002$ (see solid line) is therefore expected in the downstream region of the free surface. The waves found in figure 5.9(a) are of wavelength $\lambda \approx 12.83 - 8.85 = 3.98$ which is very close to the wavelength predicted by the linear theory.

We found that reducing the amplitude of the additional obstacle or reducing the parameter E_b, reduces the amplitude of the trapped waves. As in the gravity-capillary case, we plotted the solution branch in the $E_b - F$ plane. The branch for the fixed channel bottom configuration characterised by $A_2 = 0.1$, $A_1 = 0.05$, $L_i = 3.2$, $i = 1, 2$ is shown in figure 5.11(a). Multiple turning points are found on this branch, showing that for a critical range of Froude numbers, the trapped wave solution for a given underlying channel bottom configuration is not unique. This is comparable to our findings in chapter 4 for gravity-capillary trapped wave solutions. In figure 5.11(b) we show a comparison between the gravity-capillary and the flexural-gravity cases for a given fixed channel bottom. The solid curve shows the gravity-capillary trapped wave solution branch in the $\tau - F$ plane, and the broken curve shows the flexural-gravity branch in the $E_b - F$ plane. There are many more turning points on the gravity-capillary branch than the flexural-gravity branch. This suggests that there may be more solutions for a particular value of the Froude number in the gravity-capillary case than in the flexural-gravity case. There may be even more turning points on these branches that we were unable to obtain due to computational limitations. As in the gravity-capillary case, we were able to continue following the solution branch in figure 5.11(a) for much greater values of E_b, with F

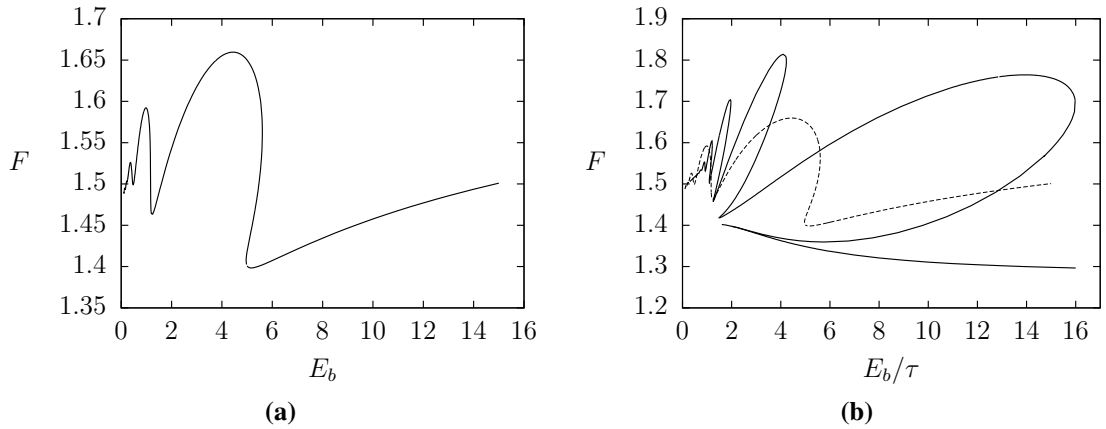

Figure 5.11: (a) The trapped wave solution branch in the E_b-F plane for flow past two fixed submerged obstructions characterised by $A_2 = 0.1$, $A_1 = 0.05$ and $L_i = 3.2$, $i = 1, 2$, with $x_d = 15$. (b) Gravity-capillary (solid line) and flexural-gravity (broken line) trapped wave solution branches in the $\tau - F$ and $E_b - F$ planes respectively, for the fixed channel bottom configuration given in (a).

increasing monotonically with E_b, corresponding to smaller and smaller channel depths. Of course, the strain of the ice in such solutions grows as E_b increases, so as we move along the branch, the solutions become more and more unphysical.

In figure 5.12 we show five different solutions for the different values of E_b when $F = 1.51$; $E_b = 0.28, 0.43, 0.54, 1.17$ and 5.51, corresponding to water depths 3.02m, 2.71m, 2.56m, 2.11m and 1.43m respectively for the physical parameters used for the experiments in Lake Saroma in Japan, and water depths 20.25m, 18.19m, 17.18m, 14.16m and 9.61m respectively for the physical parameters in the experiments in Lake Diefenbaker in Canada. The amplitude and wavelength of the trapped waves increase with increasing E_b. This result is predicted by the flexural-gravity linear dispersion relation. As one increases E_b the gradient of the downstream dispersion curve increases so that the fixed Froude number intersects the curve at a smaller wavenumber, and thus the waves have a greater wavelength. In figures 5.12(c) and 5.12(d) we plot the corresponding strain for the solutions in figures 5.12(a) and 5.12(b). One can see that the strain has increased for the larger values of E_b.

We calculated solutions for obstacles of different heights and widths, and found similar behaviours to the particular results described here. A solution with $A_1 > A_2$ is shown in figure 5.13(a). The height of the elevation over the obstacle downstream of the hydraulic fall may increase so much that it is of the same height as the upstream flow. However, figure 5.13(c) shows that the strain in this solution is also significantly greater than the strain for the solutions in figure 5.12. In order to prevent the ice from breaking in such solutions, a thicker ice and/or water depth is therefore required. Similarly, when $A_1 < 0$, trapped wave solutions may be found, see for example figure 5.13(b). Then a

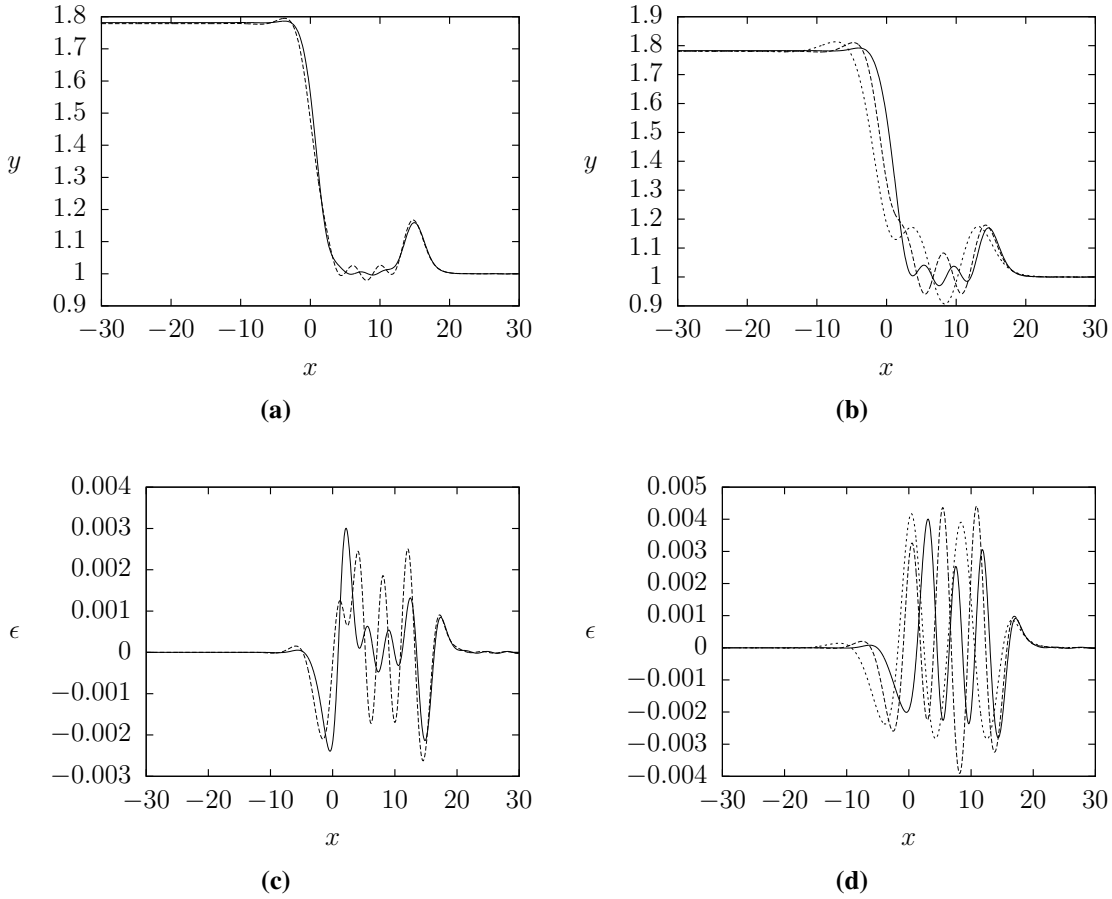

Figure 5.12: (a) and (b): Trapped wave solutions for flow past two fixed submerged obstructions characterised by $A_2 = 0.1$, $A_1 = 0.05$ and $L_i = 3.2$, $i = 1, 2$, with $x_d = 15$. The Froude number in each case is found to be $F = 1.51$. The parameter E_b is given by (a) $E_b = 0.28$ (solid line), $E_b = 0.43$ (dashed line), and (b) $E_b = 0.54$ (solid line), $E_b = 1.17$ (dashed line), $E_b = 5.51$ (dotted line). (c) and (d) show the strain on the free surface in the corresponding solutions in (a) and (b), respectively.

depression wave, instead of an elevation wave, appears over the additional obstruction downstream.

5.4.6 Hydraulic falls with a solitary type wave

Next, we place the additional obstacle upstream of the hydraulic fall and consider solutions with $F_{\rm up}$ less than the minimum of the upstream linear dispersion relation. As in the gravity-capillary case, a forced solitary type wave with small decaying oscillations in its tail is obtained over the obstruction. It is worth noting that in shallow water, for $F \approx 1$, a fifth order KdV equation was derived by Guyenne and Părău [68] and Xia and Shen [131]. It is well known that this equation admits solitary waves with decaying oscillations as solutions with $F_{\rm up} < F_{\rm up_{min}}$, see for example Grimshaw, Malomed and Benilov [63]. Forced waves with decaying oscillations for a fifth order fKdV equation have also

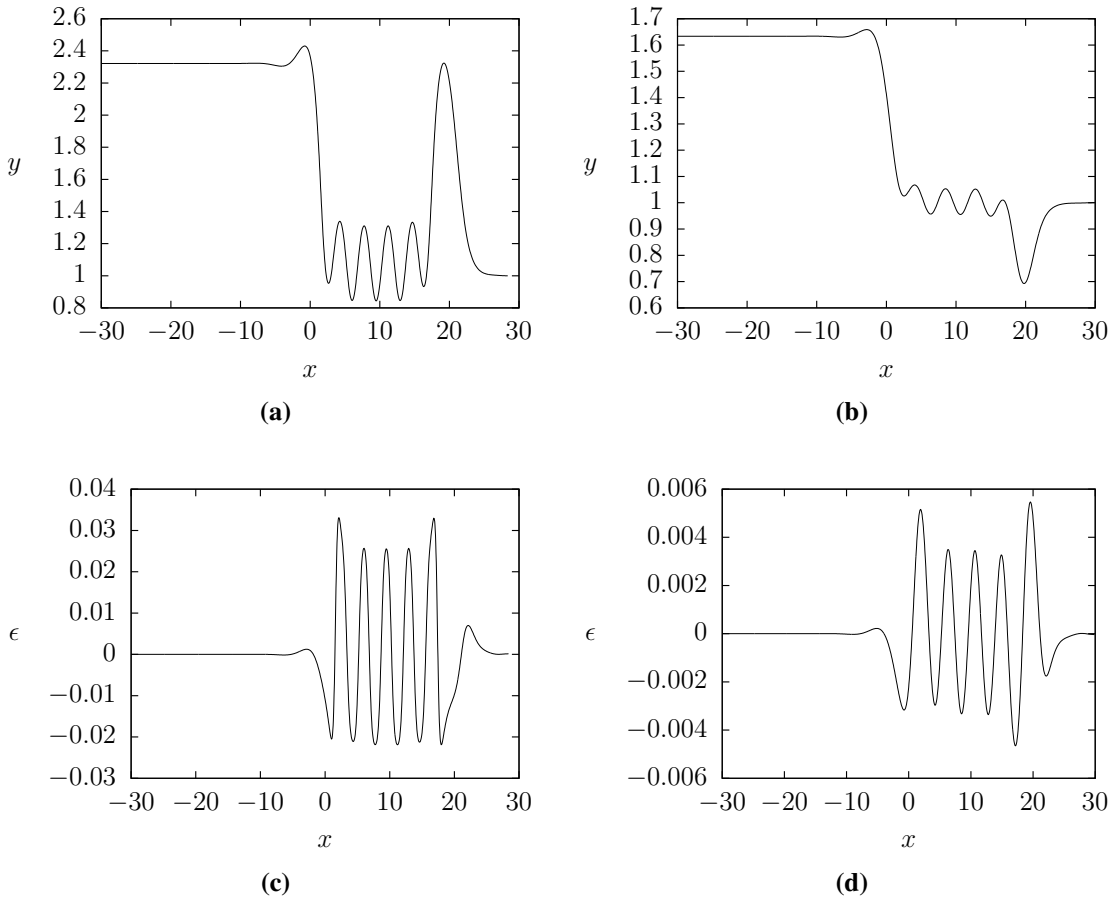

Figure 5.13: Hydraulic fall profiles over a submerged obstacle of height (a) $2A_2 = 0.2$ (b) $2A_2 = 0.1$, and width $2L_2 = 6.4$, with an additional obstacle characterised by (a) $2A_1 = 0.6$, (b) $2A_1 = -0.2$, with $2L_1 = 6.4$ and $x_d = 20$ downstream. A train of waves exists between the obstacles. The Froude numbers (a) $F = 1.8$ and (b) $F = 1.42$ are found as part of the solution, and $E_b = 0.5$ is given. (c) and (d) show the strain in figures (a) and (b), respectively.

been computed by Cho and Akylas [28]. We obtain a depression wave if $A_1 > 0$ and an elevation wave if $A_1 < 0$. Example solution profiles are shown in figure 5.14. Decreasing E_b so that the upstream Froude number approaches the minimum of the upstream linear dispersion relation, increases the number of decaying oscillations in the tails of these forced solitary type waves.

5.5 Conclusions

We have computed fully nonlinear critical flow solutions under an ice plate using the same boundary integral equation method as presented in chapter 4. The ice plate was modelled as a thin elastic shell using Cosserat theory, and due to the cubic nonlinearity in the flexural elasticity term in the dynamic boundary conditions, the solutions presented in this chapter are more complex than the comparative solutions in the gravity-capillary

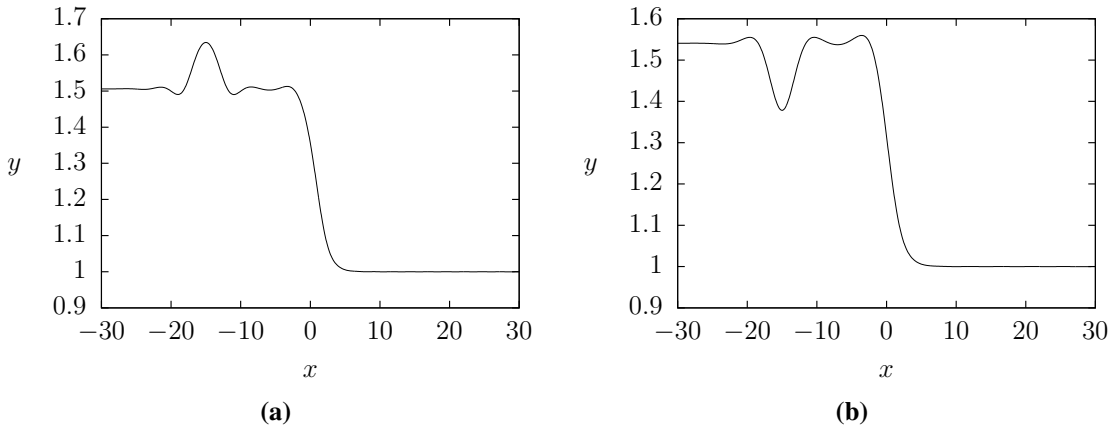

Figure 5.14: Hydraulic fall profiles over a submerged obstruction of height $2A_2 = 0.1$, and width $2L_2 = 6$, with an additional obstacle upstream at $x = -15$, characterised by (a) $A_1 = -0.1$, $L_1 = 3$ and (b) $A_1 = 0.05$, $L_1 = 3$. The Froude numbers $F = 1.34$ and $F = 1.37$ respectively, are found as part of the solution, and the parameters $E_b = 0.1$ and $E_b = 0.5$ are given.

regime.

Flexural-gravity hydraulic fall solutions are new, and we have shown that, as in the gravity-capillary case, they are not unique. For particular values of the Froude number, there exists more than one solution, which have different values of the dimensionless flexural rigidity parameter E_b. We have shown that if the obstacle is small enough, either a slight elevation before the hydraulic fall, or a train of decaying waves upstream of the fall exists in the solutions. Although a similar phenomenon was observed in chapter 4 for the gravity-capillary hydraulic falls, the phenomenon here is much more pronounced and is apparent in the majority of solutions. In the gravity-capillary case the upstream Froude number had to be very close to the minimum of the upstream linear dispersion relation to observe these results.

We then placed a second obstruction downstream of the hydraulic fall and showed that there then exists a train of waves trapped between the obstacles. As in the gravity-capillary case, these downstream trapped wave solutions are not unique. Although we found fewer turning points on the flexural-gravity trapped wave solution branch than on the gravity-capillary branch, it is possible that there exist many more turning points which we were unable to obtain due to the computational limitations that we meet near the minimum of the upstream linear dispersion relation. However, we did show that the range of Froude numbers for which multiple solutions exist, appears to be smaller in the flexural-gravity than the gravity-capillary case.

Although we did not show any computed generalised hydroelastic hydraulic falls we did speculate about the existence of such solutions. As in the gravity-capillary case, generalised hydraulic falls should exist in a flow regime where the upstream Froude number

intersects the upstream linear dispersion relation, i.e. $F_{\mathrm{up}} > F_{\mathrm{up}_{\mathrm{min}}}$. However, the resonance that then occurs between the two modes of the linear dispersion relation appears to be stronger than the resonance in the gravity-capillary case, and so the solutions are harder to compute accurately. We speculated that generalised hydroelastic hydraulic falls may therefore have, for example, Wilton type ripples upstream rather than a simple wave train. A similar problem arose in placing the second obstacle upstream of the hydraulic fall. If $1 < F_{\mathrm{up}} < F_{\mathrm{up}_{\mathrm{min}}}$ one would expect a train of trapped waves to exist between the two obstructions, as in the gravity-capillary case. Indeed, if we obtain a pure gravity trapped wave critical flow solution (as computed by Dias and Vanden-Broeck [41]), and then increase E_b by a small amount, so that $E_b = 0.001$, we obtain trapped waves of similar wavelength and amplitude to the gravity solution. However, when we attempted to increase E_b further in order to obtain a noticeable difference between the pure gravity and flexural-gravity upstream trapped wave solutions, the resonance between the two modes of the linear dispersion relation became too strong to compute solutions feasibly.

When the flexural rigidity is greater, so that $F_{\mathrm{up}} < F_{\mathrm{up}_{\mathrm{min}}}$, we showed that there exist forced solitary type waves (with small decaying oscillations in their tails) over the additional upstream obstruction. Again, such solutions look like those in the gravity-capillary flow regime.

It should be noted that the values of E_b used in our results are relatively large, and so the results presented correspond to shallow water applications, e.g. lakes and fjords, rather than deeper oceanographic situations. We have shown computed solutions for $E_b = 0.02$ to $E_b = 5$. Using all the parameters excluding the fluid depth given in table 5.1, one finds that such solutions would be physically relevant for Lake Saroma between depths 5.84m and 1.47m, and for Lake Diefenbaker between depths 39.16m and 9.85m. The mean depth of Lake Diefenbaker $H = 35$m, is included within this range, but the mean depth of Lake Saroma $H = 6.8$m is not. For our results to be valid in Lake Saroma, the depth of the lake would need to decrease further, or the thickness and/or flexural-rigidity of the ice there, would need to increase.

CHAPTER SIX

CRITICAL FLOWS AND TRAPPED WAVE SOLUTIONS IN THE RIGID LID APPROXIMATION

6.1 Introduction

In this chapter, we consider the problem involving a steady two-layer ideal fluid medium flowing in a channel of finite depth. An arbitrary submerged obstruction lies on the bottom of the channel, and the upper fluid is bounded above by a rigid lid. The effects of both gravity and surface tension are considered, and the fully nonlinear problem is solved using boundary integral equation techniques based on Cauchy's integral formula. As in the single layer case presented in chapter 4, critical flow solutions are sought so that the depths of the fluids in both layers change over the obstruction. We use a second submerged obstruction to look for 'trapped wave' solutions, where a train of waves exists, trapped between the two obstructions. These solutions are sought in both the pure gravity and the gravity-capillary regimes.

The fully nonlinear problem is formulated in section 6.2. Section 6.3 describes the numerical scheme for the rigid-lid approximation, and the linear theory is examined in section 6.4. Some results are then presented in section 6.6, and in section 6.7, the chapter ends with a summary of the findings and a concluding discussion.

6.2 Formulation

The interface of a two-dimensional, two-layer fluid medium flowing along a channel of finite depth is considered. The fluids in the two layers have constant densities ρ_1 and ρ_2, such that $\rho_2 < \rho_1$. Consequently, the fluid of density ρ_2 lies on top of the fluid of density ρ_1, in order to suppress the Kelvin-Helmholtz instability, see chapter 2. The upper fluid is

bounded above by a horizontal rigid lid; the so called rigid-lid approximation. The fluids in both layers are assumed to be incompressible and inviscid, and the flows, steady and irrotational. We introduce Cartesian coordinates (x^*, y^*) such that the x^*-axis is aligned along the horizontal undisturbed channel bottom far from the obstacle, and the y^*-axis is directed vertically upwards through a submerged obstruction. The origin is on the undisturbed bed. Gravitational acceleration g is taken to act in the negative y^* direction, and we define the surface tension on the interface between the two fluids by σ_i.

Next, we introduce the velocity potentials $\phi_1^*(x^*, y^*)$ and $\phi_2^*(x^*, y^*)$, and the stream functions $\psi_1^*(x^*, y^*)$ and $\psi_2^*(x^*, y^*)$, in the lower and upper fluid layers respectively. As the fluids in both layers are incompressible, and their flows irrotational, Laplace's equation is satisfied in the two domains;

$$\nabla^{*2}\phi_1^* = 0 \quad \text{in the lower layer,} \tag{6.2.1}$$

$$\nabla^{*2}\phi_2^* = 0 \quad \text{in the upper layer.} \tag{6.2.2}$$

As we seek hydraulic fall solutions, far upstream of the submerged obstruction(s), as $x^* \to -\infty$, the flow in both layers is assumed to be uniform. We therefore impose the condition that the fluids have constant depths h_1 and h_2, and constant velocities V_1 and V_2, in the lower and upper layers, respectively. Similarly, the flows are assumed to be uniform far downstream, as $x \to \infty$, with constant depths H_1 and H_2, and constant velocities U_1 and U_2, in the lower and upper layers respectively. A conjugate flow therefore requires $h_1 \neq H_1$ and $h_2 \neq H_2$. The rigid lid is then described by

$$y^*(x^*) = h_1 + h_2 = H_1 + H_2. \tag{6.2.3}$$

The free surface at the interface between the two fluids is given by $y^*(x^*) = h_1 + \eta^*(x^*)$, and the channel bottom, along which the arbitrary submerged obstructions lie, is given by $y^*(x^*) = B^*(x^*)$. In figure 6.1 we give a sketch of the flow domain.

The dimensionless Froude numbers in the lower and upper layers are defined by

$$F_1 = \frac{V_1}{\sqrt{gh_1}} \qquad \text{and} \qquad F_2 = \frac{V_2}{\sqrt{gh_2}} \qquad \text{upstream,} \tag{6.2.4}$$

$$F_{1d} = \frac{U_1}{\sqrt{gH_1}} \qquad \text{and} \qquad F_{2d} = \frac{U_2}{\sqrt{gH_2}} \qquad \text{downstream,} \tag{6.2.5}$$

respectively. The dimensionless Bond numbers on the interface are defined by

$$\tau = \frac{\sigma_i}{\rho_1 g h_1^2} \qquad \text{and} \qquad \tau_d = \frac{\sigma_i}{\rho_1 g H_1^2}, \tag{6.2.6}$$

upstream and downstream, respectively. We introduce the depth ratio $D = h_2/h_1$ and the

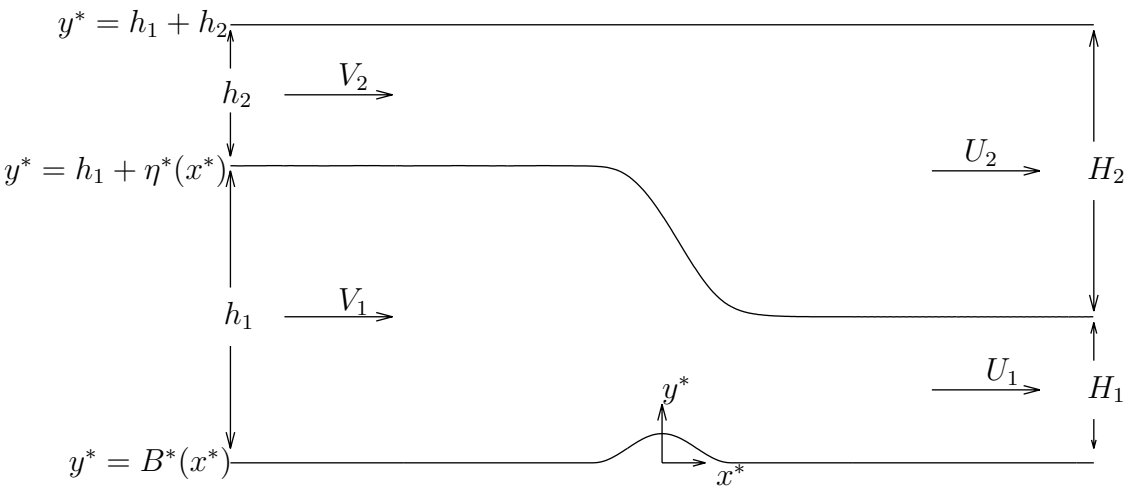

Figure 6.1: Dimensional critical flow configuration in the rigid-lid approximation, over an arbitrary obstacle on the bottom of the channel.

density ratio $R = \rho_2/\rho_1$. The critical depth ratio is then given by

$$D = \sqrt{R}. \tag{6.2.7}$$

The steady kinematic boundary conditions on the rigid lid, the interface between the two fluids, and the channel bottom are given by

$$\phi^*_{2y^*} = 0 \qquad \text{on} \quad y^* = h_1 + h_2, \tag{6.2.8}$$
$$\phi^*_{2y^*} = \phi^*_{2x^*}\eta^*_{x^*} \qquad \text{on} \quad y^* = h_1 + \eta^*(x^*), \tag{6.2.9}$$
$$\phi^*_{1y^*} = \phi^*_{1x^*}\eta^*_{x^*} \qquad \text{on} \quad y^* = h_1 + \eta^*(x^*), \tag{6.2.10}$$
$$\phi^*_{1y^*} = \phi^*_{1x^*}B^*_{x^*} \qquad \text{on} \quad y^* = B^*(x^*), \tag{6.2.11}$$

see for example, Dias and Vanden-Broeck [39].

The dynamic condition on the interface is found by applying Bernoulli's equation to each fluid at the interface $y^*(x^*) = h_1 + \eta^*(x^*)$. In the far field, as $x^* \to -\infty$, we require that $y^* \to h_1$, $u_i^* \to V_i$ and $v_i^* \to 0$, $i = 1, 2$, where $\mathbf{u}_i{}^* = (u_i{}^*, v_i{}^*)$. Thus, the Bernoulli constants $\mathcal{B}_i$ are found to be

$$\mathcal{B}_i = P_{i\infty} + \frac{1}{2}\rho_i V_i^2 + \rho_i g h_1, \tag{6.2.12}$$

for $i = 1, 2$, in the lower and upper fluids respectively. Here, $P_{i\infty}$ are the pressures in the lower and upper layers of fluid as $x^* \to -\infty$. The physical boundary condition is that $P_{1\infty} = P_{2\infty}$ on the flat interface. Then, Bernoulli's equation tells us that, for all points

on the interface $y^* = h_1 + \eta^*(x^*)$,

$$\begin{aligned}
& P_1 + \frac{1}{2}\rho_1 \mathbf{u}_1^{*2} + \rho_1 g y^* - \frac{1}{2}\rho_1 V_1^2 - \rho_1 g h_1 = P_2 + \frac{1}{2}\rho_2 \mathbf{u}_2^{*2} + \rho_2 g y^* - \frac{1}{2}\rho_2 V_2^2 - \rho_2 g h_1, \\
\Rightarrow \quad & \frac{1}{\rho_1}(P_1 - P_2) + \frac{1}{2}(\mathbf{u}_1^{*2} - R\mathbf{u}_2^{*2} - V_1^2 + RV_2^2) + g(y^* - h_1 - Ry^* + Rh_1) = 0, \\
\Rightarrow & -\frac{\sigma_i}{\rho_1}\kappa^* + \frac{1}{2}\left((\phi_{1x^*}^{*2} + \phi_{1y^*}^{*2}) - R(\phi_{2x^*}^{*2} + \phi_{2y^*}^{*2}) - (V_1^2 - RV_2^2)\right) + g(y^* - h_1)(1 - R) = 0,
\end{aligned} \tag{6.2.13}$$

where κ^* is the curvature on the interface and we have utilised the Young Laplace equation (1.2.19) in the form $P_1 - P_2 = -\sigma_i(\nabla \cdot \mathbf{n})$.

By considering the conservation of mass in both layers, we can also write

$$V_1 h_1 = U_1 H_1, \tag{6.2.14}$$

$$V_2 h_2 = U_2 H_2. \tag{6.2.15}$$

Next, we non-dimensionalise the problem by taking V_1 as unit velocity and h_1 as unit length. The upstream fluid velocity in the upper layer is defined by $\gamma = V_2/V_1$, and the depth of the upstream fluid in dimensionless variables is given by the depth ratio D. We also define $\gamma_1 = U_1/V_1$ and $\gamma_2 = U_2/V_2$. The downstream fluid velocities in the lower and upper layers are then given by γ_1 and $\gamma\gamma_2$ respectively. A sketch of the dimensionless flow configuration is shown in figure 6.2. We can now obtain relationships between the different Froude numbers (6.2.4) and (6.2.5) and write them all in terms of F_1, the upstream Froude number in the lower layer;

$$F_2 = \frac{\gamma}{\sqrt{D}} F_1, \tag{6.2.16}$$

$$F_{1d} = \gamma_1^{\frac{3}{2}} F_1, \tag{6.2.17}$$

$$F_{2d} = \frac{\gamma \gamma_2^{\frac{3}{2}}}{\sqrt{D}} F_1. \tag{6.2.18}$$

Similarly, we can write τ_d, defined in (6.2.6), in terms of τ,

$$\tau_d = \tau \gamma_1^2. \tag{6.2.19}$$

So, providing that we know γ, γ_1, γ_2 and D, the only dimensionless Froude and Bond numbers that we need to consider are F_1 and τ respectively.

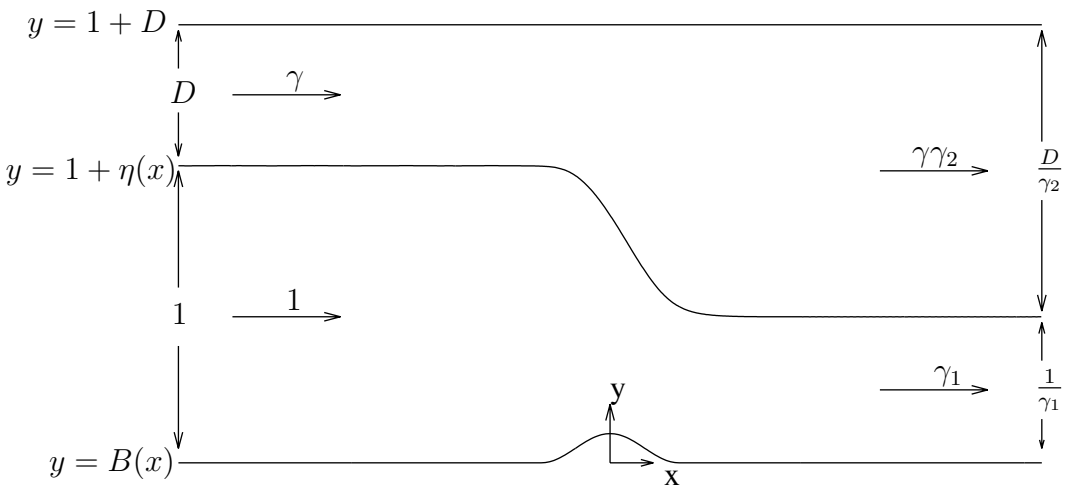

Figure 6.2: Dimensionless critical flow configuration in the rigid-lid approximation, over an arbitrary obstacle on the bottom of the channel.

We now denote dimensionless variables by non-starred variables, and write the dimensionless form of the problem as

$$\phi_{1xx} + \phi_{1yy} = 0, \tag{6.2.20}$$

$$\phi_{2xx} + \phi_{2yy} = 0, \tag{6.2.21}$$

subject to the dimensionless boundary conditions. The kinematic boundary conditions (6.2.8)-(6.2.11) become

$$\phi_{2y} = 0 \qquad \text{on } y = 1 + D, \tag{6.2.22}$$

$$\phi_{1y} = \phi_{1x}\eta_x \quad \text{on } y = 1 + \eta(x), \tag{6.2.23}$$

$$\phi_{2y} = \phi_{2x}\eta_x \quad \text{on } y = 1 + \eta(x), \tag{6.2.24}$$

$$\phi_{1y} = \phi_{1x}B_x \quad \text{on } y = B(x), \tag{6.2.25}$$

on the rigid lid, the interface, and the channel bottom respectively. The dynamic boundary condition (6.2.13) on the interface $y = 1 + \eta(x)$ becomes

$$\frac{1}{2}\left((\phi_{1x}^2 + \phi_{1y}^2) - R(\phi_{2x}^2 + \phi_{2y}^2) - (1 - R\gamma^2)\right) - \frac{\tau}{F_1^2}\kappa + \frac{1}{F_1^2}(1 - R)y - \frac{1}{F_1^2}(1 - R) = 0. \tag{6.2.26}$$

In the far field the flow must be uniform. Hence

$$\phi_{1x} \to 1, \;\; \phi_{1y} \to 0, \;\; \phi_{2x} \to \gamma, \;\; \phi_{2y} \to 0 \;\text{ and }\; \eta(x) \to 0, \quad \text{as } x \to -\infty \tag{6.2.27}$$

upstream, and

$$\left.\begin{array}{ll} \phi_{1x} \to \frac{U_1}{V_1} = \gamma_1, & \phi_{1y} \to 0, \\ \phi_{2x} \to \frac{U_2}{V_1} = \gamma\gamma_2, & \phi_{2y} \to 0, \\ \eta(x) \to \frac{H_1}{h_1} - 1 = \frac{1}{\gamma_1} - 1, & \end{array}\right\} \text{as } x \to \infty, \tag{6.2.28}$$

downstream.

Following Forbes [53], a further condition is obtained by substituting the downstream far field conditions (6.2.28) into the dynamic condition (6.2.26) on the interface, giving

$$\frac{1}{2}\left(\gamma_1^2 - R(\gamma^2\gamma_2^2) - (1 - R\gamma^2)\right) + \frac{1}{F_1^2}(1-R)\frac{1}{\gamma_1} - \frac{1}{F_1^2}(1-R) = 0, \tag{6.2.29}$$

$$\Rightarrow \qquad \frac{1}{2}F_1^2 R\gamma^2(1-\gamma_2^2) + \frac{1}{2}F_1^2(\gamma_1^2 - 1) + (1-R)\left(\frac{1}{\gamma_1} - 1\right) = 0. \tag{6.2.30}$$

The problem is now fully defined. We seek $\phi_1(x,y)$, $\phi_2(x,y)$ and $\eta(x)$, satisfying Laplace's equation in both layers, and the kinematic and dynamic boundary conditions (6.2.22) - (6.2.26), subject to the far field conditions (6.2.27) and (6.2.28), and the relation (6.2.30).

6.3 Numerical scheme

The problem is solved numerically, in a similar manner to the single layer case, by following the scheme used by Belward and Forbes [12] and Dias and Vanden-Broeck [42]. We reformulate the problem as a system of integro-differential equations, to be solved for the unknown interface over arbitrarily shaped obstructions on the bottom of the channel.

We parametrise the interface by introducing the arclength s and writing $x = X(s)$, $y = \eta(x) = Y(s)$. The parametric equation,

$$\left(\frac{dX(s)}{ds}\right)^2 + \left(\frac{dY(s)}{ds}\right)^2 = 1, \tag{6.3.1}$$

must then be satisfied on the interface. The dynamic boundary condition (6.2.26) on the interface is rewritten as

$$\frac{1}{2}(\phi_{1s}^2 - R\phi_{2s}^2 - (1 - R\gamma^2)) - \frac{\tau}{F_1^2}\kappa + \frac{1}{F_1^2}(1-R)(Y(s) - 1) = 0, \tag{6.3.2}$$

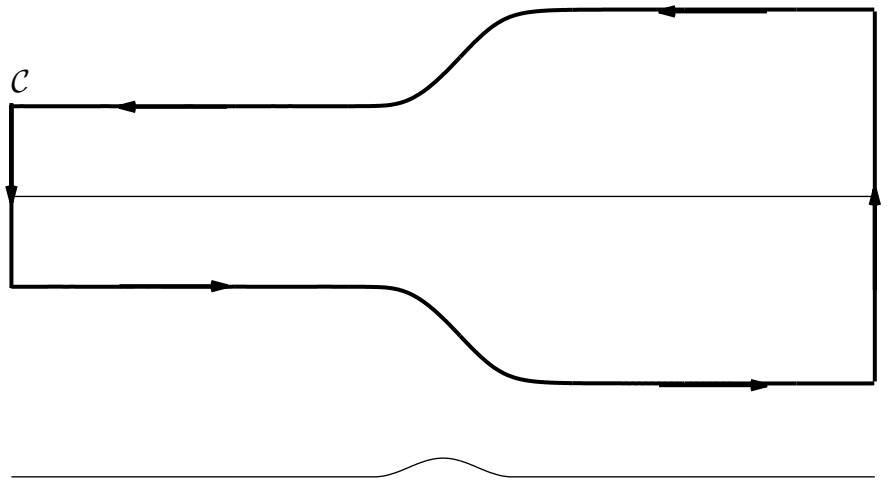

Figure 6.3: The contour $\mathcal{C}$, taken anticlockwise, consisting of the fluid interface, its image in the rigid lid, and the vertical lines joining them at $x = \pm L$.

having first parametrised the velocity components by

$$\phi_{ix} = \frac{d\phi_i}{ds}\frac{dX}{ds}, \tag{6.3.3}$$

$$\phi_{iy} = \frac{d\phi_i}{ds}\frac{dY}{ds}, \tag{6.3.4}$$

for $i = 1, 2$, as in chapter 4. Here, $\kappa = Y_{ss}X_s - X_{ss}Y_s$ is the parametrised curvature on the interface, as derived in chapter 4.

Next, we derive the integro-differential equations. Following Belward and Forbes [12], we reflect the upper fluid in the horizontal rigid lid at $y = 1 + D$ to obtain an image fluid region, bounded above by an image interface (see figure 6.3). The requirement that there is no flow through the rigid lid, given by equation (6.2.22), means that $v_2(x, 1 + D) = 0$, and so we must satisfy the reflection condition,

$$v_2(x, y) = -v_2(x, 2 + 2D - y), \tag{6.3.5}$$

in the image fluid. We apply Cauchy's integral formula to the function

$$\chi_1 = \frac{dw_2}{dz} - \gamma, \tag{6.3.6}$$

around a contour $\mathcal{C}$, shown in figure 6.3. Here, $dw_2/dz = \phi_{2x} - i\phi_{2y}$ is the complex velocity and $w_2(z) = \phi_2(x, y) + i\psi_2(x, y)$ is the complex potential in the upper fluid. The path $\mathcal{C}$ consists of the interface, the image interface, and the vertical lines $x = \pm L$ in

the limit as $L \to \infty$, as shown in figure 6.3. We obtain the integral equation

$$\int_{\mathcal{C}} \frac{\chi_1(z(\sigma))}{z(\sigma) - z(s)} z'(\sigma) d\sigma = \pi i(\chi_1(z(s))) = \pi i(\phi_{2x}(s) - \gamma - i\phi_{2y}(s)), \tag{6.3.7}$$

where σ is the arclength at integration point $z(\sigma) = x(\sigma) + iy(\sigma)$ on the contour $\mathcal{C}$. Placing the evaluation point $s = s_1$ on the interface, (6.3.7) becomes

$$\begin{aligned}
\pi i(\phi_{2x}(s_1) - \gamma - i\phi_{2y}(s_1)) &= \int_{\mathcal{C}} \frac{(\phi_{2x}(\sigma) - \gamma - i\phi_{2y}(\sigma))(x_s(\sigma) + iy_s(\sigma))}{(x(\sigma) + iy(\sigma)) - (x(s_1) + iy(s_1))} d\sigma, \\
&= \int_{\mathcal{C}} \frac{(\phi_{2s}(\sigma)x_s(\sigma) - \gamma - i\phi_{2s}(\sigma)y_s(\sigma))(x_s(\sigma) + iy_s(\sigma))A(\sigma)}{(x(\sigma) - x(s_1))^2 + (y(\sigma) - y(s_1))^2} d\sigma, \\
&= \int_{\mathcal{C}} \frac{(\phi_{2s}(\sigma)(X_s(\sigma)^2 + Y_s(\sigma)^2) - \gamma(x_s(\sigma) + iy_s(\sigma)))A(\sigma)}{(x(\sigma) - x(s_1))^2 + (y(\sigma) - y(s_1))^2} d\sigma,
\end{aligned} \tag{6.3.8}$$

where we have used (6.3.3) and (6.3.4), and have let $A(\sigma) = (x(\sigma) - x(s_1)) - i(y(\sigma) - y(s_1))$. As $L \to \infty$, the contribution to the integrals from the vertical lines tends to zero, see chapter 4 for details. Taking the imaginary part of (6.3.8), and noting that on the image interface $y(\sigma) = 2 + 2D - Y(\sigma)$ and $x(\sigma) = X(\sigma)$ so that $y(\sigma)' = -Y'(\sigma)$, (6.3.8) becomes

$$\begin{aligned}
&\pi(\phi_{2s}(s_1)X_s(s_1) - \gamma) = \\
&\int_{-\infty}^{\infty} \frac{-(\phi_{2s}(\sigma) - \gamma X_s(\sigma))(Y(\sigma) - Y(s_1)) - \gamma Y_s(\sigma)(X(\sigma) - X(s_1))}{(X(\sigma) - X(s_1))^2 + (Y(\sigma) - Y(s_1))^2} d\sigma \\
-&\int_{-\infty}^{\infty} \frac{-(\phi_{2s}(\sigma) - \gamma X_s(\sigma))(2 + 2D - Y(\sigma) - Y(s_1)) + \gamma Y_s(\sigma)(X(\sigma) - X(s_1))}{(X(\sigma) - X(s_1))^2 + (2 + 2D - Y(\sigma) - Y(s_1))^2} d\sigma.
\end{aligned}$$

For clarity, we let $\sigma = \sigma_1$ if the value of the arclength at the varying point $z(\sigma)$, on the contour $\mathcal{C}$, is on the interface. The integral equation for the upper layer is therefore given by

$$\begin{aligned}
&\pi(\phi_{2s}(s_1)X_s(s_1) - \gamma) = \\
-&\int_{-\infty}^{\infty} \frac{(\phi_{2s}(\sigma_1) - \gamma X_s(\sigma_1))(Y(\sigma_1) - Y(s_1)) + \gamma Y_s(\sigma_1)(X(\sigma_1) - X(s_1))}{(X(\sigma_1) - X(s_1))^2 + (Y(\sigma_1) - Y(s_1))^2} d\sigma_1 \\
-&\int_{-\infty}^{\infty} \frac{(\phi_{2s}(\sigma_1) - \gamma X_s(\sigma_1))(Y(\sigma_1) + Y(s_1) - 2 - 2D) + \gamma Y_s(\sigma_1)(X(\sigma_1) - X(s_1))}{(X(\sigma_1) - X(s_1))^2 + (2 + 2D - Y(\sigma_1) - Y(s_1))^2} d\sigma_1.
\end{aligned} \tag{6.3.9}$$

As in the single-layer case, discussed in chapter 4, there are two integral equations for the bottom layer. This is because the evaluation point s must be placed on both the interface and the arbitrary channel bottom. The equations are obtained by applying Cauchy's

integral formula to the function

$$\chi_2 = \frac{dw_1}{dz} - 1, \tag{6.3.10}$$

around a contour Γ consisting of the free surface, the channel bottom, and the vertical lines $x = \pm L$ in the limit as $L \to \infty$. Here, $w_1(z) = \phi_1(x, y) + i\psi_1(x, y)$ is the complex potential in the lower fluid. Following the derivation of the two integral equations in the single-layer case, we obtain the integral equation

$$\begin{aligned}
&\pi(\phi_1(s_1)X(s_1) - 1) = \\
&-\int_{-\infty}^{\infty} \frac{(u(\sigma)(1 + B_x(\sigma)^2) - 1)(B(\sigma) - Y(s_1)) + B_x(\sigma)(\sigma - X(s_1))}{(\sigma - X(s_1))^2 + (B(\sigma) - Y(s_1))^2} d\sigma \\
&+\int_{-\infty}^{\infty} \frac{(\phi_1'(\sigma_1) - X'(\sigma_1))(Y(\sigma_1) - Y(s_1)) + Y'(\sigma_1)(X(\sigma_1) - X(s_1))}{(X(\sigma_1) - X(s_1))^2 + (Y(\sigma_1) - Y(s_1))^2} d\sigma_1
\end{aligned} \tag{6.3.11}$$

when the evaluation point $s = s_1$ is on the interface. When the evaluation point $s = x$ lies on the channel bottom, we obtain

$$\begin{aligned}
\pi(\hat{u}(x) - 1) = &-\int_{-\infty}^{\infty} \frac{(\hat{u}(\sigma)(1 + B_x(\sigma)^2) - 1)(B(\sigma) - B(x)) + B_x(\sigma)(\sigma - x))}{(\sigma - x)^2 + (B(\sigma) - B(x))^2} d\sigma \\
&+\int_{-\infty}^{\infty} \frac{(\phi_1'(\sigma_1) - X'(\sigma_1))(Y(\sigma_1) - B(x)) + Y'(\sigma_1)(X(\sigma_1) - x)}{(X(\sigma_1) - x)^2 + (Y(\sigma_1) - B(x))^2} d\sigma_1,
\end{aligned} \tag{6.3.12}$$

where $\hat{u}(\sigma) = u(\sigma, B(\sigma))$ is the horizontal velocity of the lower fluid on the bottom of the channel. These two equations (6.3.11) and (6.3.12) are similar to the equations (4.3.22) and (4.3.23) obtained in chapter 4, with the exception that γ in (4.3.22) and (4.3.23) has been set equal to one, as the flow velocity upstream in the single layer case was γ but in the lower layer in the case presented here, is one. There exist singularities in all the Cauchy principal value integral equations, but these can be neglected, as in the previous chapters, by performing the integrations numerically using the trapezoidal rule (see Monacella [83]). This completes the reformulation of the problem. The three integral equations (6.3.9), (6.3.11) and (6.3.12), together with the dynamic condition (6.3.2) and the parametric condition (6.3.1), provide the system of integro-differential equations to be solved iteratively via Newton's method.

We introduce M equally spaced mesh points s_i, for $i = 1, ..., M$, on the interface, separated by an interval e, alongside the $M - 1$ mesh midpoints s_i^m, for $i = 1, ..., M - 1$. Similarly, q equally spaced mesh points x_i, for $i = 1, ..., q$ on the channel bottom, separated by an interval h, are introduced with their corresponding mesh midpoints x_i^m, for $i = 1, ..., q - 1$. We then seek the $4M + q + 3$ unknowns; $Y'(i) = Y'(s_i), X'(i) = X'(s_i), \phi_1'(i) = \phi_1'(s_i), \phi_2'(i) = \phi_2'(s_i)$ for $i = 1, ..., M$, $u(i) = u(x_i)$ for $i = 1, ..., q$, γ_1, γ_2 and F_1. However, given an initial set of values for $Y'(i)$, we can reduce the number of

unknowns by obtaining $X'(i)$ from the parametric equation (6.3.1), as in chapter 4. The rigid lid condition requires that the total depth of the fluids upstream is equal to the total depth of the fluids downstream, i.e. the rigid lid is fixed. So, we must have

$$1 + D = \frac{D}{\gamma_2} + \frac{1}{\gamma_1}. \tag{6.3.13}$$

As D is known, (6.3.13) can be used to obtain γ_2 from γ_1. Furthermore, we can obtain γ_1 by enforcing $\gamma_1 = 1/y(M)$ to satisfy the downstream far field condition. There are then $3M + q + 1$ unknowns remaining; $Y'(i) = Y'(s_i), \phi_1'(i) = \phi_1'(s_i), \phi_2'(i) = \phi_2'(s_i)$ for $i = 1, ..., M$, $u(i) = u(x_i)$ for $i = 1, ..., q$ and F_1.

Following the work of Dias and Vanden-Broeck [42], the integrals in the integro-differential equations are truncated at $\sigma = -\bar{A}$ and $\sigma = \bar{B}$, where $\bar{A}$ and $\bar{B}$ are large positive constants. As in the single layer case in chapter 4, the integrals can then be approximated numerically at the mesh midpoints, using the trapezoidal rule with summation over the mesh points. The neglected part of the integrals, from $-\infty$ to $-\bar{A}$ and from $\bar{B}$ to ∞, are approximated analytically to improve the accuracy of the solutions. As $\sigma \to -\infty$ we have that $\phi_1'(\sigma) \to 1$, $\phi_2'(\sigma) \to \gamma$, $X'(\sigma) \to 1$, $Y'(\sigma) \to 0$, $B(\sigma) \to 0$ and $u(\sigma) \to 1$. The integrals from $-\infty$ to $-\bar{A}$ therefore all approximate to zero, and so their contributions to the integro-differential equations can be neglected. As $\sigma \to \infty$ the integrals are non-zero, and thus, are determined analytically by approximating the unknowns $X'(\sigma), Y(\sigma), \phi_1'(\sigma), \phi_2'(\sigma), u(\sigma)$ and $B(\sigma)$ by their values at the last mesh midpoint on the fluid interface and channel bottom, respectively. We can also set $Y'(\sigma) = 0$ and $B_x(\sigma) = 0$.

The truncation corrections to the first integral equation (6.3.9) come from the approximations

$$\begin{aligned} &- \int_{\bar{B}}^{\infty} \frac{(\phi_{2s}(M) - \gamma X_s(M))(Y(M) - Y(s_1))}{(X(\sigma_1) - X(s_1))^2 + (Y(M) - Y(s_1))^2} \frac{d\sigma_1}{dX} dX, \\ &- \int_{\bar{B}}^{\infty} \frac{(\phi_{2s}(M) - \gamma X_s(M))(Y(M) + Y(s_1) - 2 - 2D)}{(X(\sigma_1) - X(s_1))^2 + (2 + 2D - Y(M) - Y(s_1))^2} \frac{d\sigma_1}{dX} dX, \end{aligned} \tag{6.3.14}$$

to the two integrals, respectively. The downstream truncation corrections to the integral

equations (6.3.9), (6.3.11) and (6.3.12) are then found to be

$$T_1 = -\frac{\phi_2'(M)-\gamma X'(M)}{X'(M)}\left(\pm\frac{\pi}{2}-\arctan\left(\frac{X(M)-X(s_i^m)}{Y(M)-Y(s_i^m)}\right)\right) + \frac{\phi_2'(M)-\gamma X_1'(M)}{X_1'(M)}\left(\frac{\pi}{2}-\arctan\left(\frac{X(M)-X(s_i^m)}{2+2D-Y(M)-Y(s_i^m)}\right)\right), \quad (6.3.15)$$

$$T_2 = -(u(q)-1)\left(-\frac{\pi}{2}-\arctan\left(\frac{x_q-X(s_i^m)}{B(q)-y(s_i^m)}\right)\right) + \frac{\phi_1'(M)-X'(M)}{X'(M)}\left(\pm\frac{\pi}{2}-\arctan\left(\frac{X(M)-X(s_i^m)}{Y(M)-Y(s_i^m)}\right)\right), \quad (6.3.16)$$

$$T_3 = -(u(q)-1)\left(\pm\frac{\pi}{2}-\arctan\left(\frac{x_q-x_i^m}{B(q)-B(x_i^m)}\right)\right) + \frac{\phi_1'(M)-X'(M)}{X'(M)}\left(\frac{\pi}{2}-\arctan\left(\frac{X(M)-x_i^m}{|Y(M)-B(x_i^m)|}\right)\right), \quad (6.3.17)$$

respectively. The corrections T_2 and T_3 are just the same as (4.3.28) and (4.3.29) in the single layer case, with γ set equal to one, and the explicit one in (4.3.28) and (4.3.29), representing the velocity far downstream, replaced by $u(q)$. Due to the different scales used for the non-dimensionalisation in this chapter, $u(q) \neq \gamma_1 \neq 1$. The positive sign is taken in (6.3.15) and (6.3.16) if $Y_1(M) > Y_1(s_i^m)$, the negative sign if $Y_1(M) < Y_1(s_i^m)$, and the first and last terms in (6.3.15) and (6.3.16) respectively are neglected completely if $Y_1(M) = Y_1(s_i^m)$. In (6.3.17), the positive sign is taken if $B(q) > B(x_i^m)$, the negative sign if $B(q) < B(x_i^m)$, and the first term is neglected completely if $B(q) = B(x_i^m)$.

The integral equations (6.3.9) and (6.3.11), together with their truncation corrections (6.3.15) and (6.3.16), provide $2(M-1)$ equations. A further $q-1$ equations are provided by the third integral equation (6.3.12), together with its truncation correction (6.3.17). The dynamic condition on the interface (6.3.2) provides an additional M equations. This gives a system of $3M+q-3$ equations. A further four equations are therefore required to complete the system. These come from the relation (6.2.30), and three conditions to describe the flow in the far field. We find that exactly which three far-field equations to use depends on the type of result we are looking for (see section 6.4 below). As an example, we set

$$Y'(1) = 0, \quad (6.3.18)$$

$$u(1) = 1, \quad (6.3.19)$$

$$\phi_2'(1) = \gamma. \quad (6.3.20)$$

So, we now have a system of $3M+q+1$ equations for the $3M+q+1$ unknowns, which we can solve iteratively using Newton's method.

6.4 Linear theory

We firstly consider the linear theory. In a single layered flow configuration, wave trains move with the flow speed U and are governed by the linear dispersion relation. There are no wave trains in solitary wave and hydraulic fall solutions. In a two-layer configuration, with velocities U_1 and U_2 in the lower and upper fluids respectively, if waves move with speed U_1 they will be steady in the lower fluid. When viewed in a frame of reference moving with the upper fluid however, the waves will no longer be steady. Therefore, when a solution includes a train of waves, the velocities of the two layers must be equal. However, due to their lack of a wave train, there is no such problem with hydraulic fall and solitary wave solutions.

In a flow regime where $h_1 = H_1$, the mean fluid depth of each layer in the far field is the same up and downstream. In this regime, in the absence of a forcing, the steady-flow governing equations are

$$\phi^*_{1x^*x^*} + \phi^*_{1y^*y^*} = 0 \qquad \text{in} \quad 0 < y^* < h_1 + \eta^*, \tag{6.4.1}$$

$$\phi^*_{2x^*x^*} + \phi^*_{2y^*y^*} = 0 \qquad \text{in} \quad h_1 + \eta^* < y^* < h_2 + h_1. \tag{6.4.2}$$

The kinematic boundary conditions are then

$$\phi^*_{1y^*} = 0 \qquad \text{on} \quad y^* = 0, \tag{6.4.3}$$

$$\phi^*_{2y^*} = 0 \qquad \text{on} \quad y^* = h_1 + h_2, \tag{6.4.4}$$

$$\phi_{1x^*}\eta^*_{x^*} = \phi_{1y^*} \qquad \text{on} \quad y^* = h_1 + \eta^*(x^*), \tag{6.4.5}$$

$$\phi^*_{2x^*}\eta^*_{x^*} = \phi^*_{2y^*} \qquad \text{on} \quad y^* = h_1 + \eta^*(x^*), \tag{6.4.6}$$

on the channel bottom, the rigid-lid, and the interface between the two fluids, respectively. The dynamic boundary condition on the interface is

$$-\frac{1}{\rho_1}\sigma_i\kappa^* + \frac{1}{2}(\phi^{*2}_{1x^*} + \phi^{*2}_{1y^*} - V_1^2) - \frac{R}{2}(\phi^{*2}_{2x^*} + \phi^{*2}_{2y^*} - V_2^2) + g(1-R)(y^* - h_1) = 0. \tag{6.4.7}$$

Dropping the stars, we add a small amplitude perturbation to the flow, by writing

$$\phi_1 = V_1 x + \phi_1'(x, y), \tag{6.4.8}$$

$$\phi_2 = V_2 x + \phi_2'(x, y). \tag{6.4.9}$$

Then substituting (6.4.8) and (6.4.9) into the governing equations (6.4.1)-(6.4.7), we obtain

$$\phi'_{1xx} + \phi'_{1yy} = 0 \qquad \text{in} \quad 0 < y < h_1 + \eta, \tag{6.4.10}$$

$$\phi'_{2xx} + \phi'_{2yy} = 0 \qquad \text{in} \quad h_1 + \eta < y < h_2 + h_1, \tag{6.4.11}$$

$$\phi'_{1y} = 0 \qquad \text{on} \quad y = 0, \tag{6.4.12}$$

$$\phi'_{2y} = 0 \qquad \text{on} \quad y = h_1 + h_2, \tag{6.4.13}$$

$$V_1\eta_x + \phi'_{1x}\eta_x = \phi'_{1y} \quad \text{on} \quad y = h_1 + \eta, \tag{6.4.14}$$

$$V_2\eta_x + \phi'_{2x}\eta_x = \phi'_{2y} \quad \text{on} \quad y = h_1 + \eta, \tag{6.4.15}$$

and on $y = h_1 + \eta$,

$$\begin{aligned} -\frac{\sigma_i}{\rho_1}\kappa + \frac{1}{2}\left((V_1 + \phi'_{1x})^2 + {\phi'_{1y}}^2 - V_1^2\right) \\ -\frac{R}{2}\left((V_2 + \phi'_{2x})^2 + {\phi'_{2y}}^2 - V_2^2\right) + g(1-R)(y - h_1) = 0. \end{aligned} \tag{6.4.16}$$

By considering the Taylor expansions of ϕ_1 and ϕ_2 about $y = h_1$, dropping the primes and linearising the equations, we obtain

$$\phi_{1xx} + \phi_{1yy} = 0 \qquad \text{in} \quad 0 < y < h_1, \tag{6.4.17}$$

$$\phi_{2xx} + \phi_{2yy} = 0 \qquad \text{in} \quad h_1 < y < h_2 + h_1, \tag{6.4.18}$$

$$\phi_{1y} = 0 \qquad \text{on} \quad y = 0, \tag{6.4.19}$$

$$\phi_{2y} = 0 \qquad \text{on} \quad y = h_1 + h_2, \tag{6.4.20}$$

$$V_1\eta_x = \phi_{1y} \quad \text{on} \quad y = h_1, \tag{6.4.21}$$

$$V_2\eta_x = \phi_{2y} \quad \text{on} \quad y = h_1, \tag{6.4.22}$$

and on $y = h_1$,

$$-\frac{\sigma_i}{\rho_1}\eta_{xx} + V_1\phi_{1x} - RV_2\phi_{2x} + g\eta(1-R) = 0. \tag{6.4.23}$$

Next, we seek linear sinusoidal (periodic) wave functions of the form

$$\phi_1(x, y) = \delta A_1(y)e^{ikx}, \tag{6.4.24}$$

$$\phi_2(x, y) = \delta A_2(y)e^{ikx}, \tag{6.4.25}$$

$$\eta(x) = \delta B_1 e^{ikx}, \tag{6.4.26}$$

with wavenumber k. Here, δ is an arbitrarily small constant to remind us that the functions here are all small.

Substituting the wave function (6.4.24) into Laplace's equation (6.4.17) gives

$$\begin{aligned} -k^2 A_1 + A_1'' &= 0, \\ \Rightarrow \qquad A_1 &= c_1 e^{ky} + c_2 e^{-ky}, \end{aligned} \tag{6.4.27}$$

where c_1 and c_2 are arbitrary constants. Then, from the kinematic condition on the channel bottom, (6.4.19), we find that

$$\begin{aligned} c_1 k - c_2 k &= 0, \\ \Rightarrow \qquad c_1 &= c_2, \end{aligned} \tag{6.4.28}$$

and so

$$\begin{aligned} A_1 &= 2c_1 \cosh(ky), \\ \Rightarrow \phi_1 &= 2c_1 \delta \cosh(ky) e^{ikx}. \end{aligned} \tag{6.4.29}$$

Then, from the kinematic condition on the interface in the lower fluid, (6.4.21), we obtain the relationship

$$\begin{aligned} V_1 B_1 ik &= 2kc_1 \sinh(kh_1), \\ \Rightarrow \qquad B_1 &= \frac{2kc_1 \sinh(kh_1)}{ikV_1}. \end{aligned} \tag{6.4.30}$$

Also, substituting the wave function (6.4.25) into Laplace's equation (6.4.18) gives

$$\phi_2 = \delta(c_3 e^{ky} + c_4 e^{-ky}) e^{ikx}, \tag{6.4.31}$$

where c_3 and c_4 are arbitrary constants. Then, from the kinematic condition on the interface in the upper fluid, (6.4.22), we obtain the relationship

$$(c_3 k e^{kh_1} - c_4 k e^{-kh_1}) \delta e^{ikx} = V_2 ik B_1 \delta e^{ikx}. \tag{6.4.32}$$

Now substituting B_1 from equation (6.4.30) into (6.4.32), we obtain

$$\begin{aligned} c_3 k e^{kh_1} - c_4 k e^{-kh_1} &= 2kc_1 \sinh(kh_1) \frac{ikV_2}{ikV_1}, \\ \Rightarrow \qquad c_3 &= c_4 e^{-2kh_1} + 2c_1 \gamma \sinh(kh_1) e^{-kh_1}. \end{aligned} \tag{6.4.33}$$

Thus,

$$\phi_2 = \delta \left(2c_4 e^{-kh_1} \cosh(k(y - h_1)) + 2c_1 \gamma \sinh(kh_1) e^{k(y-h_1)} \right) e^{ikx}. \tag{6.4.34}$$

Using the kinematic condition on the rigid lid, (6.4.20), and our expression for ϕ_2, (6.4.34), we find that

$$\begin{aligned} 2c_4 e^{-kh_1} k \sinh(kh_2) + 2c_1\gamma \sinh(kh_1) k e^{kh_2} &= 0, \\ \Rightarrow \qquad \frac{-c_1 \sinh(kh_1)\gamma e^{k(h_1+h_2)}}{\sinh(kh_2)} &= c_4. \end{aligned} \tag{6.4.35}$$

Therefore, (6.4.34) becomes

$$\phi_2 = \delta 2c_1\gamma \left(\frac{-\sinh(kh_1)e^{kh_2}}{\sinh(kh_2)} \cosh(k(y-h_1)) + \sinh(kh_1)e^{k(y-h_1)} \right) e^{ikx}. \tag{6.4.36}$$

In order that our expressions (6.4.29) and (6.4.36) satisfy the dynamic boundary condition, (6.4.23), we require

$$\begin{aligned} &-\frac{\sigma_i}{\rho_1}(ik)^2 B e^{ikx} + V_1 2c_1 (ik)\cosh(kh_1)e^{ikx} \\ &- RV_2 2c_1\gamma(ik)\left(\frac{-\sinh(kh_1)e^{kh_2}}{\sinh(kh_2)} + \sinh(kh_1) \right) e^{ikx} \\ &+ g(1-R)Be^{ikx} = 0. \end{aligned} \tag{6.4.37}$$

Thus,

$$\begin{aligned} &\left(\frac{\sigma_i}{\rho_1}k^2 + g(1-R) \right) \frac{2c_1 \sinh(kh_1)}{iV_1} \\ &+ i2c_1 k V_1 \cosh(kh_1) + iRV_2 2c_1\gamma k \left(\frac{\sinh(kh_1)}{\tanh(kh_2)} \right) = 0, \end{aligned} \tag{6.4.38}$$

which, multiplying by $V_1 k \tanh(kh_2)/2c_1 \cosh(kh_1)$, implies that

$$\begin{aligned} &-i\left(\frac{\sigma_i}{\rho_1}k^2 + g(1-R) \right) k \tanh(kh_1)\tanh(kh_2) \\ &+ ik^2 V_1^2 \tanh(kh_2) + iRV_2 V_1 \gamma k^2 \tanh(kh_1) = 0. \end{aligned} \tag{6.4.39}$$

Rearranging, the dispersion relation (6.4.39) becomes

$$\begin{aligned} &-\left(\frac{\sigma_i}{\rho_1 g}k^2 + (1-R) \right) \tanh(kh_1)\tanh(kh_2) \\ &+ k\frac{V_1^2}{g}\tanh(kh_2) + R\frac{V_1 V_2 \gamma}{g} k \tanh(kh_1) = 0. \end{aligned} \tag{6.4.40}$$

Then, non-dimensionalising by taking h_1 as the unit length scale, and denoting $K = kh_1$

as the dimensionless wavenumber, we obtain

$$F_1^2 K \tanh(KD) + RF_1^2\gamma^2 K \tanh(K) - \left(\tau K^2 + (1-R)\right)\tanh(K)\tanh(KD) = 0. \tag{6.4.41}$$

In the special case $\gamma = 1$, corresponding to the case that the (constant) velocities upstream are the same ($V_1 = V_2 = V$), we obtain

$$F_1^2 K \tanh(KD) + RF_1^2 K \tanh(K) - \left(\tau K^2 + (1-R)\right)\tanh(K)\tanh(KD) = 0. \tag{6.4.42}$$

Now we consider the long wave limit, $K \to 0$, in order to obtain the critical Froude number F_{bif}. This is the Froude number at which the transition between subcritical and supercritical solutions occurs. If $F < F_{\text{bif}}$, real values of the wavenumber K can be obtained. Solitary waves bifurcate from the uniform stream at this critical Froude number.

As $K \to 0$, $\tanh(K)$ can be approximated by the Taylor expansion

$$\tanh(K) \approx K - \frac{1}{3}K^3 + \frac{2}{15}K^5 - ... \approx K. \tag{6.4.43}$$

Thus, the dispersion relation (6.4.41) becomes

$$\begin{aligned} & F_1 K^2 D + RF_1^2\gamma^2 K^2 - \tau K^4 D - (1-R)K^2 D \approx 0, \\ \Rightarrow \quad & F_1^2 D + RF_1^2\gamma^2 - (1-R)D \approx 0, \\ \Rightarrow \quad & F_{\text{bif}}^2 = \frac{D(1-R)}{D + R\gamma^2}. \end{aligned} \tag{6.4.44}$$

The critical value of the interfacial tension can also be obtained by considering the linear dispersion relation at the next order. Letting $\tanh(KD) \approx KD - \frac{1}{3}K^3D^3$ and $\tanh(K) \approx K - \frac{1}{3}K^3$, the dispersion relation (6.4.41) becomes

$$\begin{aligned} & K^2\left(F_1^2 D + RF_1^2\gamma^2 - (1-R)D\right) \\ & + K^4\left(-\frac{1}{3}F_1^2 D - \frac{1}{3}RF_1^2\gamma^2 - \tau D + \frac{1}{3}(1-R)D(D^2+1)\right) \\ & + O(K^6) = 0. \end{aligned} \tag{6.4.45}$$

We satisfy this expression by letting $F_1 = F_{\text{bif}}$, and setting

$$-\frac{1}{3}F_1^2 D^3 - \frac{1}{3}RF_1^2\gamma^2 - \tau D + \frac{1}{3}(1-R)D(D^2+1) = 0.$$

Then,

$$\begin{aligned}
\tau D &= \frac{1}{3}D(1-R)(1+D^2) - \frac{1}{3}F_{\text{bif}}^2(D^3+R\gamma^2),\\
\Rightarrow\quad \tau &= \frac{1}{3}(1-R)(1+D^2) - \frac{1}{3}\frac{(1-R)}{D+R\gamma^2}(D^3+R\gamma^2),\\
\Rightarrow\quad \tau &= \frac{\frac{1}{3}(1-R)(1+D^2)(D+R\gamma^2) - \frac{1}{3}(1-R)(D^3+R\gamma^2)}{D+R\gamma^2},\\
\Rightarrow\quad \tau &= \frac{1}{3}\frac{D(1-R)(1+RD\gamma^2)}{D+R\gamma^2}.
\end{aligned} \tag{6.4.46}$$

When $R = 0$ and $D = 1$, which represents the free surface of a single-layer of fluid, (6.4.46) becomes $\tau = \frac{1}{3}$, as we would expect.

The downstream dispersion relation is similarly obtained. We find that

$$(U_1k)^2\tanh(kH_2)+R(U_2k)^2\tanh(kH_1)-\left(\frac{\sigma_i}{\rho_1}k^3+gk(1-R)\right)\tanh(kH_1)\tanh(kH_2)=0. \tag{6.4.47}$$

In the case of a hydraulic fall, downstream we will have that $U_1 \neq U_2$. Dividing (6.4.47) through by kg, we obtain

$$\begin{aligned}
&\frac{U_1^2}{g}k\tanh\left(kh_1\frac{H_2}{h_2}\frac{h_2}{h_1}\right) + R\frac{U_2^2}{g}k\tanh\left(kh_1\frac{H_1}{h_1}\right)\\
&-\left(\frac{\sigma_i}{\rho_1 g}k^2+1-R\right)\tanh\left(kh_1\frac{H_1}{h_1}\right)\tanh\left(kh_1\frac{h_2}{h_1}\frac{H_2}{h_2}\right)=0.
\end{aligned} \tag{6.4.48}$$

Now, non-dimensionalising and defining the dimensionless wavenumber as before, (6.4.48) becomes

$$\begin{aligned}
&\frac{U_1^2}{gh_1}K\tanh\left(K\frac{D}{\gamma_2}\right) + R\frac{U_2^2}{gh_1}K\tanh\left(\frac{K}{\gamma_1}\right)\\
&-\left(\frac{\sigma_i}{\rho_1 g h_1^2}K^2+1-R\right)\tanh\left(\frac{K}{\gamma_1}\right)\tanh\left(\frac{KD}{\gamma_2}\right)=0, &(6.4.49)\\
\Rightarrow\quad &F_{1d}^2\frac{K}{\gamma_1}\tanh\left(\frac{KD}{\gamma_2}\right) + RKF_{1d}^2\frac{\gamma_2^2\gamma^2}{\gamma_1^3}\tanh\left(\frac{K}{\gamma_1}\right)\\
&-\left(\tau_d\frac{K^2}{\gamma_1^2}+1-R\right)\tanh\left(\frac{K}{\gamma_1}\right)\tanh\left(\frac{KD}{\gamma_2}\right)=0, &(6.4.50)
\end{aligned}$$

where we have used that $U_2^2/U_1^2 = (U_2^2/V_2^2)(V_2^2/V_1^2)(V_1^2/U_1^2) = \gamma_2^2\gamma^2/\gamma_1^2$. Again, by expanding $\tanh x$ as a Maclaurin expansion and considering the first order of the linear dispersion relation, we can obtain F_{1d}.

So, using (6.4.41) and (6.4.50) the upstream and downstream dispersion relations can

be written in the form

$$F_1^2 = \frac{(1 - R + \tau K^2)\tanh(K)\tanh(KD)}{K(\tanh(KD) + R\gamma^2\tanh(K))}, \tag{6.4.51}$$

$$F_{1d}^2 = \frac{(1 - R + \frac{\tau_d K^2}{\gamma_1^2})\tanh(\frac{K}{\gamma_1})\tanh(\frac{KD}{\gamma_2})}{\frac{K}{\gamma_1}\tanh(\frac{KD}{\gamma_2}) + \frac{R\gamma_2^2\gamma^2 K}{\gamma_1^3}\tanh(\frac{K}{\gamma_1})}, \tag{6.4.52}$$

respectively. The upstream and downstream critical values of the Froude number are

$$F_{1\text{bif}}^2 = \frac{D(1-R)}{D + R\gamma^2}, \tag{6.4.53}$$

$$F_{1d_{\text{bif}}}^2 = \frac{(1-R)D\gamma_1^3}{D\gamma_1^3 + R\gamma_2^3\gamma^2}. \tag{6.4.54}$$

If $F_1 > F_{1\text{bif}}$, the flow in the lower layer is said to be supercritical (upstream), and if $F_1 < F_{1\text{bif}}$, the flow is said to be subcritical (upstream). When looking for critical, conjugate flow solutions there are thus four cases that we need to consider (see for example Dias and Vanden-Broeck [39]). These flow regimes are defined by:

1. Supercritical flow upstream ($F_1 > F_{1\text{bif}}$) with a thick upper layer ($D > \sqrt{R}$),
2. Subcritical flow upstream ($F_1 < F_{1\text{bif}}$) with a thick upper layer ($D > \sqrt{R}$),
3. Supercritical flow upstream ($F_1 > F_{1\text{bif}}$) with a thick bottom layer ($D < \sqrt{R}$),
4. Subcritical flow upstream ($F_1 < F_{1\text{bif}}$) with a thick bottom layer ($D < \sqrt{R}$).

6.5 Weakly nonlinear analysis

In order to choose an appropriate set of initial values for Y', we use a weakly nonlinear analysis to determine the type of hydraulic fall sought in each of the four regimes described at the end of section 6.4.

Dias and Vanden-Broeck [39] considered the pure gravity stationary fKdV equation, which is valid far from the critical depth ratio $D = \sqrt{R}$, in the rigid lid approximation. Using an appropriate choice of scaling, they showed that the classical fKdV equation in the rigid lid configuration transforms into the equation

$$\frac{1}{6}\eta_{xxx} \pm \frac{3}{2}\eta\eta_x - \mu\eta_x = -\frac{1}{2}B_x, \tag{6.5.1}$$

where $R = 1$. Here $y = B(x)$ is the equation governing the channel bottom, $\eta(x)$ is the interfacial elevation, and $\hat{\epsilon}\mu = F - 1$, where $\hat{\epsilon}$ is a small parameter with order of the square root of the height of the submerged obstruction; i.e. $\sqrt{A_2}$. Therefore, the flow is

supercritical if $\mu > 0$ and subcritical if $\mu < 0$. The plus sign in equation (6.5.1) is used in the case of a thick upper layer, $D > \sqrt{R}$, and the minus sign in the case of a thick bottom layer, $D < \sqrt{R}$.

Following Dias and Vanden-Broeck, we integrate the fKdV equation (6.5.1) with respect to x, to obtain

$$\eta_{xx} \pm \frac{9}{2}\eta^2 - 6\mu\eta = -3Q\delta(x), \tag{6.5.2}$$

where the channel bottom $y = B(x)$ has been approximated by the Dirac delta function;

$$B(x) = Q\delta(x). \tag{6.5.3}$$

Then integrating (6.5.2) between $-\epsilon$ and ϵ, in the limit as $\epsilon \to 0$, gives

$$\int_{-\epsilon}^{\epsilon} \eta_{xx} dx = -3Q \int_{-\epsilon}^{\epsilon} \delta(x) dx, \tag{6.5.4}$$

$$\Rightarrow \eta_x(0^+) - \eta_x(0^-) = -3Q. \tag{6.5.5}$$

This is known as the jump condition, and must be satisfied alongside the unforced KdV equation, (6.5.2) with $Q = 0$, i.e.

$$\eta_{xx} = \mp\frac{9}{2}\eta^2 + 6\mu\eta. \tag{6.5.6}$$

The KdV equation has an equilibrium point $x = q$ when

$$f(q) = \eta_{xx} = 0. \tag{6.5.7}$$

Thus, we see that $q = 0$ and $q = \pm\frac{4}{3}\mu$ are the only equilibrium points. Next, we multiply (6.5.6) by $2\eta_x$, and integrate once to obtain

$$\eta_x^2 = \mp 3\eta^3 + 6\mu\eta^2 + C, \tag{6.5.8}$$

for some arbitrary constant C. We can now plot the phase portraits in the (η, η_x) plane for the unforced solution trajectories. We sketch typical solution trajectories for the four different cases in figure 6.4. To obtain hydraulic falls we consider the continuous bounded solutions which satisfy the jump condition (6.5.5).

Dias and Vanden-Broeck analysed these phase portraits, to determine the behaviour of the pure gravity hydraulic fall solutions. The phase portrait in figure 6.4(a) shows that in the subcritical case with a thick upper layer, as the solution is required to be uniform upstream with $\eta = 0$, the solution trajectory must start at the fixed point $\eta = 0, \eta_x = 0$. At $x = 0$, there is then a downwards jump onto the elevation solitary wave trajectory, to satisfy the jump condition (6.5.5). The depth of the fluid in the lower layer is therefore

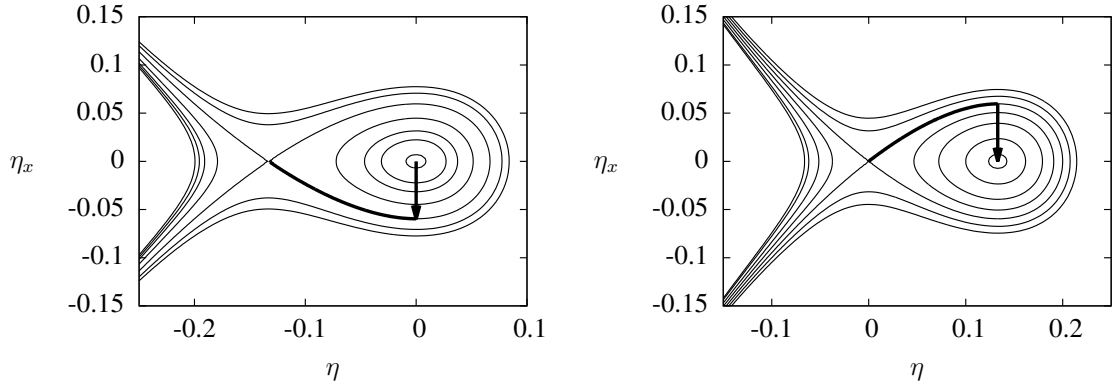

(a) Subcritical flow upstream with a thick upper layer. **(b)** Supercritical flow upstream with a thick upper layer.

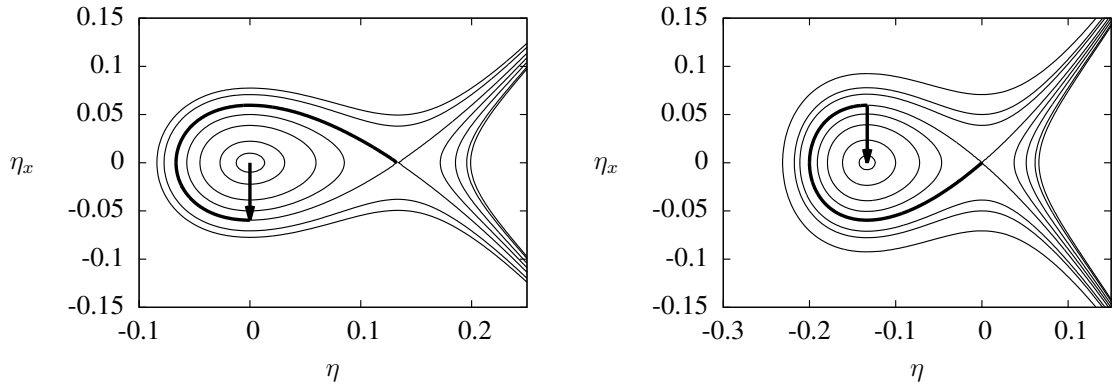

(c) Subcritical flow upstream with a thick lower layer. **(d)** Supercritical flow upstream with a thick lower layer.

Figure 6.4: Phase plane representations of the hydraulic fall solutions to the unforced pure gravity KdV equation. The hydraulic fall path in each case is shown by the thick solid line.

expected to decrease over the obstruction.

In the second case, with supercritical flow upstream and a thick upper layer, the phase portrait in figure 6.4(b) shows that, as the flow is required to be uniform upstream for $x < 0$, the solution must initially follow the elevation solitary wave trajectory. At $x = 0$ the jump condition is satisfied, so, provided that the obstacle is of the required size, the solution jumps downwards to the fixed point with $\eta_x = 0$. The depth of the lower layer is therefore expected to increase over the obstruction. Dias and Vanden-Broeck noted that a generalised hydraulic fall of the same orientation may be obtained if the solution jumps onto a cnoidal wave trajectory, rather than to the fixed point.

When the flow upstream is subcritical, with a thick lower layer, the situation is more interesting. Figure 6.4(c) shows that, as the flow is required to be uniform upstream, the solution must start from the fixed point $\eta = 0$, $\eta_x = 0$. To satisfy the jump condition the solution must jump downwards onto the depression solitary wave branch. This occurs before the solitary wave has passed its trough. The trough is therefore expected to appear on the interface over the obstruction, before the level of the lower layer increases.

Finally, when the flow is supercritical upstream with a thick lower layer, figure 6.4(d)

shows that the requirement of uniform flow upstream means that initially the flow must follow the depression solitary wave branch. To satisfy the jump condition the solution must jump downwards at $x = 0$, to the fixed point with $\eta_x = 0$. This downward jump occurs after the solitary wave has reached its trough, and so a trough is expected to appear over the obstruction before the depth of the lower fluid decreases. Dias and Vanden-Broeck note that in order to obtain this solution the obstacle must be of the exact required size. Otherwise, the solution jumps to a cnoidal wave trajectory, and a generalised hydraulic fall with waves downstream of the obstacle is predicted.

This weakly nonlinear analysis in the pure gravity case is not new (see Dias and Vanden-Broeck [39]), but is included here for completeness. We now apply the same method to the gravity-capillary fKdV equation. Following Laget and Dias [75] we obtain the KdV equation. Then, following Dias and Vanden-Broeck [39], it can be transformed into the gravity-capillary stationary fKdV equation given by

$$\frac{1}{2}(\tau^* - \tau)\eta_{xxx} \pm \frac{3}{2}\eta\eta_x - \mu\eta_x = -\frac{1}{2}B_x. \tag{6.5.9}$$

Here, τ^* corresponds to the critical value of the Bond number, given by (6.4.46). By introducing some positive constant α, with strong interfacial tension, $\tau > \tau^*$, we rewrite (6.5.9) as

$$\frac{\alpha}{6}\eta_{xxx} \mp \frac{3}{2}\eta\eta_x + \mu\eta_x = \frac{1}{2}B_x. \tag{6.5.10}$$

Integrating (6.5.10) with respect to x, we obtain

$$\alpha\eta_{xx} \mp \frac{9}{2}\eta^2 + 6\mu\eta = 3Q\delta(x). \tag{6.5.11}$$

We can then determine that the stationary points of the unforced KdV equation, $Q = 0$, are at $\eta = 0$ and $\eta = \mp\frac{4}{3}\mu$. Integrating again, we then find that the jump condition becomes

$$\eta_x(0^+) - \eta_x(0^-) = \frac{3}{\alpha}Q. \tag{6.5.12}$$

A positive, upwards jump is therefore required in the gravity-capillary cases. We sketch the solution trajectories for the four different cases in figure 6.5. As in the pure gravity case, we seek continuous, bounded solutions which satisfy the jump condition (6.5.12).

For subcritical flow with $D > \sqrt{R}$, the phase portrait 6.5(a) shows that, as the flow is uniform upstream, with $\eta = 0$, the solution must follow the depression solitary wave trajectory for $x < 0$. The solution must jump upwards to satisfy the jump condition. Provided that the obstacle is of the required size, the solution jumps to the other equilibrium point and a hydraulic fall is obtained. The depth of the lower fluid in this case is therefore expected to decrease over the obstacle. If, instead, the obstacle is such that the solution

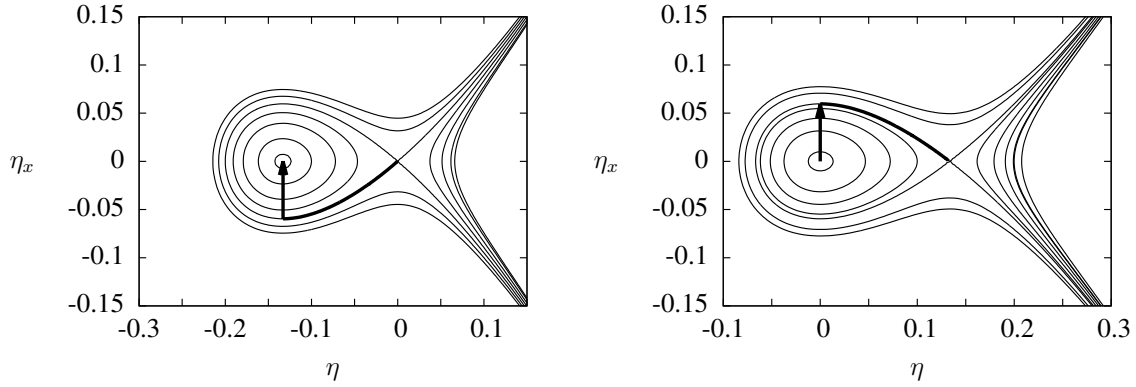

(a) Subcritical flow upstream with a thick upper layer. **(b)** Supercritical flow upstream with a thick upper layer.

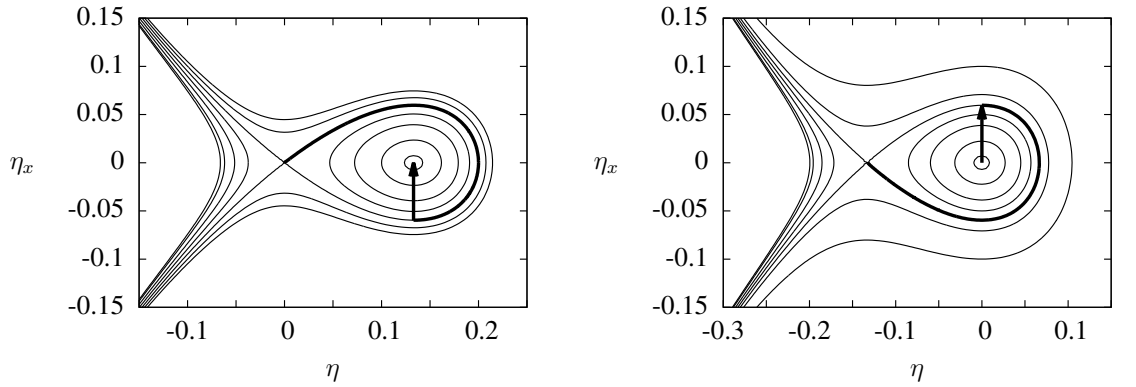

(c) Subcritical flow upstream with a thick lower layer. **(d)** Supercritical flow upstream with a thick lower layer.

Figure 6.5: Phase plane representations of the hydraulic fall solutions to the unforced gravity-capillary KdV equation. The hydraulic fall path in each case is shown by the thick solid line.

jumps to a cnoidal wave solution, then we predict generalised hydraulic falls with waves downstream of the obstacle.

When the flow upstream is supercritical with $D > \sqrt{R}$, the phase portrait 6.5(b) shows that, as we require the flow to be uniform upstream (with $\eta = 0$), the solution must stay at the equilibrium point $\eta = 0$, $\eta_x = 0$ for $x < 0$. To satisfy the jump condition the solution jumps upwards onto the depression solitary wave solution at $x = 0$, and moves to the saddle point. The depth of the lower fluid is therefore expected to increase over the obstacle.

In the case of subcritical flow upstream with $D < \sqrt{R}$, the phase portrait 6.5(c) shows that, as the flow is required to be uniform upstream with $\eta = 0$, the solution must follow the elevation solitary wave trajectory for $x < 0$. To satisfy the jump condition the solution must jump upwards, and so the peak of the solitary wave is passed before the solution jumps to the other equilibrium point at $x = 0$. Hydraulic falls in this case are therefore expected to have a peak over the obstacle, with the depth of the lower fluid being greater downstream than upstream. If the obstacle is not of the required size the solution may jump onto a cnoidal wave trajectory instead, resulting in a generalised hydraulic fall.

Finally, when the flow upstream is supercritical with $D < \sqrt{R}$, the phase portrait 6.5(d) shows that, as the flow must be uniform upstream with $\eta = 0$, the solution stays at the equilibrium point $\eta = 0$, $\eta_x = 0$ for $x < 0$. To satisfy the jump condition the solution jumps upwards onto the elevation solitary wave trajectory at $x = 0$. This happens before the peak in the solitary wave is reached, and so the hydraulic falls in this case are expected to have a peak over the obstruction before the depth of the lower fluid decreases downstream.

In each case, we now know, from the weakly nonlinear analysis, whether the depth of the lower fluid should increase or decrease over the obstacle. An appropriate set of initial values for Y' can thus be chosen accordingly.

6.6 Results

The results in this section were computed using the method described in section 6.3. We begin by setting $\gamma = 1$ so that we consider examples where the two upstream flow velocities are the same. We use the same cosine squared channel bottom configuration as presented in the previous chapters, see (4.4.1), so that the heights and lengths of the obstacles are given by $2A_i$ and $2L_i$, for $i = 1, 2$, respectively. As before, when considering flow over a single obstruction, we set $A_1 = 0$.

6.6.1 Pure gravity solutions

In the case of a single obstacle, the pure gravity hydraulic fall solutions in the rigid lid configuration have previously been obtained by Dias and Vanden-Broeck [39], and by Dias and Vanden-Broeck [40] in the critical region $D \approx \sqrt{R}$. Typical solution profiles in each of the four cases described in section 6.4 are shown in figure 6.6. We find that the solutions are very sensitive to the initial conditions we choose. An appropriate initial set of values for Y' is chosen by considering the weakly nonlinear analysis of section 6.5, but we have to manipulate the initial values of γ_1, γ_2 and F_1 carefully, in order for our code to converge. In region one, with subcritical flow upstream and a thick upper layer, we set $R = 0.6$ and $D = 2$, so that $F_{\text{bif}} \approx 0.55$. The weakly nonlinear analysis then tells us that we require $\gamma_1 > 1$ and $\gamma_2 < 1$. Therefore, we initially set $\gamma_1 = 2$, $\gamma_2 = 0.5$, $F_1 = 0.4$ and obtain the initial set of values for Y' by defining

$$Y = \frac{1}{2}\left(1 - \frac{1}{\gamma_1}\right)\left(-\tanh(\alpha\sigma)\right), \tag{6.6.1}$$

and differentiating numerically. Here α is a constant, which we take to be $\alpha = 0.05$ in this region. The three additional far field equations in this regime are given by (6.3.18)-(6.3.20). In region two, with supercritical flow upstream and a thick upper layer, the

weakly nonlinear analysis tells us that $\gamma_1 < 1$ and $\gamma_2 > 1$. Therefore, initially we set $\gamma_1 = 0.85$, $\gamma_2 = 1.2$, $F_1 = 0.55$ and we obtain the set of values for Y' by setting $\alpha = 0.5$ in (6.6.1). The three additional far field equations (6.3.18)-(6.3.20) defined in section 6.3 are replaced with the equations

$$u(1) = 1, \tag{6.6.2}$$
$$Y'(M) = 0, \tag{6.6.3}$$
$$Y'(M-1) = 0, \tag{6.6.4}$$

to ensure that the interfacial surface is uniform far downstream.

The remaining two cases are harder to determine. The flow configurations have a thick lower layer, so we choose $R = 0.6$ and $D = 0.5$. Then, we find that $F_{\text{bif}} \approx 0.43$. In region three, with subcritical flow upstream, we know from the weakly nonlinear analysis that we need $\gamma_1 < 1$ and $\gamma_2 > 1$. However, this time, we also require that there exists a depression in the free surface before the change in fluid depths occurs. We obtain such a solution by initially setting $\gamma_1 = 0.85$, $\gamma_2 = 1.2$, $F_1 = 0.5$ and $\alpha = 0.5$. The three additional far field equations (6.3.18)-(6.3.20) defined in section 6.3 are replaced with the equations

$$u(1) = 1, \tag{6.6.5}$$
$$Y'(1) = 0, \tag{6.6.6}$$
$$Y'(2) = 0, \tag{6.6.7}$$

to ensure that the interfacial surface is uniform far upstream. In region four, the flow upstream is supercritical and the weakly nonlinear analysis tells us that we need $\gamma_1 > 1$ and $\gamma_2 < 1$. We also require a depression on the free surface immediately after the hydraulic fall. We have found that this case is extremely sensitive to its initial conditions. We use $\gamma_1 = 2.5$ and $\gamma_2 = 0.5$, $F_1 = 0.48$ and $\alpha = 0.45$ initially, and take the far field equations to be

$$u(1) = 1, \tag{6.6.8}$$
$$Y'(1) = 0, \tag{6.6.9}$$
$$Y'(2) = 0. \tag{6.6.10}$$

We do not obtain a solution under these circumstances using our numerical scheme, but we do see that, after two Newton iterations, the free surface appears to be taking the desired form. The free surface is not uniform downstream as it should be, but the depression in the free surface after the hydraulic fall is shown clearly. Dias and Vanden-Broeck

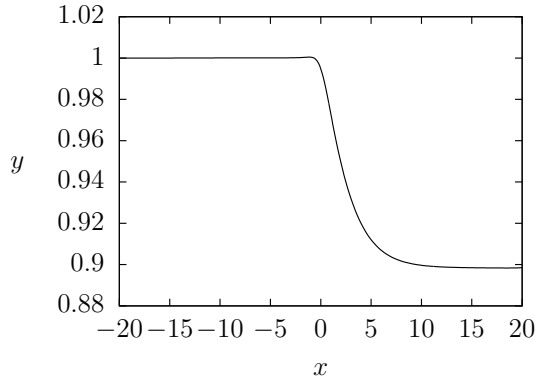

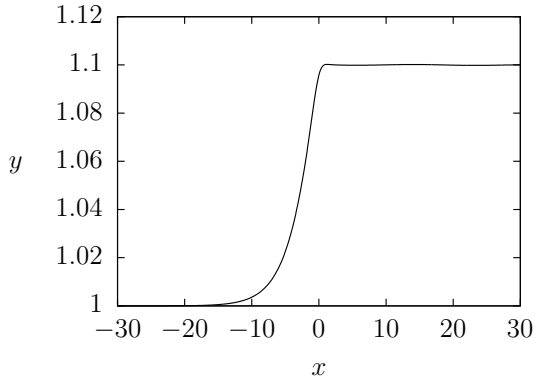

(a) Subcritical flow upstream with a thick upper layer. **(b)** Supercritical flow upstream with a thick upper layer.

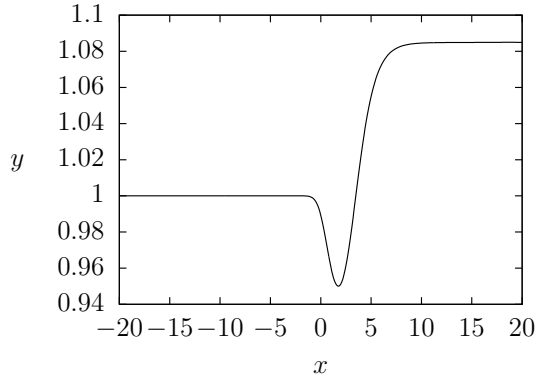

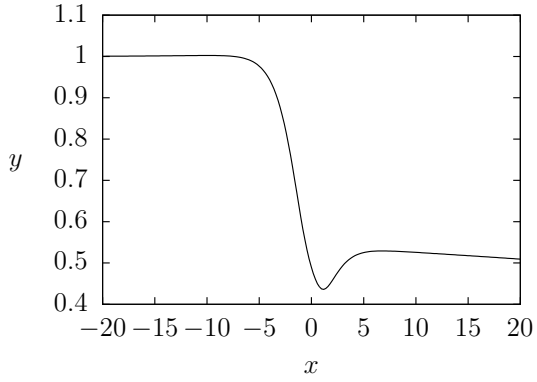

(c) Subcritical flow upstream with a thick lower layer. **(d)** Supercritical flow upstream with a thick lower layer.

Figure 6.6: Interfacial hydraulic fall profiles over an obstacle. The Froude number is found to be (a) $F_1 = 0.52$, (b) $F_1 = 0.58$, (c) $F_1 = 0.4$ respectively. The free surface profile in (d) is not a solution, but demonstrates the form of the expected solution from the weakly nonlinear analysis.

[42] show this solution in figure 18 of their paper. However, even there the solution is a generalised hydraulic fall and not a pure hydraulic fall. There are small amplitude waves downstream of the fall.

When there is just a single layer of fluid in the pure gravity case, and a second obstacle is included further upstream of the hydraulic fall, where the flow is subcritical, a train of trapped waves is found between the obstacles (Dias and Vanden-Broeck [41]). This train of waves is predicted by the linear dispersion relation, with the wavelength of the trapped waves being in rough agreement with the wavelength predicted by the linear theory. In the gravity-capillary case, unless the surface tension is very small, the additional obstacle is placed downstream of the hydraulic fall to get trapped waves to appear between the obstacles (see chapter 4).

By examining the linear dispersion relation in the four cases in the rigid lid approximation, we extend the work of Dias and Vanden-Broeck [41], by including an additional obstruction in the flow configuration, and looking for solutions with a train of waves trapped between the two obstacles.

When the flow upstream is subcritical, with a thick upper layer, the phase portrait in figure 6.4(a) shows that the solution is similar to the pure gravity single layer case. The linear theory predicts that the obstacle must be placed upstream of the hydraulic fall to obtain trapped waves. The upstream Froude number in the lower layer then intersects the lower-layer upstream linear dispersion relation, thus predicting a train of waves following the additional obstacle. Such a solution profile is shown in figure 6.7, alongside the corresponding upstream and downstream lower-layer linear dispersion relations. A train of waves, with a wavelength of $\lambda \approx 6.35$, can be seen upstream between the two obstacles. This is in good agreement with the linear theory. The solid lines in figure 6.7(c) show that the upstream Froude number F_1 intersects the upstream linear dispersion relation at $K \approx 0.99$. The linear theory therefore suggests that a train of waves of wavelength $\lambda = 2\pi/K \approx 6.35$ exists upstream.

Increasing the height of the additional obstacle increases the amplitude of the trapped waves whilst keeping the Froude number, and thus the wavelength, roughly the same. Similarly, moving the additional obstacle further upstream changes the Froude number, and thus the wavelength of the trapped waves, very little. The position of the additional obstacle therefore affects the number of waves trapped between the obstacles, but has little effect on the amplitude and wavelength of the waves. This is comparable with the results of the single layer case. See Vanden-Broeck and Dias [41] for the fully nonlinear solutions, and Pratt [95] for experimental results.

In the second case, where the flow upstream is supercritical and the fluids are such that there is a thick upper layer, the linear theory suggests that trapped waves may be obtained downstream where the flow is subcritical. We therefore place the additional obstacle downstream of the hydraulic fall and, as expected, a train of waves is found between the obstacles. A typical solution profile is shown in figure 6.8(a). The trapped waves in this case have a greater wavelength than those in the first case, and so a longer domain is required. The waves in figure 6.8(a) are of wavelength $\lambda \approx 16.35$. This is in rough agreement with the linear theory. The broken lines in the downstream linear dispersion relation in figure 6.8(c) show that, for the flow configuration of figure 6.8(a), the linear theory predicts waves with wavenumber $K \approx 0.3965$, and thus wavelength $\lambda = 2\pi/K \approx 15.85$.

When the flow upstream is subcritical and the flow configuration is such that there is a thick bottom layer, we find that the trapped waves are obtained upstream of the hydraulic fall. A typical solution profile is shown in figure 6.9(a), with waves of wavelength $\lambda \approx 3.6$. Immediately after the train of trapped waves, a trough in the interface is found before the level of the lower fluid rises downstream of the obstacle. The linear dispersion relations for the solution in figure 6.9(a) are plotted in figure 6.9(c). The solid lines show that the wavelength of the trapped waves upstream is in good agreement with the linear

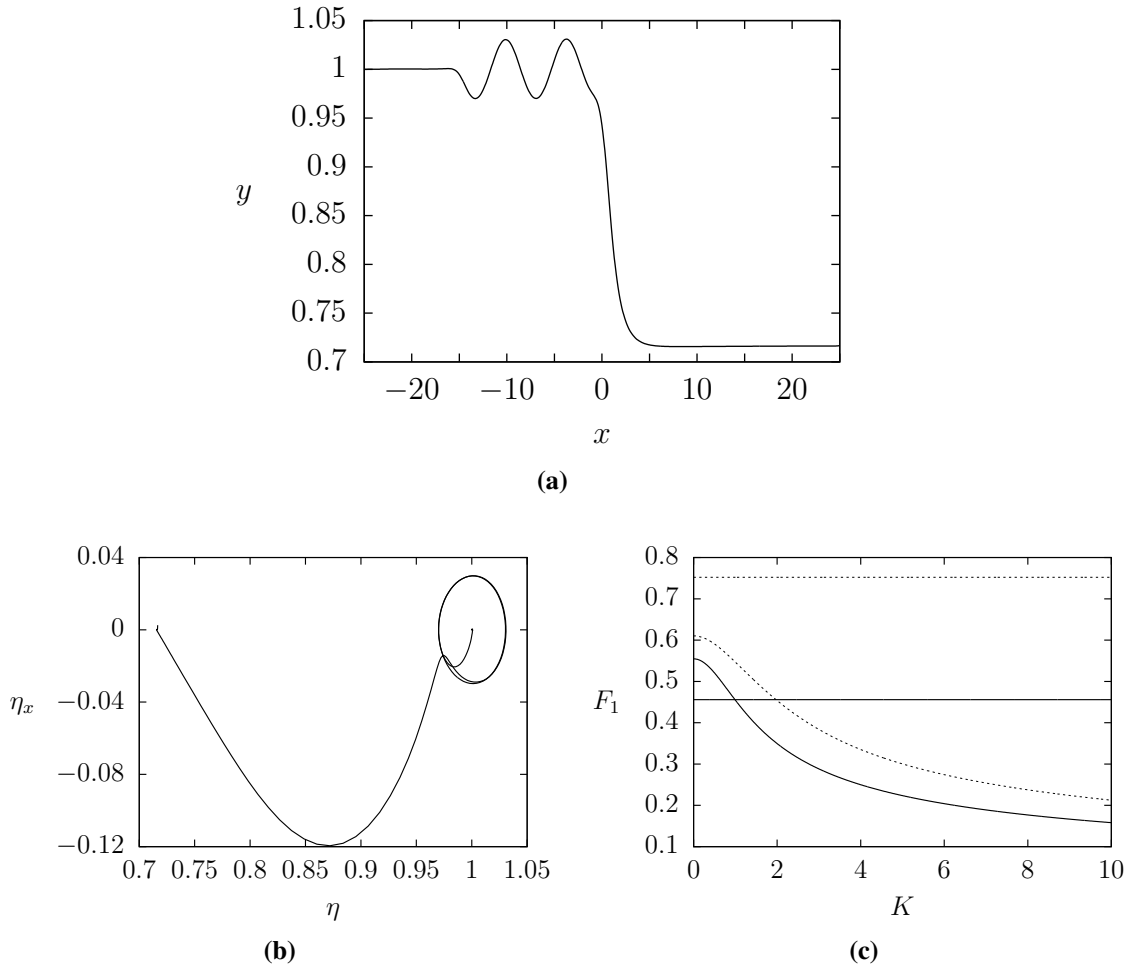

Figure 6.7: (a) Interfacial hydraulic fall profile ($D = 2$, $\sqrt{R} = 0.6$, $D > \sqrt{R}$). Waves are found trapped between the obstacles characterised by $A_2 = 0.05$, $A_1 = 0.01$, $L_1 = L_2 = 1$ and $x_d = 15$. The Froude number $F_1 = 0.46$ is found as part of the solution. The fully nonlinear phase portrait of the solution in (a) is shown in (b). In (c) we plot the upstream linear dispersion relation (curved solid line) alongside the upstream value of the Froude number F_1 (horizontal solid line) for the channel bottom configuration in (a). The broken curve is the downstream linear dispersion relation, and the broken horizontal line shows the downstream Froude number for the same bottom configuration as in (a).

theory. We see that the Froude number for the given flow configuration intersects the upstream dispersion relation at $K \approx 1.75$, corresponding to a wavelength of $\lambda \approx 3.59$.

In the fourth region, where the flow upstream is supercritical and the lower layer is thick, we would expect any trapped waves to be found downstream of the hydraulic fall, after a depression on the free surface. So, the second obstruction should be placed downstream. The downstream Froude number in this case would then be expected to intersect the downstream linear relation, resulting in waves on the free surface. Upstream, the Froude number is greater than $F_{1\mathrm{bif}}$, as the flow is supercritical, so the Froude number will not intersect the linear dispersion and no waves will appear on the free surface.

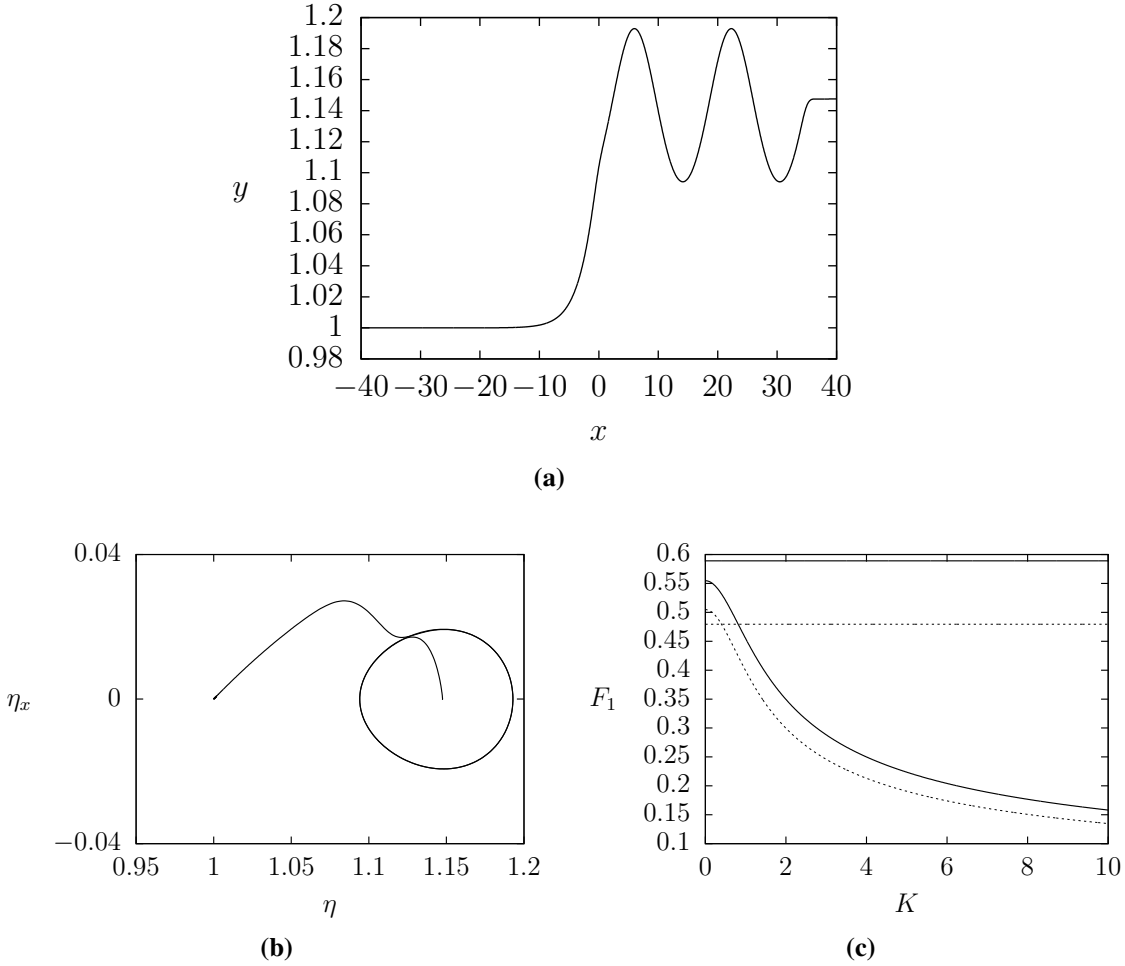

Figure 6.8: (a) Interfacial hydraulic fall profile ($D = 2$, $\sqrt{R} = 0.6$, $D > \sqrt{R}$). Waves are found trapped between the obstacles characterised by $A_2 = 0.01$, $A_1 = 0.01$, $L_1 = L_2 = 1$ and $x_d = -30$. The Froude number $F_1 = 0.59$ is found as part of the solution. The fully nonlinear phase portrait of the solution in (a) is shown in (b). In (c) we plot the upstream linear dispersion relation (solid curved line) alongside the upstream value of the Froude number F_1 (solid horizontal line) for the channel bottom configuration in (a). The broken curve is the downstream linear dispersion relation, and the broken straight line shows the downstream Froude number for the same bottom configuration in (a).

Next, we briefly examine the cases where the additional, positively orientated, obstacle is placed in the opposite region to the trapped waves, i.e. in the supercritical regions. So, in cases one and three (the flow configurations with subcritical flow upstream), the additional obstruction is now placed downstream. In figure 6.10 we show typical solution profiles. We can see, that as might be expected from considering the single layer case in chapter 4, an elevation solitary type wave is found over the additional obstruction downstream.

In the second and fourth cases, which have supercritical flow upstream, the additional obstruction must be placed upstream. In figure 6.11 we show a typical solution profile for the second case, alongside the fully nonlinear phase portrait of the solution. Again, a

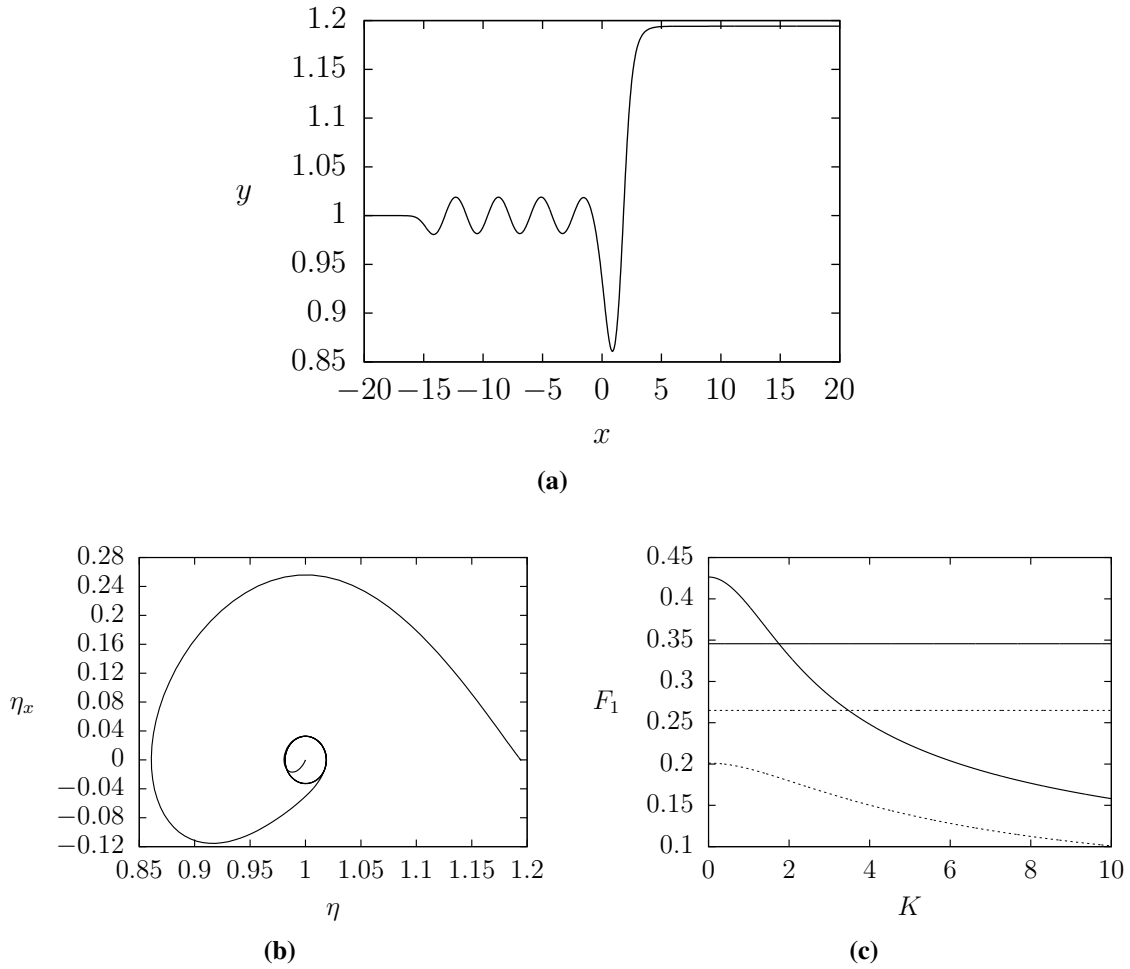

Figure 6.9: (a) Interfacial hydraulic fall profile ($D = 0.5$, $R = 0.6$, $D < \sqrt{R}$). Waves are found trapped between the obstacles characterised by $A_2 = 0.05$, $A_1 = 0.01$, $L_1 = L_2 = 1$ and $x_d = 15$. The Froude number $F_1 = 0.35$ is found as part of the solution. (c) In (c) we plot the upstream linear dispersion relation (solid curved line) alongside the upstream value of the Froude number F_1 (solid horizontal line) for the channel bottom configuration in in (a). The broken curve is the downstream linear dispersion relation, and the broken horizontal line is the downstream Froude number for the same bottom configuration in (a).

forced solitary type elevation wave appears over the additional obstruction. This solution profile shown in figure 6.11(a) is actually a type of generalised hydraulic fall as there are waves downstream, meaning that, in the phase plane, we jumped onto a cnoidal wave orbit rather than the equilibrium point.

6.6.2 Gravity-capillary solutions: Case 1

The solutions in this section were obtained using the numerical scheme described in section 6.3, with equations (6.3.18)-(6.3.20) replaced by appropriate far field conditions to obtain the required jump in the interface. The effects of interfacial tension are now included in the flow configuration.

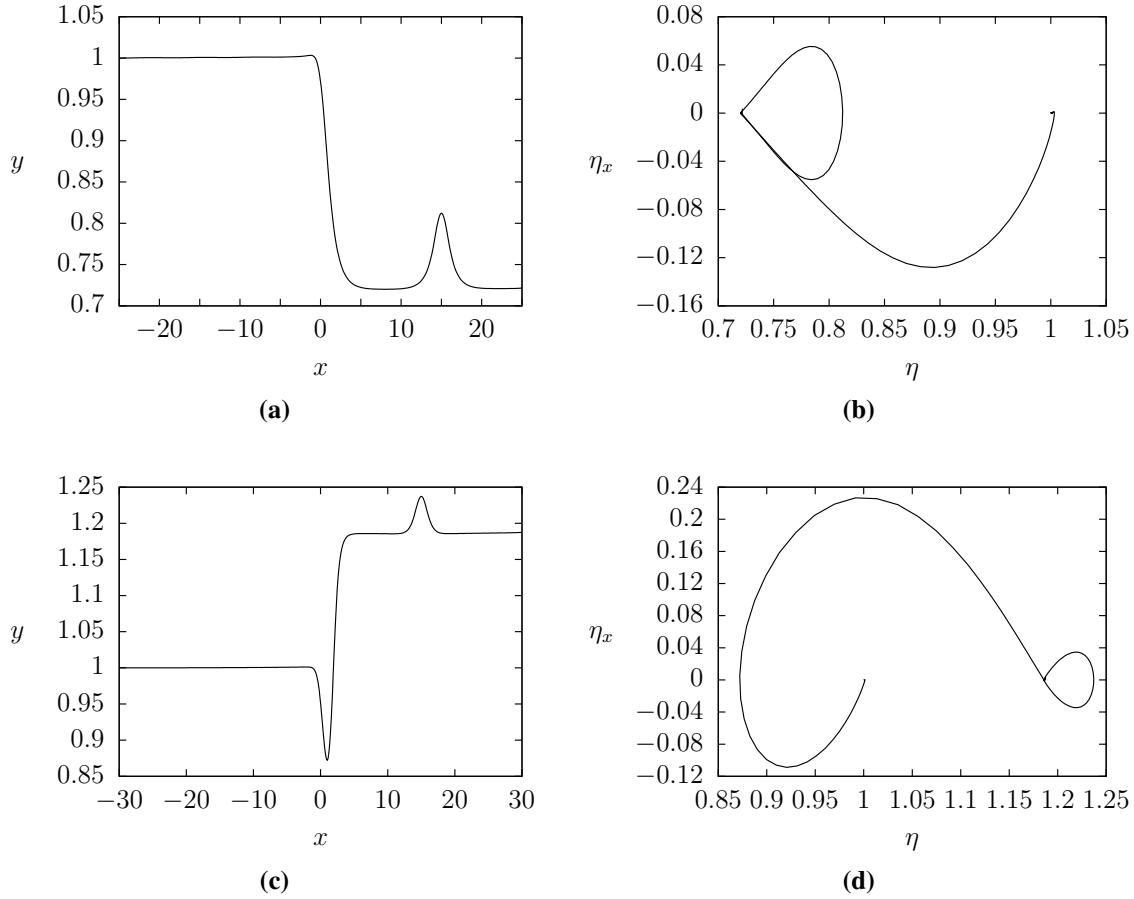

Figure 6.10: (a) and (c) show typical interfacial hydraulic fall profiles where the flow upstream is subcritical. In (a), $D > \sqrt{R}$ ($D = 2$, $R = 0.6$), and in (c), $D < \sqrt{R}$ ($D = 0.5$, $R = 0.6$). Two obstructions lie on the channel bottom, and are given by $A_2 = 0.05$ $L_1 = L_2 = 1$ and in (a) $A_1 = 0.2$, in (c) $A_1 = 0.04$. In each case, a solitary type wave is found over the additional obstruction, and the Froude number (a) $F_1 = 0.35$ and (c) $F_1 = 0.46$ is found as part of the solution. The corresponding phase portraits for the solution profiles in (a) and (c) are shown in (b) and (d) respectively.

The solutions in the first case, with subcritical flow upstream and a thick upper layer, roughly correspond to the solutions in the single layer case, discussed in chapter 4. We therefore require that $\gamma_1 > 1$ and $\gamma_2 < 1$, so initially we set $\gamma_1 = 1.2$, $\gamma_2 = 0.5$, $F_1 = 0.45$ and $\alpha = 0.3$ in (6.6.1). We replace the far field equations (6.3.18)-(6.3.20) with the equations

$$u(q) = \gamma_1, \tag{6.6.11}$$

$$Y'(M) = 0, \tag{6.6.12}$$

$$Y'(M-1) = 0, \tag{6.6.13}$$

to ensure that the free surface is uniform far downstream. Typical solution profiles for

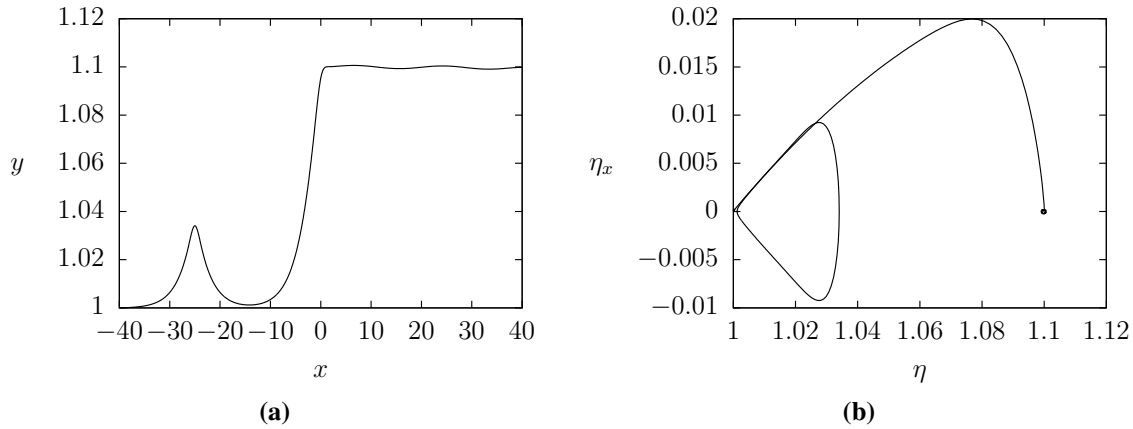

Figure 6.11: (a) shows a typical interfacial hydraulic fall profiles where the flow upstream is supercritical. In (a), $D > \sqrt{R}$, ($D = 2$ and $R = 0.6$). Two obstructions lie on the channel bottom, and are given by $A_2 = 0.05$, $A_1 = 0.01$ and $L_1 = L_2 = 1$. A solitary type wave is found over the additional obstruction, and the Froude number $F_1 = 0.58$ is found as part of the solution. The corresponding phase portraits for the solution profiles in (a) is shown in (b).

$\tau = 0.3, 0.4$ and 0.7 are shown in figure 6.12, alongside their fully nonlinear phase portraits. As the interfacial tension increases, we see that the steepness of the hydraulic fall decreases, so that, the change in depth of the interface begins further upstream. Therefore, as τ is increased further, a longer domain becomes necessary to obtain accurate solutions. Specifically, to ensure that the effects of truncating the domain, do not influence the solution. We sketch the upstream and downstream linear dispersion relations in figures 6.12(c) and 6.12(d) respectively. The horizontal lines represent the upstream and downstream Froude numbers in the lower layer in the solutions presented in figure (6.12(a)). We see that upstream, these horizontal lines do not intersect the linear dispersion relations, but downstream they do. Downstream of the hydraulic fall, small amplitude, numerical, spurious waves are sometimes found. Surprisingly, we find the wavelength of these spurious waves roughly corresponds to the wavelength that would be predicted by the linear dispersion relation. It is possible that truncating the integral equations far downstream, instead of calculating them for the infinite domain, has resulted in a form of artificial forcing downstream, which is causing these waves (see chapter 5 for further details). Our choice of far field equations (6.6.11)-(6.6.13) was chosen in order to try and minimise these spurious effects.

In figure 6.13 we show hydraulic fall profiles for smaller values of τ. As the interfacial tension is reduced, we see that a small elevation develops on the interface, immediately before the hydraulic fall. As the interfacial tension is reduced further, so that the Froude number F_1 approaches the minimum of the linear dispersion relation, the small elevation is seen to become part of a small train of decaying waves immediately before the fall.

The solution branch in the $F_1 - \tau$ plane is plotted in figure 6.14(a) for a given channel

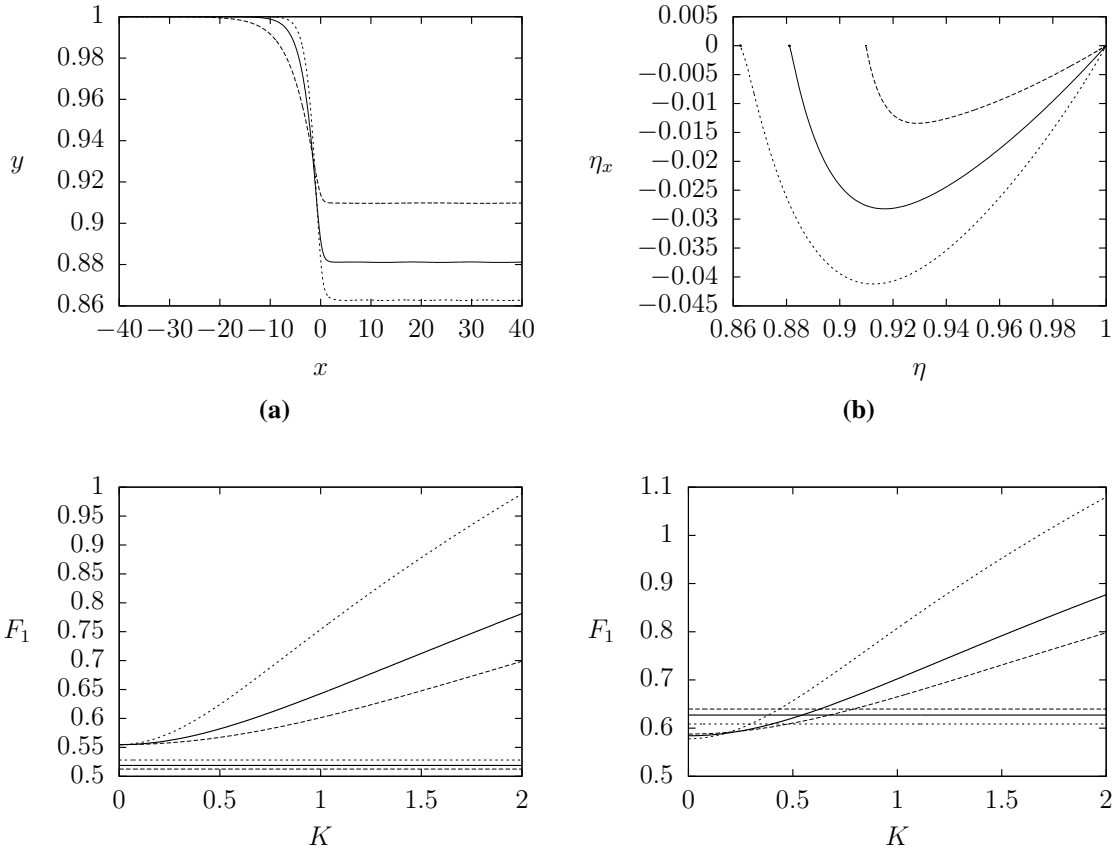

Figure 6.12: (a) Gravity-capillary hydraulic fall profiles for $\tau = 0.3$, $F_1 = 0.51$ (dotted line), $\tau = 0.4$, $F_1 = 0.52$ (solid line), and $\tau = 0.7$, $F_1 = 0.54$ (dashed line) over a submerged obstacle with $A_2 = 0.01$, $L_2 = 1$. (b) Fully nonlinear phase portraits corresponding to the solution profiles in (a). The corresponding upstream and downstream linear dispersion relations for each of the solution profiles in (a) are sketched in (c) and (d) respectively.

bottom configuration. As a longer domain is needed for increasing strengths of interfacial tension, the branch is only followed up to $\tau = 1.5$. By this point, on the domain given by $x \in [-40, 40]$, the flow has ceased to be uniform upstream, with the slope in the interface beginning even further upstream. The decrease in the steepness of the hydraulic fall as the interfacial tension increases, can clearly be seen in the hydraulic fall profiles in figure 6.14.

In the case of the free surface of a single layer of fluid, discussed in chapter 4, a turning point was found to exist on the $F - \tau$ branches of hydraulic fall solutions. It is possible that, if the domain were long enough, a turning point may also exist on the hydraulic fall solution branch, at a higher value of τ, in the case of the interface between two fluids. In such an event, two solutions with the same value of the Froude number, but different strengths of interfacial tension may exist, with one solution having a very gradual slope in the interface and the other being much steeper. Due to our current computational

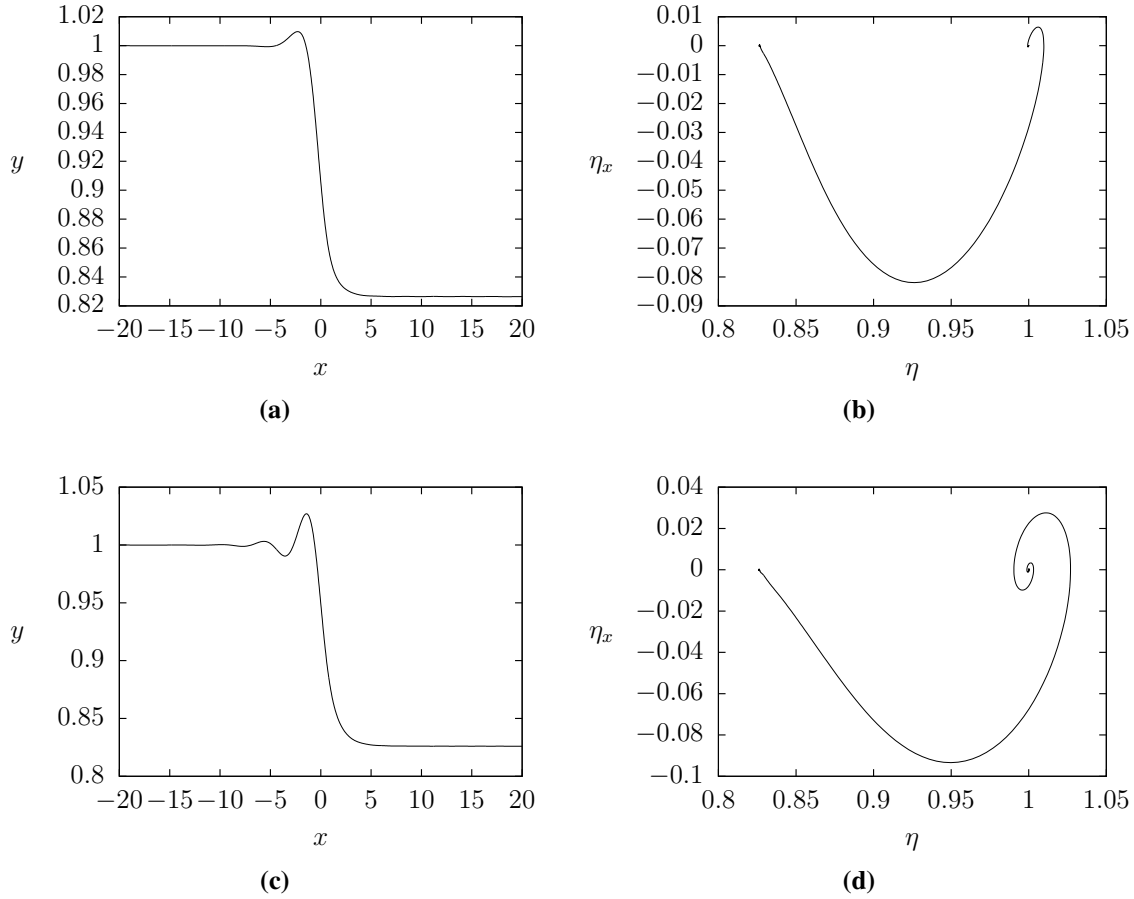

Figure 6.13: Hydraulic fall profiles over a submerged obstruction characterised by $A_2 = 0.1$, $L_2 = 1$ with (a) $\tau = 0.15$, $F_1 = 0.4997$ and (c) $\tau = 0.115$, $F_1 = 0.4995$. The corresponding fully nonlinear phase portraits are shown in (b) and (d), respectively.

limitations we have not managed to explore this possibility further, but as the results in this region are comparable to the single layer case in chapter 4, we speculate that such a turning point should exist.

Next, we seek interfacial solution profiles in this depth regime, over two submerged obstructions. Looking at the linear dispersion relations shown in figure 6.12(c) and 6.12(d), and considering the results of the single layer case presented in chapter 4, as the Froude number intersects the linear gravity-capillary dispersion relation downstream, we expect trapped waves to be obtained if we place the additional obstruction downstream. Unless the interfacial tension is very small, so that the upstream Froude number intersects the upstream linear dispersion relation, we will expect to find a solitary type wave over any additional obstruction upstream. In figure 6.15 we show a typical trapped wave solution, alongside the corresponding phase portrait and linear dispersion relation. Here, the additional obstruction downstream is centred at $x = 10$, and waves can be seen appearing between this obstruction and the hydraulic fall. We can see that the wavelength of these trapped waves is roughly $\lambda \approx 6.5 - 2.3 = 4.2$. In figure 6.15(c) we sketch the

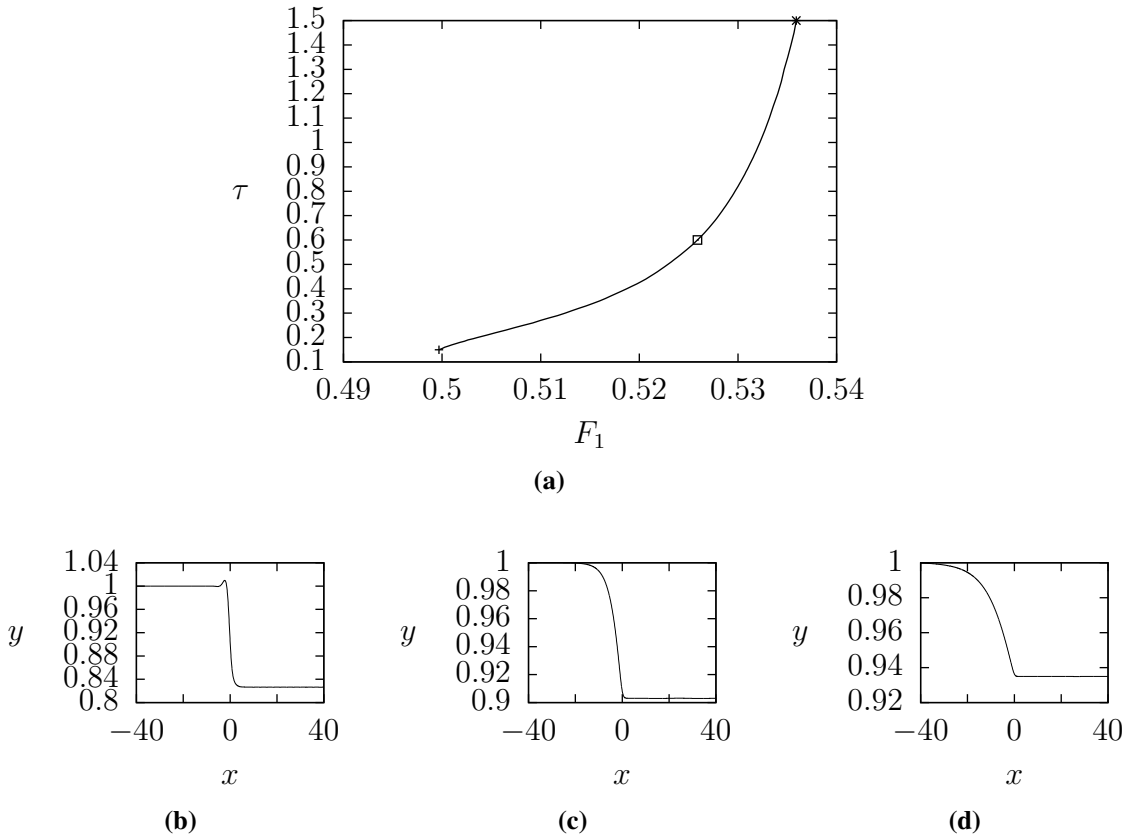

Figure 6.14: (a) Hydraulic fall solution branch in the $F_1 - \tau$ plane, over a submerged obstruction characterised by $A_2 = 0.01$, $L_2 = 1$. The points marked by the $+$, $\Box$ and $*$ correspond to the hydraulic fall profiles in (b)-(d), which from left to right correspond to $\tau = 0.15$, $\tau = 0.6$ and $\tau = 1.5$.

linear dispersion relation alongside the Froude number for the solution in 6.15(a). This shows us that the downstream Froude number intersects the downstream linear dispersion relation at $K \approx 1.54$. The linear theory therefore predicts that we should see waves with a wavelength of $\lambda \approx 4.08$ downstream. This is very close to the wavelength of the waves that we compute, and thus the linear theory supports our results.

Downstream of the second obstruction, it is clear that the interface is not actually uniform as we would expect, but a train of spurious waves exists. Again, the wavelength of these waves is in rough agreement with the linear theory; we see that the wavelength of these waves is approximately $\lambda = 27.20 - 23.28 = 3.99$ which is very close to the $\lambda \approx 4.08$ predicted by the linear theory.

As in the single layer case presented in chapter 4, we move the obstruction further downstream to see what effect this has on the solution profile. When there was just a single layer of fluid, we saw that only the number of waves trapped between the obstructions changed. The amplitude and wavelength of the waves remained consistent, and so the Froude number of the solution was shown to depend primarily on the obstruction under the hydraulic fall. We would expect to find similar phenomena here. However, upon

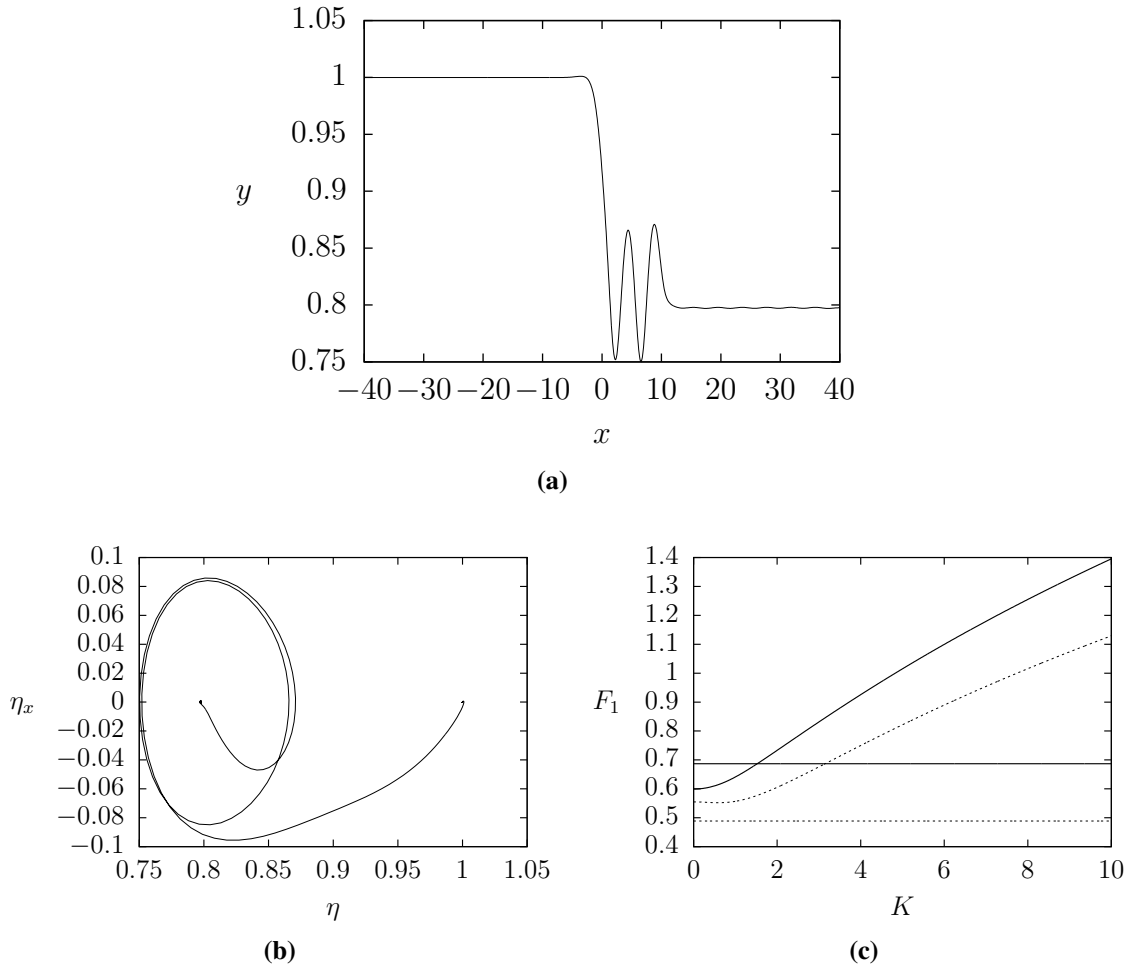

Figure 6.15: (a) Interfacial hydraulic fall profile with a train of trapped waves downstream. The interfacial tension is given by $\tau = 0.2$, and the two submerged obstructions are characterised by $A_i = 0.01$, $L_i = 1$ $(i = 1, 2)$. The Froude number $F_1 = 0.49$ is found as part of the solution. The density and depth ratios are given by $R = 0.6$ and $D = 2$ respectively. (b) shows the corresponding solution in the phase plane, and in (c) the linear dispersion relation both upstream (dashed lines) and downstream (solid lines) is shown.

moving the additional obstruction downstream, we see that F_1 increases. Therefore, the depth of the lower layer of fluid increases downstream, and the wavelength of the waves changes with the position of the second obstruction. Similarly, we found that in this rigid lid configuration, increasing the height of the second obstruction decreases the Froude number F_1, and thus, decreases the depth of the lower fluid downstream. Again, this is different to the single layer case in chapter 4, where the Froude number was dependent almost solely on the obstruction under the hydraulic fall. In figure 6.16 we show an example of this phenomenon for the case with $\tau = 0.4$. The linear dispersion relation in figure 6.16(b) shows that the downstream Froude number intersects the downstream dispersion relation at a smaller wavenumber when A_1 is increased, which will result in a greater wavelength. Similarly, when the second disturbance is moved further downstream, the

downstream Froude number intersects the linear dispersion relation at a larger wavenumber, resulting in waves with a smaller wavelength. However, we see that the difference in the wavelength is actually very small. In fact, just the addition of the second obstruction changes the Froude number. In the absence of an additional obstruction it can be shown that the flow in this configuration, with $\tau = 0.4$, has a Froude number of $F_1 = 0.519$, which is larger than the three different Froude numbers we have found for the different additional obstructions. The depth of the lower fluid downstream is therefore greater when there is just the one obstruction, over which the hydraulic fall occurs. The addition of the second obstruction has resulted in a larger fall, with a steeper gradient.

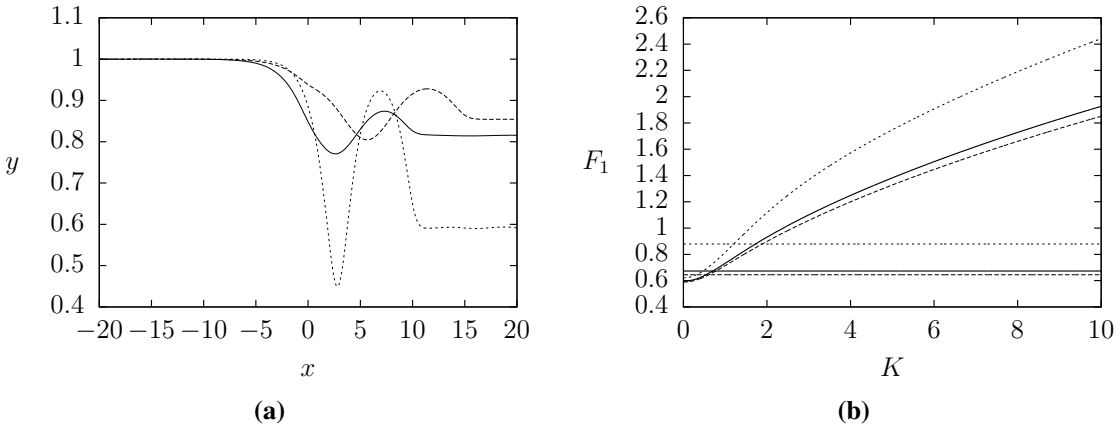

Figure 6.16: (a) Interfacial hydraulic fall profiles with trapped waves downstream. The interfacial tension is given by $\tau = 0.4$, and the two submerged obstructions are characterised by $A_1 = 0.01$ (solid and dashed lines), $A_1 = 0.05$ (dotted line) and $A_2 = 0.01$, $L_i = 1$ $(i = 1, 2)$. The downstream obstruction is centred at $x = 10$ in the solid and dotted line solutions, and at $x = 15$ in the dashed line solution. The upstream Froude numbers $F_1 = 0.496$ (solid line), $F_1 = 0.40$ (dotted line) and $F_1 = 0.51$ (dashed line) are found as part of the solution. The density and depth ratios are given by $R = 0.6$ and $D = 2$ respectively. In (b) the corresponding downstream linear dispersion relations for the solution profiles in (a) are shown.

At this point in the single layer case in chapter 4, we went on to consider the trapped wave solution branches in the $\tau - F$ plane, to determine that the trapped wave solutions were not in fact unique. We find that computing the solution branches in the $\tau - F_1$ plane in the rigid lid configuration is much harder. However, we have managed to find evidence that different solutions with the same value of the Froude number, F_1 and the same channel bottom configuration, but with different values of the Bond number τ, exist, as in the single layer case. We see that the solution profiles that we obtain are dependent on whether we compute the solution directly (i.e. we use an existing hydraulic fall profile with the same Bond number, and then simply add the additional obstacle to the channel bottom) or whether we iterate to the solution, using parameter continuation on the Bond number, from a different hydraulic fall solution profile. In figure 6.17 we sketch part of the solution branch in the $F_1 - \tau$ plane. The sketch is incomplete due to the current

computational limitations in obtaining solutions for larger values of τ. However, it does serve to show that a similar phenomenon to that observed for trapped waves in the single fluid flow configuration occurs. In figure 6.18 we show three solution profiles which have the same Bond number and the same underlying obstructions, but different values of the Froude number and different interfacial surfaces. It should be noted that there are small amplitude waves on the free surface downstream of the second obstruction, so these are actually generalised hydraulic fall solutions.

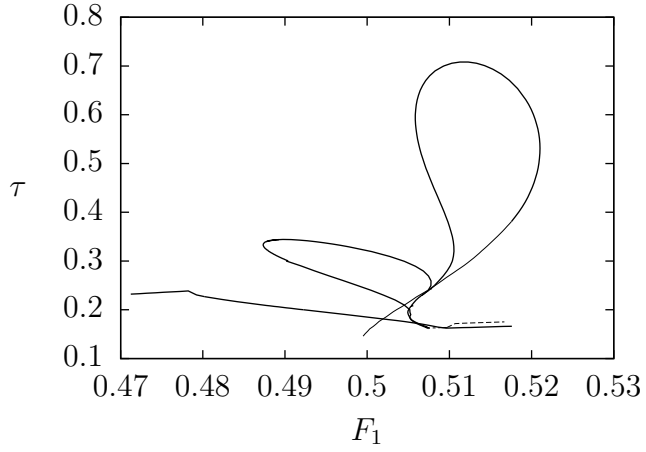

Figure 6.17: Trapped wave solutions in the $F_1 - \tau$ plane. The two submerged obstructions are characterised by $A_i = 0.01$, $L_i = 1$ $(i = 1, 2)$, where the additional obstruction is centred at $x = 15$. The density and depth ratios are given by $R = 0.6$ and $D = 2$ respectively, and the Froude number is such that $F < F_{\text{bif}}$.

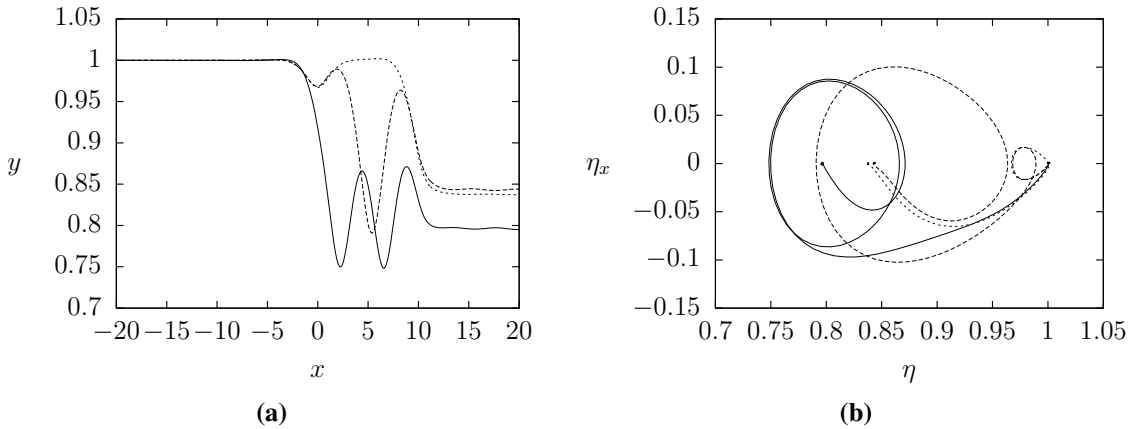

Figure 6.18: (a) Interfacial hydraulic fall profiles with trapped waves downstream. The interfacial tension is given by $\tau = 0.4$, and the two submerged obstructions are characterised by $A_i = 0.01$ and $L_i = 1$ $(i = 1, 2)$. The downstream obstruction is centred at $x = 10$, and the Froude numbers $F_1 = 0.488$ (solid line), $F_1 = 0.5035$ (dotted line) and $F_1 = 0.5059$ (dashed line) are found as part of the solution. The density and depth ratios are given by $R = 0.6$ and $D = 2$ respectively. In (b) the corresponding phase portraits for the solution profiles in (a) are shown.

Next, we add the additional obstacle to the flow configuration upstream. In figure 6.19

we show that, in this case, a solitary type depression wave appears over the additional obstruction. This is in agreement with the results presented in the single layer case in chapter 4. Interestingly, we see that, this time, the change in the Froude number from the single obstruction hydraulic fall solution to this two obstruction solution, is minimal. When the additional obstruction is placed upstream, we do not see much change in the downstream fluid depths. In terms of the linear analysis, the dispersion relation in figure 6.19(c) shows us that the upstream Froude number does not intersect the upstream linear dispersion relation in this case. However, we would expect that if the Froude number was to intersect the dispersion relation, a train of waves would appear upstream between the two obstructions, as we discovered in the single layer case.

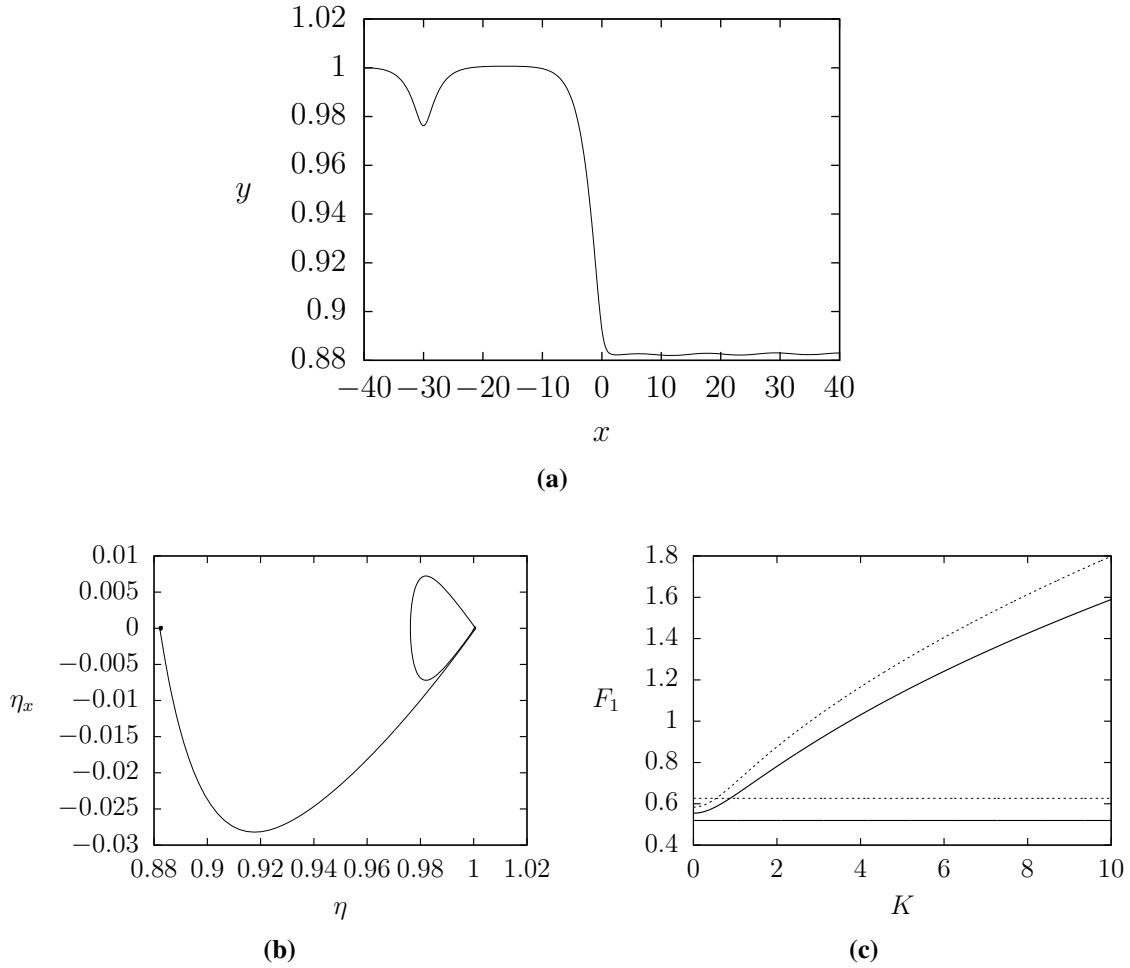

Figure 6.19: (a) Interfacial hydraulic fall profile with a depression wave upstream over a second obstruction. The interfacial tension is given by $\tau = 0.4$, and the two submerged obstructions are characterised by $A_i = 0.01$ and $L_i = 1$ $(i = 1, 2)$. The upstream obstruction is centred at $x = -30$, and the Froude numbers $F_1 = 0.519$ is found as part of the solution. The density and depth ratios are given by $R = 0.6$ and $D = 2$ respectively. In (b) the phase portrait corresponding to the solution in (a) is shown, and in (c) the upstream (solid line) and downstream (broken line) linear dispersion relations are shown alongside the upstream and downstream Froude numbers for the solution in (a).

6.6.3 Gravity-capillary solutions: Case 2

The hydraulic fall solution profile in the second case, where the flow upstream is supercritical and there exists a thick upper layer, is expected to be similar to the pure gravity interfacial solutions in this region. So, we require that $\gamma_1 < 1$ and $\gamma_2 > 1$. Initially, we set $\gamma_1 = 0.9$, $\gamma_2 = 1.2$, $F_1 = 0.55$ and $\alpha = 0.5$. We replace the far field equations (6.3.18)-(6.3.20) with the equations

$$u(1) = 1, \tag{6.6.14}$$

$$Y'(M) = 0, \tag{6.6.15}$$

$$Y'(M-1) = 0, \tag{6.6.16}$$

to ensure that the interface is uniform downstream. Then, indeed, we find solutions where the depth of the lower layer of fluid increases over the obstruction on the bottom of the channel. A typical solution profile is shown in figure 6.20(a), alongside its corresponding phase portrait in figure 6.20(b). However, as the interfacial tension is reduced, the Froude number F_1 approaches the minimum of the downstream linear dispersion relation, and a small train of decaying waves immediately after the increase in the lower fluid depth, is found. We show a typical solution profile and its corresponding fully nonlinear phase portrait in figures 6.20(c) and 6.20(d) respectively. In figure 6.21 we sketch the upstream and downstream linear dispersion relations for the solution profile in figure 6.20(a). One can see that upstream, the Froude number intersects the linear dispersion relation.

The solution branch in the $F_1 - \tau$ plane is plotted in figure 6.22(a). It shows that the Froude number increases as the interfacial tension decreases. As in the first case, increasing the interfacial tension decreases the steepness of the fall (see figures 6.22(b)-6.22(d)). We therefore require a longer domain in order to continue following the solution branch for higher values of the interfacial tension. Due to computational limitations, the solution branch here is only followed up to $\tau = 1$ for a domain in the region $x \in [-40, 40]$. The other end of the branch is followed down to $\tau = 0.19$, at which point the downstream Froude number is very close to the minimum of the linear dispersion relation.

Small numerical oscillations can be seen on the solution branch, for the larger values of τ, in figure 6.22(a). These waves are most likely due to the presence of the small numerical waves that sometimes appear upstream on the interface between the two fluids. As in the first case discussed in the previous section, where the numerical waves occurred downstream, these waves may be due to the truncation of the domain far upstream. This suggests that in order to remove or minimise the waves, our far field conditions (6.6.14)-(6.6.16) should actually include the conditions $Y'(1) = Y'(2) = 0$, to force the flow to be uniform upstream. However, we found that when we used such conditions, they did

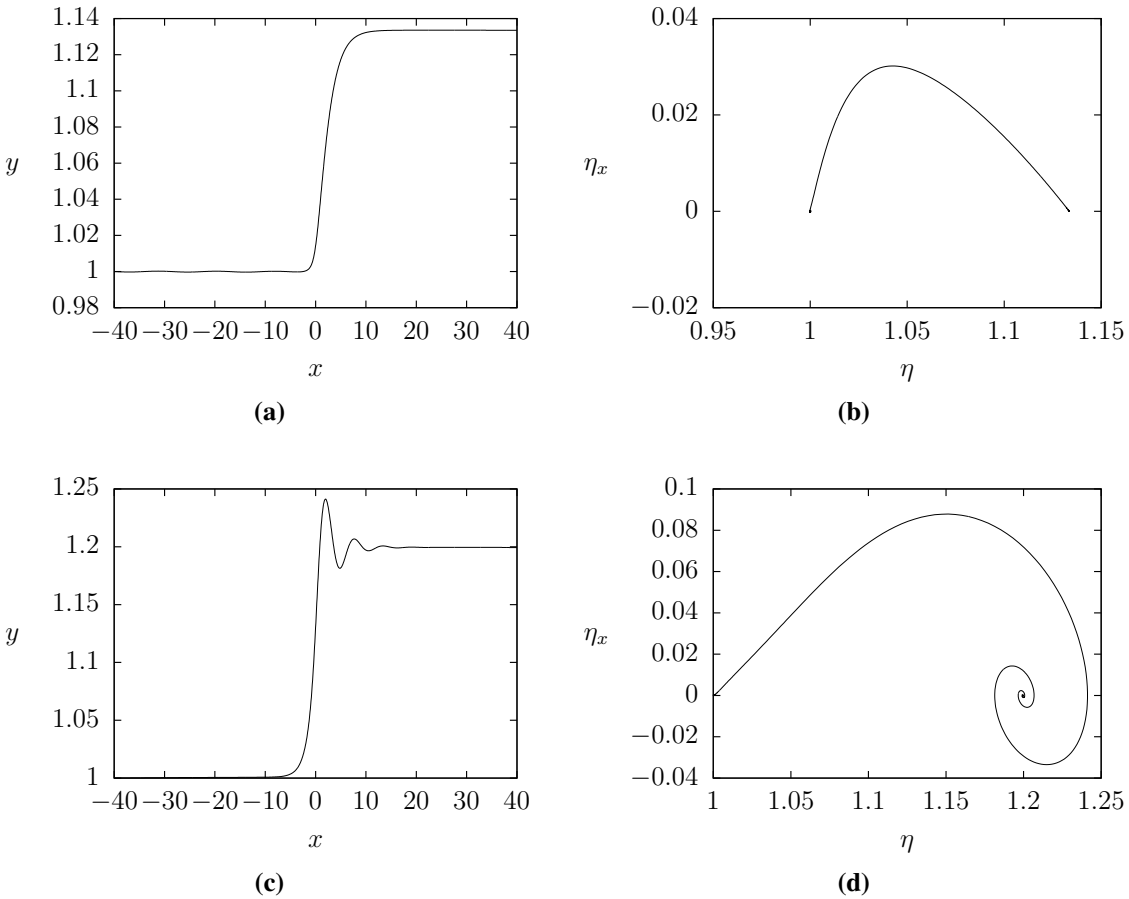

Figure 6.20: Hydraulic fall profiles over a submerged obstruction characterised by $A_2 = 0.01$, $L_1 = 1$ with (a) $\tau = 0.4$, $F_1 = 0.59$ and (c) $\tau = 0.19$, $F_1 = 0.6$. The corresponding fully nonlinear phase portraits are shown in (b) and (d), respectively.

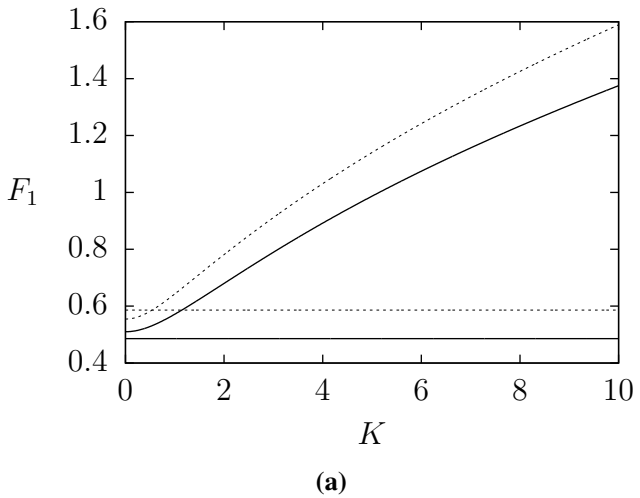

Figure 6.21: Upstream (broken curved line) and downstream (solid curved line) linear dispersion relations for the hydraulic fall profile shown in figure 6.20(a). The horizontal lines represent the values of the Froude number upstream (broken line) and downstream (solid line) in the solution profile.

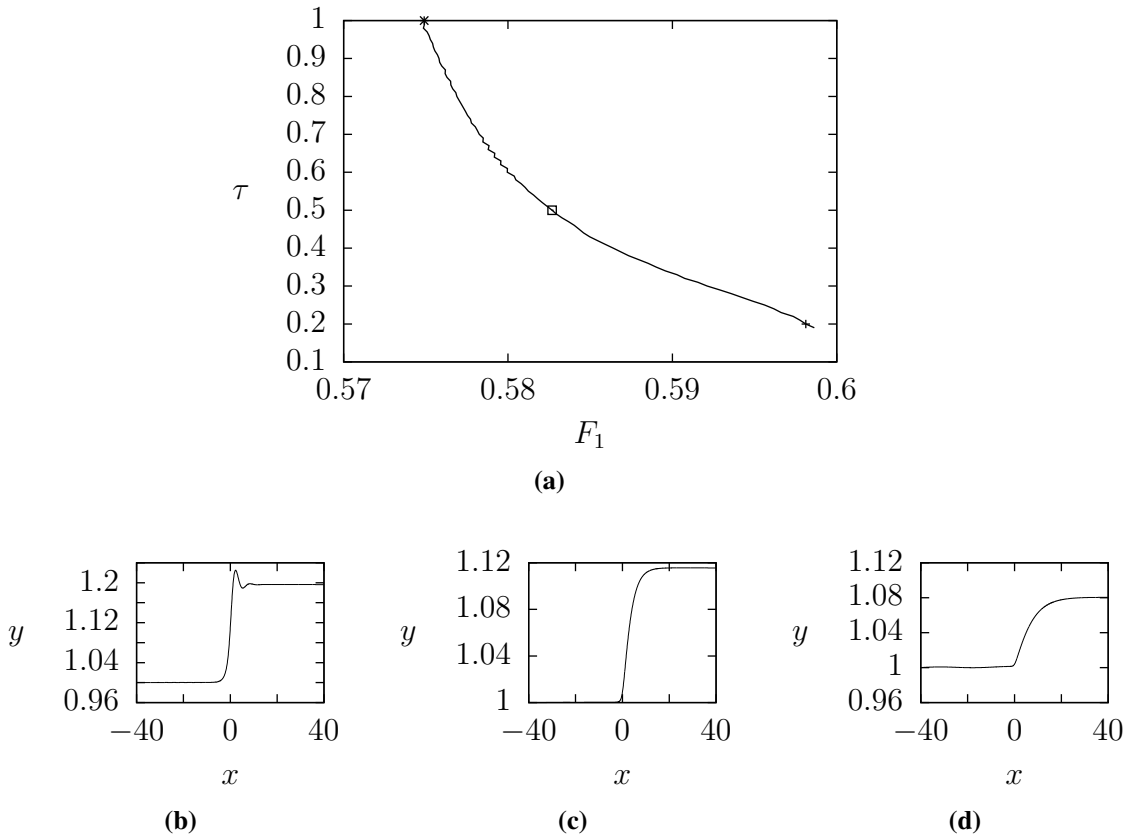

Figure 6.22: (a) Hydraulic fall solution branch in the $F_1 - \tau$ plane, over a submerged obstruction characterised by $A_2 = 0.01$, $L_2 = 1$. The points marked by $+$ $\square$ and $*$ correspond to the hydraulic fall profiles in (b)-(d), which from left to right correspond to $\tau = 0.2$, $\tau = 0.5$ and $\tau = 1$.

not always lead to a converged solution. It is possible that using a longer domain could also help to remove these waves, both on the solution branch shown in figure 6.22(a) and in the solution profiles, for example, shown in 6.22(d).

Next, we include an additional obstruction upstream of the hydraulic fall. The linear dispersion relation in figure 6.21(a) shows us that upstream, the Froude number F_1 intersects the upstream linear dispersion relation. Therefore, we would expect a train of trapped waves to appear between the two obstructions in this case. In figure 6.23 we show that this is indeed the case. Here, the additional obstacle is centred at $x = -30$. We find that the wavelength of these trapped waves is approximately $\lambda = 21 - 14.22 = 6.78$. In figure 6.23(c) we sketch the linear dispersion relations alongside the Froude numbers found for the solution in figure 6.23(a). The upstream dispersion relation shows that the upstream Froude number intersects the upstream linear dispersion relation at $K \approx 0.97$. The linear theory therefore predicts that upstream waves should have a wavelength of $\lambda \approx 6.48$. Again, this is very close to the wavelength that we observe in the solutions, and so the linear theory helps to support the existence of these upstream trapped waves.

As in the previous case, we have found evidence that there exist multiple trapped wave solutions, with the same value of the Froude number F_1 but different values of the Bond

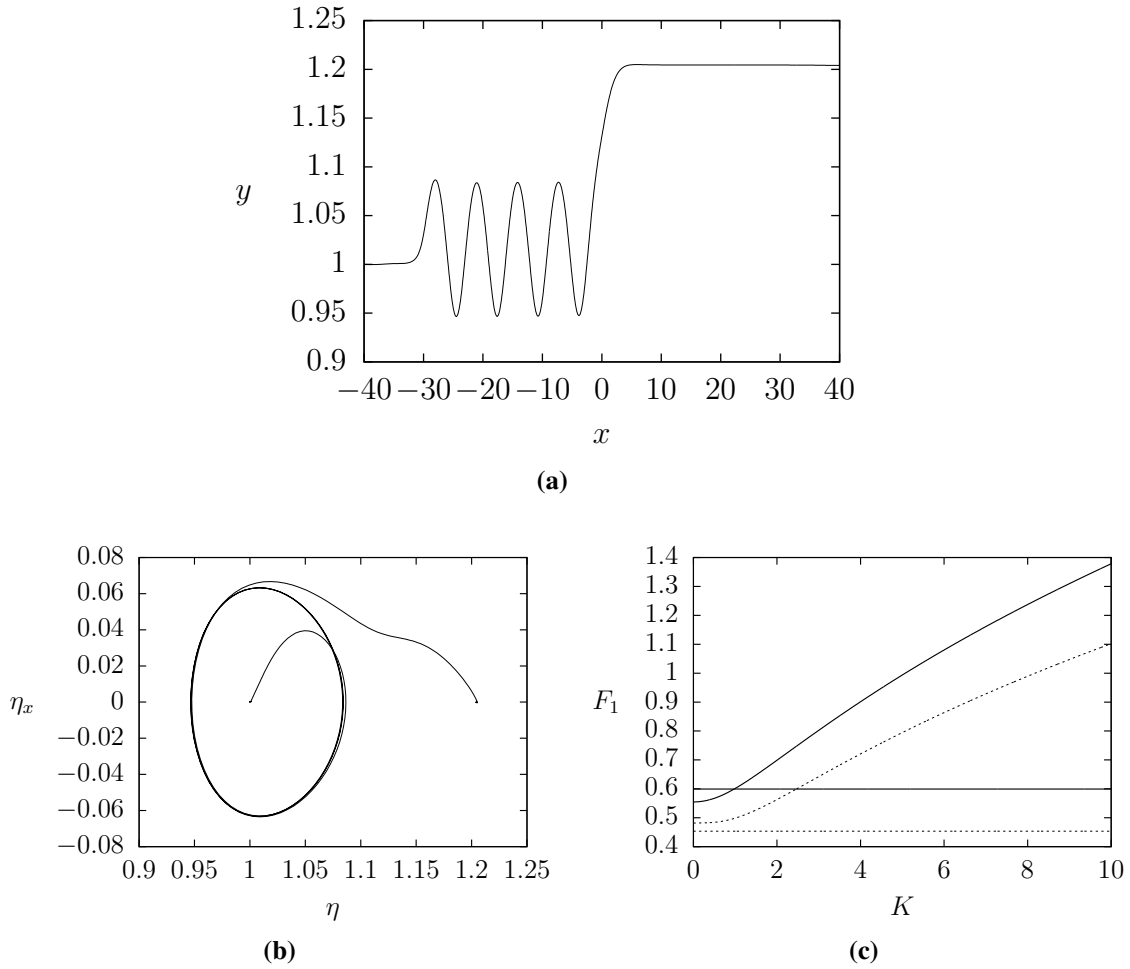

Figure 6.23: (a) Interfacial hydraulic fall solution profile with a train of trapped waves upstream. The interfacial tension is given by $\tau = 0.3$ and the two submerged obstructions are characterised by $A_i = 0.01$, $L_i = 1$ $(i = 1, 2)$. The Froude number $F_1 = 0.599$ is found as part of the solution. The density and depth ratios are $R = 0.6$ and $D = 2$, respectively. In (b) the same solution is drawn in the phase plane, and in (c), the linear dispersion relations both upstream (solid curve) and downstream (broken curve) are shown alongside the corresponding upstream and downstream Froude numbers for the solution profile shown in (a).

number τ. In figure 6.24 we sketch part of the solution branch in the $F_1 - \tau$ plane. Our current computational limitations mean that the sketch is incomplete and the accuracy of parts of the solution branches may need refining. Even so, the importance of the sketch in showing that the trapped wave solutions in this regime are not unique, is evident.

We now examine the effects of changing the size and position of the additional obstruction. We consider solutions where we place the additional obstruction used in figure 6.23(a) at $x = -15$ and $x = -12.5$ upstream, and a solution with the additional obstruction at $x = -12.5$ but with the obstruction height three times larger than the other two solutions. The solution profile in each case is plotted in 6.25(a). We see that again, the Froude number changes in each solution. This time, increasing the height of the additional obstruction increases the Froude number F_1, and thus, the depth of the lower

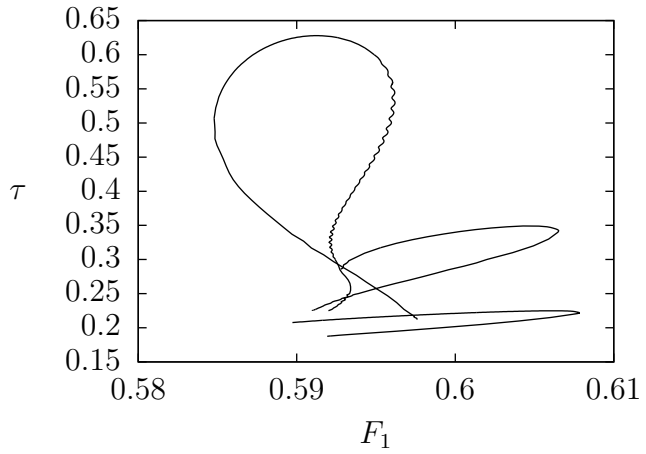

Figure 6.24: Trapped wave solutions in the $F_1 - \tau$ plane. The two submerged obstructions are characterised by $A_i = 0.01$, $L_i = 1$ $(i = 1, 2)$, where the additional obstruction is centred at $x = -15$. The density and depth ratios are $R = 0.6$ and $D = 2$, and the Froude number $F > F_{\text{bif}}$.

fluid downstream. This is the opposite to the phenomena observed in the first case with supercritical flow upstream and a thick upper layer, where increasing the obstacle height decreased the Froude number F_1. The increase in the Froude number here means that, as shown in figure 6.25(b), the linear theory predicts that the waves will have a greater wavenumber and thus a smaller wavelength for taller obstacles. We also see that changing the position of this additional obstruction has a small change on the Froude number F_1, resulting in a small change to the wavelength of the waves. In the same flow configuration in the absence of an additional obstruction, the Froude number is found to be $F_1 = 0.592$ which is smaller than the Froude numbers found in the trapped wave solutions. Although the difference in the Froude number is relatively small, it is large enough that the depth of the lower fluid downstream is significantly smaller. The second obstruction therefore appears to play an important role in determining the exact free surface profile obtained locally over the central submerged obstructions.

As the downstream Froude number does not intersect the downstream gravity-capillary linear dispersion relation in this regime, for example see figure 6.23(c), we expect that placing the additional obstruction downstream will result in a solitary type wave appearing over the additional obstruction. As the flow in the lower layer downstream is subcritical, we would expect that this solitary type wave is a wave of depression. In figure 6.26 we give a typical solution profile, where the additional obstruction is centred at $x = 12.5$, which shows that the result is as expected. However, it should be noted that, if the interfacial tension was small enough so that the downstream Froude number intersects the downstream linear dispersion relation, we would expect to find trapped waves between the two submerged obstructions.

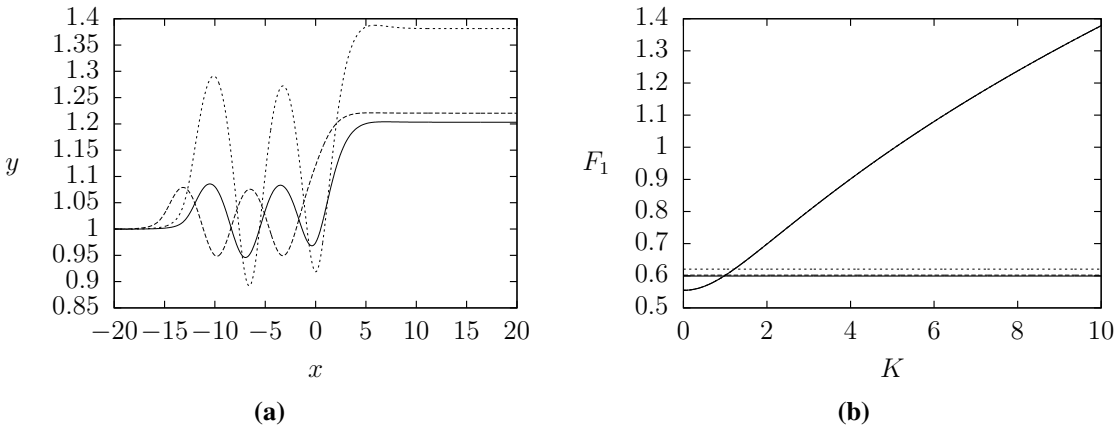

Figure 6.25: (a) Interfacial hydraulic fall solution profile with a train of trapped waves upstream. The interfacial tension is given by $\tau = 0.3$ and the central obstruction by $A_2 = 0.01$, $L_i = 1$ $(i = 1, 2)$. The additional obstruction upstream is centred at $x = -15$ with $A_1 = 0.01$ (dashed line), at $x = -12.5$ with $A_1 = 0.01$ (solid line), and at $x = -15$ with $A_1 = 0.03$ (dotted line). The Froude numbers $F_1 = 0.599$ (solid line), $F_1 = 0.602$ (dashed line) and $F_1 = 0.621$ (dotted line) are found as part of the solution. The density and depth ratios are $R = 0.6$ and $D = 2$. In (b) the upstream linear dispersion relation is plotted (solid curve), alongside the three values of the Froude number corresponding to the solutions in (a).

6.7 Conclusion

We have computed gravity and gravity-capillary critical flow solutions in the rigid-lid flow configuration, with a single submerged obstruction on the bottom of the channel. The four different types of pure gravity solutions, in either the thick upper layer or thick lower layer configurations, were already known (and computed by Dias and Vanden-Broeck [39]), but the gravity-capillary solutions are new. Where we have not computed a solution using the fully nonlinear boundary integral equation techniques, we have used a weakly nonlinear analysis, based on the fKdV equation, to show the possible interface in the given flow configuration. Solutions in the thick lower layer configuration proved to be much more difficult to compute than those with the thick upper layer, and so in the gravity-capillary case we restricted our study to the thick upper layer cases, leaving the remaining cases for future work.

We have shown that, if the interfacial tension is small enough, the gravity-capillary critical flow solutions have a small train of decaying waves on the interface immediately before (case one) or immediately following (case two) the change in fluid depths. Furthermore, we have speculated on the possibility that these critical gravity-capillary flows may not be unique. Unfortunately, due to our current computational limitations, we have been unable to investigate this possibility further.

We proceeded to present numerous pure gravity and gravity-capillary critical flow solutions in this two-layer, rigid-lid, flow configuration, with the addition of a second

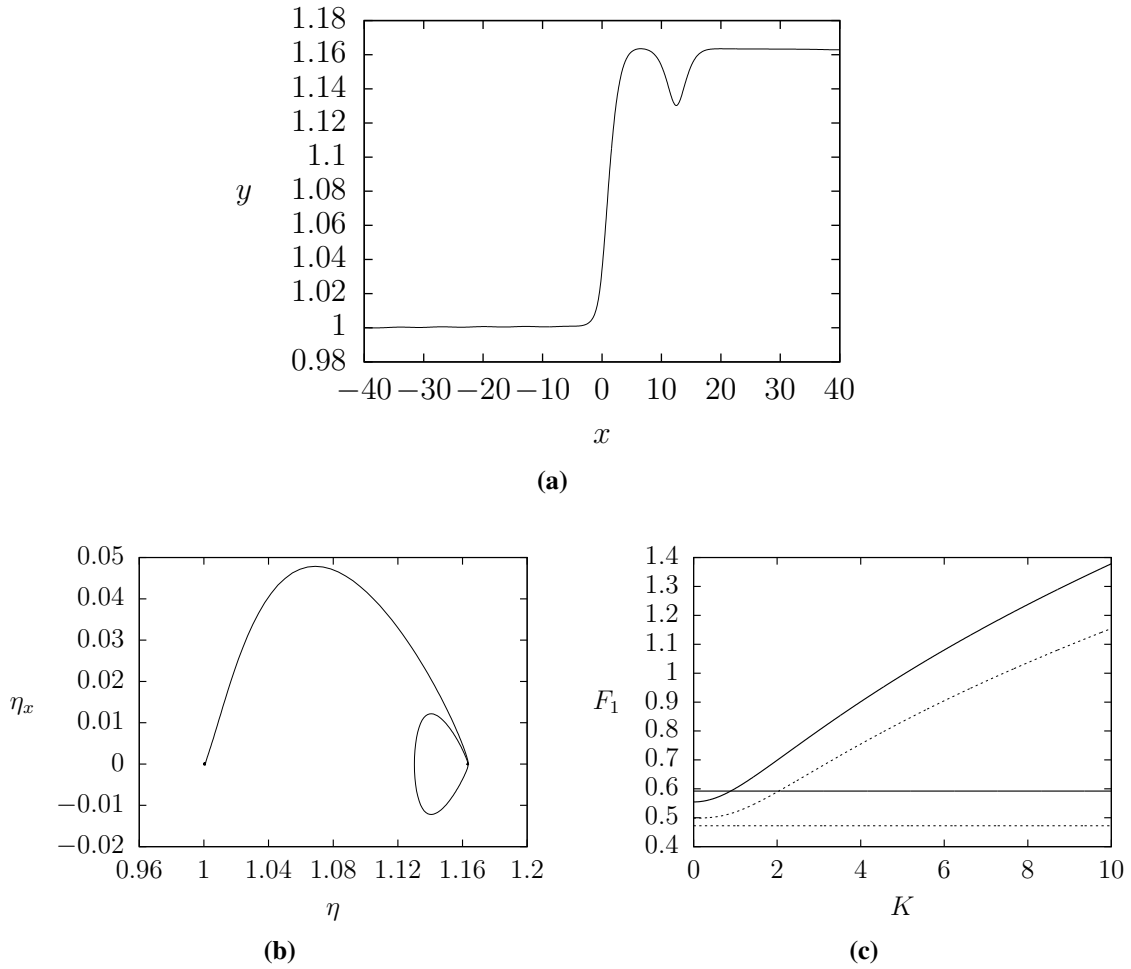

Figure 6.26: (a) Interfacial hydraulic fall solution profile with a solitary depression type wave downstream. The interfacial tension is given by $\tau = 0.3$ and the submerged obstructions are characterised by $A_i = 0.01$, $L_i = 1$ $(i = 1, 2)$. The Froude numbers $F_1 = 0.59$ is found as part of the solution. Here, $R = 0.6$ and $D = 2$. In (b) the same solution is drawn in the phase plane, and in (c) the upstream linear dispersion relation is plotted (solid curve), alongside the line $F = F_1 = 0.59$.

submerged obstruction on the bottom of the channel. The solutions, with and without surface tension, are new in this case. Using the ideas presented in chapter 4 we looked for trapped wave solutions by considering the lower fluid linear dispersion relations both up and downstream.

As shown by Dias and Vanden-Broeck in the pure gravity case, there may be further types of gravity-capillary hydraulic falls, requiring four independent parameters to characterise them. Dias and Vanden-Broeck showed that in the pure gravity, near critical case (i.e. $D \approx \sqrt{R}$), a stationary forced extended KdV equation was required for the weakly nonlinear analysis. This led to the derivation of a new critical value of the Froude number; $F_{\max}$. To provide a full picture of gravity-capillary hydraulic falls in the two-layer rigid lid approximation, the 'near critical' case would similarly have to be examined. As in the pure gravity case, we would expect to find new and different types of hydraulic fall

in this regime, and so the work presented in this chapter opens up this avenue for future research.

CHAPTER SEVEN

STABILITY OF HYDRAULIC FALLS

7.1 Introduction

In this chapter we consider the unsteady version of the problem presented in chapter 4. So, a single layer of ideal fluid in a channel of finite depth is considered, where both the effects of gravity and surface tension are taken into account. The submerged obstruction(s) on the bottom of the channel are assumed to move with time. The stability of forced solitary waves and conjugate flow solutions, which have subcritical flow upstream of the disturbance and supercritical flow downstream, are investigated. Initially, a steady solution is computed using the method outlined in chapter 4. This solution is then advanced forward in time using another modified version of the fully nonlinear boundary integral equation method discussed in chapter 3, alongside an Adams-Bashforth-Moulton scheme and a fourth-order Runge-Kutta algorithm. The evolution of the pure gravity solitary wave over a single submerged obstruction is examined with regard to the already known results, in order to ensure the accuracy of the time-stepping scheme employed in the conjugate flow case. Both the pure gravity and gravity-capillary hydraulic fall solutions obtained in chapter 4 are evolved in time, and conjectures then made as to their stability. Small perturbations to the initial steady solutions are utilised to further test these conjectures.

The fully nonlinear problem is formulated in section 7.2. Section 7.3 then describes the numerical scheme, and the results are presented in section 7.4. Finally, in section 7.5 a summary of the chapter is provided, and conclusions are drawn.

7.2 Formulation

An incompressible, inviscid, two-dimensional fluid in a channel of finite depth is considered. On the bottom of the channel one or more arbitrarily shaped submerged obstacles move to the left with speed U. Fixed Cartesian coordinates (x^*, y^*) are introduced and the x^*-axis is aligned with the flat channel bottom in the absence of the obstructions. The y^*-axis is directed vertically upwards. The origin is the initial position of one of the obstructions at time $t = 0$. The influences of gravitational acceleration g in the negative y^* direction and capillarity are included, where σ is the coefficient of surface tension on the free surface. The flow is assumed to be irrotational so that equations (3.2.1) and (3.2.2) are satisfied. Thus, there exists a velocity potential $\phi^*(x^*, y^*, t^*)$ and a stream function $\psi^*(x^*, y^*, t^*)$ satisfying (3.2.3), (3.3.4) and

$$\nabla^2 \phi^* = 0, \tag{7.2.1}$$

in the fluid domain. The positions of the free surface and channel bottom are $y^* = H + \eta^*(x^*, t^*)$ and $y^* = B^*(x^*, t^*)$, respectively. The time-dependent governing equations are

$$B^*_{t^*} + \phi^*_{x^*} B^*_{x^*} = \phi^*_{y^*} \qquad \text{on} \quad y^* = B^*(x^*, t^*), \tag{7.2.2}$$

$$\eta^*_{t^*} + \phi^*_{x^*} \eta^*_{x^*} = \phi^*_{y^*} \qquad \text{on} \quad y^* = H + \eta^*(x^*, t^*), \tag{7.2.3}$$

$$\phi^*_{t^*} + \frac{1}{2}(\phi^{*2}_{x^*} + \phi^{*2}_{y^*}) + g y^* - \frac{1}{\rho}\sigma\kappa^* = 0 \qquad \text{on} \quad y^* = H + \eta^*(x^*, t^*). \tag{7.2.4}$$

Physically, when a submerged obstruction moves through a fluid at rest, one requires that as $x^* \to \pm\infty$, any disturbances decay to zero and the fluid should be at rest. However, hydraulic fall solutions require that, locally, the depth and speed of the fluid are different far upstream and downstream. We define the constant fluid depth upstream by h and the constant upstream velocity by $V - U$. Downstream the constant fluid depth is $H < h$ and the fluid is at rest. In order to overcome this discontinuity in the flow, either up or downstream, we consider the work of Donahue and Shen [45]. Using a fKdV equation and the domain $-W < x^* < W$, where W is some constant, they let their stationary hydraulic fall solution lie in the region $-W/2 < x^* < W/2$. In order to satisfy the physical boundary condition that the flow is uniform and at rest as $x^* \to \pm\infty$, a jump must occur somewhere up or downstream in the flow. This jump must occur at $\pm W/2$. Donahue and Shen simulated the discontinuity created at the jump and found that this led to a disturbance propagating in both directions. However, provided W was large enough, they showed that this disturbance can be ignored when considering just the flow near the obstruction. We therefore assume that the interval $-W/2 < x^* < W/2$ is infinite, and let the additional jump and discontinuity start at $x^* = -\infty$. At $x^* = \pm\infty$ we can then

impose the hydraulic fall boundary conditions, and examine the flow near the obstacle. Physically, one could choose to view the problem as a moving submerged obstacle pushing a bulk of fluid upstream (with speed $V - U$) in a fluid otherwise at rest. One could then assume that there exists a sink at $x^* = -\infty$, from which this bulk of fluid could exit the system.

Next, we non-dimensionalise the equations by taking U as unit speed and H as unit length. Then, we see that the scaling for the time t is given by

$$t^* \to \frac{H}{U} t. \tag{7.2.5}$$

Unstarred variables are thus now understood to be dimensionless. The dimensionless flow configuration is sketched in figure 7.1. One can see that the dimensionless upstream flow velocity is given by $(V - U)/U = \gamma - 1$. Following the method applied in chapter 4, conservation of mass then tells us that the upstream fluid depth must be $1/\gamma$.

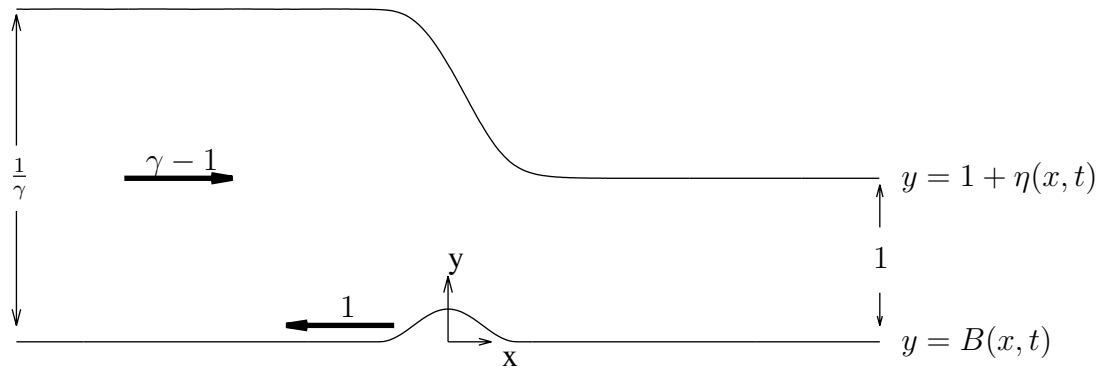

Figure 7.1: Dimensionless unsteady flow configuration over an arbitrary obstacle on the bottom of the channel.

To proceed, we follow the approaches of Longuet-Higgins and Cokelet [76] and Cooker *et al.* [32], who used mixed Eulerian-Lagrangian methods. We therefore write $(x, y) = (x, 1+\eta(x,t)) = (X(\xi,t), Y(\xi,t))$ and $\phi(x, 1+\eta(x,t), t) := \phi(X(\xi,t), Y(\xi,t), t) := \Phi(s,t)$ on the free surface, where ξ is the fluid particle label. The coordinates on the channel bottom can be denoted $(x(t), y(t)) = (x(t), B(x,t))$. The kinematic and dynamic conditions on the free surface are then expressed in Lagrangian form as

$$\frac{DX}{Dt} = \frac{\partial \phi}{\partial x}, \tag{7.2.6}$$

$$\frac{DY}{Dt} = \frac{\partial \phi}{\partial y}, \tag{7.2.7}$$

$$F^2 \frac{D\phi}{Dt} = \frac{F^2}{2}\left(\left(\frac{\partial \phi}{\partial x}\right)^2 + \left(\frac{\partial \phi}{\partial y}\right)^2\right) - Y + \tau\kappa, \tag{7.2.8}$$

where $D/Dt = \partial/\partial t + \nabla\phi \cdot \nabla$ is the material derivative, κ is the curvature of the free surface defined by (1.2.20), and the dimensionless Froude number F and Bond number τ are those defined in (2.1.6) and (2.1.2) respectively. On the channel bottom we have the dimensionless kinematic boundary condition

$$B_t + \phi_x B_x = \phi_y \text{ on } y = B(x,t). \tag{7.2.9}$$

Thus, we have three equations (7.2.6)-(7.2.8) which provide a means to advance a solution forward in time. Firstly however, the partial derivatives ϕ_x and ϕ_y on the free surface must be rewritten in terms of the tangential and normal velocity derivatives. Therefore, we write

$$\mathbf{u} = u\mathbf{i} + v\mathbf{j} = \phi_x\mathbf{i} + \phi_y\mathbf{j} = \bar{\phi}_s\mathbf{t} + \bar{\phi}_n\mathbf{n}, \tag{7.2.10}$$

where **t** and **n** are the unit vectors in the tangential and normal (out of the fluid) directions respectively. We parametrise the free surface by writing $x = X(\xi), y = Y(\xi)$, so that the tangential and normal unit vectors become

$$\mathbf{t} = \left(\frac{X'}{\sqrt{X'^2 + Y'^2}}, \frac{Y'}{\sqrt{X'^2 + Y'^2}}\right), \tag{7.2.11}$$

$$\mathbf{n} = \left(\frac{-Y'}{\sqrt{X'^2 + Y'^2}}, \frac{X'}{\sqrt{X'^2 + Y'^2}}\right), \tag{7.2.12}$$

where the $'$ denotes the derivative with respect to ξ. Thus, substituting (7.2.11) and (7.2.12) into (7.2.10) we obtain

$$\mathbf{u} = \bar{\phi}_s\left(\frac{X'}{\sqrt{X'^2 + Y'^2}}\mathbf{i} + \frac{Y'}{\sqrt{X'^2 + Y'^2}}\mathbf{j}\right) + \bar{\phi}_n\left(\frac{-Y'}{\sqrt{X'^2 + Y'^2}}\mathbf{i} + \frac{X'}{\sqrt{X'^2 + Y'^2}}\mathbf{j}\right). \tag{7.2.13}$$

Here, $\bar{\phi}_s$ denotes the derivative of ϕ with respect to the arclength of the free surface. Therefore, using (7.2.10) we must have

$$\phi_x = \frac{\bar{\phi}_s X' - \bar{\phi}_n Y'}{\sqrt{X'^2 + Y'^2}} \quad \text{and} \quad \phi_y = \frac{\bar{\phi}_s Y' + \bar{\phi}_n X'}{\sqrt{X'^2 + Y'^2}}. \tag{7.2.14}$$

Multiplying (7.2.14) by X' and Y' respectively and adding the results implies that

$$X'\phi_x + Y'\phi_y = \bar{\phi}_s\left(\frac{X'^2 + Y'^2}{\sqrt{X'^2 + Y'^2}}\right), \tag{7.2.15}$$

and thus,

$$\bar{\phi}_s = \frac{X'\phi_x + Y'\phi_y}{\sqrt{X'^2 + Y'^2}}. \tag{7.2.16}$$

Similarly, we can find that

$$\bar{\phi}_n = \frac{-Y'\phi_x + X'\phi_y}{\sqrt{X'^2 + Y'^2}}. \tag{7.2.17}$$

Next, we define the scaled derivatives in the tangential and normal directions by

$$\phi_s = \bar{\phi}_s\sqrt{X'^2 + Y'^2} \quad \text{and} \quad \phi_n = \bar{\phi}_n\sqrt{X'^2 + Y'^2}, \tag{7.2.18}$$

respectively. Then, substituting (7.2.18) into (7.2.14), (7.2.16) and (7.2.17) we obtain

$$\phi_x = \frac{\phi_s X' - \phi_n Y'}{X'^2 + Y'^2} \quad \text{and} \quad \phi_y = \frac{\phi_s Y' + \phi_n X'}{X'^2 + Y'^2}, \tag{7.2.19}$$

$$\phi_s = \phi_x X' + \phi_y Y' \quad \text{and} \quad \phi_n = \phi_y X' - \phi_x Y'. \tag{7.2.20}$$

If we define $\bar{\phi}(\xi) = \phi(X(\xi), Y(\xi))$, so that $\bar{\phi}_\xi = \phi_x X' + \phi_y Y'$. Then, using (7.2.20) we see that $\bar{\phi}_\xi = \phi_s$.

As we seek hydraulic falls, the flow must be uniform in the far field away from the obstructions. We must therefore also impose the conditions

$$\nabla\phi \to 0 \qquad \text{as } x \to \infty, \tag{7.2.21}$$

$$\nabla\phi \to \gamma - 1 \text{ as } x \to -\infty. \tag{7.2.22}$$

This completes the formulation of the problem. We need to find the unknown functions $\phi(x, y, t)$ and $\eta(x, y, t)$.

7.3 Numerical Scheme

To solve the system of nonlinear equations numerically, we employ a modified form of the boundary integral scheme used by Cooker *et al.* [32], Grimshaw, Maleewong and Asavanant [62] and Grimshaw and Maleewong [61].

At time $t = 0$ we begin by computing a steady, fully nonlinear hydraulic fall solution, using the scheme outlined in chapter 4, where the channel bottom is fixed and the fluid flows past the obstacle from left to right. We then consider the relationship between the variables in the steady and unsteady cases in order to obtain the unsteady variables X, Y and ϕ_s on the free surface at $t = 0$, and an initial guess for ϕ_x on the channel bottom. We

denote variables in the steady case with a hat ($\hat{}$), so that in dimensional form,

$$\hat{\phi}^* = \phi^* + U\hat{x}^*, \quad \hat{x}^* = x^* + Ut^*, \quad \hat{B}^*(\hat{x}^*) = B^*(x^*, t^*). \tag{7.3.1}$$

Then,

$$\hat{\phi}^*_{\hat{x}^*} = \phi^*_{x^*} + U, \quad \phi^*_{t^*} = \hat{\phi}^*_{\hat{x}^*}\hat{x}^*_{t^*} - U\hat{x}^*_{t^*} = U(\hat{\phi}^*_{\hat{x}^*} - U), \tag{7.3.2}$$

$$\hat{B}^*_{\hat{x}^*} = {B^*}_{x^*}, \qquad B^*_{t^*} = \hat{B}^*_{\hat{x}^*}U. \tag{7.3.3}$$

In the far field, as $x^* \to -\infty$, we have that $\hat{\phi}^*_{\bar{s}^*} \to U$ and $\phi^*_{\bar{s}^*} \to 0$ on the free surface, and $\hat{\phi}^*_{\hat{x}^*} = \hat{u}^* \to U$ and $\phi^*_{x^*} = u \to 0$ on the channel bottom. Therefore, after non-dimensionalising with respect to U, we obtain the relations

$$\phi_{\bar{s}} = \hat{\phi}_{\bar{s}} - 1 \quad \text{and} \quad u = \hat{u} - 1. \tag{7.3.4}$$

Using (7.2.18), we can therefore obtain ϕ_s from $\hat{\bar{\phi}}_s$;

$$\phi_s = (\hat{\bar{\phi}}_s - 1)\sqrt{X'^2 + Y'^2}. \tag{7.3.5}$$

On the channel bottom we obtain $\hat{\phi}_{\hat{x}}$ from the steady solution, so we need to find ϕ_x in terms of $\hat{\phi}_x$. But this is just equation (7.3.4).

Next, using the dimensionless form of (7.3.3), the kinematic equation (7.2.9) on the channel bottom can be rewritten so that

$$\hat{B}_{\hat{x}} + \phi_x\hat{B}_{\hat{x}} = \phi_y, \tag{7.3.6}$$

$$\Rightarrow \phi_y = \hat{B}_{\hat{x}}(1 + \phi_x) = \hat{B}_{\hat{x}}\hat{\phi}_{\hat{x}} = \hat{B}_{\hat{x}}\hat{u}, \tag{7.3.7}$$

and using $\hat{B}_{\hat{x}} = B_x$,

$$\phi_y = B_x(1 + \phi_x). \tag{7.3.8}$$

At time $t = 0$ we know $\hat{Y}$, $\hat{X}$, $\hat{\bar{\phi}}_{\hat{s}}$, $\hat{u}$ and $\hat{B}$ from the steady solution. We can then obtain the corresponding unsteady variables using equations (7.3.1) and (7.3.5) to find X and ϕ_s on the free surface, and (7.3.4) to find an initial guess for ϕ_x on the channel bottom. We also have that $Y = \hat{Y}$ and $B = \hat{B}$ initially. By numerically integrating ϕ_s, using the trapezoidal rule, we obtain ϕ on the free surface at $t = 0$. The variables B_x, X', X'', Y' and Y'' at $t = 0$ are obtained by numerical differentiation.

The remaining unknowns at $t = 0$ are ϕ_n on the free surface and ϕ_x on the channel bottom. We find them by deriving two integral differential equations. We let the evaluation point $z = X(s,t) + iY(s,t)$ be on the free surface, and $z^* = x^* + iy^*$ be the

varying point on the contour $\mathcal{C}$, consisting of the free surface, the channel bottom, and lines joining them at $x = \pm L$ in the limit as $L \to \infty$. Note that here, the starred variables are not dimensional variables. Thus, $z^* = X(s^*, t) + iY(s^*, t) = X^* + iY^*$ on the free surface, and $z^* = x^* + iB(x^*) = x^* + iB^*$ on the channel bottom. Cauchy's integral formula in principal value form is applied to the function

$$\chi = \frac{dw}{dz} = \phi_x - i\phi_y, \tag{7.3.9}$$

around the contour $\mathcal{C}$, where $w(z,t) = \phi(x,y,t) + i\psi(x,y,t)$ is the complex potential and $\psi(x,y,t)$ is the stream function. Using (7.2.19) we know that

$$\chi = \frac{(\phi_s X' - \phi_n Y') - i(\phi_s Y' + \phi_n X')}{X'^2 + Y'^2}, \tag{7.3.10}$$

on the free surface. We obtain:

$$w(z) = \frac{1}{\pi i}\int_{\mathcal{C}} \frac{w(z^*)}{z^* - z} dz^*, \tag{7.3.11}$$

$$\Rightarrow (\phi_s - i\phi_n)\frac{(X' - iY')}{(X'^2 + Y'^2)} = \frac{1}{\pi i}\int_{\mathcal{C}} \frac{w(z^*)}{z^* - (X + iY)} dz^*. \tag{7.3.12}$$

Next, we multiply (7.3.12) by $i(X' + iY')$ to obtain

$$i\phi_s + \phi_n = \frac{1}{\pi}\int_{\mathcal{C}} \frac{w(z^*)(X' + iY')}{z^* - (X + iY)} dz^*, \tag{7.3.13}$$

$$= -\frac{1}{\pi} I_1 + \frac{1}{\pi} I_2, \tag{7.3.14}$$

where

$$I_1 = \int_{-\infty}^{\infty} \frac{(\phi^*_{s^*} - i\phi^*_{n^*})(X'^* - iY'^*)(X' + iY')(X'^* + iY'^*)}{(X'^{*2} + Y'^{*2})(X^* + iY^* - (X + iY))} ds^*, \tag{7.3.15}$$

$$= -\int_{-\infty}^{\infty} \frac{(\phi^*_{s^*} - i\phi^*_{n^*})(X' + iY')((X^* - X) - i(Y^* - Y))}{(X^* - X)^2 + (Y^* - Y)^2} ds^*, \tag{7.3.16}$$

and

$$I_2 = \int_{-\infty}^{\infty} \frac{(\phi^*_{x^*} - i\phi^*_{y^*})(X' + iY')}{(x^* - X) + i(y^* - Y)} dz^*, \tag{7.3.17}$$

$$= \int_{-\infty}^{\infty} \frac{(\phi^*_{x^*} - i\phi^*_{y^*})(X' + iY')((x^* - X) - i(y^* - Y))(1 + iB^*_{x^*})}{(x^* - X)^2 + (y^* - Y)^2} dx^*, \tag{7.3.18}$$

$$= \int_{-\infty}^{\infty} \frac{(\phi^*_{x^*} - iB^*_{x^*}(1 + \phi^*_{x^*}))A(x^*, y^*)(1 + iB^*_{x^*})}{(x^* - X)^2 + (y^* - Y)^2} dx^*, \tag{7.3.19}$$

$$= \int_{-\infty}^{\infty} \frac{((\phi^*_{x^*}(1 + B^{*2}_{x^*}) + B^{*2}_{x^*}) - iB^*_{x^*})A(x^*, y^*)}{(x^* - X)^2 + (y^* - Y)^2} dx^*. \tag{7.3.20}$$

Here, $A(x^*, y^*) = (X'(x^* - X) + Y'(y^* - Y)) + i(Y'(x^* - X) - X'(y^* - Y))$ and we have used equation (7.3.8) at a given time, and the fact that $dz^* = (X'^* + iY'^*)ds^*$ on the free surface, and $dz^* = (1 + iB^*_{x^*})dx^*$ on the channel bottom. We take the real part of (7.3.14) in order to find ϕ_n, and note that $y^* = B^*$ on the channel bottom. The integral equation is therefore given by

$$\phi_n = -\frac{1}{\pi}\int_{-\infty}^{\infty} \frac{\phi^*_{s^*}(X'(X^* - X) + Y'(Y^* - Y)) + \phi^*_{n^*}(Y'(X^* - X) - X'(Y^* - Y))}{(X^* - X)^2 + (Y^* - Y)^2} ds^* + \frac{1}{\pi}\int_{-\infty}^{\infty} \frac{(\phi^*_{x^*}(1 + B^{*2}_{x^*}) + B^{*2}_{x^*})(X'(x^* - X) + Y'(B^* - Y)) + D(x^*, y^*)}{(x^* - X)^2 + (B^* - Y)^2} dx^* \tag{7.3.21}$$

where $D(x^*, y^*) = B^*_{x^*}(Y'(x^* - X) - X'(B^* - Y))$.

We can similarly obtain a second integral equation by applying Cauchy's integral formula to the complex velocity potential around the contour $\mathcal{C}$, but this time letting $z = x + iy$ be on the channel bottom. We obtain

$$I = w(z) = \phi_x - i\phi_y = \frac{1}{\pi i}\int_c \frac{w(z^*)}{z^* - z} dz^*, \tag{7.3.22}$$

$$= -\frac{1}{\pi i}\hat{I}_1 + \frac{1}{\pi i}\hat{I}_2, \tag{7.3.23}$$

where,

$$\hat{I}_1 = \int_{-\infty}^{\infty} \frac{(\phi^*_{s^*} - i\phi^*_{n^*})(X'^* - iY'^*)(X'^* + iY^*)}{(X'^{*2} + Y'^{*2})((X^* - x) + i(Y^* - B))} ds^*, \tag{7.3.24}$$

$$= \int_{-\infty}^{\infty} \frac{(\phi^*_{s^*} - i\phi^*_{n^*})((X^* - x) - i(Y^* - B))}{(X^* - x)^2 + (Y^* - B)^2} ds^*, \tag{7.3.25}$$

$$= \int_{-\infty}^{\infty} \frac{(\phi^*_{s^*}(X^* - x) - \phi^*_{n^*}(Y^* - B)) - i(\phi^*_{s^*}(Y^* - B) + \phi^*_{n^*}(X^* - x))}{(X^* - x)^2 + (Y^* - B)^2} ds^*, \tag{7.3.26}$$

and

$$\hat{I}_2 = \int_{-\infty}^{\infty} \frac{(\phi^*_{x^*} - i\phi^*_{y^*})(1 + iB^*_{x^*})}{(x^* - x) + i(B^* - B)} dx^* \tag{7.3.27}$$

$$= \int_{-\infty}^{\infty} \frac{(\phi^*_{x^*} - iB^*_{x^*}(1 + \phi^*_{x^*}))(1 + iB^*_{x^*})((x^* - x) - i(B^* - B))}{(x^* - x)^2 + (B^* - B)^2} dx^* \tag{7.3.28}$$

$$= \int_{-\infty}^{\infty} \frac{(\phi^*_{x^*}(1 + B^{*2}_{x^*}) + B^{*2}_{x^*})(x^* - x) - B^*_{x^*}(B^* - B) - iE(x^*, y^*)}{(x^* - x)^2 + (B^* - B)^2} dx^* \tag{7.3.29}$$

where $E(x^*, y^*) = B^*_{x^*}(x^* - x) + (\phi^*_{x^*}(1 + B^{*2}_{x^*}) + B^{*2}_{x^*})(B^* - B)$. Taking the real part

of the integral equation, we obtain

$$\pi\phi_y = \pi(1+\phi_x)B_x = -\int_{-\infty}^{\infty} \frac{(\phi^*_{s^*}(X^*-x) - \phi^*_{n^*}(Y^*-B))}{((X^*-x)^2+(Y^*-B)^2)} ds^* + \int_{-\infty}^{\infty} \frac{(\phi^*_{x^*}(1+B^{*2}_{x^*}) + B^{*2}_{x^*})(x^*-x) - B^*_{x^*}(B^*-B)}{(x^*-x)^2+(B^*-B)^2} dx^*, \tag{7.3.30}$$

or alternatively, taking the imaginary part:

$$\pi\phi_x = \int_{-\infty}^{\infty} \frac{\phi^*_{s^*}(Y^*-B) + \phi^*_{n^*}(X^*-x)}{(X^*-x)^2+(Y^*-B)^2} ds^* - \int_{-\infty}^{\infty} \frac{B^*_{x^*}(x^*-x) + (\phi^*_{x^*}(1+B^{*2}_{x^*}) + B^{*2}_{x^*})(B^*-B)}{(x^*-x)^2+(B^*-B)^2} dx^*. \tag{7.3.31}$$

We choose to use (7.3.31) as our second integral equation. We should point out that in deriving the integro-differential equations, as in the steady case, we have used the fact that the contribution to the integrals from the horizontal lines $x = \pm L$, in the limit as $L \to \infty$ tends to zero.

The integro-differential equations (7.3.21) and (7.3.31) are solved numerically using Newton's method. As in the steady case we discretise the free surface and the channel bottom using N and M equally spaced mesh points respectively. We then have $N+M$ unknowns; $\phi_n(i)$ for $i = 1, ..., N$ and $\phi_x(i)$ for, $i = 1, ..., M$. Here, $\phi_n(i)$ represents the values of ϕ_n at grid point i on the free surface, and similarly $\phi_x(i)$ represents the values of ϕ_x at grid point i on the channel bottom. As in the previous chapters, we must then truncate the integro-differential equations at $x^* = s^* = -\bar{A}$ and $x^* = s^* = \bar{B}$, where $\bar{A}$ and $\bar{B}$ are large positive constants. The integral equations are then evaluated at the $N+M-2$ mesh midpoints using the trapezoidal rule with summation over the mesh points. We can thus ignore the singularities in the first and second integrals in (7.3.21) and (7.3.31) respectively.

Following Dias and Vanden-Broeck [42] and our work in chapter 4, we minimise the truncation error by considering the ignored part of the integrals from $-\infty$ to $-\bar{A}$ and $\bar{B}$ to ∞. As we have no flow and no disturbance downstream as $x \to \infty$, the integrals from $\bar{B}$ to ∞ are negligible. The integrals from $-\infty$ to $-\bar{A}$ are non-zero however, and so must be evaluated analytically by approximating the unknowns by their values at the first mesh point on the free surface and the channel bottom respectively. We also have that $\phi^*_{n^*} \to 0$ far upstream when $x > \bar{A}$ (i.e. as $s^*, x^* \to -\infty$). The integrals far upstream in the first

integral equation (7.3.21) are then approximated by

$$
\begin{aligned}
&-\int_{-\infty}^{-\bar{A}} \frac{\phi^*_{s^*}(1)(X'(X^*-X)+Y'(Y^*(1)-Y))}{(X^*-X)^2+(Y^*(1)-Y)^2}ds^* \\
&+\int_{-\infty}^{-\bar{A}} \frac{(\phi^*_{x^*}(1)(X'(x^*-X)+Y'(B^*(1)-Y))}{(x^*-X)^2+(B^*(1)-Y)^2}dx^* \qquad (7.3.32)\\
&=\left[-\frac{1}{2}\phi^*_{s^*}(1)X'\log((X^*-X)^2+(Y^*(1)-Y)^2)-\phi^*_{s^*}(1)Y'\arctan\left(\frac{X^*-X}{Y^*(1)-Y}\right)\right]_{-\infty}^{-\bar{A}} \\
&+\left[\frac{1}{2}\phi^*_{x}(1)X'\log((x^*-X)^2+(B^*(1)-Y)^2)+\phi^*_{x^*}(1)Y'\arctan\left(\frac{x^*-X}{B^*(1)-Y}\right)\right]_{-\infty}^{-\bar{A}} \qquad (7.3.33)
\end{aligned}
$$

We then obtain the correction T_1 to the integral equation (7.3.21)

$$
\begin{aligned}
T_1 =& -\frac{1}{2}\phi_s(1)X'(i)\log\left((X(1)-X(i))^2+(Y(1)-Y(i))^2\right) \\
&-\phi_s(1)Y'(i)\arctan\left(\frac{X(1)-X(i)}{Y(1)-Y(i)}\right) \\
&+\frac{1}{2}\phi_x(1)X'(i)\log\left((x(1)-X(i))^2+(B(1)-Y(i))^2\right) \\
&+\phi_x(1)Y'(i)\arctan\left(\frac{x(1)-X(i)}{B(1)-Y(i)}\right) \\
&-\lim_{M\to-\infty}\left[\frac{1}{2}(\gamma-1)X'\log\left(\frac{1+\frac{(B^*(1)-Y)^2}{(M-X)^2}}{1+\frac{(Y^*(1)-Y)^2}{(M-X)^2}}\right)\right]-\frac{C}{2}(\gamma-1)Y'(i), \qquad (7.3.34)
\end{aligned}
$$

where

$$
C=\begin{cases}0 & \text{if } Y(1)<Y(i)\\ \pi & \text{if } Y(1)=Y(i)\\ 2\pi & \text{if } Y(1)>Y(i),\end{cases} \qquad (7.3.35)
$$

and we have used the fact that far upstream as $s^*, x^* \to -\infty$ we have that $\phi^*_s \to \gamma - 1$ on the free surface and $\phi^*_x \to \gamma - 1$ on the channel bottom. In the limit as $M \to -\infty$ the expression in the square brackets tends to zero. Similarly, we obtain the correction

$$
\begin{aligned}
T_2 =& \frac{\phi_s(1)}{X'(1)}\left(\arctan\left(\frac{X(1)-x(i)}{Y(1)-B(i)}\right)+\frac{\pi}{2}\right) \\
&-\phi_x(1)\left(\arctan\left(\frac{x(1)-x(i)}{B(1)-B(i)}\right)+\frac{D}{2}\right), \qquad (7.3.36)
\end{aligned}
$$

to the truncated version of the integro-differential equation (7.3.31), where

$$D = \begin{cases} -\pi & \text{if} \quad B(1) < B(i) \\ 0 & \text{if} \quad B(1) = B(i) \\ \pi & \text{if} \quad B(1) > B(i) \end{cases}. \tag{7.3.37}$$

The first integral equation (7.3.21), together with its truncation correction (7.3.34), gives $N-1$ equations, evaluated at the mesh midpoints, and the second integral equation (7.3.31), together with its truncation correction (7.3.36), gives a further $M-1$ equations. The remaining two equations come from defining the flow in the far field, and are given by

$$\phi_x(1) = \gamma - 1 \quad \text{on} \quad y = B(x), \tag{7.3.38}$$

$$\phi_n(N) = 0 \qquad \text{on} \quad y = 1 + \eta(x). \tag{7.3.39}$$

The equations (7.3.21), (7.3.31), (7.3.38) and (7.3.39) are then solved numerically at a given time to find the $N+M$ unknowns, ϕ_n and ϕ_x, on the free surface and the channel bottom respectively.

Using equations (7.2.19) we then obtain ϕ_x and ϕ_y on the free surface, and can thus march the solution forward in time using the Adams-Bashforth-Moulton scheme to solve the equations (7.2.6)-(7.2.8). This is a fourth-order predictor-corrector scheme which approximates equations of the form

$$\frac{dy}{dt} = f(t, y). \tag{7.3.40}$$

The predicted solution is given by

$$y_{1p} = y_0 + \frac{\Delta t}{24}(55f_0 - 59f_{-1} + 37f_{-2} - 9f_{-3}), \tag{7.3.41}$$

and the corrected solution, at the next time step, by

$$y_{1c} = y_0 + \frac{\Delta t}{24}(9f_{1p} + 19f_0 - 5f_{-1} + f_{-2}), \tag{7.3.42}$$

where $f_{1p} = f(t+\Delta t, y_{1p})$. See for example Longuet-Higgins and Cokelet [76]. Here, Δt is the given time step. So, this fourth-order method only requires two evaluations of the function at each time step. We apply this method to each of the equations (7.2.6)-(7.2.8). However, the scheme requires information from the three previous time steps. Therefore, we use the single step multi-variable fourth-order Runge-Kutta algorithm to obtain the first three time steps from the initial steady solution. The solution to (7.2.6)-(7.2.7) at the

next time step is therefore approximated by

$$x_{n+1} = x_n + \frac{1}{6}k_1 + \frac{1}{3}k_2 + \frac{1}{3}k_3 + \frac{1}{6}k_4, \tag{7.3.43}$$

$$y_{n+1} = y_n + \frac{1}{6}l_1 + \frac{1}{3}l_2 + \frac{1}{3}l_3 + \frac{1}{6}l_4, \tag{7.3.44}$$

$$\phi_{n+1} = \phi_n + \frac{1}{6}m_1 + \frac{1}{3}m_2 + \frac{1}{3}m_3 + \frac{1}{6}m_4, \tag{7.3.45}$$

where

$$k_1 = \Delta t \phi_x(x_n, y_n, \phi_n, t_n), \tag{7.3.46}$$

$$l_1 = \Delta t \phi_y(x_n, y_n, \phi_n, t_n), \tag{7.3.47}$$

$$m_1 = \Delta t D(x_n, y_n, \phi_n, t_n), \tag{7.3.48}$$

$$k_2 = \Delta t \phi_x \left(x_n + \frac{1}{2}k_1, y_n + \frac{1}{2}l_1, \phi_n + \frac{1}{2}m_1, t_n + \frac{1}{2}\Delta t \right), \tag{7.3.49}$$

$$l_2 = \Delta t \phi_y \left(x_n + \frac{1}{2}k_1, y_n + \frac{1}{2}l_1, \phi_n + \frac{1}{2}m_1, t_n + \frac{1}{2}\Delta t \right), \tag{7.3.50}$$

$$m_2 = \Delta t D \left(x_n + \frac{1}{2}k_1, y_n + \frac{1}{2}l_1, \phi_n + \frac{1}{2}m_1, t_n + \frac{1}{2}\Delta t \right), \tag{7.3.51}$$

$$k_3 = \Delta t \phi_x \left(x_n + \frac{1}{2}k_2, y_n + \frac{1}{2}l_2, \phi_n + \frac{1}{2}m_2, t_n + \frac{1}{2}\Delta t \right), \tag{7.3.52}$$

$$l_3 = \Delta t \phi_y \left(x_n + \frac{1}{2}k_2, y_n + \frac{1}{2}l_2, \phi_n + \frac{1}{2}m_2, t_n + \frac{1}{2}\Delta t \right), \tag{7.3.53}$$

$$m_3 = \Delta t D \left(x_n + \frac{1}{2}k_2, y_n + \frac{1}{2}l_2, \phi_n + \frac{1}{2}m_2, t_n + \frac{1}{2}\Delta t \right), \tag{7.3.54}$$

$$k_4 = \Delta t \phi_x \left(x_n + k_3, y_n + l_3, \phi_n + m_3, t_n + \Delta t \right), \tag{7.3.55}$$

$$l_4 = \Delta t \phi_y \left(x_n + k_3, y_n + l_3, \phi_n + m_3, t_n + \Delta t \right), \tag{7.3.56}$$

$$m_4 = \Delta t D \left(x_n + k_3, y_n + l_3, \phi_n + m_3, t_n + \Delta t \right). \tag{7.3.57}$$

Here, $D = \frac{1}{2}(\phi_x^2 + \phi_y^2) - y/F^2 + \tau\kappa/F^2$ and the subscripts represent the nth and $n+1$th time steps (rather than the normal derivatives). This algorithm therefore requires four evaluations of the function at each time step, so is not as efficient as Adams-Bashforth-Moulton scheme.

Following Dold [43] and Longuet-Higgins and Cokelet [76], we apply a smoothing algorithm to our results in order to attempt to remove the sawtooth instability from our

solutions. This means that we apply

$$\bar{x}_i = \frac{1}{16}(-x_{i-2} + 4x_{i-1} + 10x_i + 4x_{i+1} - x_{i+2}), \tag{7.3.58}$$

$$\bar{y}_i = \frac{1}{16}(-y_{i-2} + 4y_{i-1} + 10y_i + 4y_{i+1} - y_{i+2}), \tag{7.3.59}$$

$$\bar{\phi}_i = \frac{1}{16}(-\phi_{i-2} + 4\phi_{i-1} + 10\phi_i + 4\phi_{i+1} - \phi_{i+2}), \tag{7.3.60}$$

each time we solve the integral equations. Longuet-Higgins and Cokelet describe this procedure in depth, and derived the five point smoothing formulae given in (7.3.58)-(7.3.60).

We can now write the algorithm used to solve the problem as follows:

1. Obtain an initial steady solution using the scheme described in chapter 4 and by Dias and Vanden-Broeck [41].

2. Read $\hat{\phi}_{\hat{s}}$, $\hat{X}$, $\hat{Y}$, $\hat{\phi}_{\hat{x}}$ and $\hat{B}$ from the known steady solution. Hence, we obtain ϕ_s, X, Y and B at $t = 0$ for the unsteady problem, and initialise $\phi_n = \phi_x = 0$.

3. Approximate X', X'', Y', Y'', ϕ_s and their midpoints using X, Y and ϕ, finite differences and a four-point dyadic interpolation scheme.

4. Initialise the midpoints of ϕ_n and ϕ_x to zero.

5. Solve the integro-differential equations (7.3.21) and (7.3.31) using Newton's method, to find ϕ_n on the free surface and ϕ_x on the bed.

6. Find ϕ_x and ϕ_y on the free surface from (7.2.19), and calculate κ at $t = 0$ using (4.3.6) and (4.3.7).

   So now we have ϕ', X, X', X'', Y, Y', Y'', B, B_x, ϕ_n, ϕ_x, ϕ_y, ϕ_{Bx} and κ at $t = 0$.

7. Advance X, Y and ϕ forward in time using (7.2.6)-(7.2.8) and either the fourth order Runge-Kutta method (for the first three time steps) or Adams-Bashforth Moulton scheme, using the smoothing formulae given in (7.3.58)-(7.3.60) after each time step that the integral equations are solved.

8. Numerically differentiate X, Y, and ϕ using finite differences to obtain X', X'', Y', Y'' and ϕ_s at $t = t + \Delta t$. Analytically differentiate B_x at $t = t + \Delta t$.

9. Calculate the midpoints of X, X', Y, Y' at $t = t + \Delta t$ using a four-point dyadic interpolation scheme. Calculate the midpoints of ϕ_n and ϕ_x at time t.

10. Obtain ϕ_n and ϕ_x at $t = t + \Delta t$ by solving the integral equations (7.3.21) and (7.3.31). Apply the smoothing formulae given in (7.3.58)-(7.3.60).

11. Using ϕ_n and ϕ_s at $t = t + \Delta t$ and (7.2.19), calculate ϕ_x and ϕ_y at $t = t + \Delta t$ on the free surface. Calculate κ at $t = t + \Delta t$.

12. Repeat from step 7 for each time step.

To ensure that the results obtained are numerically accurate, the same solutions are computed on meshes of different densities and sizes, using different time steps. We vary the number of mesh points on the free surface between $N = 401, 801, 1601$ and 2401, and on the channel bottom, between $M = 201, 401, 801$, and 1201 for a given fixed domain. The mesh spacings e and h are also varied between 0.05 and 0.1, and $h = 0.1$ and 0.2, respectively. We vary the time step between $\Delta t = 0.1, 0.05, 0.025, 0.01, 0.005$ and 0.001 to ensure that the results presented are independent of the size of the time step.

7.4 Results

The results in this section were computed using the method described in section 7.3. Following Dias and Vanden-Broeck [41] and our work in chapter 4, we use the same cosine squared profile to describe the submerged obstructions. Therefore, we write

$$B(x,t) = \begin{cases} 2A_1 \cos^2\left(\frac{\pi(x-x_d+t)}{2L_1}\right) & -L_1 < x - x_d + t < L_1, \\ 2A_2 \cos^2\left(\frac{\pi(x+t)}{2L_2}\right) & -L_2 < x + t < L_2, \\ 0 & \text{otherwise}, \end{cases} \tag{7.4.1}$$

so that the heights and widths of the obstructions are given by $2A_i$ and $2L_i$, for $i = 1, 2$ respectively. The obstacle with height A_2 has been chosen so that initially, at time $t = 0$, it is centred at the origin and is a distance x_d from the other obstacle. The separation constant x_d is fixed for all time. In the case of solutions over a single submerged obstruction, we set $A_1 = 0$.

7.4.1 Solitary waves

In order to ensure that our numerical scheme is accurate, we first modify our scheme in section 7.3 so that we can look for unsteady pure gravity forced solitary waves. Therefore, in the far field as $x \to \pm\infty$, we require that there is no flow and no disturbance to the free surface. The corrections to the integro-differential equations (7.3.21) and (7.3.21) therefore both decay to zero as $x \to \pm\infty$ and can be neglected. We can thus remove the truncation corrections (7.3.34) and (7.3.36) from the numerical scheme. Furthermore, we must modify the far field conditions (7.3.38) so that there is no flow upstream as

$x \to \pm\infty$;

$$\phi_x(1) = 0 \text{ on } y = B(x). \tag{7.4.2}$$

As previously discussed, steady forced solitary wave solutions are not unique. Vanden-Broeck [122] showed that for a particular range of Froude numbers there exist two solutions with the same value of F; a small amplitude wave bifurcating from the uniform stream and a large amplitude wave bifurcating from the pure solitary wave. Grimshaw and Maleewong [61] used a moving pressure distribution as a forcing to show that, in the pure gravity case, the forced solitary waves bifurcating from the uniform stream are stable whilst those bifurcating from a pure solitary wave are unstable. We now attempt to reach these same conclusions for our submerged obstruction.

We consider pure gravity solutions over a single small obstruction characterised by $A_2 = 0.001$, $L_2 = 2$. The steady forced solution branches in the $F - y(0)$ plane are well known, and were discussed in chapter 3 in the case of gravity-capillary free surface flows past multiple pressure distributions. In figure 7.2 we show the solution branch for the pure gravity case for our given submerged obstruction. As in chapter 3, the lower part of the branch, before the turning point, corresponds to solutions bifurcating from the uniform stream. The upper part of the branch corresponds to forced solitary waves bifurcating from a pure solitary wave solution.

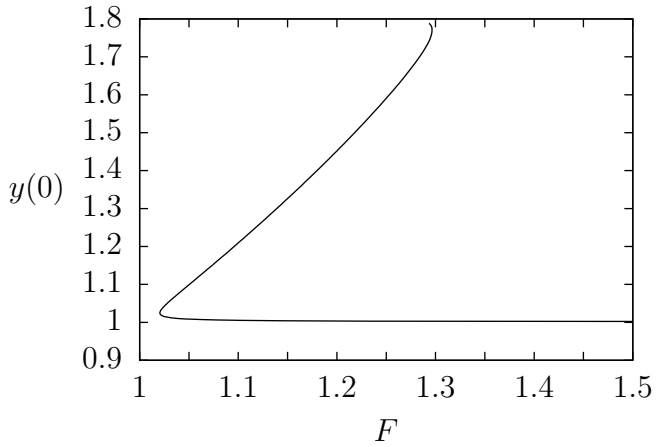

Figure 7.2: Pure gravity forced wave solution branch. The underlying obstacle is characterised by $A_2 = 0.001$, $L_2 = 2$.

Firstly, we obtain two initial steady solutions on the lower part of the branch, with $F = 1.1$ and $F = 1.32$, and advance them forward in time using the modifications to the numerical scheme, discussed above. As expected, we find that the forced wave is stable in each case. It moves upstream with the submerged obstruction without changing form. We show the solution profiles in figure 7.3. It should be noted that here, we have defined 'stable' to mean that despite the small numerical errors due to the discretisation of the

problem in the numerical scheme used, the solution does not change form. Our findings are in agreement with Grimshaw and Maleewong's [61] results and thus help to start to confirm our solutions and methodology.

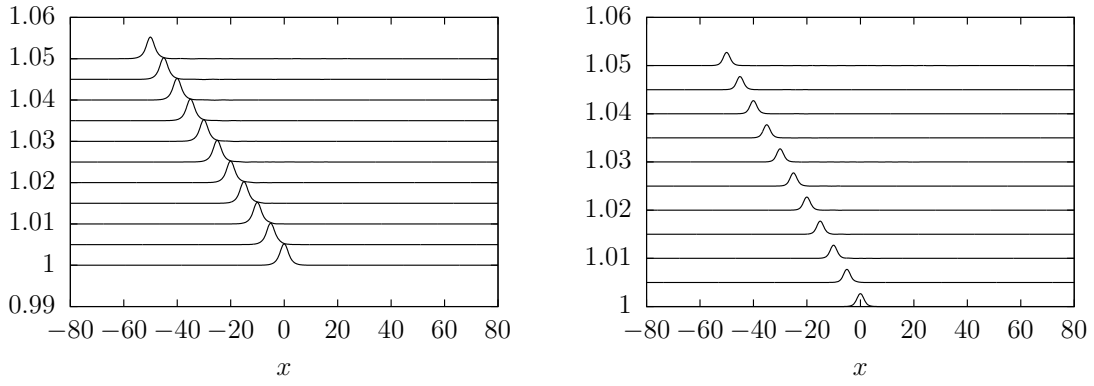

(a) $F = 1.10$ **(b)** $F = 1.32$

Figure 7.3: Time evolution of pure gravity waves with $F \approx 1.1$ and $F \approx 1.3$. Initially, a steady wave bifurcating from the uniform stream is utilised (the lowest profile). The vertical axis is then moved upwards by 0.005 for each plot shown, such that $t_n = 5n$ for plots $n = 0, ..., 10$.

Next, we start with initial steady solutions on the upper part of the solution branch in figure 7.2, with $F = 1.20$ and $F = 1.29$. We find that in each case, the forced solitary wave is unstable. When F is close to one we see that the forced solitary wave starts to move upstream away from the obstacle. For larger F, the amplitude of the solitary wave sharpens very quickly, until the solution breaks at an early time. The evolution of the free surface in each case, is shown in figure 7.4. Although it is hard to see in the figure, the solution profile at $t = 50$ in figure 7.4(a) has moved a distance of $x \approx 0.14$ upstream of the submerged obstruction. Grimshaw and Maleewong [61] observed similar phenomenon for their fully nonlinear numerical simulations of flows past a pressure distribution.

Now we try a different approach to check the stability and instability observed using the basic time evolution method. Following the ideas of Chardard *et al.* [27], we add a small perturbation to the initial steady solution. Here, we use a perturbation of the form

$$y = (1 - \alpha)y_0 + \alpha, \tag{7.4.3}$$

where $-0.1 \leq \alpha \leq 0.15$ and y_0 is the initial solution. We consider a larger obstacle than before, taking $A_2 = 0.05$ and $L_2 = 3.2$.

When the steady solution bifurcating from the uniform stream is perturbed, for every value of α we tried, we found that the forced wave recovered its original state and moved upstream with the obstruction. In figure 7.5 we show the evolution of a typical free surface profile, with $F = 1.5$ for an $\alpha < 0$ and an $\alpha > 0$. So again, we observe that this forced wave is stable, although transient waves appear downstream. This is in agreement

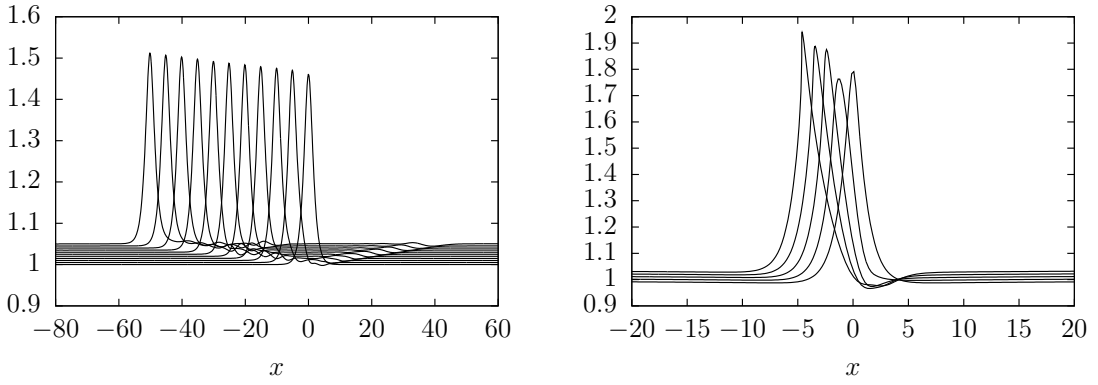

(a) $F = 1.20$ **(b)** $F = 1.29$

Figure 7.4: Time evolution of pure gravity forced solitary waves with $F \approx 1.2$ and $F \approx 1.3$. Initially, a steady forced solitary wave profile bifurcating from a pure solitary wave is utilised (the lowest profile). The vertical axis is then moved upwards by (a) 0.005 for each plot shown, such that $t_n = 5n$ for plots $n = 0, ..., 10.$, and (b) 0.01 for each plot shown, such that $t_n = n$ for plots $n = 0, ..., 4$.

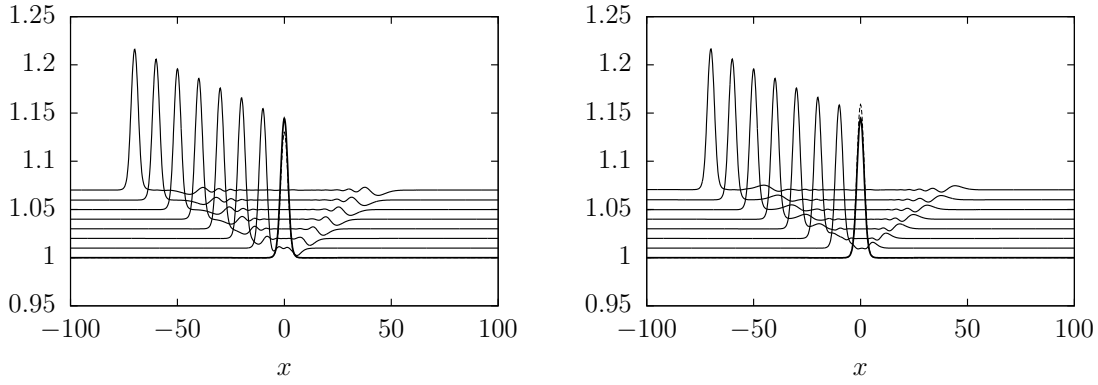

(a) $F = 1.5$ **(b)** $F = 1.5$

Figure 7.5: Time evolution of pure gravity forced waves with $F = 1.5$. Initially, a steady forced wave bifurcating from the uniform stream, perturbed by (7.4.3), is utilised. The bold solution shows the initial wave. The dashed line is the perturbed solution when (a) $\alpha = 0.1$ and (b) $\alpha = -0.1$. The vertical axis is moved upwards by 0.01 for for each plot shown, such that $t_n = 10n$ for plots $n = 0, ..., 7$.

with the findings of Chardard *et al.* who used a fKdV model to study the effect of their perturbation on an initial steady solution.

Next we add the perturbation to the initial solution bifurcating from the pure solitary wave. When $\alpha > 0$, so that the amplitude of the perturbed solution is less than the amplitude of the initial steady state solution, we find that the amplitude of the forced solitary wave decreases with time. Figure 7.6(a) shows a typical example of this behaviour for a solution with $F = 1.3$. When $\alpha < 0$, so that the amplitude of the perturbed solution is greater than the amplitude of the initial steady state solution, we find that the amplitude

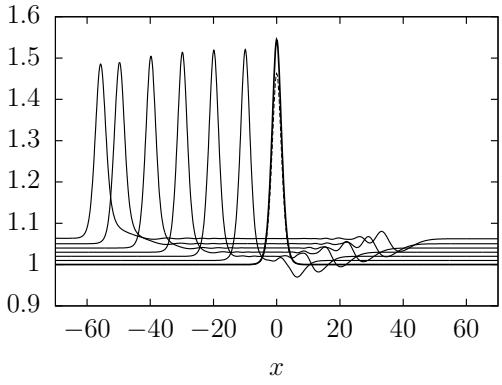

(a) $F = 1.3$

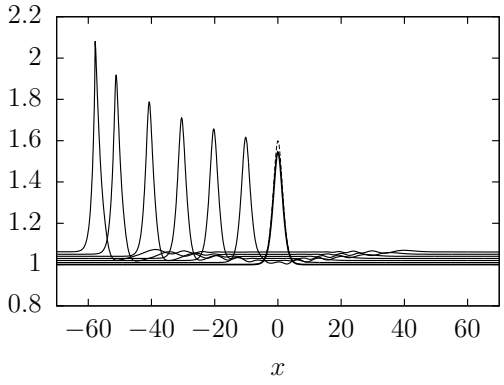

(b) $F = 1.3$

Figure 7.6: Time evolution of perturbed pure gravity forced solitary waves with $F = 1.3$. Initially, a steady, forced solitary wave bifurcating from a pure solitary wave, perturbed by (7.4.3), is utilised. The bold solution shows the initial solitary wave. The dashed line is the perturbed solution when (a) $\alpha = 0.15$ and (b) $\alpha = -0.1$.. The vertical axis is moved upwards by 0.01 for each plot shown, such that $t_n = 10n$ for plots $n = 0, ..., 5, 5.6$.

of the forced solitary wave increases with time. The crest of the wave sharpens until eventually the wave breaks. A typical example of the free surface evolution with $F = 1.3$ is shown in figure 7.6(b). Chardard *et al.*[27] observed similar phenomenon using their weakly nonlinear analysis. However, in the case where the perturbed solution is of greater amplitude than the initial steady state solution, their scheme was unable to predict wave breaking. Instead, in their solutions the large solitary wave propagated upstream away from the obstruction, leaving behind a solitary wave bifurcating from the uniform stream.

In this section we have shown that the types of solution produced in our fully nonlinear scheme for flow over a moving submerged obstruction, are in good agreement with the types of solutions obtained by Grimshaw and Maleewong [61] in the case of flow past a moving localised pressure distribution, and those in the weakly nonlinear case by Chardard *et al.* for flow over a moving submerged obstruction. This suggests that the numerical scheme presented in section 7.3 is a valid method to study unsteady free surface flows subjected to a moving obstruction on the bottom of the channel. We can now proceed to use the scheme to investigate the stability of hydraulic fall solutions, in the next section.

7.4.2 Hydraulic falls

In this section, we examine the stability of the pure gravity hydraulic fall solutions discussed in chapter 4. We therefore set $\tau = 0$, $A_1 = 0$, and take $A_2 > 0$ so that $y = B(x, t)$ describes a channel bottom along which a single submerged obstruction moves to the left.

In figure 7.7 we show the evolution of a hydraulic fall with $F = 1.34$, over an obstruction characterised by $A_2 = 0.05$, $L_2 = 3.2$. We see that the hydraulic fall moves

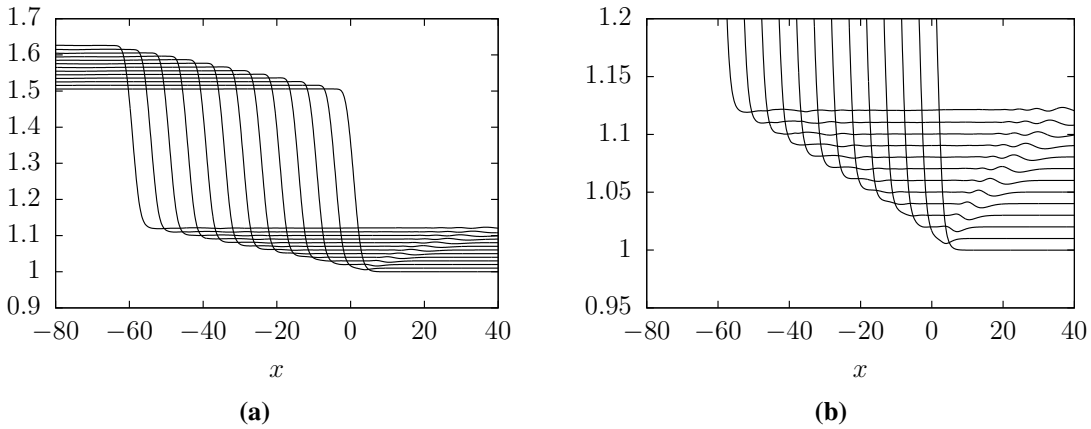

Figure 7.7: (a) Evolution in time of a pure gravity hydraulic fall with $F = 1.34$. Initially, a steady free surface is utilised (the lowest profile). The vertical axis is then moved upwards by 0.01 for each curve drawn, so that $t_n = 5n$ for plots $n = 0, ..., 12$. (b): A close-up of the downstream free surface evolution.

upstream with the submerged obstruction, whilst maintaining its shape. This suggests that the pure gravity hydraulic fall is stable. Downstream of the fall a small decaying wave train is generated and this initial transient propagates away downstream as time progresses. As time continues, more waves are shed downstream from the foot of the fall. These waves propagate slowly upstream of the initial hydraulic fall. The evolution of the downstream profiles can be seen in figure 7.7(b). It is likely that these waves are the result of implicitly perturbing the solution at $t = 0$, due to the fact that the initial solution is actually approximated because of the numerical methods involved in the scheme outlined in section 7.3.

Next, following the structure used in the unsteady solitary wave analysis in the previous section, we add a perturbation to the initial steady flow over the fall, and evolve the solution in time, to see what happens. We take this perturbation to be of the form

$$y = y_s \left(1 + \lambda \cos(\mu x) e^{-\left(\frac{x}{2}\right)^2}\right) \tag{7.4.4}$$

where $\lambda \leq 0.1$ and $\mu \leq 10$ are positive constants, and y_s is the initial steady state solution. Donahue and Shen [45] had a similar approach when using a weakly nonlinear analysis, but they perturbed their initial steady solution with white noise. Our perturbation only effects the part of the initial solution in which the gradient of the free surface is non-zero, i.e. the actual fall itself and not the uniform flows up and downstream. We find that as we advance the solution forward in time the perturbation decays and the solution moves with the underlying obstruction, and settles to the shape of the steady state hydraulic fall solution. However, a small amplitude wave train, which propagates very slowly downstream, is generated after the fall. As we evolve the solution further in

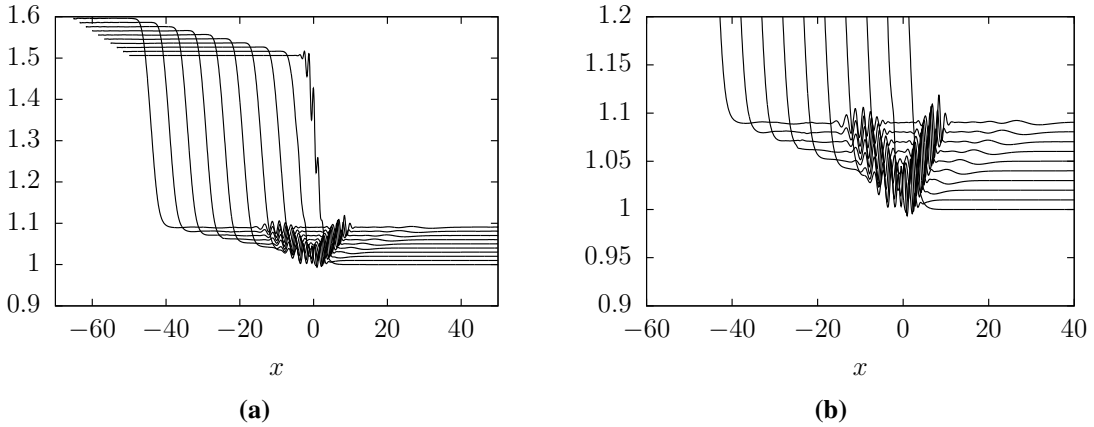

Figure 7.8: (a) Evolution in time of a pure gravity hydraulic fall with $F \approx 1.34$. Initially, a steady free surface is perturbed (the lowest profile). The vertical axis is then moved upwards by 0.01 for each plot shown, such that $t_n = 5n$ for plots $n = 0, ..., 9$. (b): A close-up of the downstream free surface.

time, another wave train is shed from the foot of the hydraulic fall. It propagates very slowly upstream. In figures 7.8 and 7.9 we show the evolution of the hydraulic fall with $F = 1.344$, over an obstruction classified by $A_2 = 0.05$, $L_2 = 3.2$. Figure 7.9 shows the free surface, at times $t = 0, 5, 17.5$ and 35. This clearly demonstrates the propagation of the waves downstream of the hydraulic fall. Locally over the obstruction, the free surface at time $t = 35$ is plotted in figure 7.9(d), and shows that the solution has become that of a classical hydraulic fall in the absence of a perturbation. Explicitly perturbing the solution has increased the disturbances shed from the hydraulic fall.

Therefore, all our results suggest that the pure gravity classical hydraulic fall is stable. This agrees with Chardard *et al.* [27] and Donahue and Shen [45] where a weakly nonlinear analysis was used.

Next, we add surface tension to our model and compute results for different values of the Bond number. Initially, we compute a steady gravity-capillary hydraulic fall solution using the method outlined in chapter 4. As in chapter 4, small amplitude waves (caused by truncating the domain downstream at some large positive constant instead of at infinity), appear downstream of the fall.

We advance forward in time, different gravity-capillary initial steady state solutions, and see that the hydraulic falls maintain their shape and move upstream with the submerged obstruction. As in the pure gravity case, a wave is shed from the fall and moves downstream away from the obstruction. The wave advances with the hydraulic fall so that far downstream, much later, the free surface appears to be uniform, without disturbances shed from the hydraulic fall. In figure 7.10 we show an advancing free surface profile with $F = 1.36$ and $\tau = 0.3$. One can see that at first, a depression wave is shed from the fall, which propagates downstream. As time progresses an elevation wave then starts to

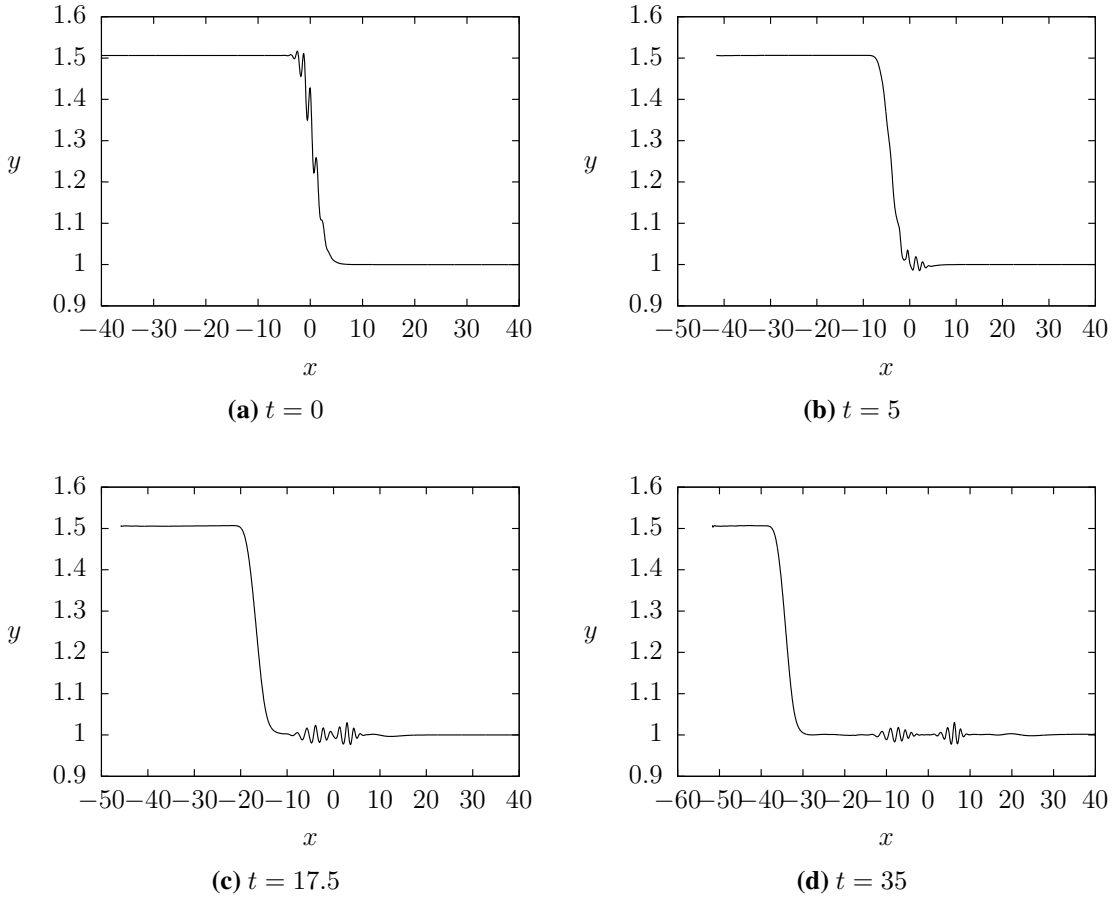

(a) $t = 0$ **(b)** $t = 5$

(c) $t = 17.5$ **(d)** $t = 35$

Figure 7.9: Free surface profiles of an initially perturbed pure gravity hydraulic fall with $F \approx 1.34$, at different time steps; (a) $t = 0$, (b) $t = 5$, (c) $t = 17.5$, and (d) $t = 35$.

emerge, which propagates steadily upstream with the fall.

When we increase the Bond number so that $\tau = 0.6$ with $F = 1.37$ we see wavetrains emerge, which are roughly symmetrical about $x = 0$. One wavetrain propagates upstream of the fall, whilst the other propagates downstream. In all the cases that we considered for $0.1 \leq \tau \leq 0.9$ (whether a depression wave, an elevation wave or multiple wave trains appeared after the fall), we saw that locally, over the submerged obstruction, the hydraulic fall maintained its shape over time. This suggests that the gravity-capillary hydraulic falls are also stable.

In chapter 4 we saw that the gravity-capillary hydraulic fall solutions were richer than the pure gravity solutions. Indeed, we showed that when the surface tension is weak, the upstream dispersion relation possesses a minimum. As the upstream Froude number of the hydraulic fall solution is increased towards this minimum, a small decaying wavetrain appears on the free surface, immediately before the hydraulic fall. Now we use such a free surface elevation as initial data, and watch it evolve with time. We see that the upstream wave train does not appear to change form as time increases. This can be seen for example in figure 7.11 where the solution with $\tau = 0.2$ and $F = 1.2$ is advanced in

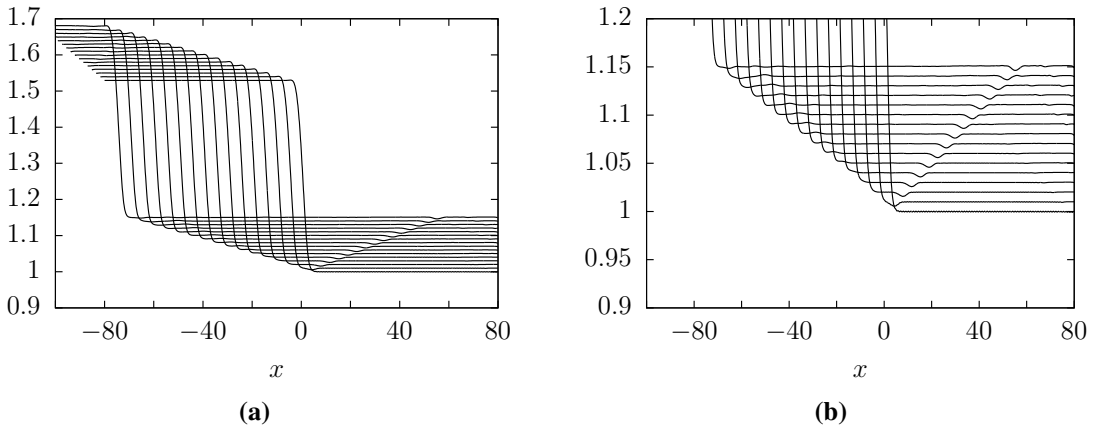

Figure 7.10: (a) Time evolution of gravity-capillary hydraulic fall profiles with $\tau = 0.3$. Initially, a steady free surface profile is utilised (the lowest profile). The vertical axis is then moved upwards by 0.01 for each plot shown, such that $t_n = 5n$, $n = 0, ..., 15$. (b): A close-up of the downstream free surface evolution.

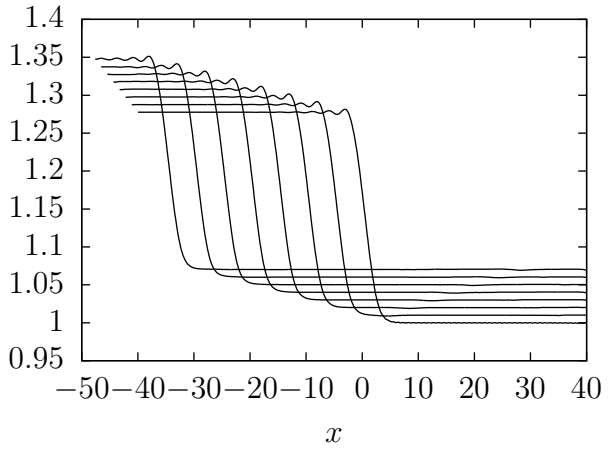

Figure 7.11: Time evolution of a gravity-capillary hydraulic fall profile with $\tau = 0.2$, $F = 1.2$, past an obstruction characterised by $A_2 = 0.015$, $L_2 = 3.2$. Initially, a steady free surface profile is utilised (the lowest profile). The vertical axis is then moved upwards by 0.01 for each plot shown, such that $t_n = 5n$ for plots $n = 0, ..., 7$. A small decaying wave train can be seen upstream of the hydraulic fall.

time. The solution profile maintains its shape, suggesting that this solution is also stable.

Next, we add the perturbation in the form given by (7.4.4) to the gravity-capillary initial steady state solutions. As the solutions advance in time the initial perturbation spreads out and radiates away very quickly, so that the local solution over the obstruction settles very quickly to the shape of the classical gravity-capillary hydraulic fall. In figure 7.12 we demonstrate this for two solution profiles, for $\tau = 0.1$ and $\tau = 0.6$. As in the pure gravity case, waves are shed downstream of the hydraulic fall. However, it appears that the capillarity dampens the waves; they are much less prominent in the gravity-capillary cases than in the pure gravity case.

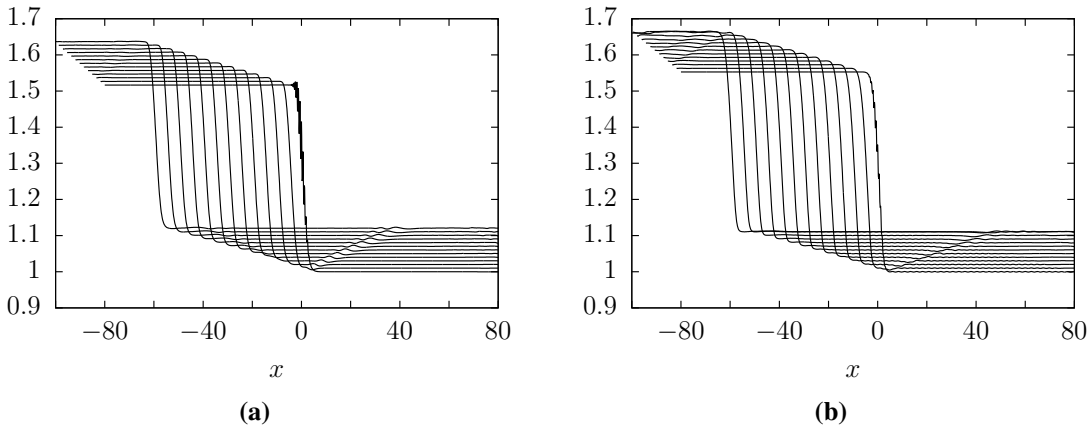

Figure 7.12: Time evolution of gravity-capillary hydraulic fall profiles; (a) $\tau = 0.1$, (b) $\tau = 0.6$. Initially, a steady perturbed free surface profile is utilised (the lowest profile). The vertical axis is then moved upwards by 0.01 for each plot shown, such that $t_n = 5n$ for $n = 0, ..., 12$.

So both methods that we have used to study the problem suggest that including surface tension does not change the stability of the hydraulic fall. The hydraulic fall is stable.

7.4.3 Trapped waves

Next, we consider the cases where a second obstruction is placed in the flow configuration, i.e. $A_1 \neq 0$. We have previously discussed how Dias and Vanden-Broeck [41] showed that in order to obtain a train of gravity waves trapped between the submerged obstruction, this additional obstruction must be placed upstream. Starting with such a steady state solution as our initial free surface profile, we see that as time evolves, the amplitude and the wavelength of the trapped waves appears to remain constant. We demonstrate this in figure 7.13 for a flow configuration with $F = 1.33$. Here, it can be seen that the free surface profile clearly maintains its shape. This suggests that the pure gravity trapped wave solutions are stable. Indeed, this is supported by the experimental work of Pratt [95] who actually observed these solutions, meaning that one would indeed expect these solutions to be stable. This is a physically realistic result.

Downstream of the hydraulic fall in figure 7.13, we see a small amplitude wave train. As time progresses the length of the flow domain which is effected by the downstream disturbances grows. The waves downstream can be seen more clearly in the close up in figure 7.13(b). A second wave train is shed from the foot of the hydraulic fall, as in the single obstruction results. This second wave train propagates upstream with the hydraulic fall.

In chapter 4 we showed that in order to obtain gravity-capillary solutions with a train of trapped waves between the two obstructions, unless the surface tension is very small, the second obstruction must be placed downstream of the hydraulic fall. Now we use

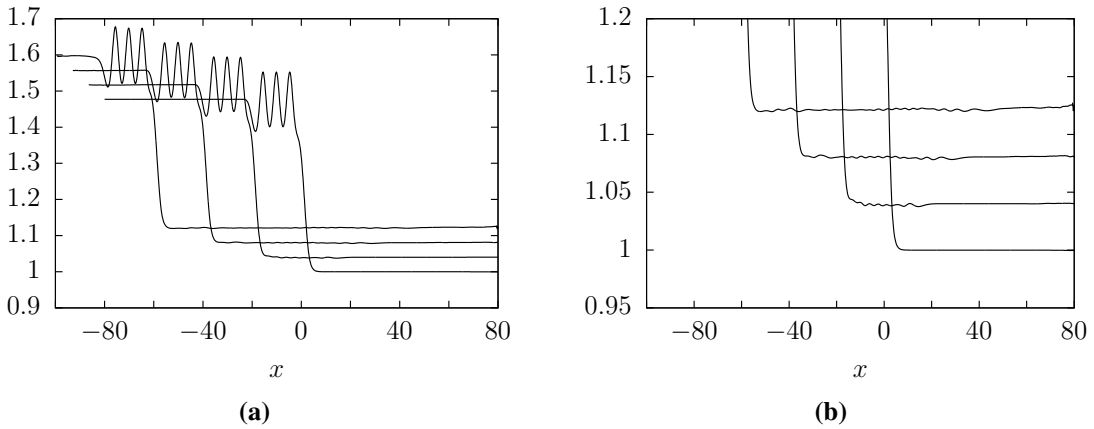

Figure 7.13: (a) Time evolution of a pure gravity hydraulic fall profile, $F = 1.33$, with a train of waves trapped between two obstructions. Initially, a steady state free surface profile is utilised (the lowest profile). The vertical axis is then moved upwards by 0.04 for each plot shown, such that $t_n = 20n$ for plots $n = 0, ..., 3$. A close-up of the downstream free surface evolution in (a) is shown in (b).

the steady state solutions obtained in chapter 4 as the initial free surface profiles for our numerical scheme here, so that we can advance the solutions in time. In figure 7.14 we show a typical solution profile with $F = 1.38$, for a strong surface tension; $\tau = 0.7$. We see that although trapped waves continue to appear on the free surface, the amplitude of the waves decreases with time. In figure 7.14(b) we show the initial solution at time $t = 0$ (the solid line), superimposed with the solution at time $t = 14$ (the dashed line) to demonstrate this point. This suggests that the trapped waves between the two obstructions are unstable. However, we do see that the hydraulic fall over the first obstruction and the elevation wave over the second obstruction appear to maintain their shape, and thus, those parts of the solution appear to be stable. Here, we have defined 'unstable' to mean that the solution does not maintain its shape when it is subjected to the small numerical errors caused by our scheme, as time increases. We speculate that, if we were not subjected to our current computational limitations, and if the solution was to be evolved even further in time, then the wave train between the submerged obstructions might vanish, resulting in a solution without waves, which is then stable.

In chapter 4, we showed that if the surface tension is weaker and the height of the downstream obstruction small enough, any trapped waves that may exist between the two obstructions, are not clearly visible. The amplitude of the waves is so small, that one would have to zoom very closely in on the downstream part of the free surface to see them. In figure 7.15 we follow a typical solution profile, with $F = 1.36$ and $\tau = 0.3$, forward in time. The solution profile appears to maintain its shape, suggesting it is stable. However, we would expect that any trapped waves found to occur between the two obstructions, would still decay with time. This is just much harder to observe because of their very

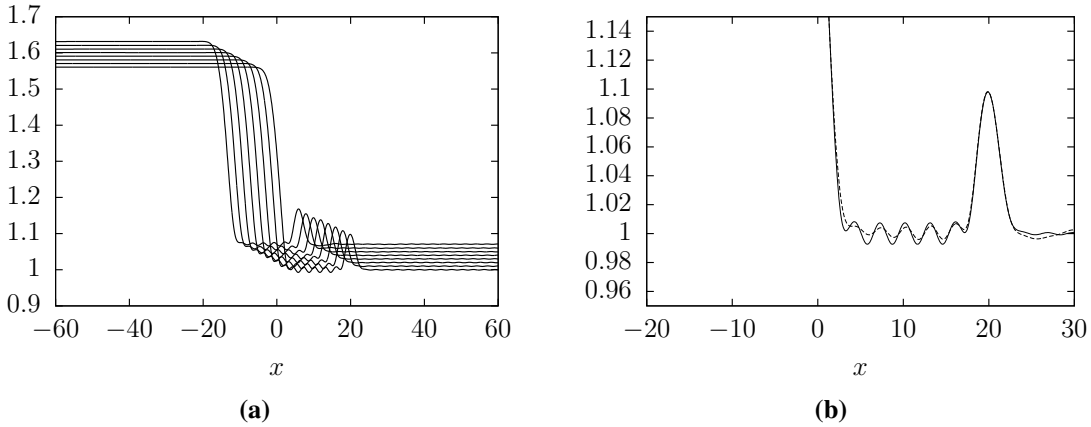

Figure 7.14: Time evolution of a gravity-capillary hydraulic fall profile with $\tau = 0.7$, $F = 1.38$, past two obstructions characterised by $A_2 = 0.05$, $L_2 = 3.2$ and $A_1 = 0.02$, $L_1 = 3.2$ with $x_d = 20$. Initially, a steady free surface profile is utilised (the lowest profile in (a)). In (a) the vertical axis is then moved upwards by 0.01 for each plot shown, such that $t_n = 2n$ for plots $n = 0, ..., 7$. In (b) the solution profiles are this time viewed in a frame of reference moving with the obstructions. The solid line shows part of the solution at $t = 0$, and the dashed line part of the solution at $t = 14$.

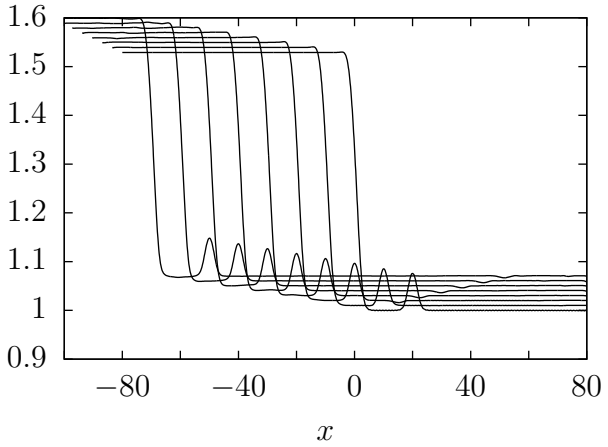

Figure 7.15: Time evolution of a gravity-capillary hydraulic fall profile with $\tau = 0.3$, $F = 1.36$, past two obstructions characterised by $A_2 = 0.05$, $L_2 = 3.2$ and $A_1 = 0.02$, $L_1 = 3.2$ with $x_d = 20$. Initially, a steady free surface profile is utilised. The vertical axis is then moved upwards by 0.01 for each plot shown, such that $t_n = 10n$ for plots $n = 0, ..., 7$.

small amplitude.

In chapter 4, we showed that when the surface tension is so small that the upstream Froude number intersects the upstream linear dispersion relation, gravity-capillary trapped waves could also be obtained by placing the second obstruction upstream of the hydraulic fall. We use this steady state solution as initial data in our numerical scheme, and evolve it in time. Figure 7.16 contains a typical solution profile with $F = 1.35$, for the weak surface tension case; $\tau = 0.1$. We obtain similar results here to the results for the downstream gravity-capillary trapped waves; the amplitude of the trapped waves decreases

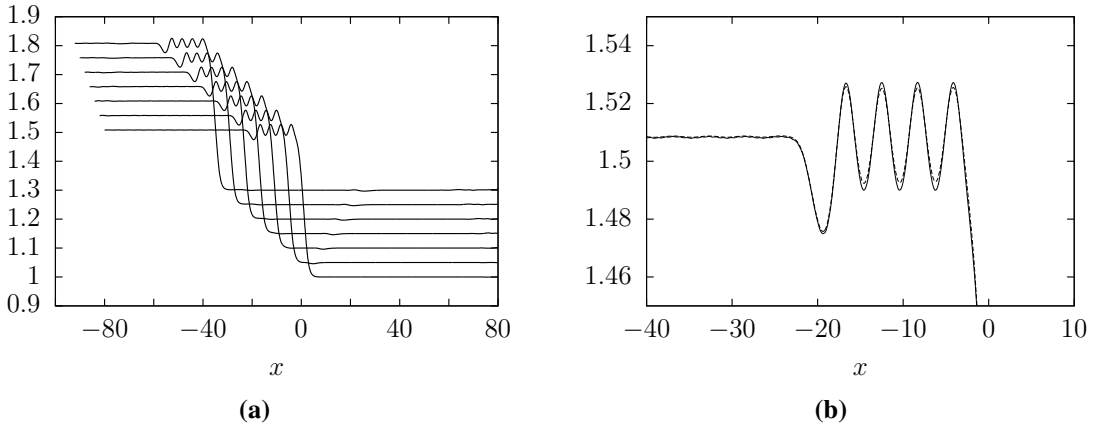

(a) **(b)**

Figure 7.16: Time evolution of a gravity-capillary hydraulic fall profile with $\tau = 0.1$, $F = 1.35$, past two obstructions characterised by $A_2 = 0.05$, $L_2 = 3.2$ and $A_1 = 0.01$, $L_1 = 3.2$ with $x_d = -20$. Initially, a steady free surface profile is utilised (the lowest profile in (a)). In (a) the vertical axis is then moved upwards by 0.05 for each plot shown, such that $t_n = 6n$ for plots $n = 0, ..., 6$. In (b) the solution profiles are this time viewed in a frame of reference moving with the obstructions. The solid line shows part of the solution at $t = 0$, and the dashed line part of the solution at $t = 20$.

with time. Again, we demonstrate this in figure 7.16(b) by superimposing the initial solution at time $t = 0$ (the solid line) with the solution at $t = 20$ (the dashed line). The amplitude of the trapped waves at $t = 20$ is clearly smaller than those at $t = 0$. So, this suggests that this type of solution is also unstable.

It therefore appears that gravity-capillary trapped wave solutions may be unstable. The amplitude of the waves, whether they occur upstream or downstream, appears to decrease with time.

7.4.4 Hydraulic falls with a solitary type wave

Now we consider the solutions which have a solitary type wave over the additional submerged obstruction, but with no trapped waves between the two obstructions. We use the results obtained by Belward [11] in the pure gravity case as our initial steady state profile. Here, the second obstruction is found downstream of the hydraulic fall. In figure 7.17 we follow a typical solution profile with $F = 1.35$ forward in time. We see that both the hydraulic fall and the solitary type wave move downstream with the submerged obstructions, suggesting that this solution is stable. The solitary wave bifurcates from the uniform stream, and we have shown in section 7.4.1 that such solutions are stable. We have shown in section 7.4.2 that the pure gravity hydraulic fall is stable, and so one could indeed expect that the hybrid solution of the pure gravity hydraulic fall followed by the solitary wave is stable, as found. Downstream of the hydraulic fall we see that a small disturbance develops. The width of this disturbance grows slowly as it advances

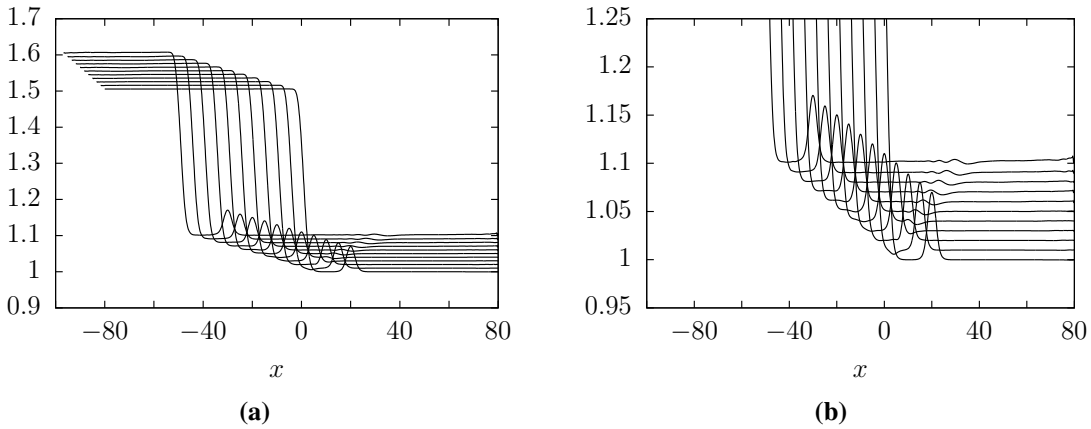

Figure 7.17: (a) Time evolution of a pure gravity hydraulic fall profile, $F = 1.35$, with a solitary type wave downstream of the fall. Initially, a steady free surface profile is utilised (the lowest profile). The vertical axis is then moved upwards by 0.01 for each plot shown, such that $t_n = 5n$ for plots $n = 0, ..., 10$. A close-up of the downstream free surface evolution in (a) is shown in (b).

downstream past the solitary type wave.

We have shown in chapter 4, for the gravity-capillary case, if the Bond number is not so small that the upstream Froude number intersects the upstream linear dispersion relation, then solitary type waves can be obtained over the additional obstruction when it is placed upstream of the hydraulic fall. A depression wave is obtained over a positively orientated obstacle, and in figure 7.18 we follow such a solution in time, with $\tau = 0.7$. We see that the depression wave and the hydraulic fall maintain their shape, whilst moving with the underlying obstructions. This suggests that this solution is stable. As in the pure gravity case, the solitary type wave is bifurcating from the uniform stream. Grimshaw, Maleewong and Asavanant [62] have shown that such gravity-capillary solutions are stable. In section 7.4.2 we showed that the gravity-capillary hydraulic fall is stable, and so again, it is feasible that the hybrid solution of the gravity-capillary solitary type wave and the hydraulic fall would be stable, as found.

When the surface tension is weak there exists a minimum in the upstream linear dispersion relation. In chapter 4, we saw that if the Froude number is close to this minimum, the solitary type wave in the steady solution has small decaying oscillations in its tail. We follow such solutions in time, where the additional upstream obstruction is negatively orientated. Figure 7.19 shows the time evolution of the free surface with $\tau = 0.19$ and $F = 1.38$, and we see that the solitary wave itself appears to maintain its shape as time evolves, but the decaying oscillations in the tail of the wave, decrease in amplitude over time. This is clearly demonstrated in the close-up of the free surface upstream at time $t = 0$ superimposed with time $t = 19$, shown in figure 7.19(b).

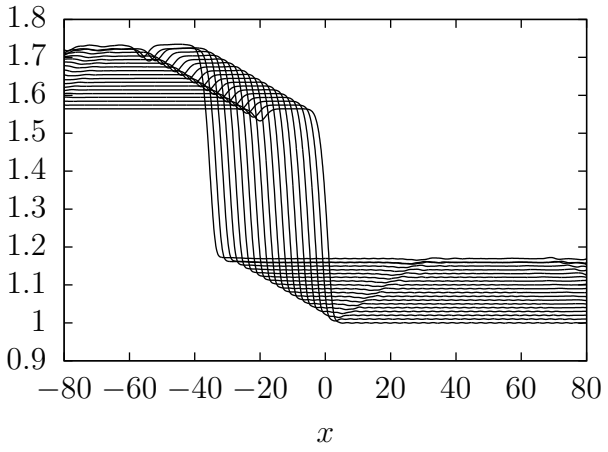

Figure 7.18: Time evolution a of gravity-capillary hydraulic fall profile. Initially, a steady free surface profile over two obstructions is utilised. The second obstruction is placed upstream of the hydraulic fall. The vertical axis is then moved upwards by 0.01 for each plot shown, such that $t_n = 2n$ for plots $n = 0, ..., 16$.

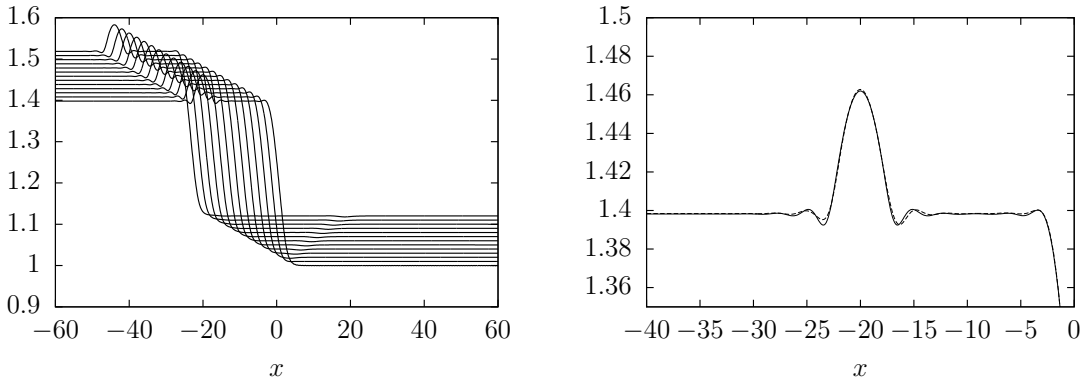

Figure 7.19: Time evolution of a gravity-capillary hydraulic fall profile with $\tau = 0.19$, $F = 1.38$, past two obstructions characterised by $A_2 = 0.03$, $L_2 = 3.2$ and $A_1 = -0.03$, $L_1 = 3.2$ with $x_d = -20$. Initially, a steady free surface profile is utilised (the lowest profile in (a)). In (a) the vertical axis is then moved upwards by 0.01 for each plot shown, such that $t_n = 2n$ for plots $n = 0, ..., 12$. In (b) the solution profiles are viewed in a frame of reference moving with the obstructions. The solid line shows part of the solution at $t = 0$, and the dashed line part of the solution at $t = 19$.

7.5 Conclusion

We have computed unsteady, forced, critical flow solutions using a fully nonlinear boundary integral equation technique, in the pure gravity and the gravity-capillary cases. Initially we used a steady state solution and then evolved the solution in time in order to assess the stability of the critical flows presented in chapter 4. We then added a small perturbation to the steady state solution which we then evolved in time and assessed what happened to the perturbation. Using these methods we showed that the pure gravity and the gravity-capillary hydraulic falls are both stable, and supported our findings in the pure gravity case by considering the weakly nonlinear findings of Chardard *et al.* [27] and Donahue and Shen [45].

In the case of two submerged obstructions moving at the same speed on the channel bottom, we showed that the pure gravity steady state trapped wave solutions found by Dias and Vanden-Broeck [41], which have a train of trapped waves upstream between the two obstructions, are stable. Furthermore, it was shown that the gravity-capillary trapped wave solutions appear to be unstable. This was the case whether the trapped waves appeared upstream or downstream. The amplitude of the waves decreased with time, and so in the absence of computational restraints, it would be of interest to follow these trapped wave solutions even further in time to see if the amplitude of the waves between the submerged obstructions decreases so much that the waves disappear completely. In chapter 4 we showed that there exist multiple families of gravity-capillary downstream trapped wave solutions. Here we have only considered the stability of one of these types of solution. It may therefore be of interest to perform a similar study on the stability of the other types of solution.

When the free surface over the additional obstruction takes the form of a solitary type wave, we showed that the gravity solution appears to be stable. In the gravity-capillary case, we saw that the solution also appeared to be stable unless the upstream Froude number was very close to the minimum of the upstream linear dispersion relation. In such an event, the decaying oscillations in the tail of the solitary wave appeared to decrease in amplitude as time evolved.

Due to their unphysical nature, we did not attempt to determine the stability of the generalised hydraulic fall solutions discussed in chapter 4. We could however speculate that the pure gravity solutions may be stable, because the associated trapped wave solutions are stable. Indeed, we have discussed how Dias and Vanden-Broeck [41] showed that the pure gravity trapped wave solution is a hybrid solution between the generalised hydraulic fall and the subcritical flow, which is uniform upstream with a train of gravity waves downstream of the solution. Grimshaw and Maleewong [61] showed that the subcritical flow is stable, so to obtain stable trapped wave solutions, we may also require that the generalised hydraulic fall is stable. Following a similar line of reasoning, we could

then speculate that both the gravity-capillary types of generalised hydraulic falls (with the waves either occurring up or downstream) are unstable, as the trapped wave solutions are unstable.

Of course, it should be noted that due to the computational limitations associated with solving such a fully nonlinear problem, we were only able to follow the free surface profiles so far in time. If we were able to advance the solutions much further in time, we might discover that some of the 'stable' solutions presented in this chapter do in fact later develop instabilities. A more rigorous analysis based on solving the eigenvalue problem would be required to absolutely determine stability.

It may be possible to remove (or reduce) the numerical oscillations visible on the free surface in some of the solutions by introducing some form of artificial damping; an absorbing beach. The principle here is that a damping layer is introduced in order to dissipate the wave energy, and thus damp any outgoing waves, before an open (artificial) boundary is reached. This method has been used for example by Cao, Beck and Schultz [24] and Părău, Vanden-Broeck and Cooker [99]. There is no internal friction in an ideal fluid so one can only absorb energy through the boundary of the fluid domain. Therefore, damping terms must be added to the free surface dynamic and/or kinematic boundary conditions. We could thus rewrite the dynamic boundary condition as

$$\frac{D\phi}{Dt} = \frac{1}{2}(\phi_x^2 + \phi_y^2) - \frac{Y}{F^2} + \frac{\tau\kappa}{F^2} + D, \tag{7.5.1}$$

where D is some additional term which vanishes outside of the absorbing layer. Cao *et al.* [24] describe how this additional term can be just an additional pressure acting on the free surface, and the energy transmission is then due to the work done by the fluid against this pressure. Cao *et al.* [24] took

$$D = \nu\phi_n \tag{7.5.2}$$

where $\nu = \nu(x)$, so that the beach always absorbs energy. Other authors, such as Cointe, Geyer, King, Molin and Tramoni [31] have used $D = \nu\phi$, but have then noted that if the damping is too strong the rate of energy absorption becomes negative, so some of the energy may be reflected back into the damping zone. Using (7.5.2) this problem should be avoided (see Cao *et al.* [24] for further details). The choice of $\nu(x)$ is still important however in determining the performance of the beach. Cao *et al.* showed that ν may be chosen to be

$$\nu(j) = \nu_0 \left(\frac{x(j) - x(\frac{N-1}{4})}{(N-1)e - x(\frac{N-1}{4})} \right)^2 \tag{7.5.3}$$

where the beach lies in the first quarter of the domain. Here, $x((N-1)/4)$ refers to the

mesh point at which the beach turns off. Outside of this damping zone, one would set $\nu(j) = 0$. Similarly, the beach may lie in the last quarter of the domain, so in the region $x \to \infty$ downstream. The constant ν_0 effects the strength of the beach.

Applying the beach to the flow in the steady case, as discussed in chapter 4, may have helped to reduce the numerical oscillations on the free surface. Then, ensuring that the beach moves with time so that it always remained next to the artificial boundary, it could be applied to the time dependent scheme discussed in this chapter. This would hopefully reduce the numerical oscillations on some of the unsteady solutions, and may even allow one to compute the free surface further in time, within the current computational limitations.

CHAPTER EIGHT

CONCLUSIONS AND FUTURE WORK

8.1 Conclusions

The free surface of an inviscid, incompressible fluid flowing along a channel of finite depth, past one or multiple disturbances in the form of localised pressure distributions or submerged obstructions on the bottom of the channel, has been studied. The effects of capillarity have been considered throughout this work, and the gravity-capillary solutions obtained have been contrasted with the known pure gravity solutions. In some cases (for example the two-layer flows over multiple obstructions) no known pure gravity solutions are available and so we have computed the simpler pure gravity solutions in such cases first, before adding capillarity to the problem.

A fully numerical method was used to solve the problem. It consisted of mapping the flow into a complex plane, and then applying Cauchy's integral equation formula to an analytic complex function around a contour enclosing the complex flow domain. This resulted in an integro-differential equation, which we solve at equally spaced mesh points on the free surface. This system of nonlinear equations, together with the dynamic boundary condition and any specific equations required for the particular flow configuration, were solved iteratively using a modified Newton's method.

However, when the forcing was in the form of an arbitrarily shaped submerged obstruction on the bottom of the channel, the free surface was first parametrised in order to avoid the need for a complex conformal map to remove any singularities. The channel bottom was then also discretised (along with the free surface), so that an additional integro-differential equation, to be solved at each mesh point on the channel bottom, was obtained. Again, the resulting system of nonlinear equations was solved using a modified Newton's method.

Forced, gravity-capillary solutions on a channel subjected to two localised pressure

distributions are new, and were found for the subcritical case, $F < 1$, with strong surface tension, $\tau > \frac{1}{3}$, in chapter 3. Multiple families of solution were found to exist for particular values of the Froude number, with solutions bifurcating from either the uniform stream or a pure solitary wave. Both non-symmetrical and symmetrical solutions about the centre of the fluid domain, $x = 0$, were obtained. The solutions were compared with the gravity-capillary waves considered by Maleewong *et al.* [77], where the forcing took the form of a single applied pressure distribution, and with the pure gravity waves considered by Binder *et al.* [18], where the forcing took the form of two submerged obstructions.

In chapter 4, gravity-capillary critical flow solutions, where the upstream flow is subcritical and downstream flow is supercritical, were found. Unlike in the pure gravity case, it was shown that multiple families of solution exist for particular values of the Froude number. The gradient of the hydraulic fall in such solutions was found to change with the surface tension τ. The case with weak surface tension, where the upstream Froude number is close to the minimum of the upstream dispersion curve $F_{up_{min}}$, was discussed, and new hydraulic falls with small decaying oscillations in front of the obstacle were found in the neighbourhood of $F_{up_{min}}$.

A new type of generalised hydraulic fall was discussed in the gravity-capillary case, where the wavetrain is found downstream of the fall rather than upstream as in the known pure gravity generalised hydraulic falls. Although the appearance of the downstream wave train is supported by the linear theory, it was shown that, as in the case of the pure gravity generalised hydraulic falls, such solutions violate the radiation condition and so lack physical relevance.

Gravity-capillary solutions with a train of trapped waves between two submerged obstructions are new. It was found that in contrast to the pure gravity case (see Dias and Vanden-Broeck [41]), unless the surface tension is very weak, the second obstruction should be placed downstream of the hydraulic fall in order to obtain trapped wave solutions. The solutions and the wavelength of the individual waves were confirmed by the linear theory. Placing the second obstacle downstream of the hydraulic fall in the pure gravity case, resulted in a solitary wave over the obstacle, with a uniform stream between the obstructions (Belward [11]). It was shown that the downstream gravity-capillary trapped wave solutions are not unique. Multiple families of solutions exist for particular values of the Froude number, where the trapped waves have different amplitudes and wavelengths dependent on the strength of the surface tension. It is not known if all the possible solutions were obtained in this case. The solution branch in the $\tau - F$ plane could have many more turning points for example, that were not found here due to computational limitations.

In chapter 5 the more complex flexural-gravity case was studied for the flow regime in

which a thin, massless sheet of ice, modelled as an elastic plate, was placed on top of the fluid. The flexural-rigidity of the ice was used alongside the Froude number to determine the nature of the solutions. Critical solutions were sought in a similar manner to the gravity-capillary critical flow solutions, and comparisons drawn between the findings for the different flow configurations. As in the gravity-capillary case of flow past a single submerged obstruction, multiple families of solutions were seen to exist for the flexural-gravity hydraulic falls. Similarly, multiple families of solution were found in the flexural-gravity case of flow over two submerged obstructions, where trapped waves appeared between the obstacles. The physical depths at which such solutions may realistically exist was discussed in relation to existing experimental work. Furthermore, the strain on the ice was computed for the solutions presented and whether the ice would break was discussed.

We then extended our numerical scheme to investigate critical flow solutions in a two-layer fluid under the rigid lid approximation. Extensive work has already considered the case of pure gravity hydraulic falls over a single obstruction. However, in chapter 6 we extended the work on these known solutions, by utilising a second obstruction to consider trapped wave solutions in this two-layer flow regime. We were able to show that the solutions in this case are richer than the counterpart solutions in the single fluid flow regime. Dependent on the parameters of the flow configuration, the pure gravity trapped waves here may exist either up or downstream.

The gravity-capillary hydraulic falls presented in chapter 6 are new. As in the single-layer case, we showed that the gravity-capillary solutions appear to be richer than those in a pure gravity flow regime. For example, solutions with a small train of waves immediately before the change in fluid depth were presented. Again, trapped wave solutions were obtainable by using a second submerged obstruction, and we presented evidence that these solutions are not unique.

Finally, in chapter 7 we considered the stability of the critical flow solutions presented in chapter 4. The stability of the pure gravity hydraulic fall had previously been considered by evolving a solution in time, in a weakly nonlinear regime. We extended this work and considered the time evolution of a pure gravity solution in the fully nonlinear regime, and showed that our results agreed with those using the weakly nonlinear theory. We extended this work further by considering the stability of the trapped wave solutions over two submerged obstructions. We showed that such solutions appear to be stable.

The work on the stability of the gravity-capillary hydraulic falls is new. We concluded that the gravity-capillary hydraulic fall is stable, but the solutions with trapped waves between two submerged obstructions in this regime, are unstable.

In the next section, we present possible avenues of future research stemming from this work. In particular, possible future work on two layer flows without the rigid lid

approximation, and flow over a step, is examined in more detail.

8.2 Future Work

There are many avenues of possible future work stemming from the work presented in this thesis. For example, we assessed the stability of the gravity-capillary flows in a single fluid, but the stability of the flexural-gravity flows presented in chapter 5 has yet to be researched. Similarly, the stability of the hydraulic fall solutions in the two-layer rigid lid approximation, in both the pure gravity and the gravity-capillary cases, is also of interest. The work on the time dependent critical flows could then be extended further by considering what happens in the case of two submerged obstructions, when the two obstacles move at different speeds. This may provide a much richer set of flows.

Guayjarernpanishk and Asavanant [66] and Binder, Dias and Vanden-Broeck [17] obtained pure gravity critical hydraulic falls over negative obstructions, and showed that an elevation wave appears over the disturbance before the depth of the fluid decreases. In figure 8.1 we show a typical free surface profile in such circumstances, alongside a solution profile in which we have included another obstacle further upstream. The free surface profiles were computed using the numerical scheme described in chapter 4. Three elevation waves of different amplitudes can be seen on the free surface between the two submerged obstructions in figure 8.1(c). In chapter 4 we showed that in the case with positively orientated obstructions, trapped waves were obtained on the free surface, but there were no additional waves directly over the obstructions. Here however, the first and the third elevation waves occur directly over the obstructions. It is thought that the second wave would form part of a train of trapped waves if the distance between the two submerged obstructions was greater. This case with negatively orientated disturbances may therefore require further work, to see if the change in polarity of the obstruction makes any further changes to the character of the flow when multiple obstructions lie on the bottom of the channel. Furthermore, we have not investigated the case of a gravity-capillary critical flow over a negatively orientated obstruction. It is thought that the nature of the flow directly over the obstruction may also change. The effect of such a change on the solutions with a small elevation or a small train of decaying waves immediately before the fall is then also of interest.

In the case of two layer flows we have only considered flows in which $\gamma = 1$, i.e. where the flows upstream in the upper and lower layers have the same velocity. It would be of much interest to be able to investigate hydraulic fall solutions where the flows were not equal upstream. In theory, this could be achieved using the scheme outlined in chapter 6, but of course, the different flow velocities would create a velocity shear between the two layers, and thus, a greater potential for the Kelvin-Helmholtz instability.

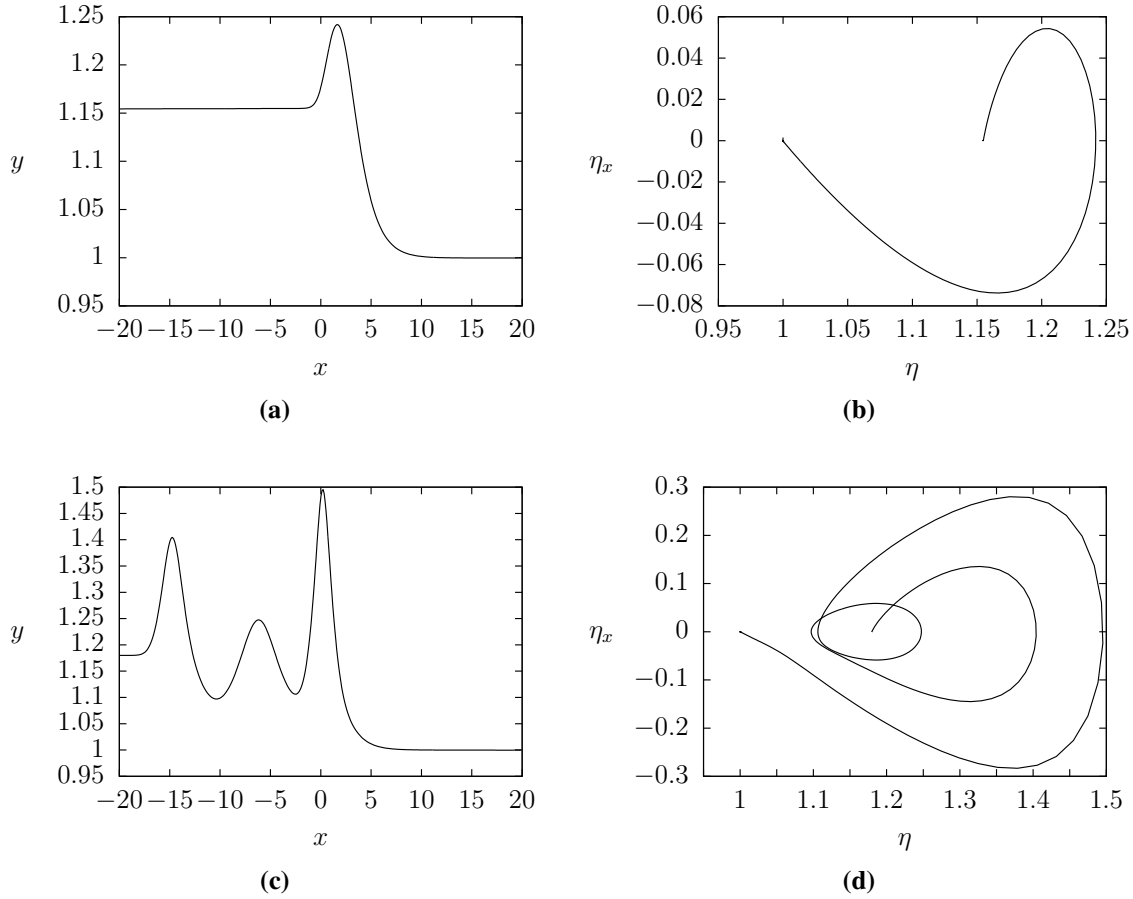

Figure 8.1: (a) Free surface profile over a negatively orientated obstruction characterised by $A_2 = -0.02$, $L_2 = 1$. The Froude number $F = 1.11$ is found as part of the solution. (c) Free surface profile over two negatively orientated obstructions characterised by $A_i = -0.05$, $L_i = 3.2$ for $i = 1, 2$. The obstructions are centred at $x = 0$ and $x = -15$, and the Froude number $F = 1.13$ is found as part of the solution. The phase portraits of the solutions in (a) and (c) are shown in (b) and (d) respectively.

Dias and Vanden-Broeck [42] showed that the critical depth ratio plays an important role in the formation of hydraulic falls in the rigid-lid approximation. More hydraulic fall solutions are found near the critical depth ratio, and Dias and Vanden-Broeck have shown that there exists a critical value of the Froude number, F_{max}, determining the maximum Froude number of hydraulic falls. The effect of this critical depth ratio on the gravity-capillary hydraulic falls is therefore of interest. Following the work of Dias and Vanden-Broeck, it is thought that one should be able to determine all the currently obtained gravity-capillary hydraulic falls in this critical region. However, we would also expect the solutions here to be richer than the solutions we have presented in chapter 6, as shown by Dias and Vanden-Broeck in the pure gravity case. Whenever the Froude number intersects the linear dispersion relation in these new critical regime solutions, we would expect that by including an additional obstruction in the corresponding flow

regime, a train of trapped waves may be found on the interface. Investigating gravity-capillary critical flows within the critical depth regime is therefore a possible avenue of future research, as we would expect to be able to find many rich solutions.

8.2.1 Two layer flow with an unbounded upper free surface

In chapter 2, we discussed the existing literature concerning the problem of a steady two-layer irrotational flow with a free upper boundary. The fluids were assumed to be ideal, with constant densities, lying one on top of the other. We discussed the pure gravity critical flow solutions that have previously been computed in this flow regime, for example, by Forbes [53]. Furthermore, we discussed some of the gravity-capillary solitary type wave results that have been computed, see for example Woolfenden and Părău [130]. However, none of the research so far considers pure gravity critical flows over multiple obstructions, or gravity-capillary critical flow solutions over one or more submerged obstructions. This is the obvious next steps to the research we have presented here.

As explained in chapter 2, the range of solutions possible in this flow regime should be much richer than those in the rigid lid approximation presented in chapter 6. Due to the existence of two free surfaces; the upper fluid boundary and the interface between the two fluids, there exist two modes which are governed by distinct linear dispersion relations. Therefore, for each critical flow solution, there are four different dispersion relations to examine; the upstream and downstream internal mode and the upstream and downstream external mode. Furthermore, when considering the gravity-capillary solutions, the surface tension can be placed on either the interface, the upper free surface, or on both free surfaces.

The problem is formulated in the same manner as in the rigid lid approximation, but instead of having a rigid lid at $y^* = h_1 + h_2$, we now have the second free surface $y^* = h_1 + h_2 + \eta_2^*(x^*)$. In figure 8.2 we give a sketch of the flow configuration. One must then solve the Laplace equations (6.2.1) and (6.2.2), the kinematic boundary conditions (6.2.9)-(6.2.11) on the interface and channel bottom respectively, and the dynamic boundary condition on the interface (6.2.13), from the rigid lid formulation in chapter 6. There are then two additional equations relating to the upper free surface; a kinematic and a dynamic boundary condition. The kinematic boundary condition on the upper free surface $y^*(x^*) = y_2^* = h_1 + h_2 + \eta_2^*(x^*)$ is given by

$$\phi_{2y^*}^* = \phi_{2x^*}^* \eta_{2x^*}^*, \tag{8.2.1}$$

and the dynamic boundary condition is found by applying Bernoulli's equation to the upper layer. As the flow is assumed to be steady and irrotational, the steady Bernoulli

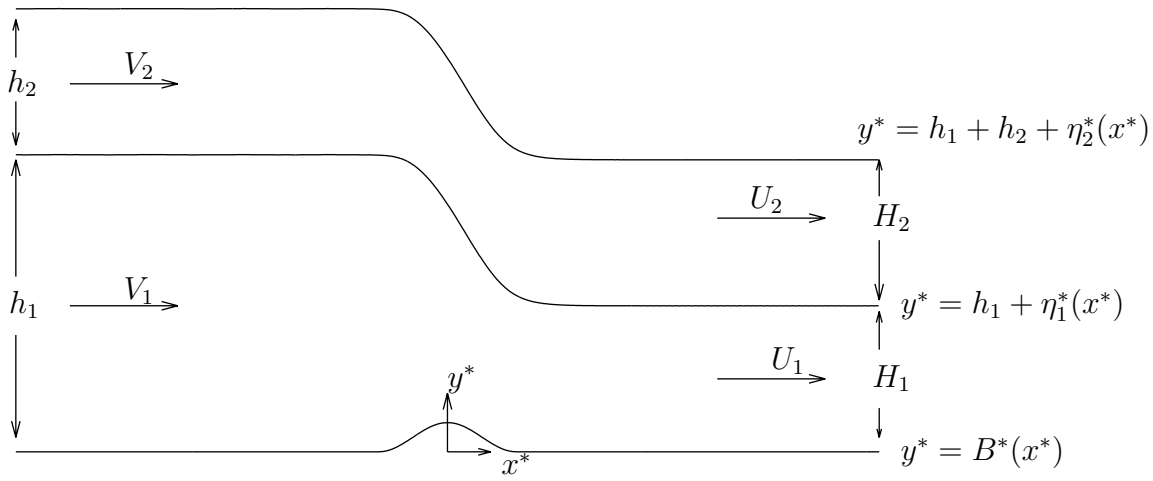

Figure 8.2: Dimensional two layer critical flow configuration with an upper free surface.

equation is satisfied everywhere in the upper fluid,

$$\frac{1}{2}\rho_2(u_2^{*2} + v_2^{*2}) + p^* + \rho_2 g y_2^* = \mathcal{B}, \tag{8.2.2}$$

where $\mathcal{B}$ is the Bernoulli constant obtained by examining the flow far upstream. As $x^* \to -\infty$ we know that $u_2^* \to V_2$, $v_2^* \to 0$, $y_2^* \to h_1 + h_2$, and $p^* \to P_\infty$. We therefore obtain

$$\mathcal{B} = \frac{1}{2}\rho_2 V_2^2 + P_\infty + \rho_2 g(h_1 + h_2), \tag{8.2.3}$$

and so (8.2.2) becomes

$$\frac{1}{2}\rho_2(\phi_{2x^*}^{*2} + \phi_{2y^*}^{*2}) + P_2 + \rho_2 g y_2^* = \frac{1}{2}\rho_2 V_2^2 + P_\infty + \rho_2 g(h_1 + h_2), \tag{8.2.4}$$

$$\Rightarrow \quad \frac{1}{2}(\phi_{2x^*}^{*2} + \phi_{2y^*}^{*2} - V_2^2) + \frac{1}{\rho_2}(P_2 - P_\infty) + g(y_2^* - h_1 - h_2) = 0, \tag{8.2.5}$$

where P_2 is the pressure in the upper fluid.

The problem is non-dimensionalised in the same manner as the rigid lid case; i.e. by taking V_1 as unit velocity and h_1 as unit length. It is now to be understood that non-starred variables are dimensionless. We introduce the upstream interfacial and upper free surface Bond numbers τ_I and τ_F, which we define by

$$\tau_I = \frac{\sigma_I}{\rho_1 g h_1^2}, \tag{8.2.6}$$

$$\tau_F = \frac{\sigma_F}{\rho_2 g h_2^2}, \tag{8.2.7}$$

respectively, so that downstream we obtain

$$\tau_{I_{down}} = \frac{\sigma_I}{\rho_1 g H_1^2} = \frac{\sigma_I}{\rho_1 g h_1^2}\frac{h_1^2}{H_1^2} = \tau_I \gamma_1^2, \tag{8.2.8}$$

$$\tau_{F_{down}} = \frac{\sigma_F}{\rho_2 g H_2^2} = \frac{\sigma_F}{\rho_2 g h_2^2}\frac{h_2^2}{H_2^2} = \tau_F \gamma_2^2, \tag{8.2.9}$$

where σ_I and σ_F are the coefficients of surface tension on the interface and upper free surface respectively. The problem therefore becomes that of satisfying

$$\phi_{1xx} + \phi_{1yy} = 0, \tag{8.2.10}$$

$$\phi_{2xx} + \phi_{2yy} = 0, \tag{8.2.11}$$

in the lower and upper fluids respectively,

$$\phi_{1y} - \phi_{1x} B_x = 0 \qquad \text{on} \quad y = B(x), \tag{8.2.12}$$

$$\phi_{2y} - \phi_{2x}\eta_{2x} = 0 \qquad \text{on} \quad y = 1 + \gamma + \eta_2(x), \tag{8.2.13}$$

$$\phi_{1y} - \phi_{1x}\eta_{1x} = 0 \qquad \text{on} \quad y = 1 + \eta_1(x), \tag{8.2.14}$$

$$\phi_{2y} - \phi_{2x}\eta_{1x} = 0 \qquad \text{on} \quad y = 1 + \eta_1(x), \tag{8.2.15}$$

and the two dynamic boundary conditions

$$\frac{1}{2}\left((\phi_{1x}^2 + \phi_{1y}^2) - R(\phi_{2x}^2 + \phi_{2y}^2) - (1 - R\gamma^2)\right) = \frac{\tau_I}{F_1^2}\kappa_1 + \frac{1}{F_1^2}(1 - R)(1 - y_1), \tag{8.2.16}$$

$$\frac{1}{2}(\phi_{2x}^2 + \phi_{2y}^2 - \gamma^2) + \frac{1}{F_1^2}y_2 = \tau_F\frac{D^2}{F_1^2}\kappa_2 + \frac{1}{F_1^2} + \frac{D}{F_1^2}, \tag{8.2.17}$$

on the interfacial and upper free surfaces respectively.

In the far field the flow is required to be uniform, so we impose the conditions (6.2.27) and (6.2.28) from the rigid lid approximation in chapter 6, alongside the additional constraints that

$$y_2(x) \to 1 + D \ \text{ as } \ x \to -\infty, \tag{8.2.18}$$

$$y_2(x) \to \frac{H_1}{h_1} + \frac{H_2}{h_1}\frac{h_2}{h_2} = \frac{1}{\gamma_1} + \frac{D}{\gamma_2} \ \text{ as } \ x \to \infty. \tag{8.2.19}$$

In the rigid lid approximation we obtained a further equation (6.2.30), relating the Froude number F_1 to the downstream flow velocities γ_1 and $\gamma\gamma_2$. This equation remains valid in this flow regime. However, following Forbes [53] we obtain yet another additional equation in this case, by this time substituting the downstream far field conditions

into the dynamic condition (8.2.17) on the upper free surface. We find that

$$\frac{1}{2}(\gamma_2^2\gamma^2-\gamma^2)+\frac{1}{F_1^2}(\frac{1}{\gamma_1}+\frac{D}{\gamma_2})=\frac{1}{F_1^2}+\frac{D}{F_1^2}, \tag{8.2.20}$$

$$\Rightarrow \quad \frac{1}{2}F_1^2\gamma^2(\gamma_2^2-1)=-\frac{1}{\gamma_1}-\frac{D}{\gamma_2}+1+D, \tag{8.2.21}$$

$$\Rightarrow \quad F_1^2=\frac{2(1+D-\frac{1}{\gamma_1}-\frac{D}{\gamma_2})}{\gamma^2(\gamma_2^2-1)}. \tag{8.2.22}$$

The problem is thus defined by the system of equations (8.2.10)-(8.2.17) along with the far field conditions (6.2.28), (6.2.27), (8.2.18) and (8.2.19), and the two relations (6.2.30) and (8.2.22).

The numerical method is then very similar to that of the rigid lid approximation, but this time we must parametrise both the interface between the two fluids, and the upper free surface. So, we write $x = X_1(s_1)$ and $y = Y_1(s_1)$ on the interface, where s_1 is the arclength on the interface, and $x = X_2(s_2)$ and $y = Y_2(s_2)$ on the upper free surface, with arclength s_2. Therefore the parametric equations

$$\left(\frac{dX_1}{ds_1}\right)^2+\left(\frac{dY_1}{ds_1}\right)^2=1, \tag{8.2.23}$$

$$\left(\frac{dX_2}{ds_2}\right)^2+\left(\frac{dY_2}{ds_2}\right)^2=1, \tag{8.2.24}$$

on the interface and the upper free surface respectively, must be satisfied.

Next, the dynamic boundary conditions (8.2.16) and (8.2.17) on the interface and the upper free surface respectively, are parametrised using the horizontal and vertical velocity components on the interface and the upper free surface in the form

$$\frac{\partial\phi_1}{\partial y}=\frac{d\phi_1}{ds_1}\frac{dY_1}{ds_1} \text{ and } \frac{\partial\phi_2}{\partial y}=\frac{d\phi_2}{ds_2}\frac{dY_2}{ds_2}, \tag{8.2.25}$$

$$\frac{\partial\phi_1}{\partial x}=\frac{d\phi_1}{ds_1}\frac{dX_1}{ds_1} \text{ and } \frac{\partial\phi_2}{\partial x}=\frac{d\phi_2}{ds_2}\frac{dX_2}{ds_2}. \tag{8.2.26}$$

The parametrised dynamic condition on the interface is given by (6.3.2), with $\tau = \tau_I$ and $Y(s) = Y_1(s_1)$, where $\kappa = \kappa_1 = Y_{1s_1s_1}X_{1s_1} - X_{1s_1s_1}Y_{1s_1}$ is the parametrised curvature on the interface. On the upper free surface we obtain

$$\frac{1}{2}\phi_{2s_2}^2+\frac{1}{F_1^2}Y_2(s_2)=\tau_F\frac{D^2}{F_1^2}\kappa_2+\frac{1}{F_1^2}+\frac{D}{F_1^2}+\frac{1}{2}\gamma^2, \tag{8.2.27}$$

where $\kappa_2 = Y_{2s_2s_1}X_{2s_2} - X_{2s_2s_2}Y_{2s_2}$ is the parametrised curvature on the upper free surface.

We are now able to derive the integro-differential equations for this free boundary

two layer case. The equations for the lower fluid are those obtained in the single layer and rigid lid cases, given by (6.3.11) and (6.3.12) with $X = X_1$ and $Y = Y_1$. The third equation in the rigid lid approximation was obtained by reflecting the upper fluid in the horizontal rigid boundary. As we now have an upper unknown boundary we are unable to use this method in this case. We therefore follow the work of Forbes [53] and apply Cauchy's integral formula to the equation

$$\chi_2 = \frac{dw_2}{dz} - \gamma, \tag{8.2.28}$$

around a contour Γ_2 consisting of the interface, the upper free surface, and vertical lines at $x = \pm L$ in the limit as $L \to \infty$. Here, $dw_2/dz = \phi_{2x} - i\phi_{2y}$ is the complex velocity. Letting σ denote the value of the arclength at the varying point $z(\sigma) = X_i(\sigma_i) + Y_i(\sigma_i)$, for $i = 1, 2$, on the contour Γ_2 and letting s denote the evaluation point we obtain

$$\pi i(\chi_2(z(s)) = \int_{\Gamma_2} \frac{\chi_2(z(\sigma))}{z(\sigma) - z(s)} dz = \int_{\Gamma_2} \frac{u_2(\sigma_i) - iv_2(\sigma_i) - \gamma}{(X_i(\sigma_i) + iY_i(\sigma_i)) - (X(s) + iY(s))} dz, \tag{8.2.29}$$

where the subscript $i = 1$ if the varying point $z(\sigma)$ is on the interface, and $i = 2$ if it is on the upper free surface. Placing the evaluation point $s = s_2$ on the upper free surface this becomes

$$\begin{aligned} \pi i(\phi_{2x}(s_2) - \gamma - i\phi_{2y}(s_2)) &= \int_{\Gamma_2} \frac{(u_2(\sigma_i) - iv_2(\sigma_i) - \gamma)(X_i'(\sigma_i) + iY_i'(\sigma_i))}{X_i(\sigma_i) - X_2(s_2) + i(Y_i(\sigma_i) - Y_2(s_2))} d\sigma_i, \\ &= \int_{\Gamma_2} \frac{(u_2(\sigma_i) - iv_2(\sigma_i) - \gamma)(X_i'(\sigma_i) + iY_i'(\sigma_i))A_i(\sigma_i)}{(X_i(\sigma_i) - X_2(s_2))^2 + (Y_i(\sigma_i) - Y_2(s_2))^2} d\sigma_i, \end{aligned} \tag{8.2.30}$$

where $A_i(\sigma_i) = (X_i(\sigma_i) - X_2(s_2) - i(Y_i(\sigma_i) - Y_2(s_2)))$, and a prime is used to denote the derivative with respect to the appropriate arclength. Taking the imaginary part we obtain

$$\pi(\phi_{2x}(s_2) - \gamma) = \int_{\Gamma_2} \frac{(Y_i(\sigma_i) - Y_2(s_2))C_i(\sigma_i) + (X_i(\sigma_i) - X_2(s_2))D_i(\sigma_i)}{(X_i(\sigma_i) - X_2(s_2))^2 + (Y_i(\sigma_i) - Y_2(s_2))^2} d\sigma_i, \tag{8.2.31}$$

where

$$C_i(\sigma_i) = -(u_2(\sigma_i) - \gamma)X_i'(\sigma_i) - v_2(\sigma_i)Y_i'(\sigma_i), \tag{8.2.32}$$

$$D_i(\sigma_i) = -v_2(\sigma_i)X_i'(\sigma_i) + (u_2(\sigma_i) - \gamma)Y_i'(\sigma_i). \tag{8.2.33}$$

Then, using (8.2.25) and (8.2.26), we see that

$$C_i(\sigma_i) = -(\phi_2'(\sigma_i)X_i'(\sigma_i) - \gamma)X_i'(\sigma_i) - \phi_2'(\sigma_i)Y_i'(\sigma_i)Y_i'(\sigma_i) = -\phi_2'(\sigma_i) + \gamma X_i'(\sigma_i), \tag{8.2.34}$$

$$D_i(\sigma_i) = -\phi_2'(\sigma_i)Y_i'(\sigma_i)X_i'(\sigma_i) + (\phi_2'(\sigma_i)X_i'(\sigma_i) - \gamma)Y_i'(\sigma_i) = -\gamma Y_i'(\sigma_i). \tag{8.2.35}$$

Thus, (8.2.31) becomes

$$\begin{aligned}
&\pi(\phi_2'(s_2)X_2'(s_2) - \gamma) = \\
&-\int_{-\infty}^{\infty} \frac{(\phi_2'(\sigma_1) - \gamma X_1'(\sigma_1))(Y_1(\sigma_1) - Y_2(s_2)) + \gamma Y_1'(\sigma_1)(X_1(\sigma_1) - X_2(s_2))}{(X_1(\sigma_1) - X_2(s_2))^2 + (Y_1(\sigma_1) - Y_2(s_2))^2} d\sigma_1 \\
&+\int_{-\infty}^{\infty} \frac{(\phi_2'(\sigma_2) - \gamma X_2'(\sigma_2))(Y_2(\sigma_2) - Y_2(s_2)) + \gamma Y_2'(\sigma_2)(X_2(\sigma_2) - X_2(s_2))}{(X_2(\sigma_2) - X_2(s_2))^2 + (Y_2(\sigma_2) - Y_2(s_2))^2} d\sigma_2.
\end{aligned} \tag{8.2.36}$$

Similarly, if the evaluation point $s = s_1$ is placed on the interface, we obtain the second integral equation

$$\begin{aligned}
&\pi(\phi_2'(s_1)X_1'(s_1) - \gamma) = \\
&-\int_{-\infty}^{\infty} \frac{(\phi_2'(\sigma_1) - \gamma X_1'(\sigma_1))(Y_1(\sigma_1) - Y_1(s_1)) + \gamma Y_1'(\sigma_1)(X_1(\sigma_1) - X_1(s_1))}{(X_1(\sigma_1) - X_1(s_1))^2 + (Y_1(\sigma_1) - Y_1(s_1))^2} d\sigma_1 \\
&+\int_{-\infty}^{\infty} \frac{(\phi_2'(\sigma_2) - \gamma X_2'(\sigma_2))(Y_2(\sigma_2) - Y_1(s_1)) + \gamma Y_2'(\sigma_2)(X_2(\sigma_2) - X_1(s_1))}{(X_2(\sigma_2) - X_1(s_1))^2 + (Y_2(\sigma_2) - Y_1(s_1))^2} d\sigma_2.
\end{aligned} \tag{8.2.37}$$

There are thus four integro-differential equations in this two-layer case; (8.2.36) and (8.2.37) in the upper fluid, and (6.3.11) and (6.3.12) in the lower fluid. Truncation corrections to the integro-differential equations may be made by approximating the integrals numerically using the trapezoidal rule as in the previous chapters. Then, the integral equations, together with the parametrised dynamic boundary conditions on the interface (6.3.2) and the free surface (8.2.27), the two parametric conditions (8.2.24) and (8.2.23), and the relations (6.2.30) and (8.2.22), complete the reformulation of the problem. We then seek the unknown functions ϕ_{1s_1}, ϕ_{2s_1},ϕ_{2s_2}, u, X_1, X_2, Y_1 and Y_2.

The upper free surface, the interface, and the channel bottom are discretised using N mesh points on the upper free surface; s_{2i}, for $i = 1, ...N$, M mesh points on the interface; s_{1i}, for $i = 1, ...M$, and q mesh points on the channel bottom; x_i, for $i = 1, ..., q$. The respective constant mesh spacings are given by e_2, e_1 and h. We now employ notation similar to that used in the previous chapters, so that, for example, $X_1(i)$ represents the value of X_1 at the ith grid point on the interface.

There are thus $4M + 3N + q + 2$ unknowns; $\phi_{1s_1}(i), \phi_{2s_1}(i), Y_1(i)$ and $X_1(i)$ for

$i = 1, ..., M$, $\phi_{2s_2}(i), Y_2(i)$ and $X_2(i)$ for $i = 1, ..., N$, $u(i)$ for $i = 1, ..., q$, F_1 and D. Given an initial set of values for Y_1 and Y_2, we use the parametric equations (8.2.23) and (8.2.24) to obtain X_1' and X_2'. Integrating numerically we obtain X_1 and X_2 and thus, we reduce the number of unknowns by $N + M$. The Froude number F_1 is also obtainable from (8.2.22), and ϕ_{2s_2} is obtainable from the dynamic condition on the upper free surface (8.2.27). This leaves $3M + N + q + 1$ unknowns.

Due to the computational limitations we encountered in the rigid lid approximation, it would be useful to be able to reduce these unknowns further. So following the idea used, for example, by Belward and Forbes [13], we use the second integral equation on the upper free surface (8.2.37) to find ϕ_2 on the interface.

We rewrite the equation in the form

$$\phi_2'(s_1) = -\int_{-\infty}^{\infty} \frac{\phi_2'(\sigma_1)(Y_1(\sigma_1) - Y_1(s_1))}{\pi X_1'(s_1)((X_1(\sigma_1) - X_1(s_1))^2 + (Y_1(\sigma_1) - Y_1(s_1))^2)} d\sigma_1 + B(s_1), \tag{8.2.38}$$

where $B(s_1)$ is given by

$$\begin{aligned}\pi X_1'(s_1)B(s_1) = \gamma\pi \\ &- \int_{-\infty}^{\infty} \frac{-\gamma X_1'(\sigma_1)(Y_1(\sigma_1) - Y_1(s_1)) + \gamma Y_1'(\sigma_1)(X_1(\sigma_1) - X_1(s_1))}{(X_1(\sigma_1) - X_1(s_1))^2 + (Y_1(\sigma_1) - Y_1(s_1))^2} d\sigma_1 \\ &+ \int_{-\infty}^{\infty} \frac{(\phi_2'(\sigma_2) - \gamma X_2'(\sigma_2))(Y_2(\sigma_2) - Y_1(s_1)) + \gamma Y_2'(\sigma_2)(X_2(\sigma_2) - X_1(s_1))}{(X_2(\sigma_2) - X_1(s_1))^2 + (Y_2(\sigma_2) - Y_1(s_1))^2} d\sigma_2.\end{aligned} \tag{8.2.39}$$

The integral is evaluated at the midpoints with summation over the mesh points, so in matrix form, this becomes

$$\phi_{2m}'(s_{1i}) = \mathbf{M}\phi_2'(s_{1j}) + B_m(s_{1i}), \tag{8.2.40}$$

where the subscript m denotes the value of the variable at the midpoint, and the matrix $\mathbf{M}$ is given by

$$M_{ij} = \frac{(Y_1(j) - Y_{1m}(i))}{\pi X_{1m}'(i)((X_1(j) - X_{1m}(i))^2 + (Y_1(j) - Y_{1m}(i))^2)} e_1. \tag{8.2.41}$$

As $\phi_{2m}'(s_{1i})$ represents the values of ϕ_2' at the mesh midpoints on the interface, it forms a vector of size $1 \times (M - 1)$. On the other hand, $\phi_2'(s_{1j})$ forms a vector of size $1 \times M$. We need a square matrix in order to be able to find the values of ϕ_2 on the interface, so

we determine $\phi'_{2m}(s_1)$ as a function of $\phi_2(s_1)$, by writing

$$\phi'_{2m}(s_{1i}) = \mathbf{A}\phi'_2(s_{1j}). \tag{8.2.42}$$

Here, $\mathbf{A}$ is a matrix obtained by noting that

$$\phi'_{2m}(s_{1i}) = \frac{\phi'_2(s_{1i}) + \phi'_2(s_{1(i+1)})}{2} \quad \text{for } i = 1, ..., M-1, \tag{8.2.43}$$

$$\phi'_2(s_{1M}) = \frac{\phi'_{2m}(s_{1(M-1)}) + \phi'_{2m}(s_{1M})}{2}. \tag{8.2.44}$$

So, $\phi'_{2m}(s_{1M}) = 2\phi'_2(s_{1M}) - \phi'_{2m}(s_{1(M-1)}) = \frac{3}{2}\phi'_2(s_{1M}) - \frac{1}{2}\phi'_2(s_{1(M-1)})$. Therefore, the matrix $\mathbf{A}$ is given by

$$A_{ij} = \begin{cases} \frac{1}{2} & \text{if } j = i+1 \text{ and } j, i < m \\ \frac{1}{2} & \text{if } j = i \neq m \\ -\frac{1}{2} & \text{if } i = m \text{ and } j = m-1 \\ \frac{3}{2} & \text{if } j = i = m \\ 0 & \text{otherwise.} \end{cases} \tag{8.2.45}$$

The matrix form of the integral equation, (8.2.40), then becomes

$$\mathbf{A}\phi'_2(s_{1j}) = \mathbf{M}\phi'_2(s_{1j}) + B_m(s_{1i}), \tag{8.2.46}$$

$$\Rightarrow (\mathbf{A} - \mathbf{M})\phi'_2(s_{1j}) = B_m(s_{1i}). \tag{8.2.47}$$

The vector $B_m(s_1)$ is evaluated at the midpoints and is given by

$$\begin{aligned} B_m(s_{1i})X'_{1m}(i)\pi &= \gamma\pi \\ &- \sum_{j=1}^{M} \frac{b_{ij}(-\gamma X'_1(j)(Y_1(j) - Y_{1m}(i)) + \gamma Y'_1(j)(X_1(j) - X_{1m}(i)))}{(X_1(j) - X_{1m}(i))^2 + (Y_1(j) - Y_{1m}(i))^2} e_1 \\ &- \gamma X'_1(M)\left(\pm\frac{\pi}{2} - \arctan\left(\frac{(X_1(M) - X_{1m}(i))}{Y_1(M) - Y_{1m}(i)}\right)\right) \\ &+ \sum_{j=1}^{N} \frac{b_{ij}((\phi'_2(s_{2j}) - \gamma X'_2(j))(Y_2(j) - Y_{1m}(i)) + \gamma Y'_2(j)(X_2(j) - X_{1m}(i)))}{(X_2(j) - X_{1m}(i))^2 + (Y_2(j) - Y_{1m}(i))^2} e_2 \\ &- \frac{(\phi'_2(N) - \gamma X'_2(N))}{X'_2(N)}\left(\frac{\pi}{2} - \arctan\left(\frac{X_2(N) - X_{1m}(i)}{(Y_2(N) - Y_{1m}(i))}\right)\right), \end{aligned} \tag{8.2.48}$$

where we have truncated the integrals in the integro-differential equation and then approximated the integrals far downstream analytically. The coefficients b_{ij} are determined by evaluating the integrals using the trapezoidal rule. The values of $B_m(s_{1i})$ therefore

form a vector with dimension $1 \times (M-1)$. In order to multiply the vector of $B_m(s_{1i})$ values by the inverse of the matrix $(\mathbf{A}-\mathbf{M})$ we require $B_m(s_{1i})$ to have dimension $1 \times M$. Therefore, we obtain an additional equation for $B_m(s_{1M})$ by introducing the artificial points $X_{1m}(M)$, $X'_{1m}(M)$ and $Y_{1m}(M)$. We write

$$X_{1m}(M) = 2X_1(M) - X_{1m}(M-1) \tag{8.2.49}$$

$$= 2X_1(M) - \frac{1}{2}(X_1(M) + X_1(M-1)) \tag{8.2.50}$$

$$= \frac{3}{2}X_1(M) - \frac{1}{2}X_1(M-1) \tag{8.2.51}$$

Similarly,

$$X'_{1m}(M) = \frac{3}{2}X'_1(M) - \frac{1}{2}X'_1(M-1), \tag{8.2.52}$$

$$Y_{1m}(M) = \frac{3}{2}Y_1(M) - \frac{1}{2}Y_1(M-1), \tag{8.2.53}$$

and so (8.2.48) can be satisfied for $i = 1, ..., M$. Thus, (8.2.47) becomes

$$\phi'_2(j) = (\mathbf{A}-\mathbf{M})^{-1}B_m(j), \tag{8.2.54}$$

from which, we may obtain ϕ_{2s_2}.

We are now left with a system of $2M + N + q + 1$ equations for the unknowns $\phi_{1s_1}(i), Y_1(i)$ for $i = 1, ..., M$, $Y_2(i)$ for $i = 1, ..., N$, $u(i)$ for $i = 1, ..., q$, and D, which can be solved iteratively as in chapter 6 using a modified version of Newton's method. The computational efficiency in obtaining $\phi'_2(s_1)$ from the integro-differential equation however is questionable. In computing $\phi'_2(s_{1i})$ for each $i = 1, ..., M$, one must invert the $M \times M$ matrix $\mathbf{A}-\mathbf{M}$ for each unknown. This results in $2M+N+q+1$ inversions of an $M \times M$ matrix for every Newton iteration, and one inversion of the $(2M+N+q+1) \times (2M+N+q+1)$ Jacobian matrix at each iteration. Alternatively, finding $\phi'_2(s_{1i})$ as an unknown in the Newton iterations requires inverting the $(3M+N+q+1) \times (3M+N+q+1)$ Jacobian matrix at each iteration. We tried a similar technique in the rigid lid approximation, and obtained ϕ'_2 at the interface from the integral equation (6.3.9). This reduced the number of unknowns in chapter 6 to $2M+q+1$. However, we found that inverting an $M \times M$ matrix $2M+q+1$ times and a $(2M+q+1) \times (2M+q+1)$ Jacobian matrix was less cost effective than inverting the full $(3M+q+1) \times (3M+q+1)$ Jacobian matrix. So in order to gain anything from obtaining $\phi'_2(s_1)$ before the Newton iterations in this upper free boundary scheme, one would need to avoid computing the $M \times M$ matrix for every unknown. Instead, it can be computed once for each iteration, for say the first unknown, and then that same matrix used for the other unknowns on that iteration. The problem is then reduced to inverting an $M \times M$ and a $(2M+N+q+1) \times (2M+N+q+1)$

matrix for each iteration, rather than inverting the full $(3M + q + 1) \times (3M + q + 1)$ Jacobian matrix at each iteration.

By manipulating the far field conditions, this numerical scheme can be modified and tested by looking for the known solitary wave solutions and contrasting the results with the work of, for example, Woolfenden and Părău [130] in the case of a single disturbance in the channel. In the case of critical flow, if the surface tension coefficients are set equal to zero, the results obtained by Forbes [53] can be used to provide further tests for the method. The scheme may then be used to further our knowledge in the area of critical flow solutions over one or multiple submerged obstructions. Trapped wave solutions can be looked for in the same manner as in the rigid lid approximation, by considering where any of the Froude numbers associated with the problem, intersect the associated linear dispersion relation.

The use of a weakly nonlinear theory, as in the rigid lid approximation (see for example Dias and Vanden-Broeck [39] in the case of the pure gravity critical flows and chapter 6 in the case of gravity capillary critical flows), may help to determine the shapes of both the interface and the upper free surfaces in the four different cases outlined in chapter 6. This would then aid in the selection of appropriate initial sets of values for Y_1' and Y_2'.

8.2.2 Flow over a step

The steady problem associated with a free surface flow over a rectangular semi-infinite step on the bottom of the channel has also received much attention. As one might expect that a change in the height of the underlying topography will result in a change in the depth of the fluid flowing over the topography, considering the gravity-capillary free surface flow over a step may be an obvious next step in the study of gravity-capillary hydraulic falls.

King and Bloor [73] showed that the pure gravity solution obtained in such a flow configuration depends on whether the flow upstream is supercritical or subcritical. If the upstream flow is supercritical, the free surface level rises over the step. If on the other hand the upstream flow is subcritical, the free surface level decreases near the step, and a wavetrain forms on the downstream surface.

In chapter 2 we briefly discussed the six different families of solutions conjectured by Trinh and Chapman [118, 119] in region five of the (F, τ)- parameter space shown in figure 2.3. Here, both the Froude number and the Bond number are small. These solutions were conjectured in the regime of flow over a step where multiple singularities (i.e. the corners of the step) occur on the underlying geometry. These singularities lead to divergence of the asymptotic expansion.

Chapman and Vanden-Broeck [26] considered the exponential asymptotics for gravity waves over a step. They showed that the important singularity is then the one generated by

the top corner of the step. The resultant truncation of the diverging asymptotic expansion results in a small error, and causes the Stokes phenomenon to occur. When the asymptotic solutions crosses a Stokes line, exponentially small corrections switch on, resulting in exponentially small gravity waves on the solution.

Following the exponential asymptotic techniques used by Chapman and Vanden-Broeck [25] (for pure capillary waves) and Chapman and Vanden-Broeck [26] (for pure gravity waves), Trinh and Chapman considered the exponential asymptotics for gravity-capillary flows. In this case they showed that the multiple singularities on the step caused multiple Stokes lines. Furthermore, the point at which the gravity and capillary waves are of equal magnitude generates a Stokes line. Each singularity can cause the switching on of exponentially small gravity and capillary waves. These waves can then interact to cause further exponentially small waves due to the secondary switchings and potentially the crossing of Stokes lines.

The physical flow domain is shown in figure 8.3(a). Here, $\hat{s}$ defines the height of the step on the channel bottom, so that far upstream we have that $H = y(\infty) - \hat{s}$. After introducing the velocity potential ϕ, one must satisfy

$$\nabla^2\phi = 0 \quad \text{in the fluid,} \tag{8.2.55}$$

$$\frac{d\phi}{dn} = 0 \quad \text{on the boundaries,} \tag{8.2.56}$$

$$\frac{1}{2}\rho\left(\left(\frac{d\phi}{dx}\right)^2 + \left(\frac{d\phi}{dy}\right)^2\right) + p + \rho g y = B \quad \text{on the free surface,} \tag{8.2.57}$$

where, as usual, ρ and p define the density and pressure in the fluid respectively and B is the Bernoulli constant defined by considering the flow in the far field. Non-dimensionalising using the fluid depth upstream divided by π as unit length, and the fluid velocity upstream as unit velocity, (8.2.57) becomes

$$\frac{1}{2}F^2((\nabla\phi)^2 - 1) + y = 1 + \tau\kappa, \tag{8.2.58}$$

where πF^2 and $\pi\tau$ are the upstream dimensionless Froude and Bond numbers respectively.

The complex potential $w = \phi + i\psi$ is introduced, as in our previous work, where ψ is the stream function chosen so that $\psi = 0$ on the free surface and $\psi = -\pi$ on the channel bottom. One can then map the physical Cartesian plane to the complex potential plane, so that the fluid is defined in the strip $-\pi < \psi < 0$, $-\infty < \phi < \infty$, as shown in figure 8.3(b). The complex velocity

$$\frac{dw}{dz} = u - iv = qe^{-i\theta} \tag{8.2.59}$$

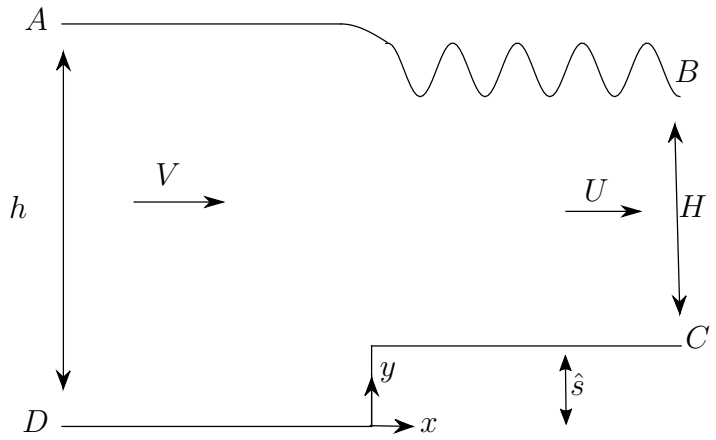

(a) Physical plane $z = x + iy$

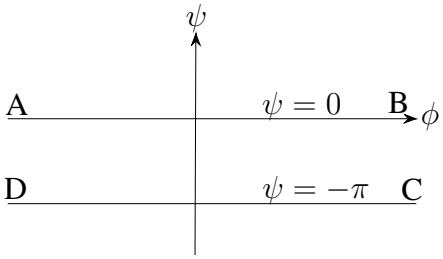

(b) Potential plane $w = \phi + i\psi$

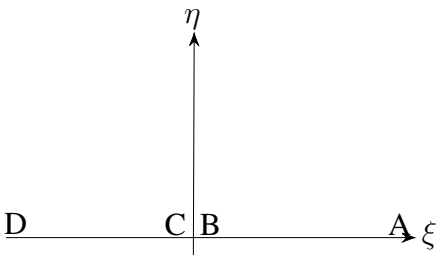

(c) Upper half plane $\zeta = \xi + i\eta$

Figure 8.3

is also introduced, where q is the flow speed and θ is the angle that the streamlines make with the x-axis. We also introduce the arclength s so that

$$\frac{dx}{ds} = \cos\theta, \qquad \frac{dy}{ds} = \sin\theta. \tag{8.2.60}$$

Following Trinh and Chapman [119], the complex potential plane is then mapped to the upper half ζ-plane, where $\zeta = \xi + i\eta$, as shown in figure 8.3(c). Then, differentiating the dynamic condition (8.2.58) on the free surface with respect to the arclength we obtain

$$F^2 q\frac{dq}{ds} + \sin\theta = \tau\frac{d\kappa}{ds}. \tag{8.2.61}$$

In chapter 4 we showed that κ can be written as

$$\kappa = Y''X' - X''Y', \tag{8.2.62}$$

where the prime denotes differentiation with respect to s. Therefore, we see that

$$\kappa' = Y'''X' - X'''Y'. \tag{8.2.63}$$

The dynamic condition (8.2.61) then becomes

$$F^2 q^2 \frac{dq}{d\phi} + \sin\theta = \tau \left(q \frac{dq}{d\phi}\frac{d\theta}{d\phi} + q^2 \frac{d^2\theta}{d\phi^2} \right), \tag{8.2.64}$$

where we have used

$$\frac{d}{ds} = \frac{d\phi}{ds}\frac{d}{d\phi} = q\frac{d}{d\phi}. \tag{8.2.65}$$

Now we apply Cauchy's integral formula to the function

$$f(\theta) = \log\left(\frac{dw}{dz}\right) = \log(qe^{-i\theta}), \tag{8.2.66}$$

around the contour defined by the ξ-axis and a semi-circle of radius R, as $R \to \infty$. Using the estimation lemma, the part of the integral along the semi-circular part of the contour can be shown to contribute nothing to the integral, and so we obtain

$$\pi i(\log q(\xi_0) - i\theta(\xi_0)) = \int_{-\infty}^{\infty} \frac{\log q(\xi) - i\theta(\xi)}{\xi - \xi_0} d\xi. \tag{8.2.67}$$

The integral in (8.2.67) is a Cauchy Principal Value. As in the previous chapters, the singularity here can be ignored by evaluating the integral at mesh midpoints on the contour, using the trapezoidal rule. Taking the imaginary part of (8.2.67) gives

$$\log q(\xi_0) = -\frac{1}{\pi}\int_{-\infty}^{\infty} \frac{\theta(\xi)}{\xi - \xi_0} d\xi. \tag{8.2.68}$$

This is now a real integral and so to analyse the problem using the known properties for complex functions, the real function is complexified by analytically continuing the function in the upper half ξ-plane. This leads to the generation of Stokes lines at the singularities in the problem. The integral equation (8.2.68) becomes

$$\log q - i\theta = -\frac{1}{\pi}\int_{-\infty}^{0} \frac{\theta(\xi)}{\xi - \zeta} d\xi - \frac{1}{\pi}\int_{0}^{\infty} \frac{\theta(\xi)}{\xi - \zeta} d\xi, \tag{8.2.69}$$

where ξ has been complexified and is thus now written as ζ. In a similar manner, we write the complexification of θ as w so that the dynamic boundary condition on the free

surface (8.2.64) becomes

$$F^2 q^2 \frac{dq}{dw} + \sin\theta = \tau \left(q \frac{dq}{dw} \frac{d\theta}{dw} + q^2 \frac{d^2\theta}{dw^2} \right). \tag{8.2.70}$$

The exponential asymptotics carried out by Trinh and Chapman [119] then go on to solve (8.2.69) and (8.2.70) for complex θ and q using the asymptotic expansions

$$\theta = \sum_{n=0}^{\infty} \epsilon^n \theta_n, \tag{8.2.71}$$

$$q = \sum_{n=0}^{\infty} \epsilon^n q_n, \tag{8.2.72}$$

where the Froude number squared and the Bond number are both of order ϵ^2, such that $F^2 = \beta\epsilon$ and $\tau = \beta B \epsilon^2$. These expansions are truncated optimally in order to see the switching on of exponentially small waves across the Stokes lines by smoothing the Stokes discontinuity. By analysing their results, this method allowed Trinh and Chapman to predict the existence of six different types of solution in the small Froude number, small Bond number limit.

It would be of interest to study this problem using fully numerical techniques, to see if any of the additional predicted solutions by Trinh and Chapman actually exist numerically. Specifically, to see if we could get different hydraulic fall solutions, i.e. with different waves on the free surface, to those that we presented in chapter 4. We follow the numerical scheme used by Chapman and Vanden-Broeck [26] for pure gravity waves. Therefore, we want to solve the integro-differential equation

$$\log q = \frac{1}{2} \log \left(\frac{\xi_0 + b}{\xi_0 + a} \right) - \frac{1}{\pi} \int_0^{\infty} \frac{\theta(\xi)}{\xi - \xi_0} d\xi, \tag{8.2.73}$$

where $-a$ and $-b$ define the images of the corners of the step in the ζ-plane, and the dynamic condition

$$\frac{1}{2} F^2 (q^2 - 1) + y = 1 + \tau\kappa, \tag{8.2.74}$$

for the unknowns θ and q. After truncating and discretising the domain, $\log q$ can be obtained at the mesh midpoints by integrating the integral in (8.2.73) using the trapezoidal rule with summation over the mesh points. Then, after some numerical manipulation and interpolation, (8.2.74) can be solved using Newton's method to find the values of θ at the mesh midpoints.

Using the full nonlinear boundary integral technique, one could investigate the different flows over a step, and look for further critical flow solutions.

References

[1] T.R. Akylas. On the excitation of long nonlinear water waves by a moving pressure distribution. *J. Fluid Mech.*, 141:455–466, 1984.

[2] T.R. Akylas. On the excitation of nonlinear water waves by a moving pressure distribution oscillating at resonant frequency. *Phys. Fluids*, 27(12):2803–2807, 1984.

[3] C.J. Amick, L.E. Fraenkel and J.F. Toland. On the Stokes conjecture for the wave of extreme form. *Acta Math.*, 148:193–214, 1982.

[4] C.J. Amick and R.E.L. Turner. A global theory of interal solitary waves in two-fluid systems. *Trans. Am. Math. Soc.*, 298:431–484, 1986.

[5] C.J. Amick and R.E.L. Turner. Small internal waves in two-fluid systems. *Archive for Rational Mechanics and Analysis*, 108:111–139, 1989.

[6] L. Armi. The hydraulics of two flowing layers with different densities. *J. Fluid Mech.*, 163:27–58, 1986.

[7] G.D. Ashton. *River and Lake Ice Engineering*. Water Resources Publications, 1986.

[8] P.G. Baines. A unified description of two-layer flow over topography. *J. Fluid Mech.*, 146:127–167, 1984.

[9] P.G. Baines. *Topographic Effects in Stratified Flows*. Cambridge Monographs on Mechanics. Cambridge University Press, 1997.

[10] A. Barker, G. Timco, H. Gravesen and P. Vølund. Ice loading on Danish wind turbines: Part 1: Dynamic model tests. *Cold Regions Science and Technology*, 41(1):1 – 23, 2005.

[11] S.R. Belward. Fully nonlinear flow over successive obstacles: hydraulic fall and supercritical flows. *ANZIAM J.*, 40:447–458, 1999.

[12] S.R. Belward and L.K. Forbes. Fully non-linear two-layer flow over arbitrary topography. *J. Engrg. Math.*, 27:419–432, 1993.

[13] S.R. Belward and L.K. Forbes. Interfacial waves and hydraulic falls: Some applications to atmospheric flows in the lee of mountains. *J. Engrg. Math.*, 29:161–179, 1995.

[14] K.Ee Bernard, R.H.J. Grimshaw, D.-H. Zhang and K.W. Chow. Steady transcritical flow over a hole: Parametric map of solutions of the forced Korteweg-de Vries equation. *Phys. Fluids*, 22(5):056602, 2010.

[15] D. Bernoulli and J. Bernoulli. *Hydrodynamics and Hydraulics*. Dover Publications Inc., 2009. Trans. by T. Carmody and H. Kobus, Preface by H. Rouse.

[16] B.J. Binder, F. Dias and J.-M. Vanden-Broeck. Steady free-surface flow past an uneven channel bottom. *Theor. Comput. Fluid Dynamics*, 20:125–144, 2006.

[17] B.J. Binder, F. Dias and J.-M. Vanden-Broeck. Influence of rapid changes in a channel bottom on free-surface flows. *IMA J. Appl. Math.*, 73(1):254–273, 2008.

[18] B.J. Binder, J.-M. Vanden-Broeck and F. Dias. Forced solitary waves and fronts past submerged obstacles. *Chaos*, 15(3):037106, 2005.

[19] M.G. Blyth and C. Pozrikidis. Buckling and collapse of heavy tubes resting on a horizontal or inclined plane. *Eur. J. Mech. - A/Solids*, 21(5):831 – 843, 2002.

[20] M.G. Blyth, E.I. Părău and J.-M. Vanden-Broeck. Hydroelastic waves on fluid sheets. *J. Fluid Mech.*, 689:541–551, 12 2011.

[21] M.J. Boussinesq. Theorie de l'intumescence liquid appellee onde solitaire ou de translation, se propageant dans un canal rectangulaire. *Comptes Rendus Acad. Sci.*, 72:755–759, 1871.

[22] P. Brocklehurst, A.A. Korobkin and E.I. Părău. Interaction of hydro-elastic waves with a vertical wall. *J. Engrg. Math.*, 68(3-4):215–231, 2010.

[23] D.C. Calvo and T.R. Akylas. Stability of steep gravity-capillary solitary waves in deep water. *J. Fluid Mech.*, 452:123–143, 2002.

[24] Y. Cao, R.F. Beck and W.W Schultz. An absorbing beach for numerical simulations of nonlinear waves in a wave tank. In *8th International Workshop on Water Waves and Floating Bodies*, pages 17–20. St. Johns, Canada, 1993.

[25] S.J. Chapman and J.-M. Vanden-Broeck. Exponential asymptotics and capillary waves. *SIAM J. Appl. Math.*, 62(6):1872–1898, 2002.

[26] S.J. Chapman and J.-M. Vanden-Broeck. Exponential asymptotics and gravity waves. *J. Fluid Mech.*, 567:299–326, 2006.

[27] F. Chardard, F. Dias, H. Nguyen and J.-M. Vanden-Broeck. Stability of some stationary solutions to the forced KdV equation with one or two bumps. *J. Engrg. Math.*, 70:175–189, 2011.

[28] Y. Cho and T. R. Akylas. Forced waves near resonance at a phase-speed minimum. *Stud. Appl. Math.*, 123(1):1–15, 2009.

[29] J.W. Choi, S.M. Sun and M.C. Shen. Steady capillary-gravity waves on the interface of a two-layer fluid over an obstruction-forced modified KdV equation. *J. Engrg. Math.*, 28:193–210, 1994.

[30] J.W. Choi, S.M. Sun and M.C. Shen. Internal capillary-gravity waves of a two-layer fluid with free surface over an obstruction-forced extended KdV equation. *Phys. Fluids*, 8(2):397–404, 1996.

[31] R. Cointe, P. Geyer, B. King, B. Molin and M. Tramoni. Nonlinear and linear motions of a rectangular barge in a perfect fluid. In *Eighteenth Symposium on Naval Hydrodynamics*, pages 85–100. The National Academies Press, Washington, DC, 1991.

[32] M.J. Cooker, D.H. Peregrine, C. Vidal and J.W. Dold. The interaction between a solitary wave and a submerged semicircular cylinder. *J. Fluid Mech.*, 215:1–22, 1990.

[33] G.D. Crapper. An exact solution for progressive capillary waves of arbitrary amplitude. *J. Fluid Mech.*, 2(06):532–540, 1957.

[34] P.G. de Gennes, F. Brochard-Wyart and D. Quere. *Capillarity and Wetting Phenomena: Drops, Bubbles, Pearls, Waves*. Springer Science & Business Media, 2004.

[35] F. Dias and A. Il'ichev. Interfacial waves with free-surface boundary conditions: an approach via a model equation. *Physica D*, 150:278–300, 2001.

[36] F. Dias and G. Iooss. Capillary-gravity solitary waves with damped oscillations. *Physica D*, 65(4):399 – 423, 1993.

[37] F. Dias and J.-M. Vanden-Broeck. Open channel flows with submerged obstructions. *J. Fluid Mech.*, 206:155–170, 1989.

[38] F. Dias and J.-M. Vanden-Broeck. Generalised critical free-surface flows. *J. Engrg. Math.*, 42:291–301, 2002.

[39] F. Dias and J.-M. Vanden-Broeck. Steady two-layer flows over an obstacle. *Philos. Trans. Roy. Soc. London Ser. A*, 360(1799):2137–2154, 2002.

[40] F. Dias and J.-M. Vanden-Broeck. On internal fronts. *J. Fluid Mech.*, 479:145–154, 2003.

[41] F. Dias and J.-M. Vanden-Broeck. Trapped waves between submerged obstacles. *J. Fluid Mech.*, 509:93–102, 2004.

[42] F. Dias and J.-M. Vanden-Broeck. Two-layer hydraulic falls over an obstacle. *Eur. J. Mech. B Fluids*, 23(6):879 – 898, 2004.

[43] J.W. Dold. An efficient surface-integral algorithm applied to unsteady gravity waves. *J. Comp. Phys.*, 103:90–115, 1992.

[44] J.W. Dold and D.H. Peregrine. An efficient boundary integral method for steep unsteady water waves. In K.W. Morton and M.J. Baines, editors, *Numerical Methods for Fluid Dynamics II*. Oxford University Press, 1986.

[45] A.S. Donahue and S.S.P. Shen. Stability of hydraulic fall and sub-critical cnoidal waves in water flows over a bump. *J. Engrg. Math.*, 68(2):197–205, 2010.

[46] V.W. Ekman. On dead water. Norwegian North Polar Expedition, 1893-1896: Scientific Results. Christiana, Ph.D. thesis, 1904.

[47] L. Euler. Principes généraux du mouvement des fluides. *Mémoires de l'Academie des Sciences de Berlin*, 11:274–315, 1757.

[48] D. Eyre. The flexural motions of a floating ice sheet induced by moving vehicles. *J. Glaciology*, 19(81):555–570, 1977.

[49] L.K. Forbes. Free-surface flow over a semicircular obstruction, including the influence of gravity and surface tension. *J. Fluid Mech.*, 127:283–297, 1983.

[50] L.K. Forbes. Surface waves of large amplitude beneath an elastic sheet. Part 1. High-order series solution. *J. Fluid Mech.*, 169:409–428, 1986.

[51] L.K. Forbes. Critical free-surface flow over a semi-circular obstruction. *J. Engrg. Math.*, 22:3–13, 1988.

[52] L.K. Forbes. Surface waves of large amplitude beneath an elastic sheet. Part 2. Galerkin solution. *J. Fluid Mech.*, 188:491–508, 3 1988.

[53] L.K. Forbes. Two-layer critical flow over a semi-circular obstruction. *J. Engrg. Math.*, 23:325–342, 1989.

[54] L.K. Forbes and L.W. Schwartz. Free-surface flow over a semicircular obstruction. *J. Fluid Mech.*, 114:299–314, 1982.

[55] Y. Fung. *Foundations of solid mechanics*. Prentice-Hall international series in dynamics. Prentice-Hall, 1965.

[56] C.S. Gardner, J.M. Greene, M.D. Kruskal and R.M. Miura. Method for solving the Korteweg-de Vries equation. *Phys. Rev. Lett.*, 19:1095–1097, 1967.

[57] D.J. Goodman. Critical stress intensity factor (KIc) measurements at high loading rates for polycrystalline ice. In P. Tryde, editor, *Physics and Mechanics of Ice*, International Union of Theoretical and Applied Mechanics, pages 129–146. Springer Berlin, 1980.

[58] D.J. Goodman, P. Wadhams and V.A. Squire. The flexural response of a tabular ice island to ocean swell. *Ann. Glaciol.*, 1:23–27, 1980.

[59] S. Grandison and J.-M. Vanden-Broeck. Truncation approximations for gravity-capillary free-surface flows. *J. Engrg. Math.*, 54:89–97, 2006.

[60] H. Gravesen, S.L. Sørensen, P. Vølund, A. Barker and G. Timco. Ice loading on Danish wind turbines: Part 2. Analyses of dynamic model test results. *Cold Regions Science and Technology*, 41(1):25 – 47, 2005.

[61] R. Grimshaw and M. Maleewong. Stability of steady gravity waves generated by a moving localised pressure disturbance in water of finite depth. *Phys. Fluids*, 25(7):076605, 2013.

[62] R. Grimshaw, M. Maleewong and J. Asavanant. Stability of gravity-capillary waves generated by a moving pressure disturbance in water of finite depth. *Phys. Fluids*, 21(8):082101, 2009.

[63] R. Grimshaw, B. Malomed and E. Benilov. Solitary waves with damped oscillatory tails: an analysis of the fifth-order Korteweg-de Vries equation. *Physica D*, 77(4):473 – 485, 1994.

[64] R.H.J. Grimshaw and D.I. Pullin. Extreme interfacial waves. *Phys. Fluids*, 29(9):2802–2807, 1986.

[65] R.H.J. Grimshaw and N. Smyth. Resonant flow of a stratified fluid over topography. *J. Fluid Mech.*, 169:429–464, 1986.

[66] P. Guayjarernpanishk and J. Asavanant. Free-surface flows over an obstacle: Problem revisited. In H.G. Bock, X.P. Hoang, R. Rannacher and J.P. Schlder, editors, *Modeling, Simulation and Optimization of Complex Processes*, pages 139–151. Springer Berlin, 2012.

[67] P. Guyenne and E.I. Părău. Computations of fully nonlinear hydroelastic solitary waves on deep water. *J. Fluid Mech.*, 713:307–329, 2012.

[68] P. Guyenne and E.I. Părău. Finite-depth effects on solitary waves in a floating ice sheet. *J. Fluids Struct.*, 49:242–262, 2014.

[69] J.K. Hunter and J. Scheurle. Existence of perturbed solitary wave solutions to a model equation for water waves. *Physica D*, 32:253–268, 1988.

[70] J.K. Hunter and J.-M. Vanden-Broeck. Solitary and periodic gravity-capillary waves of finite amplitude. *J. Fluid Mech.*, 134:205–219, 1983.

[71] T. Kakutani and N. Yamasaki. Solitary waves on a two-layer fluid. *J. Phys. Soc. Japan*, 45:674–679, August 1978.

[72] T. Kawahara. Nonlinear self-modulation of capillary-gravity waves on liquid layer. *J. Phys. Soc. Japan*, 38:265, 1975.

[73] A.C. King and M.I.G. Bloor. Free-surface flow over a step. *J. Fluid Mech.*, 182:193–208, 1987.

[74] D.J. Korteweg and G. de Vries. On the change of form of long waves advancing in a rectangular canal, and on a new type of long stationary waves. *Philos. Mag.*, 36:422–443, 1895.

[75] O. Laget and F. Dias. Numerical computation of capillary-gravity interfacial solitary waves. *J. Fluid Mech.*, 349:221–251, 1997.

[76] M.S. Longuet-Higgins and E.D. Cokelet. The deformation of steep surface waves on water. I. A numerical method of computation. *Proc. Roy. Soc. London. A.*, 350(1660):1–26, 1976.

[77] M. Maleewong, J. Asavanant and R. Grimshaw. Free surface flow under gravity and surface tension due to an applied pressure distribution: I Bond number greater than one-third. *Theor. Comput. Fluid Dynamics*, 19:237–252, 2005.

[78] M. Maleewong, R. Grimshaw and J. Asavanant. Free surface flow under gravity and surface tension due to an applied pressure distribution II Bond number less than one-third. *Eur. J. Mech. B Fluids*, 24(4):502 – 521, 2005.

[79] M.J. Mercier, R. Vasseur and T. Dauxois. Resurrecting dead-water phenomenon. *Nonlinear Process. Geophys.*, 18(2):193–208, 2011.

[80] H. Michallet and F. Dias. Numerical study of generalized interfacial solitary waves. *Phys. Fluids*, 11(6):1502–1511, 1999.

[81] P.A. Milewski and J.-M. Vanden-Broeck. Time dependent gravity-capillary flows past an obstacle. *Wave Motion*, 29(1):63 – 79, 1999.

[82] P.A. Milewski, J.-M. Vanden-Broeck and Z. Wang. Hydroelastic solitary waves in deep water. *J. Fluid Mech.*, 679:628–640, 2011.

[83] V.J. Monacella. *On Ignoring the Singularity in the Numerical Evaluation of Cauchy Principal Value Integrals*. Report. Washington DC Naval Ship Systems Command, 1967.

[84] J.N. Moni and A.C. King. Guided and unguided interfacial solitary waves. *Q. J. Mech. Appl. Math.*, 48(1):21–38, 1995.

[85] F. Nansen. *Farthest North*. Modern Library Exploration. Modern Library, 1999.

[86] C.L.M.H. Navier. Mémoire sur les lois du mouvement des fluides. *Mem. Acad. R. Sci. Paris*, 6:389–416, 1823.

[87] V.D. Naylor. The stream function and the velocity potential function. *The Mathematical Gazette*, 38:30–34, 1954.

[88] C. Page, S. Grandison and E.I. Părău. The influence of surface tension upon trapped waves and hydraulic falls. *Eur. J. Mech. - B/Fluids*, 43:191 – 201, 2014.

[89] C. Page and E.I. Părău. Hydraulic falls under a floating ice plate due to submerged obstructions. *J. Fluid Mech.*, 745:208–222, 2014.

[90] C. Page and E.I. Părău. Time dependent hydraulic falls and trapped waves over submerged obstructions. *Phys. Fluids*, 26(12):126604, 2014.

[91] C. Page, E.I. Părău and S. Grandison. Gravity-capillary water waves generated by multiple pressure distributions. *J. Nonlinear Science and Applications*, 6:137–144, 2013.

[92] A.S. Peters and J.J. Stoker. Solitary waves in liquids having non-constant density. *Commun. Pure Appl. Math.*, 13(1):115–164, 1960.

[93] P.I. Plotnikov and J.F. Toland. Modelling nonlinear hydroelastic waves. *Philos. Trans. Roy. Soc. London Ser. A*, 369(1947):2942–2956, 2011.

[94] C. Pozrikidis. Buckling and collapse of open and closed cylindrical shells. *J. Engrg. Math.*, 42(2):157–180, 2002.

[95] L.J. Pratt. On nonlinear flow with multiple obstructions. *J. Atmospheric Sci.*, 41(7):1214–1225, 1984.

[96] E. Părău and F. Dias. Ondes solitaires forces de capillarit-gravit. *Comptes Rendus de l'Acadmie des Sciences - Series I - Mathematics*, 331(8):655 – 660, 2000.

[97] E. Părău and F. Dias. Interfacial periodic waves of permanent form with free-surface boundary conditions. *J. Fluid Mech.*, 437:325–336, 2001.

[98] E.I. Părău and F. Dias. Nonlinear effects in the response of a floating ice plate to a moving load. *J. Fluid Mech.*, 460:281–305, 2002.

[99] E.I. Părău, J.-M. Vanden-Broeck and M.J. Cooker. Time evolution of three-dimensional nonlinear gravity-capillary free-surface flows. *J. Engrg. Math.*, 68(3-4):291–300, 2010.

[100] E.I. Părău and H.C. Woolfenden. Gap solitary waves in two-layer fluids. *IMA J. Appl. Math.*, 77:399–407, 2012.

[101] Lord Rayleigh. On waves. *Philos. Mag.*, 1:257–279, 1876.

[102] Lord Rayleigh. The form of standing waves on the surface of running water. *Proc. Lond. Math. Soc.*, 15:69–78, 1883.

[103] J.S. Russell. Report on waves. *Annual Report British Association for the Advancement of Science*, 14:311–390, 1845.

[104] H. Sha and J.-M. Vanden-Broeck. Two-layer flows past a semicircular obstruction. *Phys. Fluids A*, 5(11):2661–2668, 1993.

[105] S.P. Shen, M.C. Shen and S.M. Sun. A model equation for steady surface waves over a bump. *J. Engrg. Math.*, 23:315–323, 1989.

[106] S.S.P. Shen. Locally forced critical surface waves in channels of arbitrary cross section. *J. Applied Math. and Physics ZAMP*, 42:122–138, 1991.

[107] S.S.P Shen. Forced solitary waves and hydraulic falls in two-layer flows. *J. Fluid Mech.*, 234:583–612, 1992.

[108] S.S.P. Shen. On the accuracy of the stationary forced korteweg-de vries equation as a model equation for flows over a bump. *Q. Appl. Math.*, LIII:701–719, 1995.

[109] V.A. Squire. The breakup of shore fast sea ice. *Cold Regions Science and Technology*, 21(3):211 – 218, 1993.

[110] V.A. Squire. Past, present and impendent hydroelastic challenges in the polar and subpolar seas. *Philos. Trans. Roy. Soc. London Ser. A*, 369(1947):2813–2831, 2011.

[111] V.A. Squire, R.J. Hosking, A.D. Kerr and P.J. Langhorne. *Moving Loads on Ice Plates*. Solid Mechanics and its Applications. Springer, 1996.

[112] G.G. Stokes. On the theory of oscillatory waves. *Trans. Camb. Phil. Soc.*, 8(441):441–455, 1847.

[113] G.G. Stokes. *Mathematical and Physical Papers*, volume 1. Cambridge University Press, 1880.

[114] H. Sundqvist and G. Veronis. A simple finite-difference grid with non-constant intervals. *Tellus*, 22(1):26–31, 1970.

[115] T. Takizawa. Deflection of a floating sea ice sheet induced by a moving load. *Cold Regions Science and Technology*, 11(2):171 – 180, 1985.

[116] T. Takizawa. Response of a floating sea ice sheet to a steadily moving load. *J. Geophys. Res.*, 93(C5):5100–5112, 1988.

[117] J.F. Toland. On the existence of a wave of greatest height and Stokes's conjecture. *Proc. Roy. Soc. London. A.*, 363(1715):469–485, 1978.

[118] P. Trinh and S.J. Chapman. New theoretical gravity-capillary waves. part 1: Linear theory. *J. Fluid Mech.*, 724:367–391, 2013.

[119] P. Trinh and S.J. Chapman. New theoretical gravity-capillary waves. part 2: Nonlinear theory. *J. Fluid Mech.*, 724:392–424, 2013.

[120] R.E.L. Turner and J.-M. Vanden-Broeck. Broadening of interfacial solitary waves. *Phys. Fluids*, 31(9):2486–2490, 1988.

[121] A. Ugural. *Stresses in Plates and Shells*. McGraw Hill Book Company, New York, 1981.

[122] J.-M Vanden-Broeck. Free-surface flow over an obstruction in a channel. *Phys. Fluids*, 30(8):2315–2317, 1987.

[123] J.-M. Vanden-Broeck. Wilton ripples generated by a moving pressure distribution. *J. Fluid Mech.*, 451:193–201, 2002.

[124] J.-M. Vanden-Broeck. *Gravity-Capillary Free-Surface Flows*. Cambridge Monographs on Mechanics. Cambridge University Press, 2010.

[125] J.-M. Vanden-Broeck and E.I. Părău. Two-dimensional generalized solitary waves and periodic waves under an ice sheet. *Philos. Trans. Roy. Soc. London Ser. A*, 369(1947):2957–2972, 2011.

[126] E. Ventsel and T. Krauthammer. *Thin Plates and Shells: Theory, Analysis, and Applications*. CRC Press, 2001.

[127] P.-L. Viollet, J.-P. Chabard, P. Esposito and D. Laurence. *Mécanique des Fluides Appliquée.* Presses de l'Ecole Nationale des Ponts et Chaussées, 1998.

[128] G.B. Whitham. *Linear and Nonlinear Waves*. Wiley-Interscience, 1974.

[129] J.R. Wilton. On ripples. *Philos. Mag.*, 29(6):688–700, 1915.

[130] H.C. Woolfenden and E.I. Părău. Numerical computation of solitary waves in a two-layer fluid. *J. Fluid Mech.*, 688:528–550, 2011.

[131] X. Xia and H. T. Shen. Nonlinear interaction of ice cover with shallow water waves in channels. *J. Fluid Mech.*, 467:259–268, 2002.

[132] V.E. Zakharov. Stability of periodic waves of finite amplitude on the surface of a deep fluid. *J. Appl. Mech. Tech. Phys.*, 9:190–194, 1968.

[133] V.E. Zakharov and A.B. Shabat. Exact theory of two-dimensional self-focusing and one-dimensional self-modulation of waves in nonlinear media (Differential equation solution for plane self focusing and one dimensional self modulation of waves interacting in nonlinear media). *Sov. Phys.*, 34(3):62–69, 1972.